

A novel device for interrogation of neuron
connectivity in acute brain slices

A thesis presented in fulfilment of the requirements for
the degree of

Doctor of Philosophy

by

Douglas A. Young

Department of Physics
University of Strathclyde

2019

This thesis is the result of the author's original research. It has been composed by the author and has not been previously submitted for examination which has led to the award of a degree.

The copyright of this thesis belongs to the author under the terms of the United Kingdom Copyright Acts as qualified by the University of Strathclyde Regulation 3.50. Due acknowledgement must always be made of the use of any material contained in, or derived from, this thesis.

Signed:

Date:

Abstract

The complexity and scale of inter-neuron communication in the human brain presents an immense obstacle to understanding the mechanisms of information processing and how changes to neuronal connectivity are associated with pathological states. Neuron interactions underlie functional roles of local brain networks, for instance memory and cognitive abilities, which are often detrimentally impacted in cognitive states. Therefore, elucidating connectivity in the brain, between numerous subtypes of cell and in different functional regions, can provide a physiological model of appropriate neuronal behaviour. This could potentially be used to identify neuronal behaviours indicative of pathological states such as Alzheimer's disease.

Advancements in imaging technologies, such as calcium imaging and fMRI, have greatly enhanced studies of neuronal networks. However, the temporal and spatial resolution of these methods are limited in precisely determining activity observed across hundreds of neurons simultaneously. Similarly, patch clamping techniques have provided a wealth of knowledge in terms of ion channels and single-cell responses, yet are not currently operable across hundreds of neurons simultaneously.

Presented here is a novel microelectrode array (MEA) with high spatial resolution (60 μm electrode pitch) combined with a data acquisition setup capable of sampling electrical signals at a frequency of 20 kHz, enabling precise recording of neuronal activity in acute rat brain slices. Electrode tips were exposed at the tips of silicon needles designed to bypass cellular damage resulting from tissue preparation to record from viable neurons. The device demonstrated a signal-to-noise ratio of 10:1 in the presence of tissue and platinised electrode impedances of 200 k Ω , which are appropriate electrical characteristics with which to perform extracellular electrophysiological recordings. The device was integrated into a custom data acquisition system and, through a robust spike sorting process, successfully identified individual neurons. Neuronal signals were then assessed for temporal and amplitude features to discriminate subtypes of neurons to indicate functional roles within the network. This data was then used to develop several approaches to connectivity analysis afforded by the resolution of the device. Finally, the effectiveness of the needles in bypassing damaged tissue was evaluated histologically. These findings suggested that the preparation used here resulted in extensive cellular damage at the section surface. However, these results indicate potential for this approach to study of neuronal connectivity across hundreds of viable neurons.

Table of Contents

Abstract	3
List of Figures	6
List of Tables	8
List of Equations.....	9
List of Diagrams.....	9
List of Images	9
List of Abbreviations	9
1. Introduction	10
2. Literature Review	14
2.1 Electrophysiology.....	15
2.1.1 The Cell Membrane.....	16
2.1.2 The Resting Membrane Potential	18
2.1.3 Neuronal Currents Can be Described using Equivalent Circuit Model.....	20
2.1.4 Postsynaptic Potentials Can Summate	22
2.1.5 The Action Potential.....	25
2.1.6 Neurons communicate via Synapses: Neurotransmission	27
2.2 Microelectrode Arrays: Technological Developments.....	29
2.2.1 Intracellular Recording Methods	30
2.2.2 Extracellular Potential Recording Methods.....	32
2.2.3 MEAs: Materials and Technical Requirements	34
2.2.4 Neuroinflammation and Biocompatibility.....	36
2.3 Spike Sorting of Extracellular Waveforms.....	38
2.3.1 Principal Component Analysis	40
2.3.2 Connectivity.....	44
3. Electrical Characterisation of a Novel Microelectrode Array	47
3.1 Fabrication Summary of the 512-Needle Microelectrode Array.....	48
3.2 Investigations of Electrode Platinisation and Impedance Measurements	50
3.3 Platinization protocol.....	52
3.4 Data Acquisition System	53
3.4.1 Application-Specific Integrated Circuits of the Neuroboard	54
3.5 Platinised Electrodes have Appropriate Impedance to Detect Neuronal Activity	56
3.6 Readout Channels Not Capacitively Coupled.	59

Chapter 1

3.7	Biological and System Noise.....	60
3.8	Discussion: Electrical Characterisations.....	62
4.	Neuron Identification and Population Evaluation.....	64
4.1	Experimental Setup and Spike Sorting.....	65
4.1.1	Dissection Procedure.....	65
4.1.2	Recording Procedure.....	67
4.1.3	Spike Sorting and Neuron Identification.....	69
4.2	System Noise and Signal Evaluation and During Recordings.....	74
4.3	Neuron Activity is Limited to 2 Hours of Recording in this Preparation.....	77
4.3.1	Decrease in Neuronal Spike Frequency.....	78
4.3.2	Neuron Spike Amplitude Does Not Decrease.....	81
4.4	Discussion: Neuron Identification.....	84
5.	Neuronal Spike Features and Temporal Characteristics.....	87
5.1	Classification of Cell Types: Excitatory or Inhibitory.....	92
5.1.1	Analysis of Averaged Neuron Waveforms.....	95
5.1.2	Neuron Subtypes Discrimination via Waveform Analysis.....	97
5.2	Spike Train Temporal Properties Indicate a High Proportion of Bursting Neurons 106	
5.2.1	Inter-spike Interval Distributions.....	107
5.2.2	High Frequency Spike Rates Identify Distinct Activity in a Subset of Neurons 109	
5.2.3	Coefficient of Variation of Inter-Spike Intervals.....	111
5.3	Defined Periods of Bursting Behaviour.....	114
5.3.1	Mean Inter-spike Interval Method.....	115
5.3.2	MBISI analysis.....	117
5.4	Discussion: Spike Features and Temporal Characteristics.....	121
6.	Connectivity Analysis of Recorded Neurons.....	127
6.1.	Peristimulus Time Histograms.....	128
6.2.	EI mapping.....	133
6.2.1	Proximal Correlated Activity.....	134
6.2.2	Signal propagation.....	138
6.3	Discussion: Connectivity.....	140
7.	Histological Evaluation of Acute Slice Damage.....	142

Chapter 1

7.1 Summary of Experimental Procedures	144
7.2 Propidium Iodide Demonstrates Extensive Damage to Tissue Surfaces	146
7.2.1 Validation of Propidium Iodide Staining of Free-Floating Sections	147
7.2.2 Incubation in aCSF Demonstrated Limited Impact on Fluorescence Signal	149
7.2.3 Baseline Propidium Iodide Fluorescence Signal Determined by TritonX Incubation	151
7.3 Assessing the Impact of Microneedle Insertion.	152
7.4 Cross-section Imaging of Agar-embedded Tissues	154
7.5 Neuron Tracing with Dil Lipophilic Dye	157
7.6 Optical clearing.....	159
7.6.1 SeeDB Optical Clearing	161
7.6.2 ClearT2 Optical Clearing	165
7.7 Discussion: Histological Evaluation.....	168
8. Conclusions & Discussion.....	172
8.1 Discussion: Electrical Characterisations	173
8.2 Discussion: Neuron Identification.....	174
8.3 Discussion: Spike Features and Temporal Characteristics	175
8.4 Discussion: Connectivity Analysis of Recorded Neurons	177
8.5 Discussion: Histological Evaluation of Acute Slice Damage.....	178
8.6 Summary & Future Directions	182
Acknowledgments.....	184
Bibliography.....	185
Appendices	206

List of Figures

Figure 2. 1. Cellular membranes are composed of two symmetric layers of phospholipids.	17
Figure 2. 2. Ionic currents across a neuronal membrane can be represented as a resistor-capacitor electronics circuit.	21
Figure 2. 3. Temporal and spatial summation.....	23
Figure 2. 4. Schematic of a typical action potential.....	26
Figure 2. 5. Patch clamp techniques aim to detect current changes across the membrane in as small an area as possible.....	31
Figure 2. 6. Extracellular voltage potentials exhibit inversed phases of action potentials.....	33
Figure 2. 7. Initial stages of spike sorting	41
Figure 2. 8. Identifying, and applying, an appropriate amplitude threshold is a common second step for spike sorting.....	42

Figure 2. 9. PCA clustering of data was performed in 5 dimensions exhibiting the greatest variance across the data.....	43
Figure 2. 10. Three forms of connectivity can be used to describe neuron interactions within a network..	46
Figure 3. 1. Fabrication of the MEA.....	49
Figure 3. 2. The MEA was glued into a PCB board populated with the PlatChips and NeuroChips of the acquisition system.	53
Figure 3. 3. The 512 needle MEA is integrated on a PCB, with the acquisition system consisting of 16 ASICs.....	55
Figure 3. 4. Electrode impedance as a function of frequency.....	57
Figure 3. 5. Six electrodes were individually platinised in turn, and a current of 100nA, 150nA or 200nA was applied.....	58
Figure 3. 6. The capacitance between electrode readout channels	59
Figure 3. 7. The RMS noise input	61
Figure 3. 8. Histogram of electrode noise distribution excluding two disconnected, high noise, channels..	62
Figure 4. 1. Coronal sections were taken from rat brains allowing access to a large portion of cortex which could be easily arranged over electrodes.....	67
Figure 4. 2. Experimental layout for electrophysiological recordings.....	69
Figure 4. 3. Flow chart schematic of spike sorting.....	70
Figure 4. 4. The average spike waveform for each neuron in a spike sorting parameter dataset which identified 78 unique neurons.....	73
Figure 4. 5. RMS input noise of electrodes during first minute of recording from brain tissue.	75
Figure 4. 6. Average spike amplitudes per neuron.....	76
Figure 4. 7. The average spike amplitude per neuron divided by the RMS noise input value recorded on the associated electrode indicates the SNR of the system.	77
Figure 4. 8. Neuron spike rates.....	79
Figure 4. 9. Percentage of spikes elicited by neuronal units.....	80
Figure 4. 10. Average neuron spike amplitude.	81
Figure 4. 11. Comparing average neuron spike amplitudes between 0-2hrs and 2-4hrs.....	82
Figure 4. 12. Example of individual neuron spike amplitude analysis over time.....	83
Figure 5. 1. Example of an averaged neuron waveform.....	88
Figure 5. 2. Example of verification analysis of amplitude over time and spike rate.....	91
Figure 5. 3. The average spike waveform for each neuron.....	93
Figure 5. 4. Features used in waveform analysis.....	94
Figure 5. 5. Averaged neuron waveforms.....	96
Figure 5. 6. The average peak to trough ratio per neuron and average trough to peak time.....	98
Figure 5. 7. Temporal features of average waveforms.....	100
Figure 5. 8. The end slope of the waveform	101
Figure 5. 9. Histograms and k-means clustered scatterplots of average waveform end slopes.....	102
Figure 5. 10. Amplitude and temporal ratios.....	104
Figure 5. 11. Histograms and k-means clustered scatterplots of clustered width ratios compared to peak to trough ratios.....	105
Figure 5. 12. Counts of inter-spike interval values.	108
Figure 5. 13. Histograms of ISI values per neuron plotted on a logarithmic scale.....	109
Figure 5. 14. Percentage of ISI values under a given limit.	110
Figure 5. 15. The variation of counts of ISI values per neuron were evaluated.	111
Figure 5. 16. Coefficient of variation over the 2hour recording.....	112
Figure 5. 17. Coefficient of variation values, per neuron, calculated with ISIs above or below the median ISI value for each neuron.	113
Figure 5. 18. Comparison of CV values per neuron at relatively high and low frequencies.	114
Figure 5. 19. Example of the MISI method of burst detection.	116

Figure 5. 20. Evaluation of the MISI method of bursting activity detection.....	117
Figure 5. 21. MN burst analysis indicates the proximity of high frequency periods within a temporal sequence	119
Figure 5. 22. Frequency of burst count identifies discrete populations of bursts at varying limiting ISI values..	120
Figure 5. 23. Temporal qualities of neurons measured using the NBISI method.	121
Figure 6. 1. Excerpt of a raster plot of neurons #52 & 2 with corresponding PSTH plots calculated over the 2 hours of recording.	129
Figure 6. 2. Colourmap of the percentage spikes per neuron occurring within a given PSTH time window.	131
Figure 6. 3. Increasing spike count results in a trend of increasing numbers of neuron combinations	132
Figure 6. 4. Electrophysiological mapping of neuron locations across the MEA.	134
Figure 6. 5. The percentage of each neuron’s spikes included within the PSTH time window of each other neuron compared to the distance between seed electrodes.	135
Figure 6. 6. Example of a digraph plot utilised to demonstrate activity correlations across neuron positions on the MEA device.....	136
Figure 6. 7. Directed graph based on neuron locations.....	137
Figure 6. 8. Directed graph based on neuron locations	137
Figure 6. 9. Signal propagation across the MEA.....	139
Figure 6. 10. The average amplitude of every electrode at each spike time for an individual neuron can indicate the path of signal propagation.	140
Figure 7. 1. Free-floating sections were effectively stained by PI.	149
Figure 7. 2. Impact of aCSF incubation on PI fluorescence in free-floating tissue sections.....	150
Figure 7. 3. Comparison of TritonX-treated and aCSF-incubated slices.....	152
Figure 7. 4. Visualisation of silicon needle punctures in tissue sections.....	153
Figure 7. 5. Stitched images of PI-positive cells in a 50 µm thick cross section of brain tissue.	156
Figure 7. 6. Cross-sectioned tissues imaged following sample needle penetration..	157
Figure 7. 7. Staining of brain sections with cell tracer dye Dil.....	158
Figure 7. 8. Dil staining of brain tissue	159
Figure 7. 9. SeeDB optically cleared sections.....	162
Figure 7. 10. Particle analysis of SeeDB optically -cleared sections.....	163
Figure 7. 11. Analysis of SeeDB-cleared sections.....	164
Figure 7. 12. ClearT2 optically cleared sections..	166
Figure 7. 13. Analysis of ClearT2 optically cleared sections.....	167

List of Tables

Table 2. 1. The discrepancy of ionic concentrations between the cytoplasm and extracellular matrix creates a voltage potential.....	19
Table 2. 2. The chemical structures of neurotransmitters are diverse.	28
Table 3. 1. Summary of the electrical characteristics of the 512-needle MEA.....	63
Table 4. 1. Summary of numbers of neurons identified using different spike sorting parameters.....	72
Table 4. 2. Average neuron population properties and system noise.	84
Table 5. 1. Summary of neuron spiking features.....	126
Table 7. 1. Protocol summary for propidium Iodide staining of free-floating sections.....	148
Table 7. 2. Summary propidium Iodide staining protocol.....	151
Table 7. 3. SeeDB optical clearing protocol.	160

Table 7. 4. ClearT2 optical clearing protocol	160
---	-----

List of Equations

Equation 2. 1. The Nernst Equation..	19
Equation 2. 2. The Goldman-Hodgkin-Katz equation.	20
Equation 2. 3. The electrochemical driving force.....	21

List of Diagrams

Diagram 4. 1. Schematic of the positioning of slices on the MEA.	68
Diagram 7. 1. Secondary sectioning of agar-embedded sections.....	155

List of Images

Image 7. 1. Surplus silicon-based needles produced during trials of etching fabrication techniques.....	153
Image 7. 2. Optical clearing of brain tissue with the ClearT2 method.....	165

List of Abbreviations

AAD	<i>Acute Axonal Degeneration, 37</i>	<i>Inter-Spike Interval, 87</i>
aCSF	<i>Artificial Cerebro-Spinal Fluid, 63</i>	LFP
AP	<i>Action Potential, 15</i>	<i>Local Field Potential, 30</i>
ASIC	<i>Application-Specific Integrated Chip, 46</i>	MEA
ATP	<i>Adenosine Tri-Phosphate, 15</i>	<i>Micro Electrode Array, 10</i>
CMOS	<i>Complementary Metal-Oxide Semiconductor, 35</i>	PCA
CV	<i>Coefficient of Variation, 87</i>	<i>Principal Component Analysis, 39</i>
EAP	<i>Extracellular Action Potential, 32</i>	PFA
ECM	<i>Extra-Cellular Matrix, 16</i>	<i>Paraformaldehyde, 142</i>
EPSP	<i>Excitatory Postsynaptic Potential, 23</i>	PI
FF	<i>Free-Floating (sections), 140</i>	<i>Propidium Iodide, 140</i>
IPSP	<i>Inhibitory Postsynaptic Potential, 23</i>	PSTH
ISI		<i>Peri-Stimulus Time Histogram, 125</i>
		RC
		<i>Resistor-Capcitor, 20</i>
		RMP
		<i>Resting Membrane Potential, 17</i>
		RMS
		<i>Root Mean Square, 47</i>
		SD
		<i>Standard Deviation, 79</i>
		VGCC
		<i>Voltage-Gated Calcium Channel, 28</i>
		WD
		<i>Wallerian Degeneration, 37</i>

1. Introduction

The human brain processes information through complex mechanisms and understanding the relevance of neuronal interactions is critical to advancing contemporary neuroscience. Connectivity between neurons underlies cognitive functions such as learning and memory¹, therefore, it is important to elucidate these mechanisms to fully understand the impact of neurodegenerative diseases on neural network systems. Presented here is an approach to obtain and analyse high quality recordings of neuronal activity over multiple cells in acute rodent brain slices. These recordings were made using a novel microelectrode array (MEA) of 512 electrodes possessing high spatial resolution (60 μm), processed at 20 kHz, and exhibiting an appropriate signal-to-noise ratio (10:1) to record extracellular neuronal signals. A key novelty of the MEA design are the pyramidal silicon needles on top of which the exposed electrode tips are situated. The design goal is to penetrate beyond tissue damaged by the brain slice preparation procedure and record from healthy neural networks and obtain data representative of physiological connectivity. The aim of the project was to provide a validated experimental system capable of precisely resolving hundreds of neurons over an area of 1x2mm and analysing a high proportion of a local functional network in the cortex. Furthermore, the intact network architecture would reflect the physiological arrangement of neuronal networks.

Neural circuits of millions of densely packed cells exist throughout the brain, each eliciting electrical signals propagated to numerous target cells. This poses a daunting technical challenge, as the importance of subtle changes in electrophysiological currents is not fully understood, while the diversity of neuronal subtypes throughout the brain increases this complexity, for example, at least 16 neuron types have been identified in the human cortex² and recently 133 types have been defined in the mouse neocortex³. Current approaches to analysing connectivity via electrophysiological activity include EEG⁴ or fMRI⁵ imaging techniques. These techniques provide a holistic view of brain states and record from millions of cells simultaneously. These approaches can define functional areas but lack the resolution to determine the activity of individual neurons and their connections. Conversely, patch clamping techniques enable a highly detailed analyses of the ionic currents impacting individual cells⁶, yet they are invasive and limited to only being able to simultaneously record from a handful of cells while being technically challenging to perform.

Advances in photolithography techniques have enabled the generation of closely-packed electrodes capable of recording small amplitude electrophysiological signals propagated through the extracellular fluid surrounding neurons⁷. In parallel, computing advancements have facilitated the differentiating of these signals to identify and allocate these signals to individual neuronal units via the process of spike sorting⁸. These developments have progressed the application of MEAs in studies of neuronal connectivity, which possess the advantage of being able to continuously record electrophysiological activity from a large population of cells simultaneously over periods of days⁹. Additionally, MEA recordings afford greater temporal precision than imaging techniques, such as calcium imaging, and can spatially determine the source of individual signals due to the proximity of electrodes. The density of neurons requires high spatial resolution of electrodes to differentiate signals and determine correlated connectivity between cells. Yet many neurons exhibit such low frequency activity they are difficult to detect due to data processing parameters which require a large number of spikes to define the electrical activity of individual cells. These “dark neurons”¹⁰ are therefore an obstacle in defining local networks and their function within a broader system. To overcome this, electrodes are increasingly arranged in greater densities to improve the electrode : neuron ratio. Alternatively, cell numbers are decreased by culturing neurons on top of MEAs, however, this method does not maintain a physiological network architecture. Neural probes consisting of multiple recording sites have been developed which can be inserted *in vivo*, but to access deep brain structures such as the hippocampus, the invasive nature of this technique inherently damages cells and disrupts the network. Therefore, MEAs of 512 electrodes have been developed to record from acute brain slices, which allows for access to specific structures and maintains network architecture, by fabricating electrodes at the tips of silicon needles capable of penetrating beyond tissue damaged by the sectioning procedure¹¹.

The aims of this project consisted of characterising the electrical characteristics of the MEA and developing an experimental protocol to reliably record from hundreds of neurons in the rat cortex. After the data is analysed and determined as suitably high-quality, discriminatory features could then be applied to provide parameters of typical behaviour of neurons with the aim of differentiating neuronal subtypes. This approach has been applied successfully to visual cortex recordings in previous reports¹² and the applicability of these features to the data presented here was attempted. Finally, changes to neuron behaviour can be assessed

following a validated system change, for instance, stimulation of targeted cells through optogenetics or the application of a pharmacological agent.

This thesis describes the characterisation of a novel device designed to record from hundreds of neurons simultaneously and the methods through which the extracted electrophysiological information can be analysed to highlight properties of neurons. In many instances, the approaches outlined in this work have not previously been applied to recordings of acute brain slice preparations and, although based on previous studies, further analysis was required to overcome limitations in the data. It is hoped the analytical approaches to the data may provide insight for further investigations that incur similar obstructions.

Initially, the electrical properties of the device were characterised and found to exhibit excellent signal to noise ratio at levels appropriate to detect neuronal signals. These levels were achieved via the common method of platinisation of the electrodes to reduce their impedances. The acquisition system^{13,14} and fabrication of the device¹⁵ are also described. The setup and experimental recording procedures are described in chapter 4 which summarises the key population data: number of neurons identified, frequency of activity and the noise of the system. It also highlights a recurring difficulty in the dataset and justifies the use of parameters used to prioritise quality of the data over quantity. Neurons are a highly heterogeneous class of cell and differentiating their activities based on electrophysiological signals would be highly advantageous for neural network interrogation. Although narrow spikes have been associated with interneurons, there is currently no accepted approach¹⁶ to further identify subtle differences in waveform signature. Chapter 5 demonstrates several analyses of features of waveforms based on previous reports of their successful application in distinguishing neuron types. The temporal characteristics of neuron activity is addressed in chapter 6, where the variation exhibited by each neuron is evaluated. Periods of relative high activity, known as “bursting”, were assessed using two methods in this chapter, one of which was developed by the author. The device records over an area which potentially consists of hundreds of neurons. Therefore, direct connectivity was difficult to define, however, several approaches to neuron connectivity analysis are described in chapter 6 which were developed to identify highly correlated activity relative to the network. This method was adapted to account for spike count and the distance between neurons to generate directed graphs of neuron location and the likely direction of information

transmission between activity-correlated cells. The time lag of signal detection across electrodes was also used to highlight the initial segment of the axon output structure. Using an electrophysiological image consisting of waveforms temporally correlated to identified somatic spikes, and constructed based on neuron refractory periods, propagated signals from individual neurons were traced across multiple electrodes and detected at distances of up to 180 μm from the site of the identified cell body. This method therefore provides a means to validate models of effective connectivity between neurons. A critical novelty of the device is its structure, which is designed to enable electrode insertion into brain tissue. Therefore, chapter 7 assesses the appropriateness of this design and how effectively it can be combined with the experimental setup. Extensive tissue damage was observed via a combination of propidium iodide staining and optical clearing techniques which suggested the sectioning procedure potentially impacted the validity of recordings. Chapter 8 summarizes the key achievements and suggests future directions of investigations into neuron connectivity.

2. Literature Review

Signal transduction through networks of connected neurons is the basis of cognition. How these signals are generated, modulated and integrated to encode memories or perceive stimuli is a critical factor in understanding the functions of brain structures. Furthermore, disturbances to normal network functions may underlie pathological neurodegenerative disease states and defining a physiological state of neuron connectivity may aid in early diagnosis, for instance, in cases of Alzheimer's and Parkinson's disease. This section will provide context for the characterisation of a novel high-density MEA designed to investigate neuronal connectivity in acute rat brain slices.

Localised neuron networks, at a scale of hundreds of neurons, have been previously studied *in vitro*^{9,17}. However, cultured cells do not retain the complex physiological architecture of the mature mammalian brain and therefore provide limited descriptions of the electrophysiology in neuronal networks. Electrophysiology studies can be approached by several methods, largely through intracellular or extracellular means. Intracellular methods provide detailed data regarding the activity of an individual cell, while extracellular methods can record activity from multiple units simultaneously. Technological advancements have enabled the generation of tools to probe localised networks and study network characteristics in terms of both connectivity and with a resolution capable of discriminating neuronal subtypes¹² (GABAergic, glutamatergic etc.). However, limitations regarding long-term biocompatibility remain an impediment for this approach¹⁸.

Simultaneous extracellular recordings of hundreds of neurons provide a means of interrogating connectivity throughout a network but raises the additional problem of filtering a variety of electrophysiological signals which are to be correctly assigned to individual neuronal units. Advancements in computing have allowed large-scale analysis of extracellular voltage waveforms, termed spike sorting⁸, to improve the resolution of neuron electrophysiology and enable detailed investigations into the properties of each cell. Spike sorting approaches have greatly enhanced the speed of analysing large datasets and, although many variations of the process exist, consist of stages of feature selection and dimensionality reduction to maximise variation in signal waveforms; the uniqueness of each voltage potential can be used to discriminate the signal source (an individual neuron).

Neuronal connectivity is an expansive topic and details of many of its elements, such as graph theory^{19,20}, are beyond the scope of this work. However, generalised descriptions of structural, effective and functional connectivity are firmly accepted in neuroscience and can

be used to identify interactions between neurons^{21–23}. Structural connectivity refers to the direct anatomical interactions between neurons, while effective connectivity assesses the weighting of these synapses – a preferential responsiveness of a neuron to a specific input suggests a more critical role for that connection. Functional connectivity relates to indirect correlations of activity, where unconnected neurons play similar roles within the same network.

This chapter will outline the principles of electrophysiology, specifically the generation of voltage potentials and how these signals are propagated throughout a neuronal network. Investigative methods, such as intracellular recordings, will then be discussed to provide a context for describing MEA technologies used to study hundreds of neurons simultaneously. The advantages and limitations of this approach are summarised, before describing the method of neuron identification used in this body of work. Finally, forms of neuronal connectivity – structural, functional and effective - are briefly discussed in the context of MEA investigations.

2.1 Electrophysiology

Neurons propagate signals throughout their membranes using the flow of ions to produce an electrical voltage potential. These voltage potentials are generated at dendrites, the “inputs” to the cell, in response to chemical stimulations. Dendritic potentials can flow in a bidirectional manner. Backpropagation, towards the postsynaptic site of initiation, is believed to impact synaptic efficiency and provide local synaptic feedback^{24,25}, while current flow towards the cell body (soma) can initiate a larger signal called an action potential (AP) where integrated dendritic signals exceed a voltage threshold. The AP is generated at the base of the axon, the output anatomical structure of a neuron.

The ability of neurons to generate voltages derives from the cellular membrane and the selectively permeable proteins embedded within it. Orchestrating the flow of charged ions across this resistive barrier can create electrochemical and electrostatic forces to regulate local electrical potentials. This is achieved by transmembrane proteins which can actively drive ionic flow against the concentration gradient using adenosine triphosphate (ATP) as an energy substrate. When required, other proteins allow ions to flow passively towards concentration equilibrium. Neurons integrate dendritic potentials and, provided input voltage criteria are achieved, propagate an AP to neurons within the network. Therefore,

the mechanisms of generating and propagating voltage potentials are important in understanding the relaying of information between neurons.

Electrophysiology is an expansive topic and of great interest to contemporary neuroscience research. Neurons do not function solely as a relay of information but integrate a vast number of inputs from dendrites that are filtered before a further stimulation of the network occurs. Each neuron acts as a switchboard for the network and can inhibit, amplify or regulate the activities of other neurons. Neuronal networks act cohesively in processes such as learning and memory, therefore fully understanding the mechanisms of neuronal communication is highly desirable for determining pathophysiological states such as Alzheimer's disease.

This project concerns the characterisation of a tool with which to investigate inter-neuron communication, at the scale of tens to hundreds of neurons, by obtaining high-quality extracellular electrophysiological recordings. Therefore, this section will focus upon: membrane contributions to generating electrical potential, how differences in ionic currents are regulated and directed, and how electrical potentials can be summated to an AP, information which can be transmitted between neurons.

2.1.1 The Cell Membrane

Neurons can generate a voltage potential by conducting the movement of charged ions against concentration gradients through a resistor. This resistance is the form of the semi-permeable cellular membrane which separates the extracellular space from the intracellular cytosol. This structure compartmentalizes the cell into an individual unit and plays a role in regulating cellular homeostasis.

Biological membranes are composed of a phospholipid bilayer 8-10nm thick^{26,27}. Two symmetrical layers contain a hydrophobic lipid portion repelled by the cytosol and ECM and a polar, hydrophilic, glycerol-phosphate group (Fig. 2.1). Membranes are commonly described as selectively permeable: specific conditions and proteins are required to facilitate the movement of molecules across the barrier. However, smaller and less charged molecules more readily diffuse across the barrier. For instance, oxygen molecules dissolve and pass through the lipid tails easily and small uncharged polar molecules such as H₂O can diffuse through, although at a slower rate²⁸. Importantly, lipid bilayers are highly impermeable to charged ions regardless of molecular size and this property is crucial in producing voltage potentials across membranes. Membranes are highly dynamic, and a myriad of processes

occur across this structure. These processes are generated by proteins embedded in the membrane which, in response to stimuli, alter conformation and instigate a specific mechanism. Cellular membranes therefore act as a mediator between the individual cell and the extracellular environment.

This communication between neurons occurs in many ways, such as via hormones (e.g. growth hormone-releasing hormone²⁹ and even gases (such as nitric oxide³⁰), but the two main distinctions are whether a stimuli (i.e. the binding of a chemical messenger) results in the fluctuation of molecules across the membrane through an ionotropic receptor (through an ion channel or transporter) or causes a phosphorylation reaction through a G-protein (metabotropic) receptor embedded in the membrane. Metabotropic receptors mediate protein cascades and are involved in numerous cellular processes, but act over a longer time scale than ionotropic receptors. The kinetic speed at which ionotropic receptors alter configurations enables the rapid movement of ions across the membrane. These receptors are important in neurotransmission across synapses, however similar structures exist which respond to voltage changes rather than chemical binding and generate the resting membrane potential (RMP) and APs.

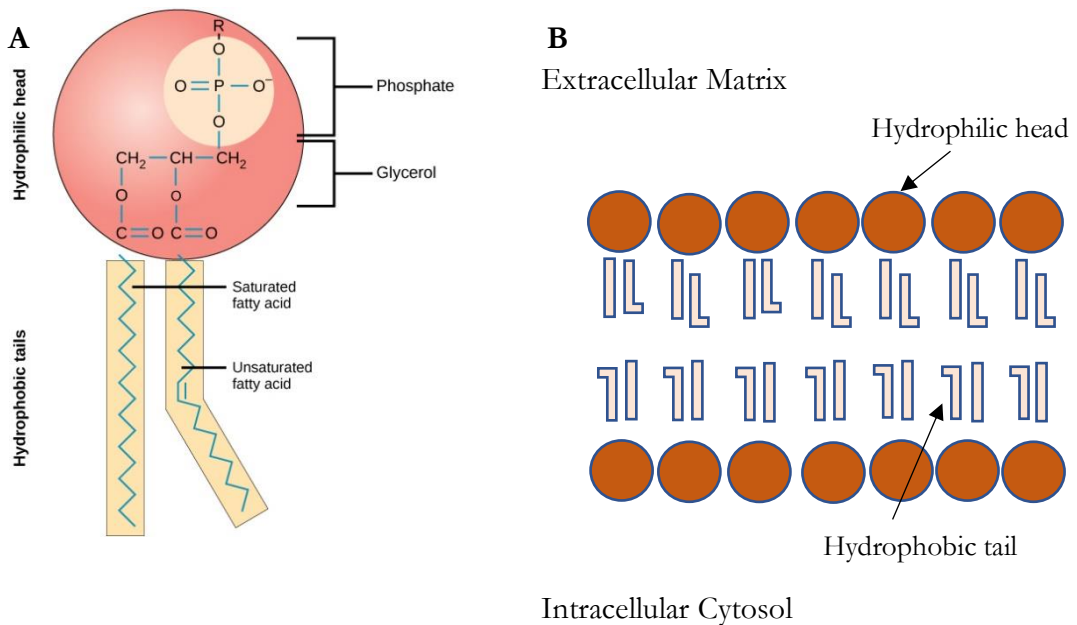


Figure 2. 1. Cellular membranes are composed of two symmetric layers of phospholipids. (A) Each layer consists of a hydrophilic portion, containing a polar phosphate group, electrostatically drawn to either the cytosol or the extracellular space. Hydrophobic tails of

fatty acids are repelled from water-based medium. Image source: OpenStax College³¹. (B) This structure compartmentalises the cell and channels spanning the membrane regulate the flow of ions into, and out of, the cell.

Differences in concentrations of charged molecules generate a voltage potential. Rapid electrophysiological changes to this voltage difference are attributable to two types of membrane transport proteins: ion channels allowing the passive flow of specific ions down a concentration gradient, and ion pumps which act against the gradient. Ion channels quickly alter their conformational state and mediate neuronal signalling, while ion pumps establish and maintain ionic concentrations necessary to propagate an AP.

Ion channels are a large class of transmembrane proteins which, in response to a stimulus e.g. a voltage threshold or a pharmaceutical agonist, can re-configure into either an “open” or “closed” state, thus controlling the passive flux of a specific ion species across the otherwise impermeable lipid barrier of the membrane. Other means of ionic flow across the membrane are via exchangers (e.g. Na-Ca exchanger, NCX, ³²) and ion pumps (i.e. ATP-sensitive channels, ³³) which utilise energy rather than passive movement.

2.1.2 The Resting Membrane Potential

In the absence of stimulation, the cytoplasmic surface of the membrane is more negative than the extracellular side. The discrepancy in ionic concentration generates a voltage potential (the RMP) in the range of -60 mV to -70 mV. This concentration gradient is maintained by the sodium/potassium ATPase ($\text{Na}^+/\text{K}^+\text{ATPase}$) pump, an anti-port ion channel which exchanges two extracellular K^+ ions into the cell for three Na^+ ions out of the cell resulting in a net loss of positive charge. The $\text{Na}^+/\text{K}^+\text{ATPase}$ channel is phosphorylated following the binding and hydrolysis of adenosine triphosphate (ATP) which provides the energy to pump Na^+ and K^+ ions across the membrane. These concentration gradients create an imbalance of electrochemical and electrostatic forces due to the selective permeability of the membrane. Electrochemical forces are the result of unequal concentration gradients of ion species while electrostatic forces are generated by the attraction and repulsion of these ions to each other (positively or negatively charged).

The continual loss of positive charge driven by the $\text{Na}^+/\text{K}^+\text{ATPase}$ results in the cell being negatively charged relative to its surroundings and attracts positive ions to the extracellular surface. The elevated intracellular concentration of K^+ generates an outward directing

electrochemical force down the concentration gradient to act on K^+ to exit the cell. However, the positively charged ions are additionally attracted to the negative environment of the cell. For as long as the electrochemical force exceeds the electrostatic force K^+ would exit the cell via ion channels but, the increased loss of positive charge conversely increases the negativity of the cell (electrostatic force). The level at which both these forces acting on an ion are exactly balanced creates an equilibrium state where the net flux of the ion species is zero. The equilibrium (or reverse) potential (E_k) of these forces is described by the Nernst equation (Equation 2.1).

$$E_k = - \frac{RT}{zF} \ln \frac{[K]_{in}}{[K]_{out}}$$

Equation 2. 1. The Nernst Equation is a useful approximation of the contributions of individual ion species towards electrical potential differences caused by concentration differences. In the example shown above, the movement of potassium (K^+) ions is described which generate a considerable electrical potential difference (E_k) owing to large cytoplasmic and extracellular concentration discrepancy. The value of E_k at which there is no net flux of the ion species is the ionic equilibrium potential; where electrostatic and electrochemical forces are balanced. R is the gas constant (8.31 J/kmol), T is absolute temperature (310K), F is equal to Faraday's constant (96500 coulombs/mol) and Z is the valence of the ion.

Ion	[Cytoplasm], mM	[Extracellular], mM	E_k , mV	P_i cm/s
K^+	135	4	-92	1×10^{-7}
Na^+	12	140	+64	1×10^{-9}
Cl^-	4	116	-88	1×10^{-8}

Table 2. 1. The discrepancy of ionic concentrations between the cytoplasm and extracellular matrix creates a voltage potential, the contribution of each ion species to this potential can be calculated by the Nernst equation to provide the equilibrium potential (E_k). P_i refers to the typical permeability for that ion. These are hypothetical values representative of mammalian neurons³⁴.

The Nernst equation represents an idealized situation – membranes are selectively permeable to numerous inorganic ions and alterations to an ionic concentration gradient will consequently affect the electrical gradient. For neurons, the ions which exert the most

significant bioelectric effect are K^+ , Na^+ and Cl^- . Rather than including the gradients of all inorganic ions, the Nernst equation can be modified to become more physiologically representative by combining the equilibrium potentials of these three important ions. The resulting equation is the Goldman-Hodgkin-Katz equation, commonly called the Goldman equation (equation 2.2³⁵).

$$V_m \cong \frac{RT}{F} \ln \frac{P_k[K]_{out} + P_{Na}[Na]_{out} + P_{Cl}[Cl]_{in}}{P_k[K]_{in} + P_{Na}[Na]_{in} + P_{Cl}[Cl]_{out}}$$

Equation 2. 2. The Goldman-Hodgkin-Katz equation is a modified version of the Nernst equation which accounts for the behaviour of several ion species in response to electrochemical and electrostatic forces.

The Goldman equation accounts for the permeability of several ion species and is useful for calculating the influence of extracellular effects on the membrane potential. The discrepancies between equilibrium potentials of these significant ions means that altering the intracellular concentration gradient of one (e.g. increasing Na^+) can affect another (e.g. the membrane is less polarised, therefore the electrostatic attraction of extracellular Cl^- to the cell increases). The Goldman equation reflects the complex dynamics of ion currents across the cell membrane and the constant flux of electrical potential that occurs. The RMP is maintained by homeostatic mechanisms and the role of cellular structures, such as the membrane and ion channels, can be utilised to model cellular responses to changes in ion concentrations.

2.1.3 Neuronal Currents Can be Described using Equivalent Circuit Model.

The Nernst and Goldman equations can be used to calculate interactions between the membrane potential and ion concentrations but are limited in describing changes to membrane permeability, i.e. the opening and closing of ion channels. Resistance, capacitance and conductance of a neuron can be described by a resistor-capacitor (RC) circuit to illustrate the flow of current³⁶ (Fig. 2. 2, A). This model is useful to understand how membrane resistance and capacitance impacts the propagation of electrical signals across the cell.

The phospholipid bilayer of the membrane insulates the conductive intracellular environment and generates electrical capacitance. A neuron can therefore contain charge and generate an electrical field. However, membranes act as leaky capacitors because the

ion channels embedded within it can conduct charge when in an open state. Furthermore, increasing the number of open channels allows more ions to flow, i.e. resistance to current is reduced, and conductance is increased. In the absence of a concentration gradient, single channel conductance would be calculated by Ohm's Law. However, the ionic gradient additionally creates an electromotive force, represented in the equivalent circuit as a battery; a source of electrical potential generated by the difference in chemical potentials. The relationship between current and voltage is therefore shifted towards the Nernst potential of the ion species the channel is selective to (Fig. 2.2, B).

There is a chemical force driving the movement of ions (concentrated gradients shown by the Nernst potential, E_k) as well as voltage across the capacitance of the membrane (V_m , an electrical force). Both forces result in currents should ion channels open. Combined, they determine the driving force acting on an ion to reach equilibrium potential (Equation 2.3).

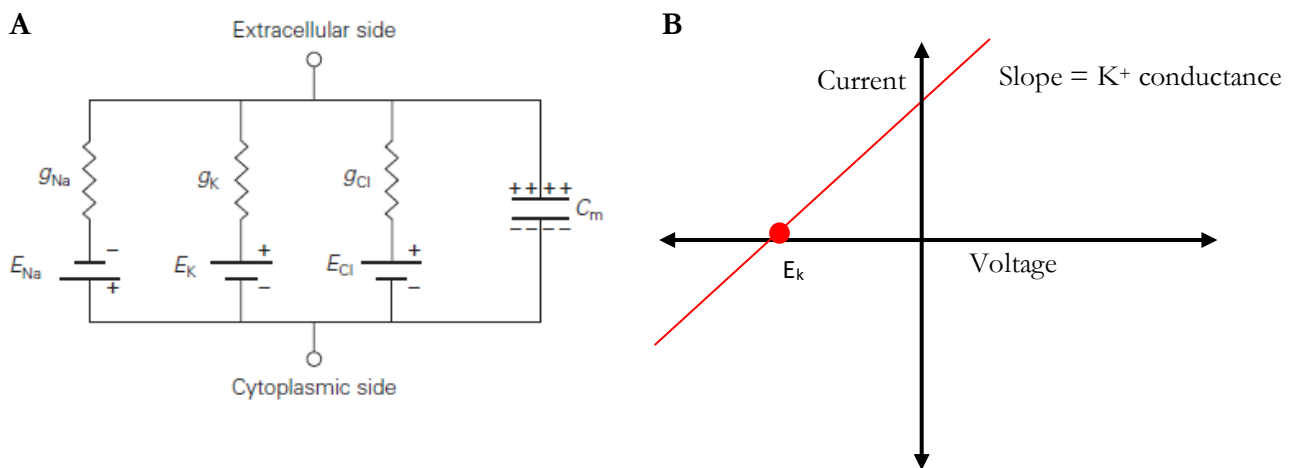


Figure 2. 2. Ionic currents across a neuronal membrane can be represented as a resistor-capacitor electronics circuit. (A) The membrane acts as an insulating capacitor storing charge (C_m) and ion channels as variable resistors conducting ion flow ($g_{Na}/g_K/g_{Cl}$). Ionic gradients also generate a chemical electromotive force represented as a battery ($E_{Na}/E_K/E_{Cl}$). Image adapted from Dabrowski et al.³⁶ (B) The electrochemical driving force acting upon an ion species is determined by electrochemical and electrostatic forces, which shift the current-voltage relationship towards the Nernst potential of that ion species.

$$\text{Electrochemical Driving Force} = V_m - E_k$$

Equation 2. 3. The electrochemical driving force refers to the electrostatic and chemical forces acting upon ions across a membrane and can be calculated as the difference between the membrane voltage potential (V_m) and the Nernst potential (E_k).

The electrochemical driving force, and equating cellular properties to electrical components, enables the modelling of currents in a neuron in the form of the equivalent circuit model. This provides a means of modelling the effects of altering parameters such as density of ion channel expression, which can then be incorporated into a more complex model describing neurons with different characteristics. This model was further developed³⁸ to incorporate synapses, and other forms include representations of neurons in a network³⁹ which form the basis of network modelling simulations. The biophysical properties of membranes and ion channels can describe the mechanisms which generate electrical potentials. These potentials can be propagated throughout a network depending on how each signal is integrated and processed at the cell body.

2.1.4 Postsynaptic Potentials Can Summate

Neurons exist as individual units within a larger network circuit. The equivalent circuit describes the electrical state of a neuron and its responses when presented with a stimulus. Chemical receptors localized on dendrites receive a signal from a neighbouring neuron in the form of a neurotransmitter (see section 2.1.6). Binding of a transmitter to a ligand-gated ion channel initiates a change in receptor configuration to an open state. Subsequently the conductance of the specific ion increases, the electrochemical gradient is shifted and the charge across the membrane capacitor is adjusted. Subsequently a transient postsynaptic potential (PSP) is generated. These potentials are the input signals which are modified and integrated to determine further processing of the signal and are therefore important in evaluating connectivity between neurons.

Postsynaptic potentials are transient voltage fluctuations with peak amplitudes ranging from 30-665 μV ⁴⁰. Depending on postsynaptic receptors present, PSPs can be excitatory (EPSPs, i.e. depolarizing a dendrite) or inhibitory (IPSPs, i.e. polarising a dendrite) and the effect on membrane potential is propagated towards the cell body. EPSPs are typically elicited by increased Na^+ conductance into the cell and IPSPs are commonly the result of Cl^- entry, however other ions, such as Ca^{2+} , also contribute to PSPs⁴¹.

Dendritic branches encounter more synapses as the projections approach the cell body; therefore, PSPs more proximal to the cell body filter the preceding signal. Such alterations may be reliant on specific frequencies as simulations of extracellular signals indicate that low frequency signals (~ 1 Hz) experience less attenuation when propagated from distal dendrites, while signals ~ 100 Hz are reduced by approximately a factor of 100 at the soma⁴².

However, it has been reported that dendrites located further from the soma of hippocampal CA1 neurons exhibit increased EPSP amplitudes which may counterbalance downstream filtering⁴³. Integration of PSPs can occur along dendritic trees with the final, modified, signal being further processed at the soma. The amplitude and frequency of signals impact how input signals are summated and define whether the cell body will be depolarised to threshold and consequently generate an AP signal. Temporal summation occurs when a high frequency input from few (or a single) sources incrementally lower the polarisation of the cell (Fig. 2.3, A). An individual signal of this amplitude would not cause the soma to reach threshold, but before the membrane potential can return to rest an additional input occurs and reduces the polarity of the cell. Therefore, high frequency dendritic potentials are more likely to elicit an AP even at low amplitudes. Spatial summation is the result of simultaneous stimulation by several neurons where precise timing can result in the summation of sub-threshold signals to induce an AP (Fig. 2.3, B). This mechanism creates highly complex computations as the precision of these interactions are related to how the local network behaves holistically and may underly a highly regulated function.

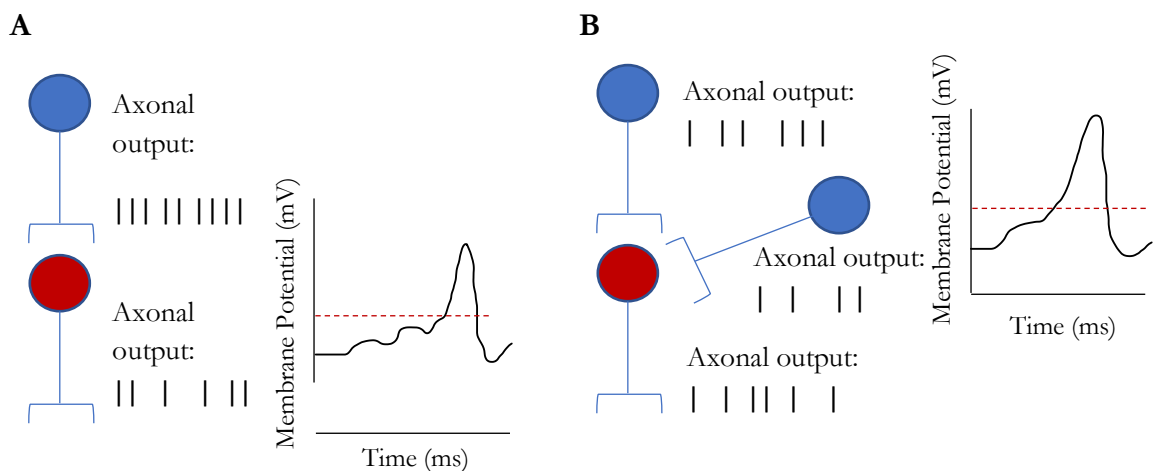


Figure 2.3. Temporal and spatial summation. (A) Temporal summation occurs following high intensity stimulation from a single source. The high frequency of impulses stimulating the postsynaptic membrane means it does not fully return to resting potential, therefore a smaller amplitude signal at high frequencies can elicit a postsynaptic action potential. (B) Spatial summation occurs following near simultaneous stimulation of a synapse by two sources which sum amplitudes and achieve threshold voltage. Red dashed line; action potential threshold voltage.

The filtering and integration of potentials across even a small neuronal network produces highly complex interactions. The morphology of dendrites can influence summation by attenuating and filtering signals that are propagated towards the soma, as dendritic architecture can impact the probability of changes to the membrane resistance and capacitance. For instance, a greater degree of dendritic branching proximal to the soma would reduce the axial resistance, reducing the length constant of a potential and slowing signal propagation⁴⁴. Therefore, any additional postsynaptic potentials occurring in this region are more likely to temporally summate with the slowed potential. To determine the significance of a neuron's behaviour within a network, the behaviour of numerous neighbouring cells also need to be accounted for. Therefore, studying the neural code within a local network requires a high spatial resolution capable of defining as many neighbouring cells as possible combined with the temporal precision to indicate the mechanisms of signal summation occurring.

Small amplitude dendritic potentials are difficult to study in large numbers simultaneously to these criteria; however calcium imaging techniques have been shown to be able to record from multiple synapses simultaneously *in vivo* and capable of resolving electrical activity on individual dendritic spines⁴⁵. Two-photon microscopy imaging at the single cell level can provide high spatial resolution regarding the summation of dendritic signals but is often limited by low signal to noise ratio (~2:5) and temporal kinetics of the calcium dyes (sampling rates of ~1 kHz)⁴⁶. Dyes with greater temporal definition are expected to be developed in the near future, while the combination with wide-field microscopy has enabled the visualisation of the electrical activity of ~1000 neurons *in vivo*⁴⁷. This achievement required extensive image processing and data analysis, while improved temporal resolution would greatly enhance the analysis of connectivity in these studies.

Small amplitude potentials cannot be utilised via extracellular recordings to define neurons as the distance from the membrane enhances attenuation of these small signals while the variety of currents present in the extracellular space generate noise, further masking signals⁹. These factors obfuscate the identification of subthreshold interactions suggestive of temporal or spatial summation. Extracellular neuronal recordings therefore focus on large amplitude potentials generated at the cell body which can be used to identify the activity of an individual neuron, however, spatial and temporal characteristics of neurons can be used to estimate connectivity in a network provided the resolution of these features is

appropriately high. The number of connections, and how signals interact, means the integration of neural codes is particularly problematic in understanding neuronal networks. Connectivity is discussed further in 2.3.2

2.1.5 The Action Potential

Sub-threshold dendritic potentials are difficult to study due to limitations in allocating small potentials to an individual anatomical structure. However, the integrated output of the cell is generated from the easily identifiable cell body and consists of a large amplitude (mV range) signal termed the action potential (AP). This potential has been extensively studied, and the key aspects of its generation are outlined below.

At rest, the membrane voltage of the cell body is maintained at around -70 mV relative to the extracellular space; however slight fluctuations to this value occur constantly depending on various factors such as the availability of extracellular ions and other intracellular processes. Dendritic signals are integrated as they arrive at the soma and contribute to these fluctuations. The initial segment of the axon (the “output” component of a neuron) is the axon hillock where action potentials are generated and propagate signals through other neurons in the network. The high density of voltage gated Na⁺ channels in this area reflect the ability to mediate large voltage changes, and may also function as a feedback mechanism (backpropagation). EPSPs have been shown to be amplified in a sodium channel-dependant manner around the axon hillock⁴⁸, and channels >30 μm beyond the initial axon segment have exhibited increased excitability. These properties determine a neuron’s threshold voltage – if integrated, potentials reduce the polarisation of the axon hillock membrane sufficiently to reach a voltage threshold, an action potential is initiated. Threshold values are between -40 mV and -55 mV and this discrepancy is due to the properties and density of ion channels, diameter of the axon (affecting resistance and time constant), which in turn affects the summation of EPSPs to trigger the opening of voltage gated sodium channels⁴⁹ which initiate a cascade of ionic currents.

Ion channels are generalised into either ligand-gated (opening mechanism controlled by a specific molecule) or voltage-gated. Voltage gated channels respond to a specific transmembrane potential and alter the conformation of subunits to an open state. At a transmembrane potential specific to the type of channel, the subunit conformation of the channel alters, increasing or decreasing the conductance of ions across the membrane. In the context of the AP, the threshold potential refers to the transmembrane voltage at which

voltage-gated sodium channels begin to open. Sodium rapidly enters the cell to attain concentration equilibrium and the cell is further depolarised, inducing more channels to increase conductance in a positive feedback loop. Action potentials can be described as “all or nothing” events – they occur only if threshold voltage is reached and the process will always initiate once these criteria is achieved. Potentials with insufficient amplitude to open multiple sodium channels will not elicit an AP and are failed initiations (Fig. 2.4). The membrane returns to RMP following these sub-threshold potentials.

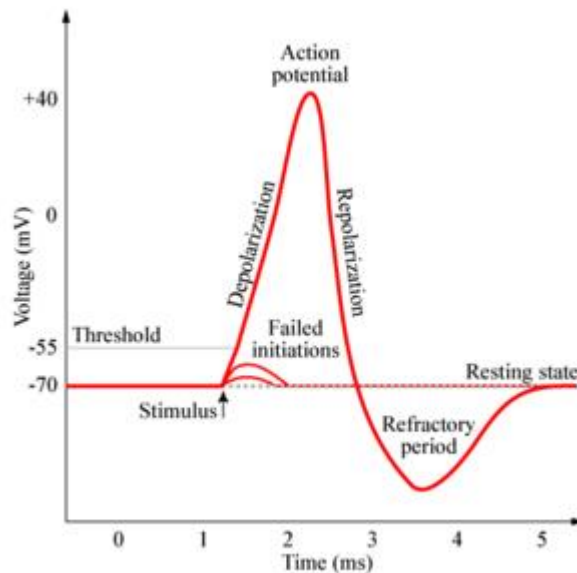


Figure 2. 4. Schematic of a typical action potential. Integrated voltage potentials open sodium channels of the axon hillock (stimulus): positively charged sodium ions flow into the cell, decreasing polarity across the membrane. Integrated potentials stimulating enough current to raise the resting membrane potential to threshold voltage initiate a positive feedback mechanism in voltage-gated sodium channels, causing more channels to open (depolarisation). Sodium channels become inactivated, but depolarisation triggers voltage-gated potassium channels to open and potassium flows out of the cell down its concentration gradient (repolarisation) driven towards equilibrium potential (~-90 mV). During the refractory period ion channels are inactivated; as channels begin returning to resting state the membrane voltage remains too negative, and active channels too few, to generate enough current to reach threshold. The sodium/potassium ATPase channel pump returns the membrane to resting voltage.

Positively charged sodium ions enter a neuron and reduce the polarity relative to the extracellular environment. Once threshold voltage is achieved, a positive-feedback

mechanism is induced opening more sodium channels and further depolarising the cell. This process continues and eventually achieves a positive bias of approximately +60 mV. This process is the depolarisation phase of the action potential. Very quickly (~ 0.5 ms) all axon hillock sodium channels have opened, yet the kinetics of their protein configurations limit the time they can remain open. As these channels are temporarily inactivated, the neuron cannot quickly return to RMP by expelling sodium. Instead, the depolarisation causes voltage-gated potassium channels open, permitting K^+ ions to flow outward towards equilibrium potential. This subsequently re-polarises the neuron (repolarisation in Fig. 2.4). Potassium channels continue to open, and the continual loss of positive ions polarises the membrane potential beyond the RMP, hyperpolarising the membrane. This is the refractory period where no AP can be stimulated during this time (typically ~ 2 ms) due to the greater amplitude required to reach threshold and few sodium channels have reverted to their original configuration. However, this period is suggested to vary across cell types as mossy fibers of the cerebellum have been observed to elicit APs at $\sim 1\text{kHz}$ ⁵⁰, indicating a refractory period of <1 ms occurs in this class of neurons. Refractory periods are a useful parameter in spike sorting analysis (see section 2.3) as this provides an upper frequency limit with which to filter neuronal spiking and spike timing correlation parameters are used in the analysis presented here.

2.1.6 Neurons communicate via Synapses: Neurotransmission

Neurons relay action potentials to each other via synapses- junctions between axon terminals and dendrites. The signal is transduced into vesicles of neurotransmitters, transported in discrete organelles of chemicals, which bridge the synaptic cleft and elicit a response from the postsynaptic cell. Release of vesicles into the cleft is the result of calcium-dependent exocytosis, whereby voltage gated calcium ion channels in the presynaptic terminal open in response to depolarisation⁵¹. The calcium flux then initiates exocytosis through a series of protein interactions⁵² which fuse the vesicle membrane with the cell membrane and release neurotransmitters into the synapse. This mechanism enables dendrites to receive multiple inputs in a changeable, but highly regulated, fashion.

Postsynaptic cells can be affected by various types of transmitter released at concentrations dependent on the electrical amplitude induced at the presynaptic cell. At an axon terminal, voltage-gated calcium channels (VGCCs) are expressed at the active zones of presynaptic membranes which initiate the exocytosis of neurotransmitters. These channels are co-

localised with vesicle docking and priming sites for fast coupling of APs to calcium-dependant exocytosis. As VGCCs open in response to membrane depolarisation, extracellular Ca^{2+} is electrochemically driven into the cell. A series of protein interactions initiated by the presence of calcium promotes vesicles of neurotransmitters to be chaperoned towards the synaptic membrane. Vesicular and cellular membranes then fuse to release neurotransmitters into the synaptic cleft. There are a variety of neurotransmitters released across synapses which can initiate different responses in the postsynaptic neuron. Broadly, neurons can be classified as excitatory or inhibitory based on the neurotransmitters they emit. Table 2.2 identifies examples of well-established neurotransmitters grouped by their chemical structure. Neurotransmitters diffuse across the synaptic cleft and bind to corresponding receptors located on postsynaptic dendrites. The effect may be to open ion channels or initiate a second messenger cascade, subtly generating and mediating electrical potentials conducted towards the cell body.

Chemical Group	Examples
Choline ester	Acetylcholine (ACh)
Monoamines	
Catechol	Dopamine (DA), Noradrenaline (NA)
Indole	5-Hydroxytryptamine (5-HT, serotonin)
Imidazole	Histamine
Amino acids	
Acidic	Glutamate (Glu)
Basic	γ -Aminobutyric acid (GABA), glycine
Peptides	Enkephalins, endorphins, cholecystokinin, substanceP
Purines	Adenosine triphosphate (ATP)
Retrograde Transmitters	
Steroids	Pregnenalone
Nitric oxide	Nitric oxide
Eicosanoids	Prostaglandins

Table 2. 2. The chemical structures of neurotransmitters are diverse, reflecting the versatility of synaptic communication. Retrograde transmitters can act at the presynaptic terminal. Adapted from *Neurotransmitters, Drugs and Brain Function*⁵³.

Although neurotransmitters are often described as exerting a postsynaptic effect, it is important to note that they can also act in a presynaptic manner to modulate activity. For example, glutamate is a classic transmitter with a postsynaptic excitatory effect, but it also partly inhibits ionotropic receptors presynaptically in a feedback mechanism⁵⁴. A further complication is the heterogeneity of transmitters that can be released into the synaptic cleft from a single neuron. These are often termed primary and co-transmitters; for example, interneurons of the striatum are known to transmit primarily GABA, but also substance P across synapses⁵⁵. However, this combination only exists in certain brain structures (as do other combinations) which indicate modulatory functions specific to that population of cells. Neurotransmission is the chemical transduction of signals between neurons and is the mode of communication which elicits voltage changes at the dendrites of neurons, however, there are a variety of different mechanisms involved which can impact the postsynaptic input. Gene expression of receptors and production of transmitters determines the basic function of a neuron within a network, yet the role of individual neurons and its weighting within a network are poorly resolved. To examine this, technologies have been developed to examine the function of neuronal subtypes within a network by studies large numbers of neurons simultaneously.

2.2 Microelectrode Arrays: Technological Developments

To understand the functional connectivity of neuronal circuits, and how these relationships relate to physiological (and pathological) states, experiments need to consider a range of electrophysiological parameters. For example, the effectiveness of neuron-neuron communication is influenced by ion currents²², sub-threshold potentials⁵⁶, local field potentials⁵⁷, synaptic weighting⁵⁸ and functional connectivity²¹. Presently, intracellular recording methods can only be applied to a limited number of cells even *in vitro*, with simultaneous recordings of 8-12 neurons representing a significant achievement^{59,60}, while technologies which can monitor hundreds of neurons at once are constrained to investigating extracellular potentials – removing the ability to assess the impact of sub-threshold potentials⁹. As such, technical approaches are often compared and combined to limit these discrepancies and it is necessary to evaluate these methodologies in relation to each other. Intracellular recording methods have been developed over several decades with increasing sophistication. This has been partly driven by the pharmaceutical industry's interest in high-throughput screening of ion channel characterisations⁶¹ as investigating the properties of

individual ion channels and responses to changes in ion currents provides insights into electrophysiology at the molecular level. However, although these methods are useful for evaluating the activities of neurons, they remain largely inapplicable in assessing functional connectivity of a large-scale neuronal network⁶² as the necessity of bulky precision pipette manipulators and visualisation of the target cell makes this cumbersome setup unfeasible to study 100s of neurons simultaneously.

The electrical fields generated by summated postsynaptic potentials can be detected extracellularly as voltage potentials (V_e). These signals can be interpreted via an electroencephalogram (EEG, potentials recorded from the scalp), electrocorticogram (ECoG, from the cortical surface using electrodes placed sub-durally) and as local field potentials (LFPs, electrodes placed within the brain). These techniques are useful in determining the synchronous activities of large numbers of neurons across brain structures, yet their spatial resolution is insufficient to identify individual neurons.

To compromise, mesoscale technologies have been developed to identify large numbers of neurons simultaneously yet maintain the resolution to record the electrophysiology of individual units⁹. An electrode placed proximally to a neuronal membrane allows for detection of field potential waveforms from which it is possible to define and reconstruct voltage potentials from individual neurons. Therefore, MEAs have been developed which can record the electrophysiological activity of hundreds of neurons simultaneously.

Electrophysiological methods demonstrate a variety of spatial resolutions and the scale of neuronal populations they can investigate. This chapter will outline the development of intracellular techniques, before focussing upon MEAs - including the device presented in this project - and highlight the technological advancements in other methodologies designed to address the same problem.

2.2.1 Intracellular Recording Methods

Following the work of Hodgkin and Huxley (1952)³⁷, electrophysiological techniques focussed on how to study single-cell currents in smaller preparations. Using a micropipette and forming a high resistance seal on a small area of membrane (Fig. 2.5), accurate measurements of potential changes occurring across individual ion channels can be achieved⁶³. The value of this technique, known as patch clamping, is indicating the “open” or “inactive” (and “closed”) states of ion channels in response to stimuli. Applying a constant voltage to the setup and measuring resultant current, Ohm’s law indicates any change in resistance would reflect a change in ion channel state.

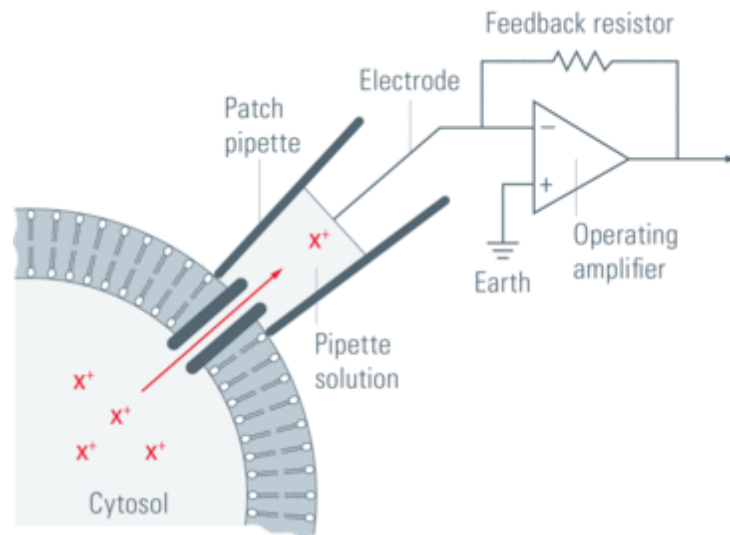


Figure 2. 5. Patch clamp techniques aim to detect current changes across the membrane in as small an area as possible, ideally limited to a single channel. A pipette filled with electrolyte solution is used to form a high resistance seal around the area, and isolates currents crossing the membrane caused by the flow of ions. These currents can be detected by an electrode and the signal amplified for analysis (image source adapted from Leica Microsystems⁶⁴).

Patch clamping enables low noise measurements of currents through ion channels with low conductance (in the range of pS) by sealing off a portion of the membrane containing as few ion channels as possible, ideally a single channel. Ensuring the current flows only into the pipette and not through the seal necessitates a GΩ seal⁶⁵ to distinguish a single ion channel current. This requires a micropipette 0.5 μm - 2 μm in diameter to minimize the number of channels present but, additionally, decreased surface area increases the seal resistance and reduces current leakage. Gentle suction further increases resistance. Various configurations of patch clamping exist: cell-attached, whole-cell, inside-out, outside-out²⁷, as well as automated systems for performing patch clamp *in vivo*⁶⁶. The cell-attached method is employed as described above with the membrane intact. In contrast, the whole-cell configuration ruptures the membrane at the pipette opening, allowing the voltage of the entire cell to be measured and also modified via solutions introduced into the cytosol via the pipette²⁷. Removing the portion of the membrane that has been sealed onto the pipette from the rest of the membrane can enable greater interrogation of intracellular, or extracellular, properties of ion channels, for instance channel gating by a specific molecule. The inside-out and outside-in methods are examples of how the membrane can be manipulated to study specific properties of membrane ion channels⁶⁷. These techniques are used to obtain precise measurements of voltage changes across membranes or current flow

through individual channels; for example, assessing the impact of pharmaceuticals upon the activities of specific channel subtypes^{68,69}. However, they are technically challenging, and bulky micromanipulators limit the number of clamping setups that can be applied simultaneously. As such, a more appropriate approach is required to analyse the connectivity of hundreds of neurons.

2.2.2 Extracellular Potential Recording Methods

The electrical fields generated by action potentials possess sufficient magnitude to be detected extracellularly as voltage potentials (V_e) with the use of a reference potential – provided the electrode is proximal to the membrane. These extracellular action potentials (EAPs) are also termed “spikes”, from which information regarding the flow of charge across a membrane can be inferred (Fig 2.2). Recordings of extracellular voltage fluctuations will exhibit several sources of biophysical signals, depending on the density, and electrode proximity, to the cells. High neuronal density results in the detection of potentials from several units and complicates the identification of neurons from the waveforms they produce, however, this has the advantage of identifying and recording from multiple neurons simultaneously. The collective electrical fields generated across a network are known as local field potentials (LFPs)- low frequency oscillations <100 Hz which represent the fluctuation of charge in the extracellular space⁴². LFPs are implicated in neuronal synchronicity – the collective activity of hundreds of neurons^{70,71} - and are often monitored using technologies surveying structures of the brain (e.g. EEG). However, if an electrode is proximal to an individual neuron, its electrical activity would dominate the signal at higher frequencies and bandpass filtering can further improve resolution of spikes from individual neurons.

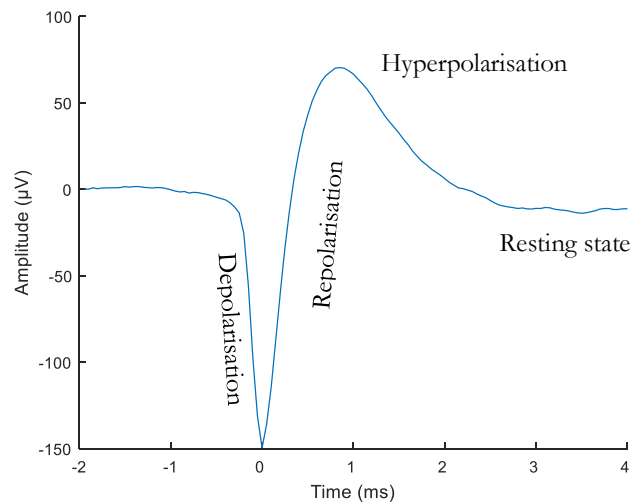


Figure 2. 6. Extracellular voltage potentials exhibit inversed phases of action potentials. As the intracellular portion of the membrane becomes more positive during the depolarisation phase of the action potential, the extracellular surface becomes more negative. The detected amplitude changes in potential also depend on the distance of the electrode from the membrane.

In contrast to intracellular techniques, extracellular electrodes are less invasive as the membrane and connections remain largely unperturbed, however, signal amplitude is rapidly attenuated over distance while electrical and biological noise reduces the ability to reliably isolate individual signal sources. As such, extracellular electrodes need to be located within $\sim 100 \mu\text{m}$ of a neuron to be identified^{72,73}. Extracellular currents generated by large hippocampal cells have been detected up to a distance of $140 \mu\text{m}$ from an electrode⁷⁴, however, a volume with a radius of $140 \mu\text{m}$ from an electrode site in the same CA1 hippocampal region is calculated to contain ~ 1108 recordable neurons, therefore only a fraction of cells in a given volume can be identified⁷⁵. This discrepancy is the result of methodological limitations in attributing waveforms to individual units, the density of electrodes used and the low spiking frequency of some neurons.

Traditionally, extracellular recording methods are limited to only providing information on whether a neuron fires an AP or not, without direct observation of the neuronal subtype. Employing optogenetic techniques in parallel to electrophysiology has great potential to increase the specificity of studies⁷⁶, whereby transgenic cells can be optically stimulated to induce an action potential, although artificially evoking spikes would not necessarily reflect communication in a physiological circuit. An alternative approach is to retrospectively match

fluorescence imaging of specific cell types to waveforms detected in the vicinity of an electrode. Becchetti *et al.* (2012)⁷⁷ expressed a fluorescent protein in inhibitory GABAergic cells cultured on an MEA in order to identify electrophysiological criteria and eliminate the need for subtype distinction in future studies. Their results indicate the Fano factor (here defined as the ratio of spike count variance to the mean of the neuron spike count⁷⁸) to be the most reliable means of inhibitory/excitatory distinction with inhibitory neurons exhibiting significantly greater spike count variance, however, contention for these parameters remains. The variability of literature-reported electrophysiological classifications of neuronal subtypes is, often to a large degree, due to un-standardised methodologies and recording conditions (e.g. electrode types, recording temperatures, spike sorting algorithms). Attempts are being made to normalise this data⁷⁹ although heterogeneous techniques will doubtless persist for some time. A further complication for extracellular recordings is “silent” (or dark) neurons which exhibit low spike frequency and can therefore be problematic in spike sorting. This artefact occurs where insufficient data is acquired to allocate spikes to an individual neuron and data is therefore excluded from further analysis. Although the prevalence of such neurons varies across brain regions, silent neurons may constitute ~90% of cells in cortical regions¹⁰.

2.2.3 MEAs: Materials and Technical Requirements

The recordings presented in this work were acquired using a 512-electrode MEA with a high spatial resolution (electrode pitch of 60 μm) and resolved at a temporal rate of 20 kHz. These characteristics are effective to investigate acute slices of brain tissue. Microelectrode array technologies have been developed for a range of functions with specific requirements. Implantable arrays have been used to study and alleviate symptoms of pathological diseases such as Parkinson’s disease - where a stimulating electrode is implanted into effected areas of neurodegeneration⁸⁰ - and investigated as a method of restoring vision following retina degeneration⁸¹. The development of technologies to examine extracellular electrophysiology has enabled stimulation and recording of multiple neurons simultaneously. Arrays of small metal electrodes are becoming commonly used to investigate neuronal function, integrated with both *in vivo* and *in vitro* experimental setups⁹. These devices are required to produce a high signal to noise ratio (SNR) and remain biocompatible for long periods of time. Design and fabrication of MEAs is an expansive topic with much research devoted to material development, biocompatibility, and electrical design and fabrication techniques. This section

will briefly outline the requirements, development and materials used in devices comparable to the technology presented in this work, with an emphasis on *in vitro* research.

Electrodes can be inserted at multiple spaced points in the brain, but MEAs require a high electrode spatial resolution to effectively record from a localized network of neurons. Increased resolution additionally helps to differentiate multiple electrophysiological signals and triangulate the signal. Traditionally, MEAs have been limited in their spatial resolution and number of electrodes, but the advancement of technologies based on micro-electromechanical systems (MEMS) and complementary metal-oxide-semiconductor (CMOS) fabrication techniques, has helped to overcome some of these limitations^{82,83}. MEAs consisting of 519⁸⁴, 3600⁸⁵, and recently even 26,400⁸⁶, electrodes have been demonstrated and electrode-electrode pitches of <20 μm realised. These devices are commonly used either in preparations of retinal ganglion cells or have neurons cultured on the device to study, for example; network maturation⁸⁷, activities in pathological states⁸⁸ and pharmacology⁸⁹.

The necessity of electrodes to be small enough to be arranged in high densities results in higher electrode impedance, which can impact the signal to noise ratio of the system. Charge carried by physiological electrolytes is transferred to electrodes via capacitive mechanisms. As the electrode is decreased in size the spread resistance (the resistance to current flow from solution to the electrode) increases⁹⁰ and the interfacial capacitance of the system (in parallel with charge transfer resistance) becomes less dominant (see Diagram 3.1). At a (material-specific) voltage limit, alternative mechanisms of charge transfer begin to occur, typically reduction-oxidation reactions resulting from increased charge transfer resistance, which can alter the behaviour of the system. To effectively record small amplitude neuronal activity, the effective electrode impedance (the sum of metallic resistance, spread resistance and at the electrode interface) needs to be less than the input impedance at the front end amplifier of the recording system or signals will be significantly attenuated^{91,92}. To adjust system limitations, metal electrodes are electroplated with materials that increase the surface area required for charge transfer and decrease occurrences of unwanted reactions. Increased surface area reduces the electrical impedance of the electrode, improving the neuron/electrode interface. Impedance values for electrodes $\sim 5 \mu\text{m}$ in diameter are typically between 200 k Ω and 800 k Ω at 1 kHz frequency. The electrodes presented in this work were coated with platinum-black, a granular form of platinum which exhibits high capacitance at low current densities⁹³, resulting in low impedance values. It is a commonly used material to plate electrodes due to its limited biological reactivity⁹⁴ and mechanical stability^{90,93}.

A major obstacle to obtaining electrophysiological data from chronic implantations is the immune response to foreign materials in the brain (section 2.2.4). To overcome this, numerous materials have been evaluated for their biocompatibility. However, these materials must retain appropriate conductivity and low impedance to record neuronal signals with effective SNR. Electrodes are typically fabricated from conductive metals such as gold, titanium nitride or platinum due to their conductivity and low biological reactivity. Methods of increasing the conductive surface areas of electrodes often utilise conductive structures such as carbon nanotubes (CNTs) and conductive polymers⁹⁵. The device presented in this work is not implantable and is designed to study *ex vivo* tissue over periods of up to 5 hours. MEAs are among the forefront of technologies used to investigate electrophysiological properties of neuronal networks and have been combined with other technologies such as patch clamp⁶⁰, and integrated with optical outputs for use in optogenetic studies⁷⁶. Many studies that utilise MEAs commonly investigate neuronal cells *in vitro*, where cell densities are lower and network properties can be examined in greater detail. However, the network architecture of cultured cells is not representative of the physiological brain, therefore these studies are limited in neuronal connectivity on the scale of hundreds of neurons. Alternative approaches use organotypic slices - where a section of brain tissue is cultured before being recorded from – however, despite a more representative architecture, the boundaries of cortical layers and hippocampal regions become blurred during time required for culturing⁹⁶. Here, we attempt to record from an acute slice of brain tissue with connectivity and architecture intact to resolve the electrophysiology of a representative neuronal network.

2.2.4 Neuroinflammation and Biocompatibility

A novelty of the MEA characterised in this project is the arrangement of 3-dimensional needle electrodes. Although MEAs with 3D electrode structures have been previously demonstrated⁹⁷, these investigations have primarily focussed on recording the electrophysiology of cultured cells or variations in electrode geometry and material. Sectioning of brain tissue allows access to regions otherwise difficult to access *in vivo*, or to recreate *in vitro*, such as the hippocampus or striatum. Organotypic slices, where brain sections are cultured, retain much of this original structure, however, the boundaries between structures become less defined during culturing, reducing this advantage⁹⁶. In contrast, the motivation for the presented device is to record from acute slices of brain tissue to ensure the connectivity of neuronal networks is as representative as possible. As such, the

reason for developing 3D needle electrodes is to penetrate beyond damaged layers of cells inherent in the sectioning procedure.

It is important to consider the effects on the electrical activities of neurons resulting from mechanical damage to brain tissues. In response to acute stress, immunological responses initiate molecular cascades resulting in necrosis or apoptosis. Additionally, directly affected cells release cytokines and other chemical messengers which diffuse to neighbouring, unaffected, neurons and illicit responses. This section will summarise how neurons respond to the preparation of acute slices: directly (e.g. axotomy), indirectly (through biochemical messenger signals) and how these can influence the electrophysiology of the network. However, most immunological investigations concern physiological responses over the time scale of 6-12hours, while experiments discussed in this work typically last ~4hours. Therefore, the major mechanisms of apoptosis will be omitted and instead this chapter will focus on acute trauma and the immediate electrophysiological consequences of transecting neuronal projections.

Severe mechanical damage to the soma will lead to catastrophic cell death, leaching cellular debris which will be later phagocytised by microglia – a ubiquitous immunological cell type in the brain. In many ways more problematic, however, are the extensive arborisations and protrusions of neurites. In the central nervous system, nerve fibres can extend a relatively large distance from the cell body and, on average, are 20,000 times larger than the soma in length and total surface area⁹⁸ therefore neurons distal to an area of damage can still incur cellular trauma. Of concern is damage to the axon – the diameter and elongation of which makes it especially vulnerable.

Neuronal projections can be degenerated in a controlled manner via several mechanisms; e.g. pruning (involved in embryonic developmental plasticity, ⁹⁹) or apoptosis (programmed cell death, ^{100,101}). In response to trauma, neuronal responses act to limit damage and promote neurite regrowth via Wallerian degeneration (WD ¹⁰²). This process spans several days, therefore the relevance to this project is limited to the initial responses, known as acute axonal degeneration (AAD). Although AAD and WD are distinct mechanisms in terms of where and when they occur, many characteristics are indistinguishable. For instance, Kerschensteiner *et al.* (2005) demonstrated that, once initiated, both processes fragment damaged axon portions at equivalent speeds (70 $\mu\text{m}/\text{min}$) while calpain proteases, key mediators of cytoskeletal degradation, are essential for both responses. As the time-course

relevant for recording from acute slices in the presented setup spans <12hours, this covers both AAD and the early stages of WD.

Transection of an axon, axotomy, has been mostly studied in an *in vitro* context owing the technical difficulties in sectioning and monitoring a specific axon, although *in vivo* imaging of degenerative processes have been performed in both spinal cord nerves and optic nerves^{103,104}. The immediate consequences are extended disintegration from the site of injury (~300 μm distally, Kerschensteiner et al. 2005) in a process spanning between 5 and 60minutes. This is accompanied by vigorous spiking and an increased calcium influx¹⁰⁵. Increased calcium concentration promotes the modulation of proteins which will be retrogradely transported to the soma and initiate apoptotic or protective cascades. The intra-axonal rise in calcium is critical for AAD progression, as Ca^{2+} blockers attenuate this mechanism¹⁰⁴. During this acute stage, components of the axonal cytoskeleton, such as neurofilaments and microtubules, are disassembled via Ca^{2+} -dependant activation of the serine-threonine protease calpain. Through Western blotting and histological techniques, Kampfl *et al.* (1996) observed increased calpain activation, and accumulation of calpain-mediated break-down products, 15minutes from the onset of injury.

Increased intracellular calcium and increased spiking frequency will additionally affect electrochemical gradients, particularly Na-Ca exchanger membrane proteins. As sodium accumulates during high-frequency spiking, its gradient assumes an outward direction and Na-Ca exchangers invert their operation; driving more calcium into the cell attempting to rectify sodium concentration.

These findings indicate that degenerative processes are initiated at a relevant timescale to data presented in this project and alter the electrophysiology of neuronal networks through increased calcium and sodium load. However, it is undefined to what extent neurons downstream in the network from an axotomised cell are influenced by these factors. Therefore, bypassing acutely damaged cells using 3D needle-geometry electrodes reduces the likelihood of recording from cells adversely impacted by mechanical damage.

2.3 Spike Sorting of Extracellular Waveforms

Spike sorting is method used to filter electrophysiological signals and assign extracellular waveforms to an individual neuronal unit. This is necessary when recording from multiple electrodes as duplicate signals are detected, while multiple signal sources can distort

recordings and limiting the reliability of high-quality neuronal recordings. There are several approaches to overcome these problems which have developed through the use of MEAs and acute slices¹⁰⁶. However, this section will expand on the method described in Litke *et al.*¹⁴ with which the data presented in this project was analysed.

Analysis of neuronal spikes recorded with extracellular methods requires a means to separate multiple signals detected on a single electrode. Spike sorting, assigning a waveform potential to an individual neuron, requires a high signal to noise ratio (SNR) ideally with signals unambiguously separated temporally and spatially across several electrodes. In addition to the biological noise of distant, low-amplitude potentials, electrical noise introduced into the preparation via the amplifier of the recording system must be filtered and discarded. In the case of high density MEAs, several electrodes may detect a voltage potential from an individual neuron¹⁰⁷, therefore the sampling rate of extracellular voltages is required to be performed at sub-millisecond timescales to provide temporal resolution capable of differentiating sources of individual action potentials.

As commercially available MEAs are now commonly developed with hundreds of electrodes⁸¹ the computational time required to process such large datasets - often in the range of a terabyte for a recording of several hours – can be a major factor in choosing a spike sorting method. The processing time for spike sorting algorithms increases with electrode number as more electrical signals are being recorded for processing, therefore this has become a major limitation for investigations with large numbers of electrodes. Computational time also increases due to manual adjustment by human verification – increasingly sorting methods are shifting towards a greater reliance on full automation to reduce human bias and this time-consuming manual phase. Differences in experimental setup are an important consideration before deciding on a spike sorting method as acquisition systems, electrode number and pitch, and electrode material could have varying degrees of sorting reliability.

Due to the desire to automate identification of thousands of waveforms, methods of spike sorting have focussed on Principal Component Analysis (PCA), whereby features are extracted and the maximum variations between the data are highlighted as a means of clustering data of a similar class together, i.e. data from an individual neuron. Other methods utilise independent component analysis (ICA)¹⁰⁸, which acts on the assumption that all signals are statistically independent, and wavelet transformation, which is more commonly used in analysis of low frequency signals and is useful if amplitude analysis is not an applicable approach^{96,109}.

Although frequency and amplitude of spiking events can alter, waveforms retain a characteristic shape, which can be identified using feature extraction techniques. This shape is also partly defined by the refractory period (see section 2.1.5) which is defined by the kinetics of ion channels and results in a waveform with defined biological parameters. Problems with spike sorting and the need for manual adjustment due to alterations to waveform shape over time continue to be an issue. For instance, neuroinflammation has been shown to result in neuron hyperexcitability¹¹⁰, while axotomized cultures of cortical cells have demonstrated long-term changes to AP amplitudes¹¹¹.

Reliable and robust spike sorting is critical to investigating neuronal connectivity- not just for identification of neurons but for ensuring good, isolated, recordings of spike times. Overlapping or miss-assigned spikes cause difficulties in analysing probabilities of connectivity. However, this difficulty arises from the relative temporal and spatial similarities from two connected neurons. This is also true in instances of spatial summation, where two proximal neurons are innervated by the same presynaptic neuron and could exhibit similar temporal and spatial waveform properties.

2.3.1 Principal Component Analysis

Filtering of appropriate frequencies is typically performed in the range of 300-3000 Hz¹¹² for spike analysis after which the RMS noise of the raw data is evaluated. From this, a suitable threshold is selected which spike amplitudes will pass, and then return past (Fig. 2.7). A typical threshold used in here would be 60 μV ¹⁴, although suitability depends on the noise of the system used. If the employed threshold is too low, false-positive signals would be included for further processing and obfuscate neuronal identification; too high, and spikes may be omitted, reducing statistical power crucial to spike sorting (Fig. 2.8).

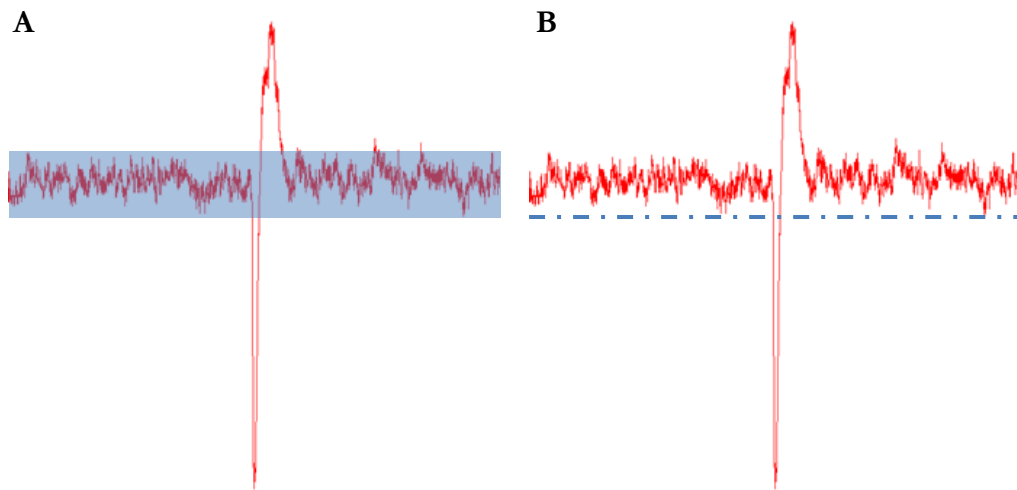


Figure 2. 7. Initial stages of spike sorting involve identifying voltages that exceed, and then return to, the RMS noise detected on the electrode (left), which is done by calculating a suitable threshold voltage (right). When a threshold value is too low, irrelevant background noise will be included for further analysis, which can contaminate identified neurons, while a high value reduces the number of spikes identified.

PCA is a method of dimensionality reduction. As multiple waveform attributes are included for analysis the observed dimensions increase, however this makes separating data with common features more difficult. The dimensions that exhibit the highest variability in the data (the principal components) are then used to maximise the variance of the dataset. These components are based on orthogonal vectors of the variables which essentially re-fit the data to dimensions that highlight the greatest variance.

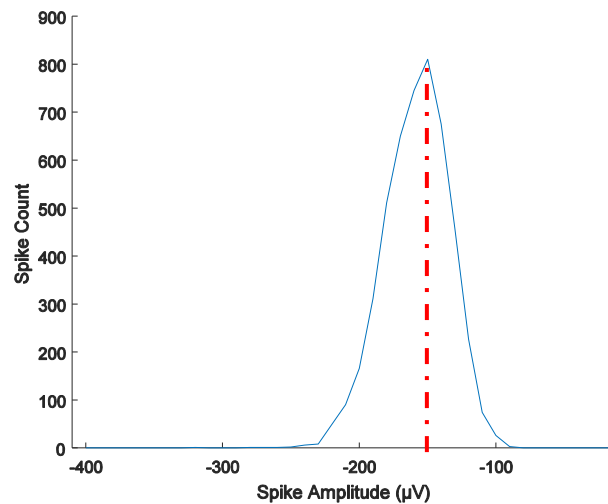


Figure 2. 8. Identifying, and applying, an appropriate amplitude threshold is a common second step for spike sorting. A high threshold will clearly identify neurons; however, this requires neurons to exhibit high amplitudes spikes and many spikes may be omitted, reducing the power of the statistics needed to cleanly separate signals during PCA. In the above example, the threshold (red dashed line) is $-150 \mu\text{V}$ identifying the bulk of detected spikes, yet hundreds of spikes will be discarded from further processing. Bin width $10 \mu\text{V}$.

As a spike is identified on an electrode, all data points 0.5 ms prior and 0.8 ms after the spike time are included from that electrode (the “seed” electrode) and its six surrounding neighbours. The electrodes on the MEA presented are arranged hexagonally, and this accounts for each equidistant electrode. For a spike identified on each electrode, and its neighbours, a 182-dimensional vector is generated from the analogue waveform with each vector representing the recorded voltage at each time point included in analysis. As the numbers of dimensions now represent a large amount of data, PCA is performed to reduce these dimensions down to 5 and the more observable variations can be used to cluster data together.

Clustering is carried out using The Expectation Maximization algorithm, which separates data based on the assumption that clusters represent individual classes, which are fitted to a 2D Gaussian distributions for each of the 5 dimensions (i.e. PCA dimension 1: PCA dimension 2, Fig. 2.9). This stage of spike sorting involves manual validation primarily due to electrode drift or non-stationary background noise which cause difficulties in Gaussian fitting⁸.

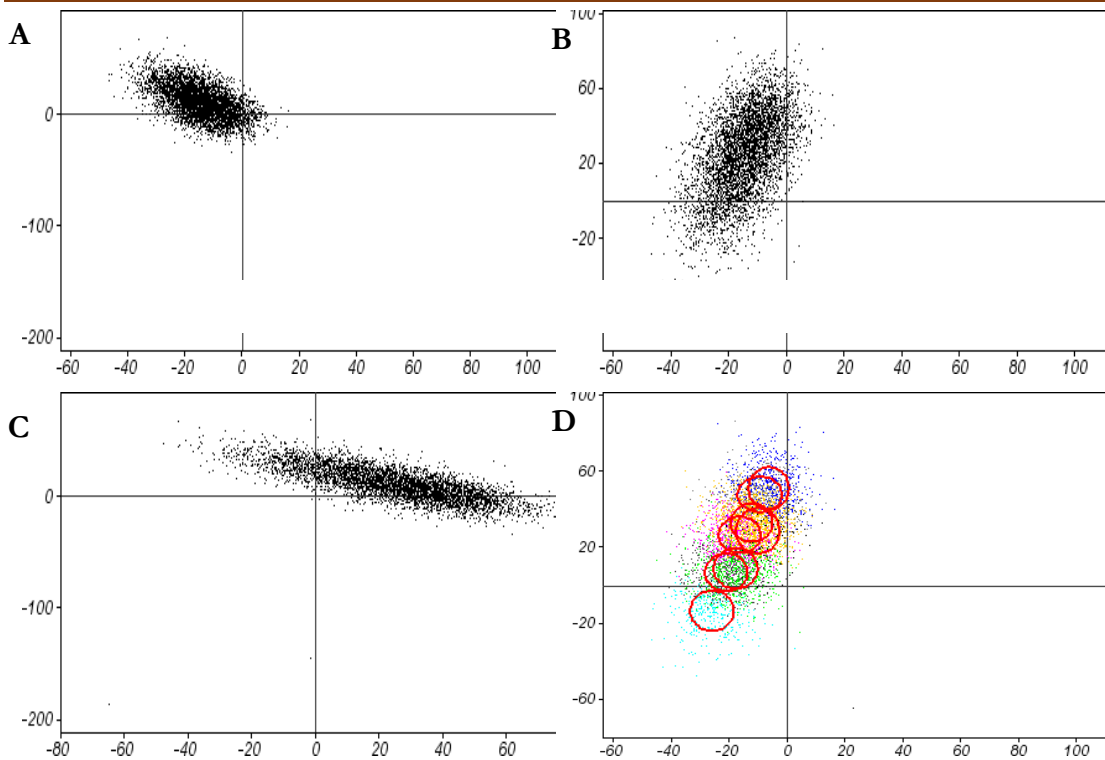


Figure 2. 9. PCA clustering of data was performed in 5 dimensions exhibiting the greatest variance across the data. Clustering examples of the same dataset (A, B, C) are PCA dimensions 1-3 represented in 2-dimensional plots. Data are clustered by calculations assuming the distribution is Gaussian; occasionally data do not fit this assumption, e.g. electrode drift from original neuron-electrode interface, resulting in over-clustering (D). This requires manual validation and is a motivation for improved spike sorting methods.

The clusters then undergo neuron cleaning – very similar features could be reasonably included in a cluster which cannot physiologically belong to the same neuron. Multi-unit activity that has been incorrectly clustered can be identified using the absolute refractory period (section 2.1.5) by applying an autocorrelation function which analyses the inter-spike intervals of the reconstructed neuron and applies a limit of feasible re-activation based on a physiological limit of ~ 1.5 ms¹⁴. Histograms of inter-spike intervals associated with a cluster are generated to highlight spikes detected from more than one neuron, where intervals less than the refractory period (~ 1.5 ms) must originate from more than one source. Data which defy the limits of this inter-spike interval threshold are defined as contaminated, are not associated with a single neuron, and are discarded.

2.3.2 Connectivity

Advancements in MEA technologies have enabled the recording of electrophysiological activity from hundreds of neurons simultaneously and allowed for analysis of local network connectivity properties^{113,96}. Neuronal connectivity relates to how information is relayed throughout the network and how the integration of communicated signals produce a coherent output. Large scale connectivity analysis has been performed over entire brain regions, for instance with magnetic resonance imaging¹¹⁴, however the resolution afforded by new MEAs enables enhanced interrogation of network properties on the scale of individual neurons. Understanding neuronal connectivity can explain mechanisms of information processing and how this can be impacted in neurodegenerative diseases, whilst also elucidating adaptive plasticity mechanisms which underlie learning and memory.

Large brain structures are understood to be functionally segregated as certain structures have defined roles, e.g. the hippocampus is strongly associated with learning and memory. However, the role of an individual neuron within a local network is less defined. An approach to characterise the function of a neuron in the context of a network is to discriminate forms of connectivity (Fig. 2.10). Structural connectivity concerns the anatomical connection between neurons at a synapse; this feature identifies an interaction, but not the role of the neuron within the network. Further characterisations include functional connectivity, where remote neuronal events exhibit a statistical dependency, or *effective connectivity*, the direct influence of a neuron upon another²².

Functional connectivity is based on time dependant correlations and can be determined if the activity of one neuron can predict the activity of another. Effective connectivity relates to the synaptic weighting of a structural connection – the impact one neuron's activity upon another. Defining the anatomical architecture of a network enforces a parameter enabling the clear identification of effective connectivity and has been incorporated into algorithms to adjust analyses of connectivity⁹⁶. Therefore, effective connectivity acts as a means of weighting synaptic connections by highlighting architectural features most probable to contribute to information propagation. This form of connectivity is more relevant to local network electrophysiology on the scale of hundreds of neurons; however, the area covered by the array presented in this work (1x2mm) implies assessments of indirect, functional, connectivity could be performed.

Effective connectivity is typically studied *in vitro*^{115,21} as cell densities, network architecture, cell accessibility and cell type can be manipulated and designed to simplify investigations.

Additionally, such studies concern the flow of information throughout a network and are therefore condition-dependent. Stimulating the network at a known location, at a specific time, provides context to downstream activity. This can be performed with an electrical stimuli introduced into the extracellular space, while contemporary studies are increasingly utilising optogenetic techniques in a neuron-specific manner to evaluate networks in a more physiological environment¹¹⁶. Although providing useful insights, the conditional stimulation of network nodes does not reflect the physiological behaviour of neurons and the corresponding output of the holistic network.

To accurately reconstruct correlated network activity of individual cells, MEAs have been used to characterise functional connectivity by inferred correlated activity states. This is performed by evaluating the network in the context of graph theory, a mathematical model with a large range of parameters which can indicate the behaviours of the network²¹. Properties of the graph (network) can then be assessed for commonalities. Example parameters include node degree (how many correlated connections for each neuron), cluster coefficient (how segregated the neuron is from other neurons) and path length (the number of neurons which a signal must traverse to reach another neuron). Node degree has been shown to be a useful metric in determining scale-free networks (where a smaller population of neurons have a high degree of connectivity, i.e. population connectivity exhibits a power law distribution¹¹⁷) characterised by highly connected hub neurons¹¹⁸ which are believed to be critical for information processing¹¹³. Scale-free networks correlate with robustness of the system, suggesting redundancy mechanisms exist to maintain the reliability of signal propagation in these pathways.

The use of MEAs to study neuron connectivity is becoming widespread due to their ability to record from multiple neurons simultaneously, while increased spatial resolution achieved by technological advancements affords greater detail of direct neuron interactions. However, the difficulties associated with recording from acute slices has limited analyses of representative network connectivity in healthy, intact, neuronal networks. This work demonstrates a device with high electrode spatial resolution with a recording area of 2mm² integrated in an acquisition system capable of accurately defining hundreds of individual neuronal units. The connectivity analysis presented here aims to evaluate several approaches to assessing connectivity across a functional cortical network with a focus on effective connectivity.

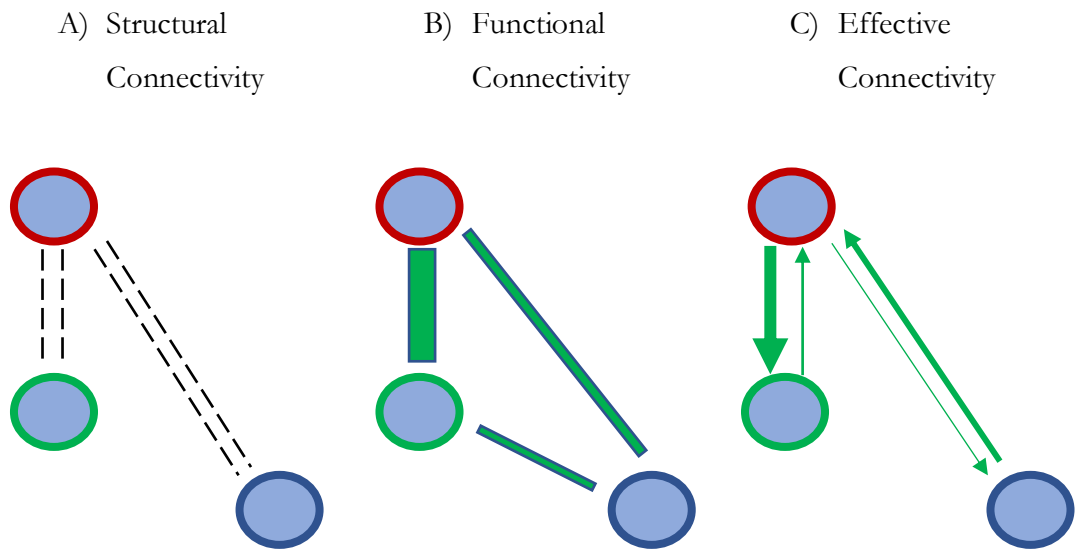


Figure 2. 10. Three forms of connectivity can be used to describe neuron interactions within a network. (A) Structural connectivity refers to the anatomical connections at synapses. (B) Functional connectivity is time-dependant correlations in activity where the state of one neuron can predict the state of another. (C) Effective connectivity relates to synaptic weighting; a measure of the causal impact the activity of one neuron can directly affect a neighbour.

3. Electrical Characterisation of a Novel Microelectrode Array

Monitoring hundreds of neurons simultaneously within a local network requires high temporal and spatial resolution to effectively sort spikes and investigate connectivity between cells. Prior to electrophysiological recordings, the electrical properties of the MEA and recording system were evaluated. This section will briefly outline the fabrication of the MEA, fabricated by Dr. Gunning at the Institute of Photonics (University of Strathclyde) using photolithography techniques¹¹, and describe the electronic components of the recording system. Aspects of the system which can limit the quality of recordings are then discussed and evaluated for their appropriateness to perform electrophysiological recordings of neurons.

The impedances of electrodes at the electrode-electrolyte (the physiological solution) interface were assessed to determine the SNR and sensitivity to low amplitude neuronal spikes. High impedances limit the detection of low amplitude signals and constrain the electrical grounding of electrodes through the electrolyte solution which increases background noise, obscuring neuronal signals. To overcome this, the surface areas of electrodes were increased by electroplating with a biologically inert material. Electroplating is commonly used to lower electrode impedance values (see section 2.2.3) and the MEA presented here was electroplated with platinum black. The effect of platinisation upon electrode impedances, and resultant system noise, was investigated both by addressing electrode channels individually and, once the recording system was fully assembled, via software which initiates an application-specific integrated chip (ASIC). The impedances of tungsten electrodes were successfully reduced by the platinisation protocol to below 300 k Ω which is suitable value to match the system requirements and obtain an appropriate signal to noise ratio. No trend was observed following changes to current densities and time parameters used, therefore the minimum combination of these parameters (100nA / 20s) was used for future electroplating which resulted in a reliable impedance decrease across several electrodes.

The MEA was then integrating into the acquisition system and root mean square (RMS) noise of electrodes measured in saline solution with a brain slice applied to the electrodes. The noise of 72% of the electrodes was measured to be between 14 and 16 μ V, with no channels exhibiting an RMS noise greater than 18 μ V. A total of 20 channels exhibited significantly lower noise and were confirmed as electrically shorted by direct measurements. The noise input from both the electrical system and in the presence of a brain slice immersed in saline

was found to be stable at an appropriate level to perform electrophysiological recordings. These initial evaluations were important to ensure the device behaves comparably to previous MEA developments and that devices could be reliably fabricated without defects occurring.

3.1 Fabrication Summary of the 512-Needle Microelectrode Array

The system presented in this work progressed from investigations of retinal ganglion cells which utilised an MEA with indium tin oxide electrodes based on a glass substrate^{7,119,84}. However, the requirements to investigate acute slices required alterations to the MEA design. A novel combination of semiconductor fabrication methods were used to produce a device from a silicon substrate, as previously reported in the development of a 64-needle electrode MEA¹¹, with tungsten electrodes exposed at the tips of silicon needles (figure 3.1, B & C). An 8-fold increase in the number of high-density electrodes may have decreased uniformity across electrodes due to low process capability of a novel photolithography process, however this was found not to be the case. Fabrication steps are visualised in Fig. 3.1A, with Fig. 3.1B&C displaying scanning electron micrographs (S.E.M.) of the resultant needle electrodes. The fabrication of the 512-needle MEA was performed by Dr Gunning¹²⁰, and their development is beyond the scope of this work (see appendix 1 for further details of array fabrication). Briefly:

- 1) Photoresist is applied to a silicon wafer to pattern an array of circles, where photoresist is absent, which indicate electrode positions (60 μm pitch) and base diameters (25 μm). Exposed areas of silicon undergo deep reactive ion etching (DRIE) to produce tapered holes.
- 2) Silicon dioxide is applied to the lining of the holes and adjoining surface as an insulation layer, and tungsten deposited on top of the silicon dioxide by chemical vapour deposition.
- 3) Excess tungsten on the wafer surface is removed, using photolithography and etching techniques, to pattern the electrode tracks.
- 4) Polysilicon is deposited in the etched holes to provide mechanical stability, and the surface excess is etched to expose the tungsten tracks.
- 5) Aluminium is sputter deposited, patterned and etched so that it coats the exposed tungsten and enhances the electrical contact with tungsten at the needle tip.

- 6) The wafer is inverted and most of the original silicon is removed (leaving $\sim 100 \mu\text{m}$ thickness for physical support) using a solution of tetra methyl ammonium hydroxide. The underlying silicon dioxide remains intact to act as an etch stop and allowing the formation of the needles. The extent of silicon removal during this stage determines the length of the needles.
- 7) The tungsten needle tips are then exposed by removing silicon dioxide with hydrofluoric acid.

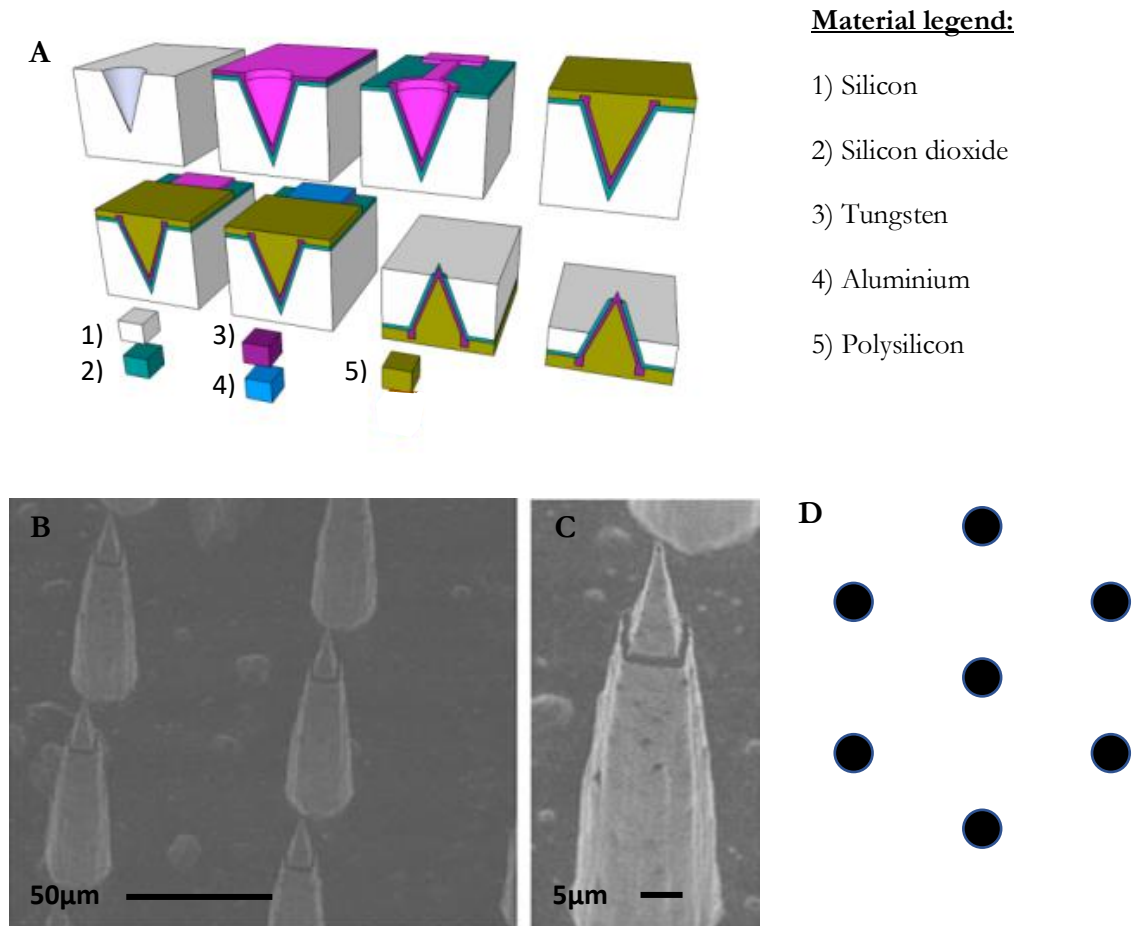


Figure 3. 1. Fabrication of the MEA. (A) Arrays were fabricated from silicon using photolithography techniques which can etch defined areas into which conductive materials can be deposited. Specifically the microfabrication technique can be found in appendix 1. (B) The microelectrode needles can be produced in high-density arrays of $60 \mu\text{m}$ pitch and heights up to $250 \mu\text{m}$; example image of $\sim 50 \mu\text{m}$ high needles. (C) These needles are insulated in silicon dioxide (also providing mechanical support) with a tungsten electrode exposed at the tip. (D) Electrodes are arranged in a pattern to make each electrode equidistant to its neighbours and form a rectangle $1 \times 2 \text{mm}$ in size.

The array of electrodes is arranged in a rectangular geometry, but individual electrodes are laid out in a hexagonal arrangement (Fig. 3.1, D) with each electrode equidistant to each of its 6 neighbours. The electrodes were spread over an area of 1x2mm with 60 μm pitch between needles. This fabrication process can produce needles up to 250 μm in height, however the needles which recorded neuronal signals in this work were 90 μm in height with a 30 μm diameter base and pyramidal tungsten electrode tips 5x5x20 μm in size.

The heights of the needles are a critical property, as the novelty of the device is the ability to bypass damaged tissue – an inherent consequence of acute slice preparation. Additionally, a compromise between the diameter of the needles and mechanical stability must be considered as large electrodes (and needle support) inserted into tissue would likely cause severe damage to brain tissues yet needles too fragile may fracture upon insertion. However, the size of the electrode tips is important to consider as the conducting surface area determines the impedance of the electrode which must be matched to the recording system to achieve high-quality recordings.

3.2 Investigations of Electrode Platinisation and Impedance Measurements

The surface area of each pyramidal tungsten electrode tip was $\sim 200 \mu\text{m}^2$. Electrode surface area is inversely related to impedance (as area decreases, impedance increases) therefore the small size of these electrodes limits current flow and increases electrical noise. However, single-cell resolution becomes more difficult with a large electrode detecting multi-unit activity, as the large surface area would attenuate signals through spatial averaging¹²¹. In contrast to patch clamp, where a high electrode resistance amplifies voltage deflections, impedances of electrodes for extracellular recordings require low impedances. Electrodes are coupled to the electrical grounding (in this case, a platinum wire) through the electrolyte solution and impairing the connection of electrodes to grounding causes the electrodes to be “floating” – with no reference, the system will record a higher noise input. The impedances of electrodes is critical in detecting the extracellular currents generated by neurons.

The electrode and input amplifier impedances are connected in series. The effective electrode impedance is the sum of the spread resistance (electrolyte conductivity through the surface of the electrode), the impedance associated with electrode surface (charge transfer resistance in parallel with interfacial capacitance) and the metallic resistance of the electrode. To preserve signal quality and reduce signal reflection, the front-end amplifier is

designed with an impedance greater than the impedance of the electrode because the signal will be attenuated where this is less than the electrode impedance (see equation 3.1).

These parameters have previously been used to model optimal impedance values⁷ and application-specific silicon chips, integrated into the recording system presented here¹²², are designed to function at an electrode impedance of ~300 kΩ at 1 kHz. To match electrode impedances to the system design, and ensure a high SNR, impedances were measured, surface areas were increased by electroplating with granular (black) platinum.

$$V_{in} = \frac{V_e}{1 + \left(\frac{Z_e}{Z_a}\right)}$$

Equation 3. 1. The recorded voltage (V_{in}) is determined by the impedances of the electrode and front-end amplifier (Z_e and Z_a , respectively). The voltage input will be attenuated if Z_a is not substantially greater than Z_e . V_e is the voltage at the electrode interface.

Electrode impedances were measured in their initial state following fabrication, where tungsten is the conductive material, followed by independent platinisation of several individual electrodes. These initial evaluations were performed before the MEA was integrated into the neuroboard, in a custom setup with the function of keeping the device physically stable whilst allowing access to individual readout channels on the opposite side to the electrodes (see Appendix 2).

The etching process to expose the tungsten tips of electrodes may not have resulted in complete or uniform exposure, further decreasing the surface area. As discussed previously biologically inert materials are commonly used to coat electrodes (see section 2.2.3), specifically those which form nanostructures⁹ and increase the electrode-electrolyte interface area. Here, electrodes are plated with platinum black which is a granular form of platinum. This form of platinum possesses well characterised catalytic properties and, compared to other metals used as electrodes like gold, is reportedly less reactive¹²³ in electrolyte solutions.

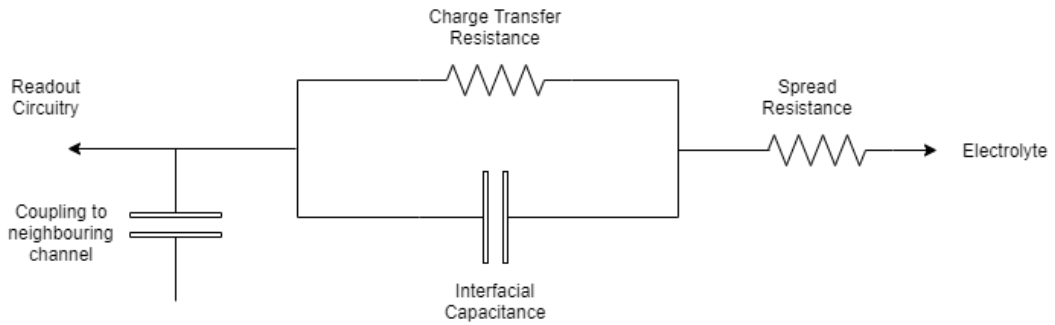


Diagram 3. 1. A simple electrical model of electrode impedance showing the major factors affecting electrode impedance at the electrode-electrolyte interface. Spread resistance refers to the area and resistivity of the electrolyte solution. Charge transfer resistance is determined by the charge transfer rate and the redox reactions that occur at the interface, while the interfacial capacitance consists of layers of charged ions ($\sim 15 \mu\text{F}/\text{cm}^2$). Additionally, there may be coupling to a neighbouring channel which is determined by distance between channels, surface area and the permittivity through the dielectric medium.

3.3 Platinization protocol

Platinization of the 3D needle arrays was performed with caution. Previous experiments using planar electrode arrays had utilised a current density of $4\text{nA}/\mu\text{m}^2$ applied for 20s to platinize flat electrodes $20 \mu\text{m}^2$ in size⁷. However, the pyramidal structure of the 512 MEA electrodes presented an electrode surface area of $\sim 200 \mu\text{m}^2$ ($5 \mu\text{m} \times 5 \mu\text{m}$ base and $20 \mu\text{m}$ height). Uncertainty of how uniformly electrodes would be plated, depending on how thoroughly tungsten had been exposed in the etching process, meant further investigations of platinisation were required.

For initial platinisation attempts, electrodes were individually platinized using a Yokogawa multi-channel source measurement unit (GS820) connected to a single channel probe applied to a channel readout bondpad. The electrodes were immersed in a 1% chloroplatinic acid solution (PtCl). Chloroplatinic acid solution (8% in water, Sigma Aldrich, 262587) was diluted with 0.08% lead (II) acetate trihydrate (Sigma, 316512) in distilled water to provide 1% solution. The platinum reference wire encircling the chamber was then connected to the source measurement unit to complete the circuit and a current of $0.004 \mu\text{A}$ at a 1volt compliance limit was applied. Further investigations into the effect of platinisation were performed at 0.004 , 0.008 and $0.012 \mu\text{A}$, each for either 20 or 30seconds. Later, when the array was integrated into the neuroboard, tungsten electrodes were electroplated using input commands from custom-made labview software (National Instruments), which

initiated the platchips located on the neuroboard to ensure appropriate parameters. Electrode impedances were measured using an LCR meter (Iso-Tech 800), in the same setup as platinisation, at 0.1V across a frequency range of 0.1: 100 kHz.

3.4 Data Acquisition System

The MEA was then integrated into the neuroboard, containing the PlatChips and NeuroChips^{14,122,124,125}, and shielded in an aluminium box which acted as a Faraday cage (Fig. 3.2, B). A circular gap in this box was present over the electrode portion of the array and the electrode area was surrounded by a plastic cylinder 1cm in height. The plastic cylinder functioned as a chamber to contain the electrophysiological solution and tissue, isolating conductive physiological solutions from sensitive electronic components.

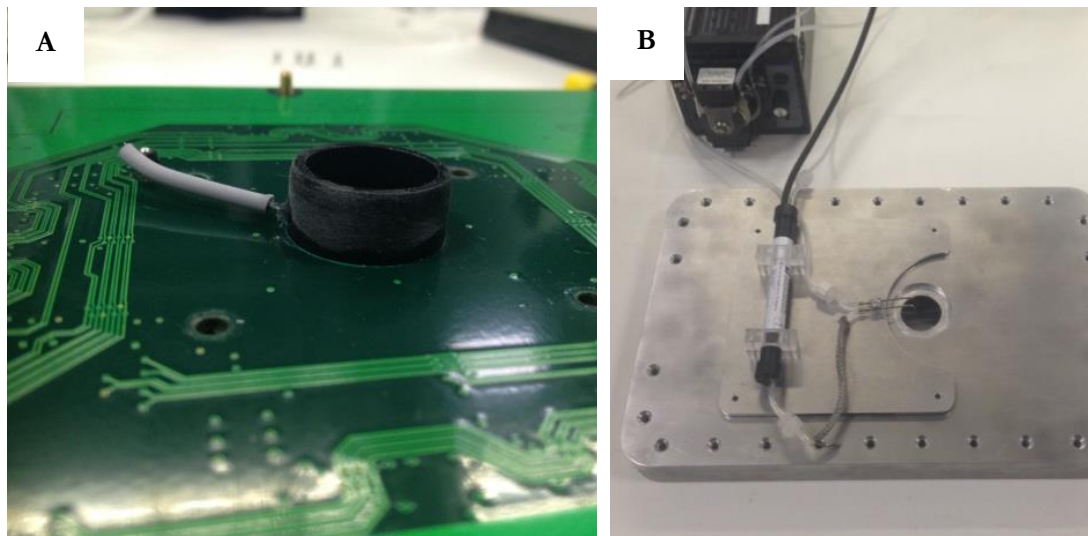


Figure 3. 2. (A) The MEA was glued into a PCB board populated with the PlatChips and NeuroChips of the acquisition system located on the underside of the board. A cylinder of Delrin plastic formed a chamber around the needles of the MEA to contain physiological solution. A platinum wire surrounded the inner wall of the chamber to function as an electrical reference which led out of the chamber and was soldered to a grounding pin. (B) The neuroboard was sealed within an aluminium box to shield the system from electrical static and physical damage. A hole in the box allowed access to the MEA chamber and to insert perfusion tubes into the chamber to continually refresh the chamber with warmed solution (seen attached to the lid of the box with an in-line heater and the pump in the background).

3.4.1 Application-Specific Integrated Circuits of the Neuroboard

The acquisition system was developed at the AGH University of Science and Technology, Krakow, Poland, and University California Santa Cruz, U.S.A.^{14,122,124,125}, critical components of which are the PlatChips and NeuroChips which populate a PCB board termed the “neuroboard”. The electrode voltage is amplified, filtered and multiplexed by the electronics of the neuroboard, which is connected to an interface board with a 68-pin shielded cable (NI SH68-68-EPM). The interface board acts as a conduit for power supplies, providing +/- 2.5V and +/-5V, with currents controlled by variable resistors on the board. The interface board also enables commands for recording and platinisation protocols to be transmitted from a PC running Labview software (National Instruments) to the neuroboard via a digital input/output cable, while the analogue multiplexed signals from the neuroboard are relayed to the PC via two separate analogue output cables.

Within the PC, two ADC boards, with 4 ADC channels each, digitized the input analogue signals at a sampling rate of 20 kHz for each channel. Each ADC channel is 12-bits, providing 4096 voltage levels over a 5V range (+/-2.5V). Amplification by NeuroChips (gain of 1500) before processing results in a resolution of 0.814 μV per ADC count. With a sampling rate of 20 kHz, the system can record voltage changes of 0.814 μV at 50 μs intervals.

The number of electrodes that can be included in an array is limited by the readout electronics required to amplify and filter electrical signals from electrodes. Low noise electronics are required which process amplitudes of 50-500 μV in a 30-3000 Hz frequency spectrum with a multichannel readout. In the work presented here, ASICs required for data pre-amplification, filtering, and platinisation of electrodes, was primarily divided between two functionally different 64-channel ASIC chips; PLAT-64 and NEURO-64¹²².

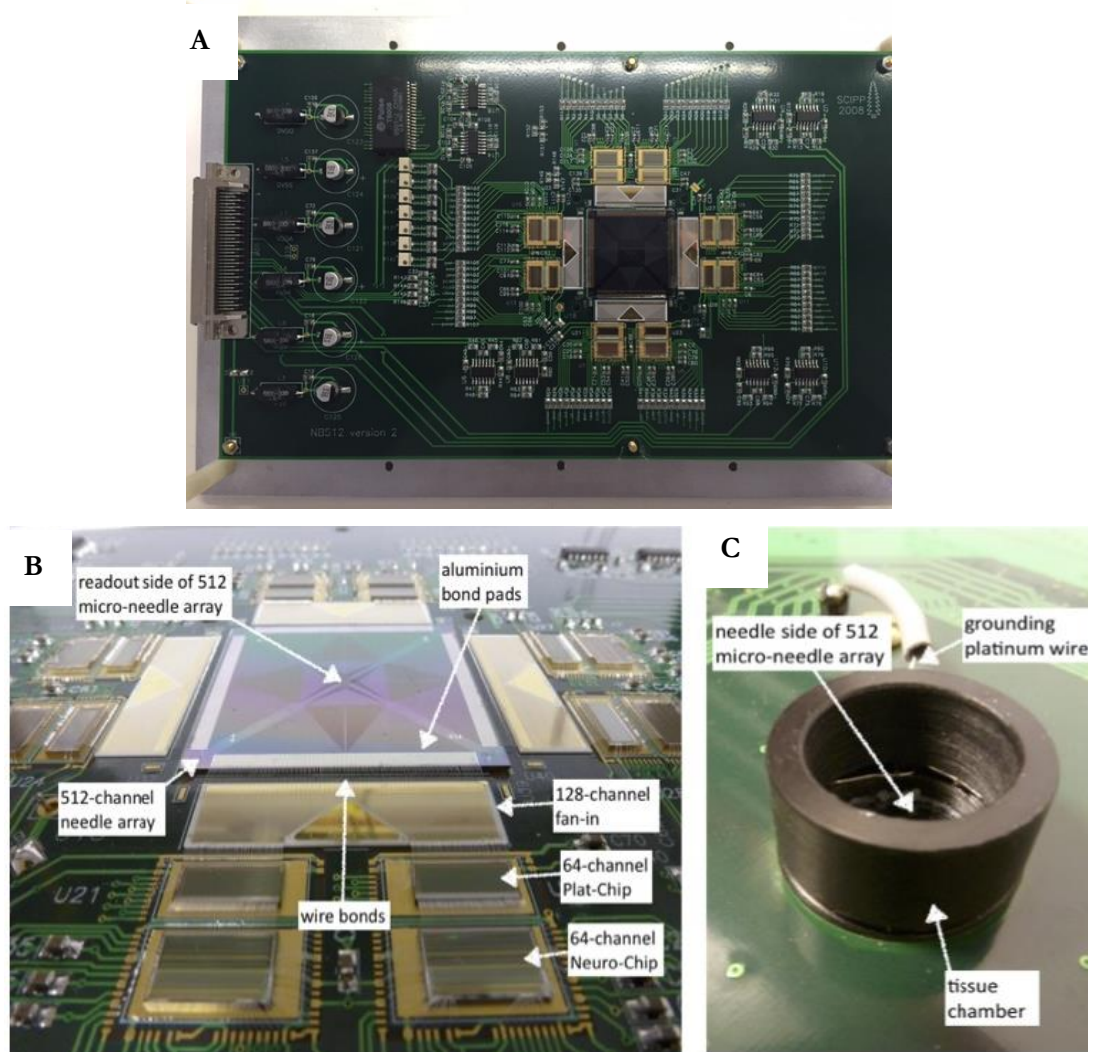


Figure 3. 3. The 512 needle MEA is integrated on a PCB, with the acquisition system consisting of 16 ASICs; eight PLAT-64 chips couple to eight NEURO-64 chips. (A & B) Each of the 64 channels per chip correspond to individual electrodes which are situated on the inverse side of the PCB surrounded by a chamber (C) with which to contain electrophysiological solution, and a ring of platinum wire to function as ground.

An electrode is AC-coupled to a capacitor before the readout connects to the PLAT-64 chip. This is because the reference platinum wire and electrodes sit at slightly different potentials - as electrodes would charge in attempting to match the potential of the reference, the capacitor prevents the chip's amplifier from being saturated. Eight PLAT-64 chips couple the electrodes to eight NEURO-64 chips (Fig. 3.3, B) and act as a switch and supply currents for platinisation of electrodes in the range of 0-500nA controlled by a 5-bit DAC (block diagram of a single PLAT-64 channel can be found in appendix 3). Each of the 64 channels contains a

current generator with a 150pF capacitor; therefore, channels can be individually platinised as required.

During recordings, signals are relayed to a corresponding NEURO-64 chip of 64 channels and a multiplexer requiring a rate of up to 5M Hz¹²². Signals are driven through preamplification, a bandpass filter and a final output amplification stage before a 64:1 multiplexer reduces the number of outputs from 512 to 8 before being relayed to a computer for processing. This acquisition system has demonstrated an input system noise of 7 μ V RMS with 512 electrodes with a passband of 50-2000 Hz¹²². This system has been shown to record neuronal activity across 512 planar electrodes at a rate of 20 kHz in previous investigations of retinal ganglion cells and organotypic slice cultures¹²⁴.

3.5 Platinised Electrodes have Appropriate Impedance to Detect Neuronal Activity

Initial platinisation procedures were performed on a minimum number of electrodes to minimise impact to the entire array. Tungsten electrodes (n = 3) exhibited an average impedance of 480.6 k Ω (\pm 0.74 S.D.) at 1 kHz (Fig. 3.4), corresponding to 1 ms and an appropriate comparison for AP frequencies. As expected, impedance values decreased with increased frequency, demonstrating an AC capacitive coupling between the electrodes and electrolyte interface. After platinisation at 0.004 μ A for 20seconds, the impedance of the electrode at 1 kHz decreased by 51% to a mean of 245 k Ω (\pm 3 S.D.). For comparison, platinised needle electrodes have been previously reported to exhibit a typical impedance of 300 k Ω at 1 kHz¹¹.

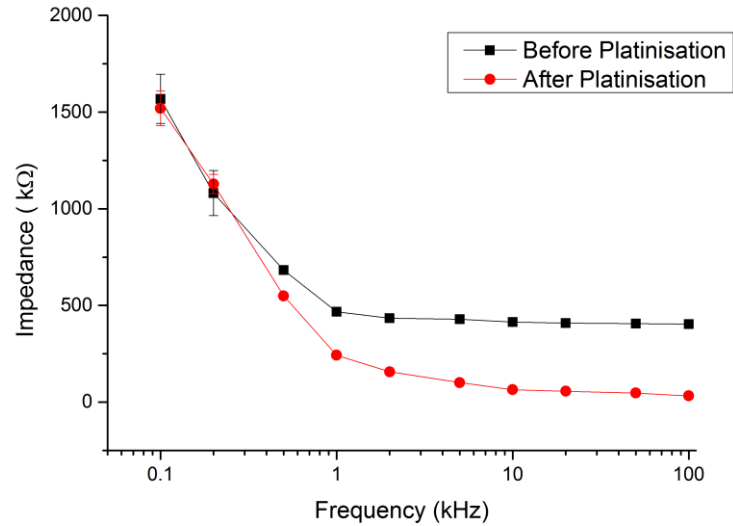


Figure 3. 4. Electrode impedance as a function of frequency. Impedance values for 3 electrodes measured before and after electroplating with platinum at a current density of $0.04 \mu\text{A}$ applied at 1V. For voltage applied at 1 kHz, the electrode's impedance is reduced from $480.6 \text{ k}\Omega$ to $245.6 \text{ k}\Omega$ following the formation of granular platinum black at the electrode surface. Black = tungsten electrode, red = platinum electrode. Error bars S.D.

Following successful platinisation of 3 electrodes, alternative currents were applied to investigate an optimal protocol for platinisation. Tungsten electrodes ($n= 6$) exhibited impedances of 390 to $599 \text{ k}\Omega$ (Fig. 3.5, A) and were electroplated using current densities of 0.5 , 0.75 or $1 \text{ nA}/\mu\text{m}^2$ (current input of 100 nA , 150 nA and 200 nA) applied for either 20s or 30s on individual electrodes. All electrodes exhibited a decrease in impedance following platinisation, ranging from 227 - $269 \text{ k}\Omega$. Higher current densities did not produce a greater decrease in impedance. Similarly, increasing the duration of electroplating did not result in a greater decrease in impedance at any of the attempted current densities (Fig. 3.5, B) and impedances were reduced by an average of 52.4% . Following platinisation, electrode impedances demonstrated less variation ($\pm 16.6 \text{ k}\Omega$ compared to $\pm 74.4 \text{ k}\Omega$ for tungsten electrodes prior to platinisation) suggesting platinisation also improves uniformity of performance across electrodes.

Low current densities were used as a precaution – an excessively large surface area leads to inaccuracies in local potential events as the recorded signal is averaged over a relatively large area and can impact recorded signal amplitudes¹²¹. This spatial averaging can attenuate amplitudes and has a greater impact on electrical sources closer to the electrode, for example

it has been shown that 11 μm and 86 μm diameter electrode detect the same signal amplitude at a signal source distance of 20 μm , but at 1 μm this signal is attenuated by 25% at the larger electrode¹²⁶. Briefly electroplating with a current of 100nA for 20s reduced impedances to appropriate values of 150-300 k Ω and was found to consistently reduce impedances by \sim 50% (Appendix 4). Therefore, this was determined as a suitable platinisation protocol for microelectrodes.

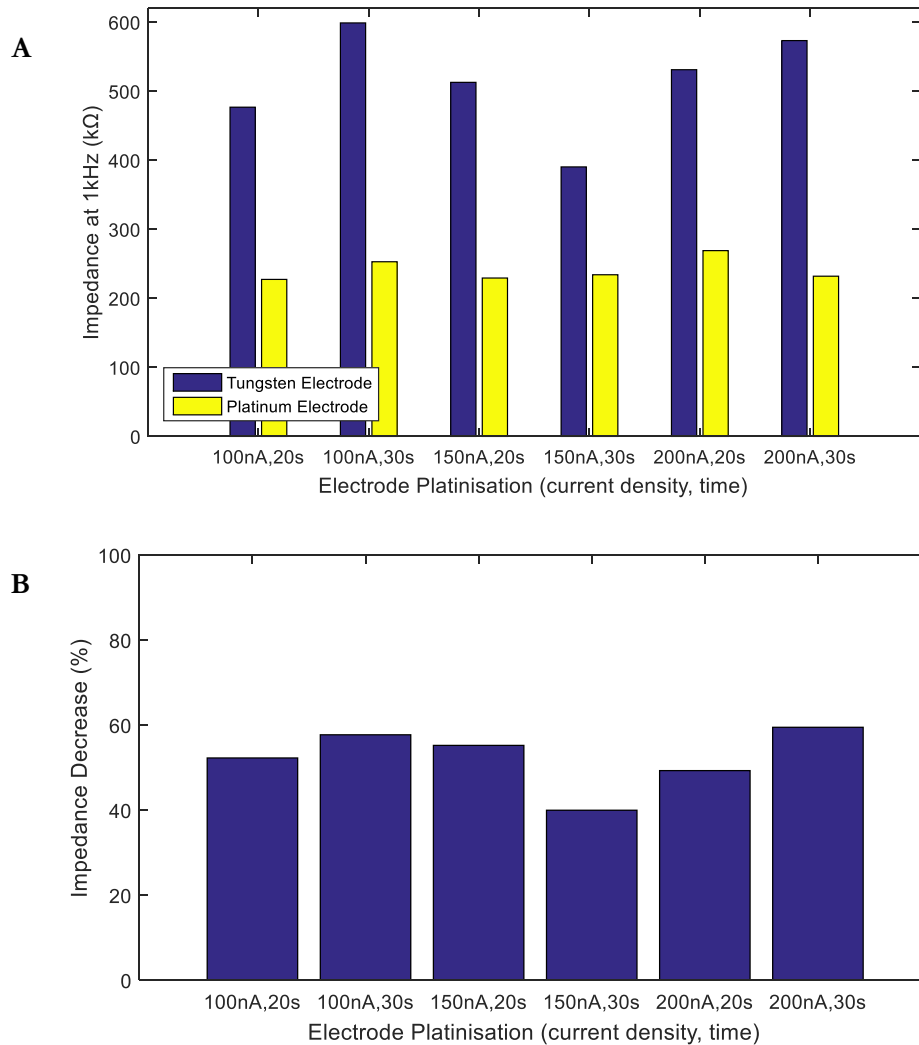


Figure 3. 5. (A) Six electrodes were individually platinised in turn, and a current of 100nA, 150nA or 200nA was applied. Tungsten electrode surface area was calculated to be 200 μm^2 , corresponding to current densities of 0.5, 0.75 or 1nA/ μm^2 , and electrodes were platinized for either 20 or 30 seconds. Electrodes impedances were measured at 1 kHz. Each platinisation protocol reduced impedances below 300 k Ω , indicating a suitable impedance level to record extracellular neuronal signals. (B) No trend was observed across platinisation protocols. Increasing current density and time of current application did not enhance the

decrease in impedance following these protocols. Electrode impedances were reduced on average by 52%, ranging from 49.3% to 59.5%. Error bars (S.D.) were excluded due to the stability of measurements resulting in very low values.

3.6 Readout Channels Are Not Capacitively Coupled.

Prior to integrating the MEA into the acquisition system, the inter-channel capacitances of the MEA channel readouts were investigated to determine if parasitic capacitance was evident and could impact recordings. This was due to concern that the semi-conductive properties of the silicon substrate would carry charge between the insulated electrode channels. Two probes were applied to bond pads, capacitances measured using an LCR meter (Iso-Tech 800), then one probe was moved to the next bond pad and measurements repeated. This was repeated at several locations on the readout side of the MEA as the readout tracks differed in length depending on the location of the corresponding electrode. Capacitances between bondpads remained stable across the array with a typical range of 8.5-11pF. Measurements representative of capacitances seen across the array are presented in Fig. 3.6; there was no change in capacitance over distance between bondpads and different track lengths did not exhibit a bias in this property. This indicates that channels in the MEA do not demonstrate direct capacitance, as there is no correlation between readout track distance, but suggests that channels display capacitance to the substrate itself in the range of 20pF (a 20pF inter-channel capacitance would be recorded as ~ 10 pF capacitance to substrate as observed). This low value capacitance would not significantly impact recording quality.

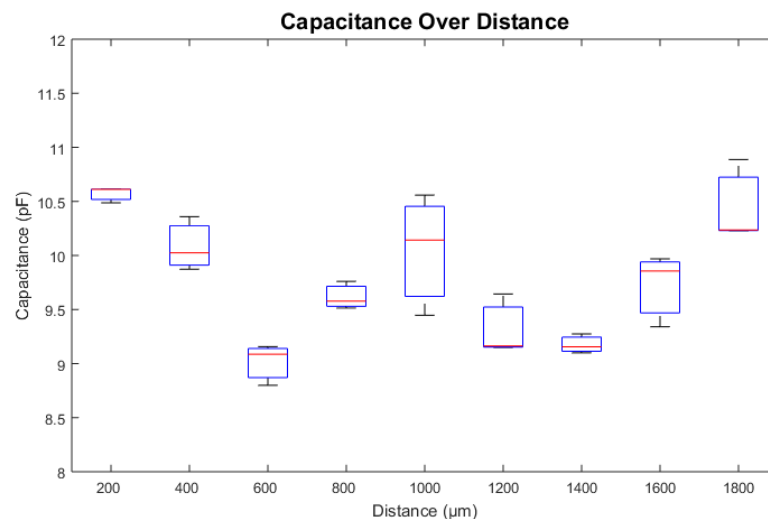


Figure 3. 6. The capacitance between electrode readout channels was measured by applying probes to channel bondpads. Measurements typically ranged from 8.5 pF to 11 pF and was

consistent across distance between channels and the different lengths of channels required for the readout of 512 electrodes. This figure is a representative example, where one probe remained at contact and the other was moved to successively distal contacts.

3.7 Biological and System Noise

Previous experiments using a similar setup with 61 recording electrodes have determined the electronics of the system to contribute ~ 5 μV RMS input noise and a ~ 7 μV noise level recorded from electrodes immersed in saline solution¹⁴. Measured in 0.1M saline solution (0.9% NaCl) in the absence of tissue, the system presented here recorded an RMS noise of ~ 10 - 12 μV . These measurements are more relevant when brain tissue is applied to the electrodes and setup is more complete, as non-stationary biological noise is additionally present. Therefore, the data presented here is of electrode noise recorded in the presence of a rat brain slice. During the initial minutes, brain slice recordings exhibit very low (or complete absence of) neuronal activity. Therefore, a noise evaluation of 15 seconds of recorded data was performed which corresponds to 300,000 samples per electrode channel. The combined biological and system noise across all electrodes accounted for a mean of 15.35 μV RMS input (± 0.1 μV S.D.). This includes two disconnected electrodes exhibiting high noise values (black boxes, Fig. 3.7) which are likely either broken or the result of a defect during fabrication. Exclusion of these channels from analysis does not significantly alter the average noise, which ranges from 11.8-17.8 μV (Fig. 3.7). Several channels exhibited significantly lower noise and were suspected of being electrically shorted (red dashed boxes, Fig.3.7). Using a 32-channel probe card and a data acquisition system (Keithley, 2701), resistances between electrode channel bond pads were measured to identify these electrodes. A total of 20 channels displayed low resistance to a neighbouring channel (10-900 Ω) compared to the remainder, measurement of which was limited by the maximum measurement of the acquisition system. Of these shorted channels, 3 triplets and 4 pairs were found, suggesting poor insulation of these channels on the MEA readout.

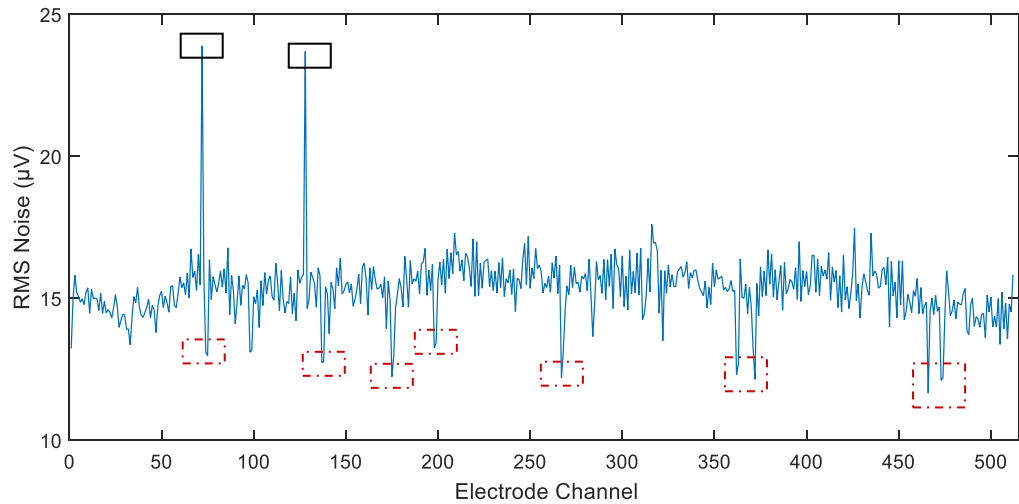


Figure 3. 7. The RMS noise input averaged over 15seconds with tissue placed on the array immersed in physiological solution. The average noise over all channels was $15.35 \mu\text{V}$ with an average standard deviation of $0.1 \mu\text{V}$ (not shown). Channels 72 and 128 (black boxes) are disconnected and therefore exhibit higher noise values, while most of the electrodes that measured noticeably lower noise (dashed red boxes) were paired neighbours, suggesting these channels had been shorted together.

The spread of electrode noise can be seen in Fig. 3.8 (excluding disconnected channels) and 72% of the 512 channels exhibited an RMS noise value between 14 and 16 μV . An electrode RMS input noise of $\sim 15 \mu\text{V}$ is sufficiently low enough to detect neuronal spikes with a peak amplitude $>80 \mu\text{V}$. As the tissue becomes more active in the presence of the solutions used during recordings, it is reasonable to expect an increase in the background biological activity and a subsequent increase in RMS noise; however, a further 15s noise analysis taken 20minutes into recording from tissue showed this increase was observed to be on average $0.86 \mu\text{V}$ ($\pm 1.2 \mu\text{V}$ S.D.) which is slight enough to be negligible.

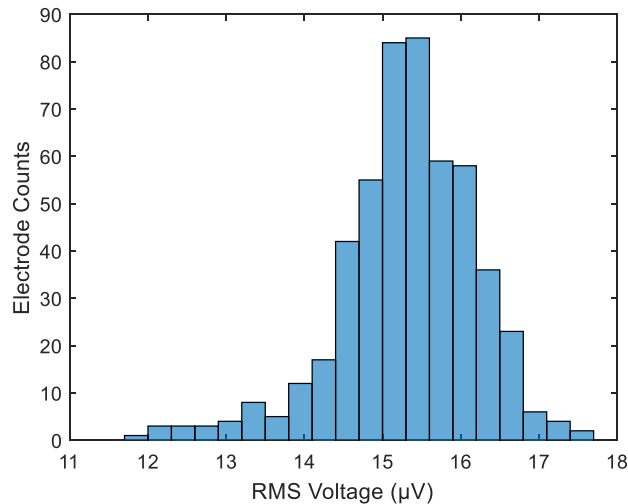


Figure 3. 8. Histogram of electrode noise distribution excluding two disconnected, high noise, channels. The mean RMS input noise for each electrode was measured over a 15second recording period; corresponding to 300,000 samples. Electrodes exhibited a mean noise of 15.35 μV (± 1 S.D.), while electrodes with a recorded noise level in the range of 14 to 16 μV accounted for 72% of channels.

3.8 Discussion: Electrical Characterisations

The novel MEA presented here was fabricated at the University of Strathclyde using photolithographic techniques. The device consisted of 512 tungsten electrodes, each insulated in a 3-dimensional needle of silicon dioxide, with 60 μm pitch. The tips of the needles were etched to expose the tungsten electrodes which measured a 5x5x20 μm pyramid. The electrodes covered an area of 1mx2mm, and readout channels were etched on the opposite side. The fabrication of 512 high-density needle MEAs did not compromise the properties of electrodes, which demonstrated electrical characteristics suitable for the extracellular recording of multiple neurons simultaneously.

Tungsten electrodes can be uniformly and effectively platinised at a current density of 0.5nA/ μm^2 for 20seconds to reduce electrode impedance by $\sim 50\%$. Increasing the current input, and applying for longer periods, did not enhance this effect. The deposition of granular platinum may reach a saturation point on exposed tungsten. The etching process (see section 3.1) may not have been uniform across electrode tips, therefore, increased platinum surface area would have limited impact on impedance

. Capacitances measured between electrode read out channels did not exhibit correlation with distance, indicating that the capacitances measured are the result of channel

capacitance with the silicon substrate and not directly between readout channels. The low values for this capacitive mechanism (~ 10 pF) indicates the MEA fabrication process can successfully insulate readout channels and did not impact the quality of recordings.

The input noise generated by the system was a critical factor in verifying the suitability of the system as excessive RMS noise would obscure electrophysiological events. The system presented here exhibited an RMS noise of ~ 10 - 12 μV , comparable to previous studies using a similar setup¹⁰. In the presence of brain tissue, this increased to an electrode average to 15 μV , however, this value is still an appropriate level with which to identify extracellular spikes which are commonly greater than 100 μV in amplitude.

The scale and fragility of the microneedles and the electrode readout channels makes the device prone to damage or fabrication defects. Only 20 channels of the 512 electrodes were found to be electrically shorted (3.9%), indicating a reliable process of fabrication. These electrodes can be consistently and uniformly platinised to provide the required impedance values, which decreases the input noise of the system to suitable levels to recording extracellular neuronal activity.

Characteristic	Average Values	Summary
Tungsten impedances at 1 kHz(kΩ)	490 \pm 74	
Platinum Impedances at 1 kHz(kΩ)	250 \pm 17	Not reduced below 200k Ω at any attempted parameters
Impedance reduction (%)	52	
Capacitive coupling (pF)	9.8	
System noise (μV) at 1 kHz	11.5 (1:11)	Interface and front-end amplifier
Biological noise (μV) at 1kHz	15.35 (1:15)	SNR of 1:15 reported in comparable device ¹¹
Shorted Channels (%)	3.9	20 channels out of 512

Table 3. 1. Summary of the electrical characteristics of the 512-needle MEA. The device exhibits appropriate properties with which to achieve the experimental aim and compares favourably to previously evaluated devices of similar design.

4. Neuron Identification and Population Evaluation

This chapter will detail the experimental procedures that were used to characterise electrophysiological recordings of acute brain slices with the novel MEA and the spike sorting parameters used to identify distinct individual neurons. This process consisted of: the preparation of acute slices and the means used to maintain viability during recordings; the analytical approach to spike sorting using a custom-designed software from University California Santa Cruz¹⁴; and justification for the use of certain parameters in further analyses. Features of the recording, for example evaluating electrical and biological noise of the setup, will be summarized before a broad discussion of the spike amplitudes and frequencies exhibited by the neurons. This information was then used to refine parameters to use for connectivity analyses.

Dissections were performed according to a previously described method¹²⁷, but modified to provide acute coronal slices. The procedure allowed access to a large portion of cortex which could be easily arranged over electrodes. Slices were maintained in solutions of artificial cerebrospinal fluid (aCSF), which is commonly used for *in vitro* neuronal studies to substitute physiological cerebrospinal fluid¹²⁸. These aCSF solutions contained different concentrations of specific salts depending on the stage of their preparation; for instance, during sectioning, tissues were immersed in a solution containing a high sucrose concentration. Warmed artificial cerebrospinal fluid with elevated potassium content was oxygenated and perfused over the tissue for the duration of recordings, which typically lasted 4 hours.

Numerous recording attempts were made, however, the data for this chapter is limited to the recording which identified the highest number of neurons effectively separated from noise. Comparisons between datasets were not completed as most recordings were impacted by electrical noise artifacts or acquired insufficient electrophysiological data to identify neurons. These challenges are discussed in chapter 8.

The approach to spike sorting was based on PCA, a method of feature extraction and dimensionality reduction (see 2.3.1), but additional stages of data analysis are required to identify neurons. Briefly: a voltage threshold is applied to waveforms recorded on electrodes and separates electrical events unlikely to be the result of noise; PCA is then performed on data derived from groups of electrodes to cluster events with similar attributes; further thresholds are then applied to remove duplicate spikes and to improve PCA clustering of electrical signals. Resulting waveforms are then manually evaluated prior to further analysis. Several spike sorting parameters were applied to the data to maximise the quality and

number of neurons identified. The optimum parameters were found to be a threshold setting of 6, which was multiplied by the RMS input noise measured on each individual electrode, with a small allowance for correlation and contamination of signals. These parameters initially identified 74 neurons and, following manual assessment of average waveforms and clusters, an additional 4 neurons were identified to provide a total of 78.

The SNR of neurons to electrodes were found to be at an appropriate level to cleanly detect neuronal signals (~10:1). This was consistent across each neuron and corresponding electrode – indicating the device’s stability in recording neurons and a successful fabrication technique. An evaluation of changes to each neurons’ spike rate over time indicated that most neurons displayed a dramatic decrease in spike rate following the initial 2 hours of recording. However, the amplitudes of spikes remained constant over the full 4 hours of recording suggesting the reduced frequency was not the result of a deteriorating interface between electrode and neuron. Parameters with which to further assess neurons were then compiled and the characteristics of each individual neuron was assessed. Comparisons between neurons highlight the variety of neuronal properties across the population and provided an estimation of parameters with which to approach connectivity analysis.

4.1 Experimental Setup and Spike Sorting

To record spike activity which reflects normal connectivity, slices must be maintained in solutions with appropriate oxygen, glucose and ion species content in order to mimic physiological conditions and to remain viable. However, the trauma of dissection, and subsequent sectioning, initiates molecular inflammatory responses which alter the electrophysiological behaviours of neurons (see section 2.2.4). Therefore, alterations are made to aCSF solutions to limit changes in activity and maintain normal functionality. Previous studies have modified the concentration of solutes and temperature of solutions to optimise cell survival^{1,2,3} by including a sucrose-rich solution as an equimolar replacement. Therefore, three different solutions were used during tissue preparation for electrophysiological recordings.

4.1.1 Dissection Procedure

Animals were maintained at the Biological Procedures Unit at the University of Strathclyde and procedures were performed according to protocols outlined by UK Home Office

legislation. Sprague Dawley rats (p14-21) were sacrificed by cervical dislocation, the brain was removed and placed directly into a vial of ice-cold artificial cerebrospinal fluid (aCSF). This solution consisted of 124nM NaCl, 3mM KCl, 2mM MgSO₄, 1.25 mM NaH₂PO₄, 26mM NaHCO₃, 10mM D-glucose and was oxygenated with carbogen (95% O₂, 5%CO₂) for 15-20 minutes prior to addition of 1mM CaCl₂. Brains were kept in aCSF for 3 minutes to allow the entire organ to cool and lower metabolic rate with the aim of minimising excitotoxic and apoptotic mechanisms.

Brains were then placed onto a filter paper moistened with a sucrose-modified version of aCSF (206mM sucrose, 2mM KCl, 1mM MgCl₂, 2mM MgSO₄, 1.25mM NaH₂PO₄, 26mM NaHCO₃, 10mM D-glucose, 1mM CaCl₂) where the cerebellum was removed, and the two hemispheres separated medially (dotted line in Fig. 4.1, A). Tissues were then fixed to a vibratome stage on an anterior-dorsal vertical axis (dorsal fixed to the stage) and bathed in oxygenated sucrose-aCSF. Next, a vibratome (Intracel 1500) was used to section 350 µm thick coronal slices starting ~0.5 Bregma.

Brain sections were taken from each hemisphere and transferred to a custom-made incubation chamber (Fig. 4.1, B). This was developed in response to earlier experiments highlighting that even low-pressure oxygenation could induce a vortex in the solution, potentially physically damaging slices. Partially trapping oxygen bubbles allowed for low-pressure oxygenation to be used and increase oxygen solubility. However, an oxygen sensor was not available to verify this. Sections were kept in the chamber at room temperature aCSF for 60 minutes to allow equilibrium in the new medium to occur.

Sections were then transferred to the MEA chamber using a shallow plastic scoop, taking care to limit contact with tissues. While floating in the chamber, liquid was carefully removed via a syringe which allowed the tissue to contact the electrodes. The cortex was positioned over the needles during the solution removal and approximately the same area was used during each experimental repetition (Fig. 4.1, A, white box). Recordings aimed to provide an assessment of the acquisition system, rather than focussing on a specific cortical area.

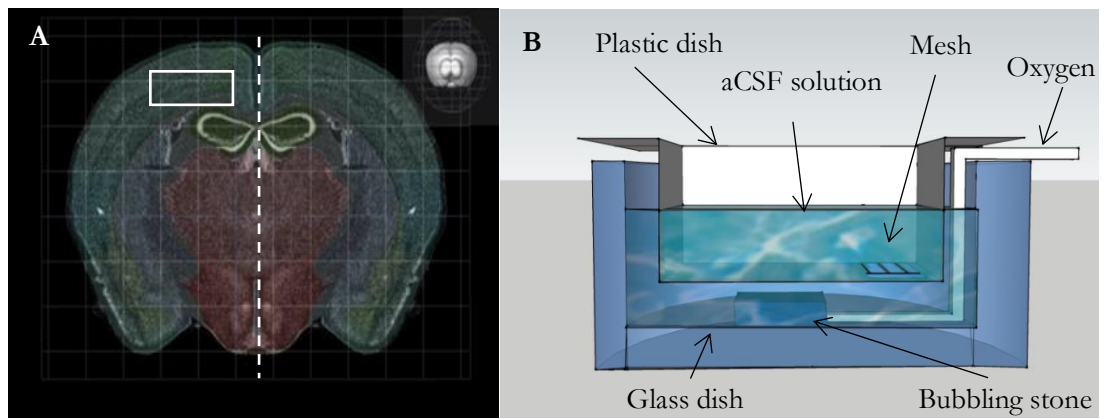


Figure 4. 1. Coronal sections (A) were taken from rat brains allowing access to a large portion of cortex which could be easily arranged over electrodes. Prior to sectioning, hemispheres were separated as the recording chamber could not easily accommodate sections of this size (dotted line). Sections were arranged over electrodes to record from approximately the same cortical area for each attempt (white box). Image sourced from Allen Brain Atlas². (B) Sections were incubated in oxygenated aCSF for one hour at room temperature in a custom-made incubation chamber before recordings began. Oxygen was supplied from a pressurised oxygen tank and fed through tubing to a bubbling stone in the incubation chamber. The oxygen source (bubbling stone) was separated from direct contact with sections by a plastic dish, but oxygenated solution could be refreshed via a mesh at the base.

4.1.2 Recording Procedure

Once excess solution had been gently removed with a syringe, a resistance seal with an osmotic membrane was placed over the tissue and aCSF applied over the membrane (Diagram 4.1). Care was required to lower this seal – the tissue could float and not contact the electrodes or could be crushed by excessive force.

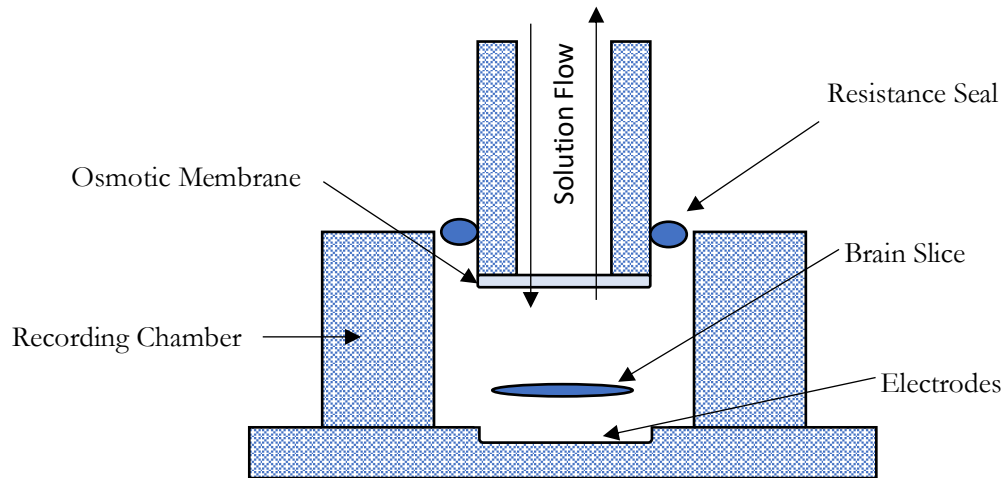


Diagram 4. 1. Schematic of the positioning of slices on the MEA. Electrodes are located at the base of a chamber which was filled with eCSF. Sections were placed in the chamber and positioned over electrodes, before liquid was carefully removed using a syringe. A resistance seal with an osmotic membrane was then placed on top to secure the tissue against electrodes and eCSF perfused over the tissue.

During recordings, acute slices were perfused using a perfusion pump (Cole Parmer, Masterflex C/L) at a rate of 2ml/min with oxygenated excited-aCSF (eCSF). This solution resembles aCSF but with increased KCl content (increased to 5mM from 3mM) to stimulate neuronal activity. Before reaching the array chamber, perfused eCSF was heated with an in-line heater (Warner Instruments, TC-324C) and a thermistor connected to the heating system was used to ensure the solution at the bottom of the chamber was 37°C. The supply of eCSF was continually oxygenated and solution was circulated through separate perfusion tubings.

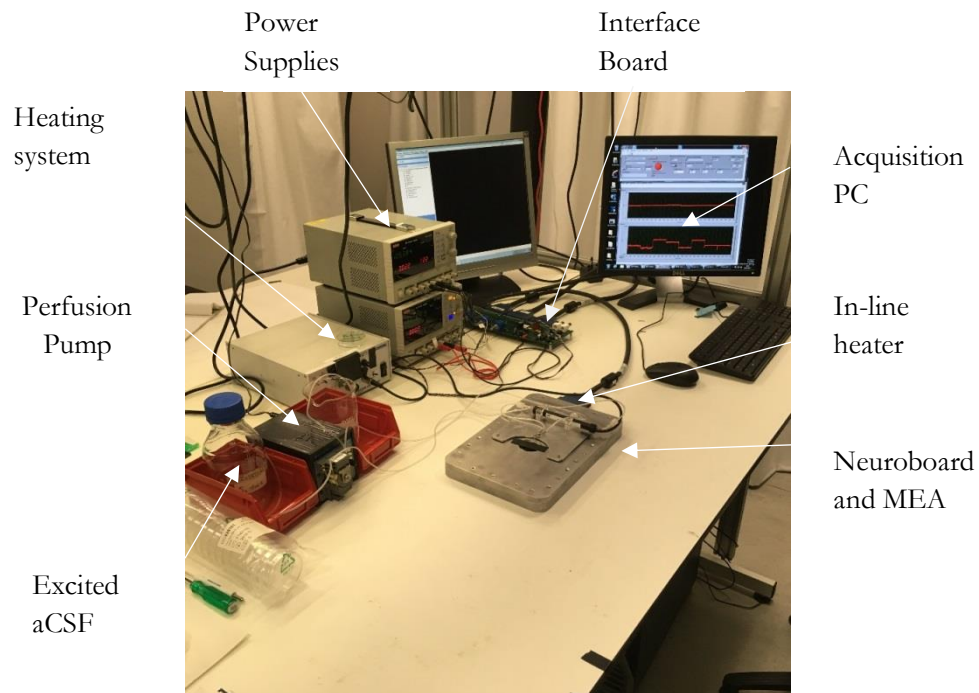


Figure 4. 2. Experimental layout for electrophysiological recordings. Excited aCSF is perfused through the in-line heater before reaching the array chamber and is circulated using the same pump. The interface board relays raw data (bandpass filtered) from the neuroboard, which the MEA is wire bonded to. The interface board also connects and filter voltages from both power supply units ($\pm 5V$ and $\pm 2.5V$) required by the neuroboard. Signals are then digitized by two ADC boards, each with 4x 12-bit channels, and processed using LabView software.

4.1.3 Spike Sorting and Neuron Identification

Presented in the following sections is a high-quality recording from an acute slice of rat cortex which identified 78 unique neurons. Acute slice recordings were typically four hours long. The time limitation of four hours is a result of a significant drop in activity which is discussed in the following sections. Many experiments did not exhibit a sufficiently high SNR to identify discrete neurons (further discussed in chapter 8), however, the data presented here demonstrate clear clustering of well-defined neuronal spikes. This indicates that the spike sorting method is appropriate for interpreting data derived from acute slices via the needle MEA and processed through the neuroboard system. This section outlines the capability of the spike sorting method used and provides justification for the use of parameters on which further analytical investigations were based. The impact of electrical and biological noise was then evaluated to demonstrate an appropriate SNR to record neurons is achievable with this

system. As the activity (spiking frequency) of most neurons significantly decreases after 2 hours of recording, a brief outline of the overall population activity is provided as justification for subsequent chapters focussing on the initial 2 hours of recording. Additionally, a summary of neuron properties, such as spike amplitude, during this time period is included.

The spike sorting process occurs over several stages (Fig. 4.3) and several example parameters and results are listed below (table 4.1). Initially, a sigma value is chosen to represent the deviation from RMS noise spike voltages are likely to be detected at – a voltage significantly more negative than the noise. This estimated value was multiplied by the threshold setting to generate a threshold voltage, i.e. a voltage value which, ideally, has a low probability of resulting from system noise. Next, 5-dimensional PCA clustering is performed (as described in section 1.3) to reduce the dimensionality of data. After identifying clusters of neuron waveforms, and defining them as an individual unit, further contamination and correlation thresholds are applied. Contamination and correlation values indicate how cleanly the spikes are identified and separated from each other and lower values maintain a more stringent threshold of identification. Contamination refers to the Gaussian clustering of data during PCA – the clusters with significant overlap indicates electrodes have detected electrical events which cannot be easily attributable to an individual neuron. The autocorrelation function is applied based on a neuron refractory period of ~ 1.5 ms¹⁴ and neurons that have highly correlated spike times may not be discrete cells as initially processed but duplicates detected by several electrodes.

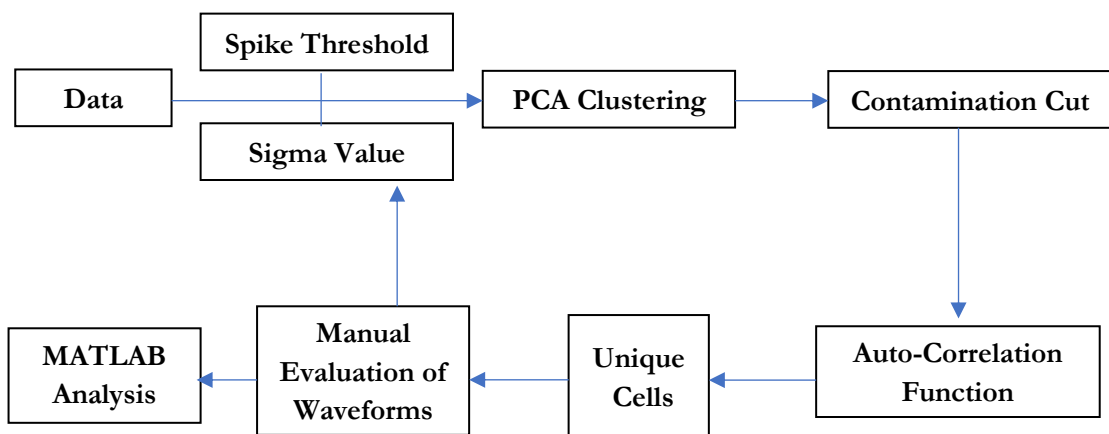


Figure 4. 3. Flow chart schematic of spike sorting. A voltage threshold value is multiplied by a sigma value derived from the RMS input of each individual electrode; a signal which goes beyond, and then returns past, this value is incorporated into the next stage of analysis. After

PCA clustering, correlation and contamination thresholds are applied to the clusters to ensure spikes are clearly identified and allocated to an individual neuron and not duplicated. The results are evaluated manually and re-assessed for further processing.

Initially, threshold voltage and sigma values could be chosen arbitrarily to ensure only spikes were included. This was used as an initial evaluation of how appropriate chosen parameters were, however, more accurate was to use the RMS noise value calculated for each electrode, which accounts for discrepancies between electrode RMS noise input values. The variation of these RMS noise values can be seen in section 3.7 and averaged $\sim 15 \mu\text{V}$.

Ideally, neuron clusters would be highly distinct, and exhibit a correlation value (determined through the auto-correlation function) and contamination value (determined by how effectively PCA clustering separates the signals) of zero. Although minimising contamination and correlation parameters ensured highly defined neurons, these parameters can be set too stringently to identify many units (see parameter combinations #1, 2 and 3 in table 4.1). Following discussions with the developers of the spike sorting software, a recommended relaxation of the correlation and contamination parameters (relating to spike timing differences and the overlap of Gaussian distributions of PCA clustered samples) still maintained a realistic means of defining individual units whilst increasing the number of units identified; as can be seen from parameter combinations # 4, 5, 7, 9 and 10 in table 4.1 (combinations #6 and 8 are included for comparison of higher parameter values only).

Parameter	Sigma Value	Threshold Setting	Correlation	Contamination	Raw Neurons	Processed Neurons	Unique Cells	Average Spikes/Cell
1	6	10	0	0	4	1	1	300
2	6	8	0	0	72	18	18	569
3	RMS	8	0	0	41	16	7	986
4	RMS	7	0.25	0.3	128	31	31	982
5	RMS	6	0.25	0.3	300	74	74	531
6	RMS	6	1	0.85	300	73	73	562
7	RMS	4	0.25	0.3	2844	1419	1414	106
8	RMS	4	1	0.85	2844	1419	1414	106
9	RMS	5	0.25	0.3	925	206	205	179
10	RMS	3	0.25	0.3	3230	1564	1559	101

Table 4. 1. Summary of numbers of neurons identified using different spike sorting parameters. Strict parameters resulted in a low number of highly defined neuronal units; while relaxing these settings allowed for more units to be identified, more noise is introduced into the analysis which degrades the quality of recordings. Quality of recordings was assessed by manually reviewing the PCA clusters of spike data points and the average waveforms generated. Parameters using the electrode noise value and threshold setting of 6 resulted in 78 unique neurons which satisfied the criteria of high-quality neurons (bold outline). Further analysis proceeded using this dataset.

The parameters in row 5 were used for further analysis. Similar parameter settings could produce varied results; for example, comparing rows 5 and 9 in table 4.1 shows that increasing the threshold setting increases the likelihood of identifying cells, but drastically limits the average number of spikes allocated to that cell. In this comparison, with an average RMS noise value of 15 μV (see section 4.2) row 5 has a spike amplitude threshold of 90 μV and row 9 a threshold of 75 μV . Therefore, settings in row 9 detect more signals and subsequently suggests a large number identified neurons. However, this larger dataset makes clustering less defined and to accurately assign spikes to discrete units the number of spikes per cell is consequently much smaller than results from row 5 settings. As cells with < 100 spikes/cell would be discounted from further analysis, it was decided that the results in row 9 did not provide sufficient data. Spatial temporal qualities of the array and their usefulness regarding connectivity investigations were therefore considered. A small number

of neurons detected over distal locations on the array are less likely to share functional connections, however, a reasonably high number of spikes per neuron (~ 200) are required to make connectivity investigations relevant. The spread of neurons across the array in the selected parameter dataset is discussed in a later section (section 6.2), while spike frequencies and amplitudes are summarized below.

Quality of recordings was assessed by manually reviewing the PCA clusters of spike data and the average waveforms generated. Parameters using the electrode RMS noise value and threshold setting of 6 (Table 4.1, bold outline) resulting in 74 unique neurons. Additional manual assessment of the clustering (using custom software CellFinder to examine dimensional clusters in 2 dimensions) produced a further 4 neurons for analysis. The 78 neurons had been allocated a reasonable minimum spike rate (minimum 100 per neuron) and coherent extracellular waveforms were observed (Fig. 4.4). This dataset satisfied the criteria of a reasonable number of high-quality neurons to investigate connectivity. Further analysis proceeded using this dataset and was performed using Matlab software.

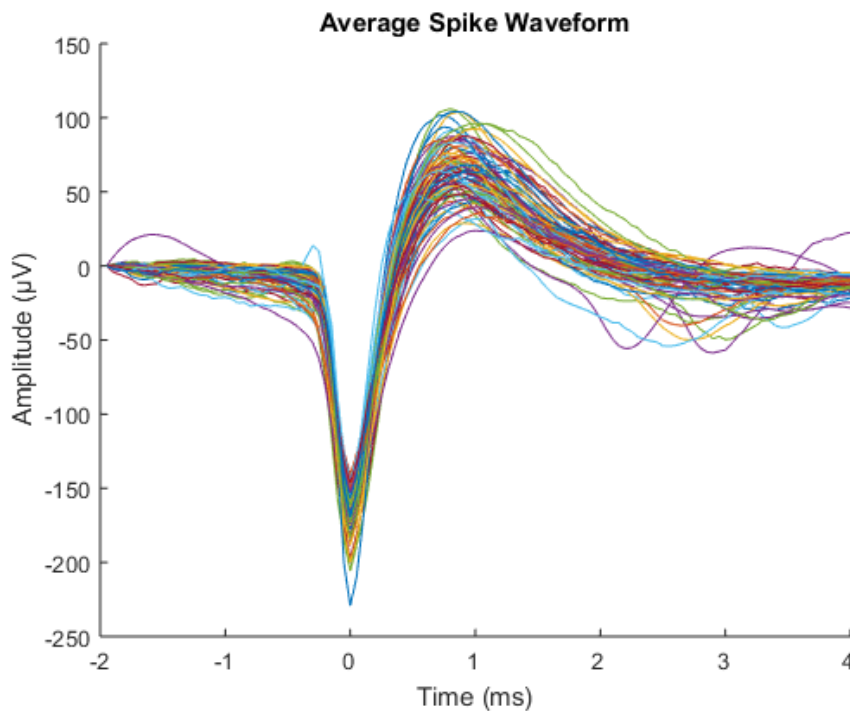


Figure 4. 4. The average spike waveform for each individual neuron in a spike sorting parameter dataset which identified 78 unique neurons (dataset #5 in table1). Individual units were identified by PCA clustering and subjected to a correlation, contamination and spike count limit, had each spiking event attributed to it plotted as a function of time and amplitude with the minimum recorded amplitude centred at $t = 0$ ms. The spike amplitude was recorded

from the electrode which first detected an electrical event which was attributed as a spike and assigned to the respective neuron. All spiking events per neuron were plotted this way and averaged to provide an average spike waveform for each neuronal unit. Further analysis of waveform characteristics is provided in chapter 5.

4.2 System Noise and Signal Evaluation and During Recordings

As discussed in chapter 3, the input RMS noise of the acquisition system in the presence of tissue was appropriately low enough to detect neuronal signals and previous experiments achieved quality recordings with a similar range of noise values. To assess whether neuron detection was limited to electrodes with exceptional SNR, the RMS noise of electrodes that identified neurons (termed “seed” electrodes) were evaluated using seconds of recorded data. This corresponds to 300,000 samples per electrode channel (20 kHz sampling rate). The mean noise of seed electrodes ($15.5 \mu\text{V} \pm 0.4$) was comparable to that of non-seed electrodes ($15 \mu\text{V} \pm 0.7$), while the mean noise across all electrodes was $15.32 \mu\text{V} \pm 0.8$. The seed and non-seed electrodes groups exhibited significantly different RMS noise ($p < 0.05$, student’s t-test), and this excludes groups of shorted, low-noise, non-seed electrodes and two ungrounded, electrically floating, electrodes, however this difference is likely due to the difference in population numbers (74 seed to 438 non-seed). Seed electrodes did not exhibit outlier noise values which could indicate a bias in detecting spikes (Fig. 4.5, A). The seed electrode noise ranged from 14.64 - 16.07 μV (Fig. 4.5, B) which was an appropriate level to detect neuron spike amplitudes.

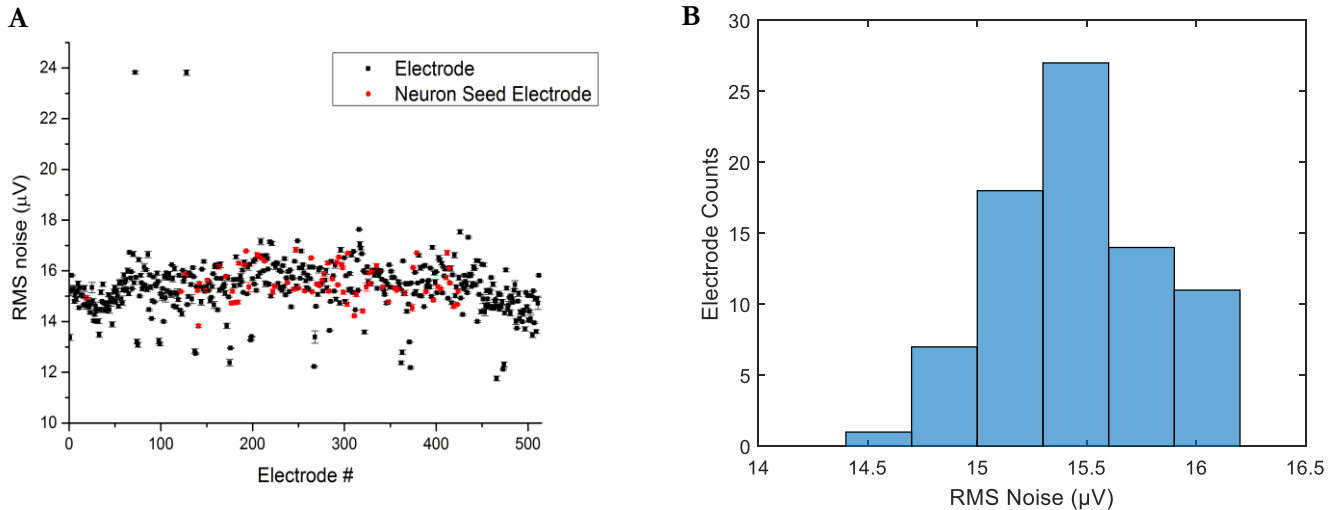


Figure 4. 5. RMS input noise of electrodes over three 5 second periods during first minute of recording from brain tissue. (A) Each point represents the RMS noise of an electrode: red points are seed electrodes which detected peak spike amplitudes of neurons; black dots correspond to electrodes not associated with neurons (error bars standard deviation). Seed electrodes did not exhibit outlier noise values. (B) Histogram of the RMS noise on each seed electrode. Over half electrodes (44) exhibited an RMS noise value of 15.04 μV - 15.64 μV .

The average spike threshold value for spike sorting parameters is 92.76 μV (this varies based on electrode RMS) and most spike amplitudes exceeded 100 μV (Fig. 4.6, A). The spike amplitude count per neuron (Fig. 4.6, B) demonstrates the distribution of spike amplitudes for each neuron. There is a clear discrepancy between neurons with high spike count detected by the MEA and most cells that have a peak of less than 200 spikes. However, the range of amplitudes is relatively consistent across all neurons (from \sim -100 μV to \sim -250 μV). The large variation in spike amplitudes may be the result of spike rate changes over time as spike amplitude has been shown to significantly reduce in the majority (86%) of substantia nigra neurons in response to increased firing rates¹²⁹. Yet, amplitudes in these neurons were not found to significantly increase following a dramatic reduction in spike rate in the second half of recordings (see Fig. 4.10). Potentially, perturbations in the incubation chamber (due to, for instance, the perfusion system) could cause the tissue to oscillate and result in attenuation of the signal amplitude.

The RMS noise value for each seed electrode was then compared to the average spike amplitude for each associated neuron to calculate the specific SNR for each neuron: electrode interface (Fig.4.7). The average SNR was 10.4 ± 1 which is an appropriate ratio to

discern high amplitude spikes to cluster neurons and consistent with earlier reports using a similar system¹⁵.

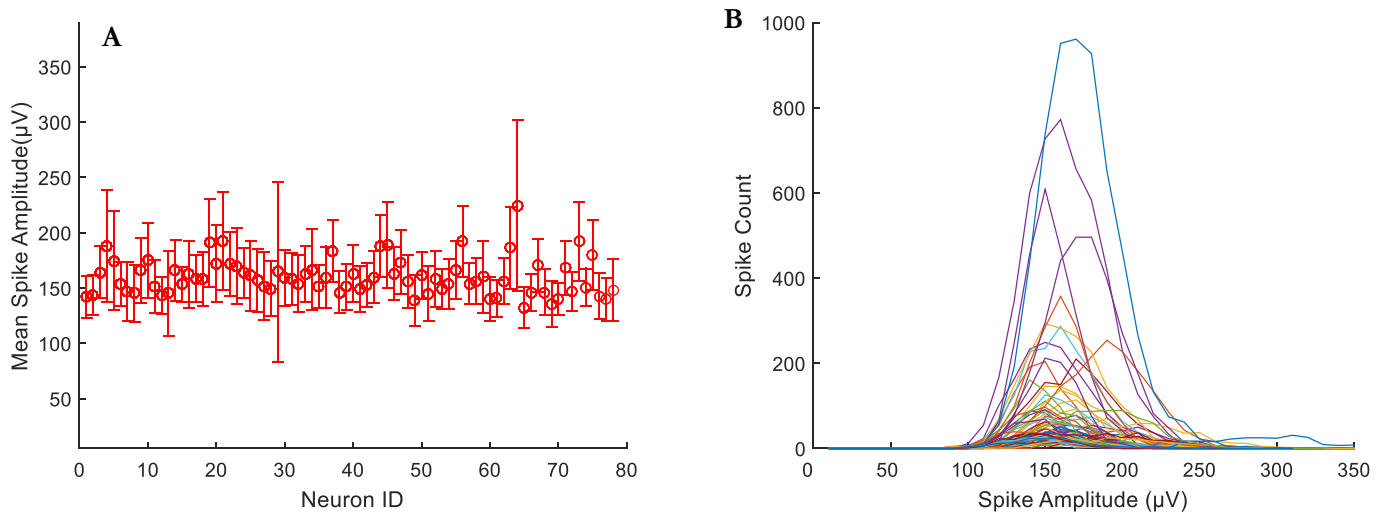


Figure 4. 6. (A) Average spike amplitudes per neuron, error bars S.D. The range of amplitudes was relatively consistent across the population. (B) Counts of spike amplitude values, where each line represents a neuron (bin width 10 μV). Four neurons exhibit a distinctly higher number of spikes (peak >400 counts), however the variation in amplitudes is largely consistent and the most active neuron (peak \sim 1000counts) envelopes most of this variation.

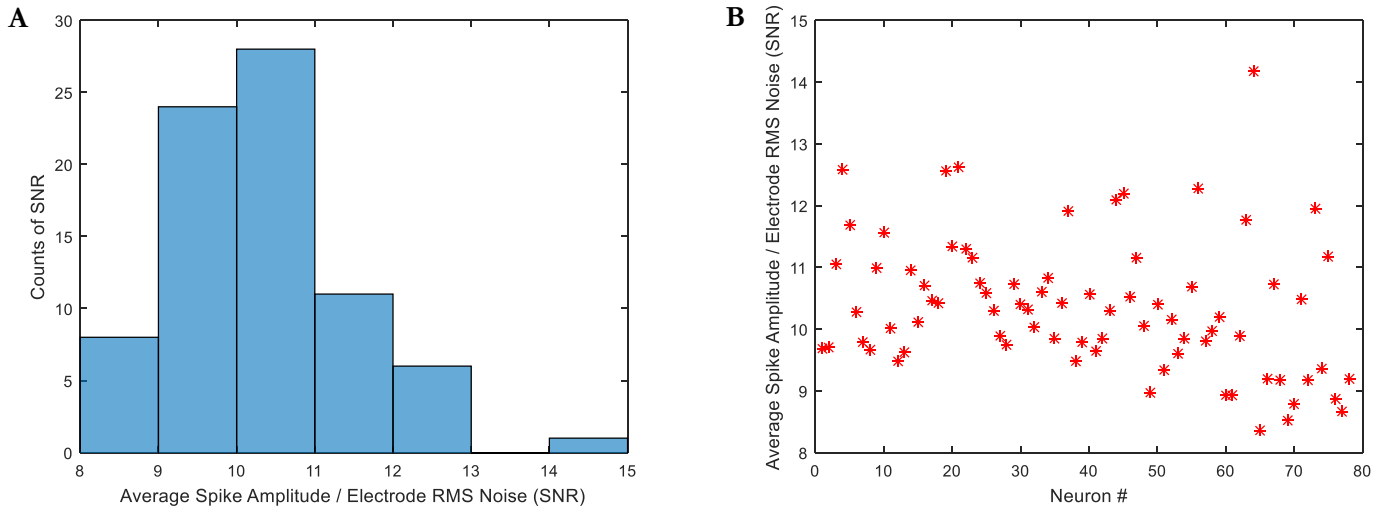


Figure 4. 7. The average spike amplitude per neuron divided by the RMS noise input value recorded on the associated electrode indicates the SNR of the system. (A) Histogram of neuron amplitudes divided by their respective electrode noise demonstrates 52 neurons displayed an SNR value of between 9 and 11 to 1. (B) Average neuron spike amplitude divided by corresponding electrode noise for each neuron.

4.3 Neuron Activity is Limited to 2 Hours of Recording in this Preparation

Continuous spiking activity was recorded for 4 hours. Previous electrophysiological recordings from acute slices of hippocampus and neocortex have demonstrated robust viability beyond 4 hours and in some preparations have remained validated beyond 36 hours^{130,131}. However, in the data presented here, there is a drastic decrease in neuron firing rate following the first two hours of recording. The combined spike rate of all neurons rapidly increased for the first hour (peaking 75-80 minutes) before steadily decreasing. The high frequency peak of activity at ~3.5 hours (starting ~12000s) is attributable to a single neuron, which exhibits very low frequency spiking except during this period (lasting ~20min). The initial rise in activity was observed across most neurons and explicit examples are provided in later sections.

Although neuron activity was detected over a 4-hour period, later sections of this work will focus on the data obtained in the first 2 hours of recording where a clear majority of cells exhibit greater activity. This section will briefly compare and summarise the differences between the first and second halves of recording (termed *0-2hr* and *2-4hr* respectively) to justify this decision. Due to the drastic change in spiking frequency, and consequent loss of useful data, further analyses focussed on the initial 2 hours of recording. The reduction in

spike rate is observed across the population and is unlikely to be related to inter-neuron communication.

4.3.1 Decrease in Neuronal Spike Frequency

The spike rate per neuron for the duration of the 4-hour recording demonstrates very low spike frequency across the population (Fig. 4.8, A) due to long periods of quiescence between spikes. Neuronal activity was detected and recorded for 4-hours, however 71% of all recorded spikes are elicited within the first two hours of recording. The disparity in activity between the first and second halves of the recording can be seen from the combined population spike rate (Fig. 4.8B) and the activity differences between these periods (Fig. 4.8 C & D) were assessed in greater detail.

The percentage of each neuron's spikes elicited in either half of recording (Fig. 4.9, A) demonstrates half (39) of all neurons exhibit >75% of activity 0-2hr, while 12 neurons elicit >50% of spikes during 2-4hr. While a minority of neurons demonstrate increased activity after 2 hours of recording, this figure highlights that most of the recorded data is obtained in the initial 2 hours of recording. A smaller ISI value suggests a higher frequency of activity (Fig. 4.9, B). Apart from seven neurons (#20, 25, 29, 41, 71, 72, 73), the average ISI value 2-4hrs is larger than the preceding two hours, suggesting a general decrease in spike frequency in addition to percentage of elicited spikes. Additionally, at 0-2hrs, 4 neurons exhibited an average ISI of >100s while this number increases to 49 neurons in the 2-4hr period. This does not reflect the variation in spikes per neuron but is an indication of the change in behaviour over the duration of recording.

The later high frequency neuron (discussed in Fig. 4.8) can be identified in figure 4.9 (A) as neuron #71, which highlights a larger inter-spike intervals (ISIs) in the initial two hours (black) with a shorter periodicity in the second half of recording (red). This outlier is also evident in figure 3.6, showing 94.4% of this neuron's spikes occur within 2-4hours. Neuron #72 also elicits very few spikes in the initial half of recordings (1.74% of total recorded neuron spikes), however, this neuron has a small number of attributed spikes (117 total), only marginally more than the spike count cut-off value of 100 spikes used as a neuron clustering criterion.

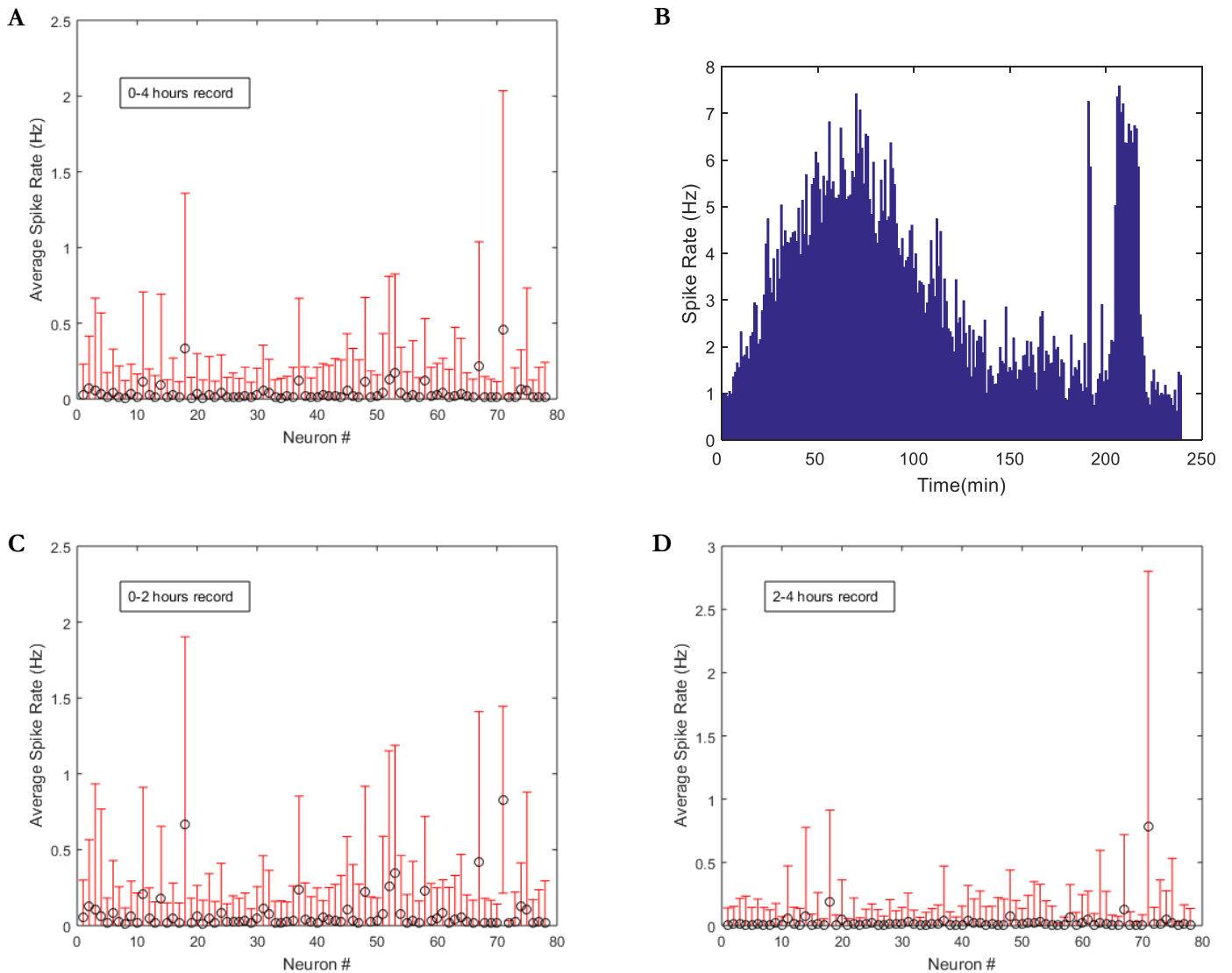


Figure 4. 8. Neuron spike rates. (A) Combined neuron population firing rate for the duration of the 4-hour MEA recording from an acute cortical slice. Binned at a rate of 1min, the population of recorded neurons showed a peak in activity ~ 75 -80minutes into the recording which then decreased at a similar rate until ~ 145 minutes. The population activity remains in the range of 1-2 Hz except for a single neuron exhibiting ~ 20 minutes of high frequency activity. (B) Neuron spike frequency for the total population during 4 hours of recording. (C) Individual neuron spike frequency during the initial two hours of recording. (D) Individual neuron spike frequency during the last two hours of recording; error bars S.D.

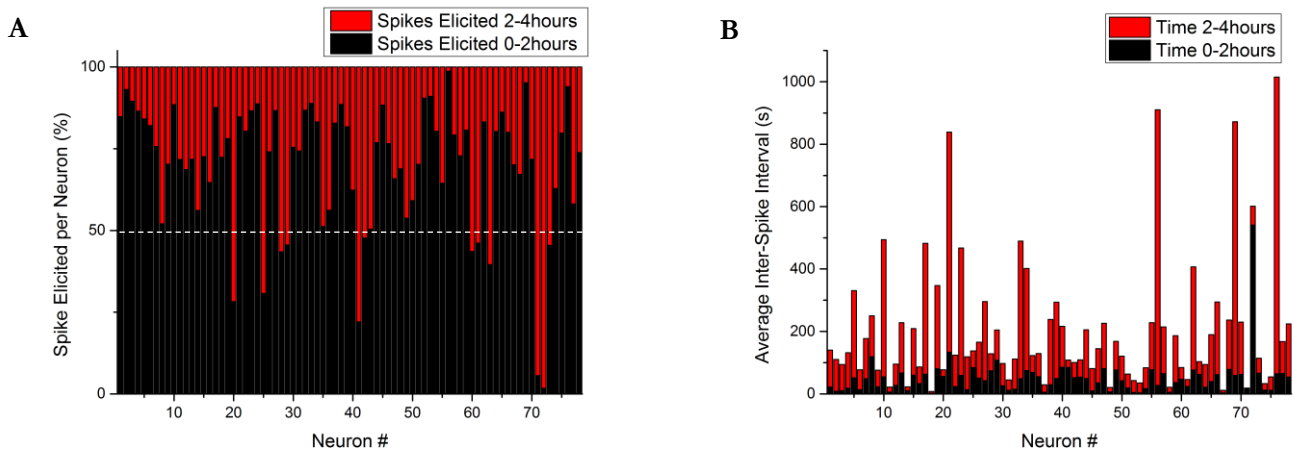


Figure 4. 9. Neuron activity alters over time with most neurons eliciting more spikes, at a higher frequency, during the first 2 hours of recording. The reduced quantity of spikes recorded in the second half of recording makes this period of activity difficult to evaluate (A) Percentage of spikes elicited by neuronal units during the initial 120minutes of recording and the latter 120minutes of recording. Of the 78 neurons, 12 neurons were more (>50%) active during 2-4hrs, but half (39neurons) elicited over 75% of their spikes in the first 0-2hrs; highlighting the discrepancy in neuron activity during these intervals. (B) Average inter-spike-interval (ISI) for each neuron in the first 2 hours of recording and the second 2 hours of recording. The increased ISI 2-4 hours into recording highlights the lower firing rate in the second half of recording.

An initial summary of the dataset indicates a distinct variation in both total spike count, and average spike frequency, per neuron over the course of the entire 4-hour recording. For instance, the average spike count for the population in 0-2hrs is 382 spikes/cell, yet there is a large degree of variation across neurons. Therefore, generalisations regarding the entire population activity (and assuming similar behaviour) are not easily reconciled. Although this variation decreases over 2-4hrs, this is due to fewer spikes being identified. This population is not targeted (i.e. specific cortical cell types) and is instead based on distinct activity. Decreased variation could indicate synchrony and an alignment of activity behaviour, yet it is proposed here that the decreased spike rate seems unlikely to be representative of normal, healthy, network communication.

4.3.2 Neuron Spike Amplitude Does Not Decrease

In addition to high temporal resolution, the acquisition system is also capable of high resolution of spike amplitudes. Further analysis was performed to assess if the decrease in spike frequency is accompanied with a corresponding decrease in spike amplitude. Decreasing amplitude could suggest a change to the electrode-electrolyte interface, for instance due to increased distance or cellular injury. The average spike amplitude for each neuron was measured for 0-2hours and 2-4hours (Fig. 4.10, A&B). Average amplitudes ranged from 132.5 : 224.2 μV during 0-2hrs and 129.7 : 225.2 μV during 2-4hrs, and no significant difference between datasets was identified ($p = 0.2$, t-test).

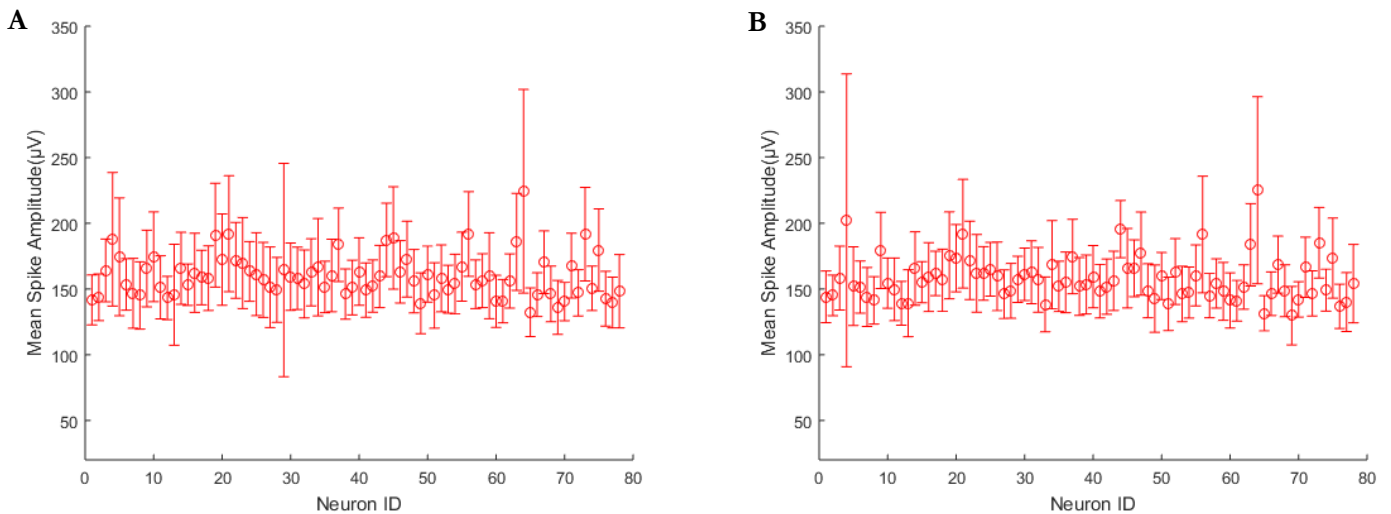


Figure 4. 10. Average neuron spike amplitude 0-2hrs (A) and 2-4hrs (B); error bars are standard deviation. The average amplitude 0-2hrs ranges from 132-224 μV with an average of 161 μV and an average deviation of 28 μV . During 2-4hrs, average amplitudes ranged from 130 to 225 μV with an average of 158 μV and an average standard deviation of 25 μV . The change in amplitude deviation in spikes attributed to neurons #4 and #29 is noticeable, and in each case can be attributed to a single outlier spike (see Appendix 5).

Changes to individual neuron spike amplitudes were further investigated. An average amplitude decrease of >10 μV s was exhibited by 14 neurons in the second half of recording, while 4 neurons increased by >10 μV (Fig. 4.11, A). Overall, more average spike amplitudes decreased in the second half of recording, but did not indicate catastrophic degradation of the electrode-electrolyte interface as the behavioural response over time is not uniform across all neurons. Additionally, the change in standard deviation of the spike amplitudes (Fig. 4.11,B)

exhibited minimal changes, indicating that the variation of spike amplitudes remains constant. Two exceptions are neuron #4 (S.D. increased by 70 μV , average amplitude increase of 17 μV) and #29 (S.D. decrease of 98 μV , average amplitude decrease of 15 μV). In both instances this change in deviation results from a single outlier spike compared to other spikes attributed to the neuron (see Appendix 5). The population change in deviation over the two time periods did not significantly change ($p = 0.11$, student's t-test).

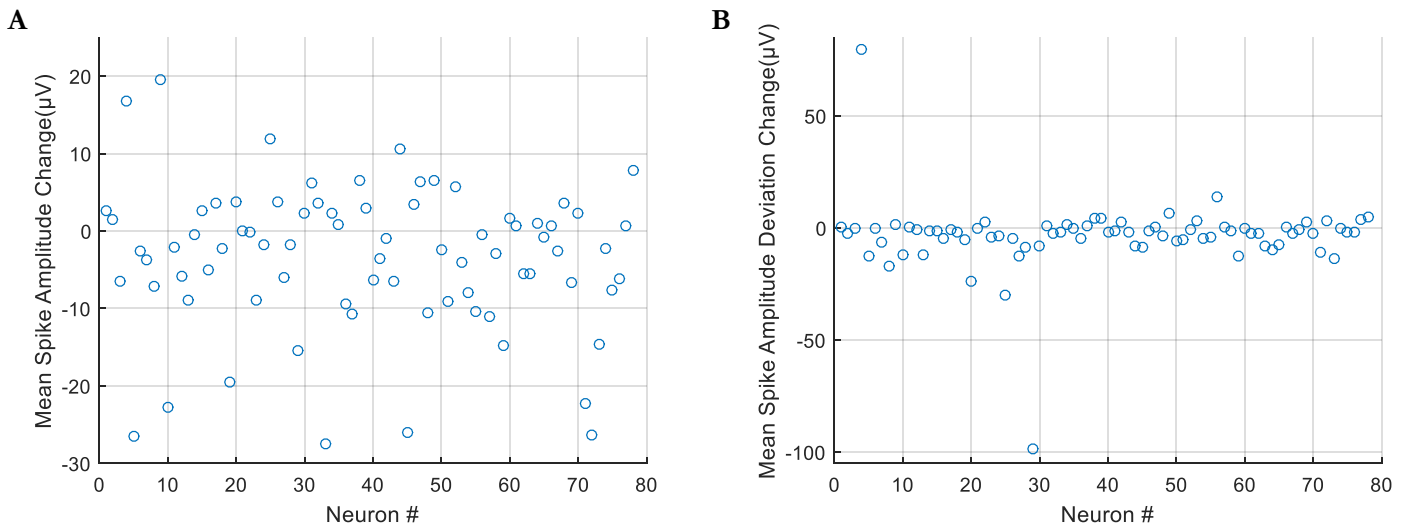


Figure 4. 11. (A) Comparing average neuron spike amplitudes between 0-2hrs and 2-4hrs, a total of 14 neurons exhibited an average amplitude decrease of more than 10 μV between 0-2hrs and 2-4hrs, while only 4 neurons displayed an increase of more than 10 μV . The mean spike amplitude per neuron did not significantly change across the two time periods ($p = 0.2$, student's t-test). There was an overall decrease in average neuron amplitude in the second half of the recording (48 neurons decreased in average amplitude), however, these small changes are not indicative of a significant degeneration of the electrode-electrolyte interface. (B) Change in spike amplitude standard deviation per neuron between 0-2hrs and 2-4hrs. Overall, variation in spike amplitude decreased in the second half of recording, but the deviation in 0-2hrs was not significantly different to the deviation 2-4hrs ($p = 0.11$ student's t-test). Both neuron #4 and #29 showed large changes in spike amplitude variation are attributable to single outlier spikes (see appendix 5).

In order to ensure averaging of amplitudes did not obscure transient periods of rapid changes in spiking behaviour, manual evaluation of individual neurons was performed to verify the initial summary of spike amplitudes between 0-2hrs and 2-4hrs (Fig. 4.12); similar analyses were performed between hours 1, 2, 3 & 4. No differences in amplitudes were identified

between comparisons of hours 1 and 2 or between 3 and 4. These results indicate that the decrease in spike frequency, exhibited by the majority of neurons, is not accompanied by a corresponding decrease in amplitude and suggests that no periodic changes in amplitude impacted the identification of spikes.

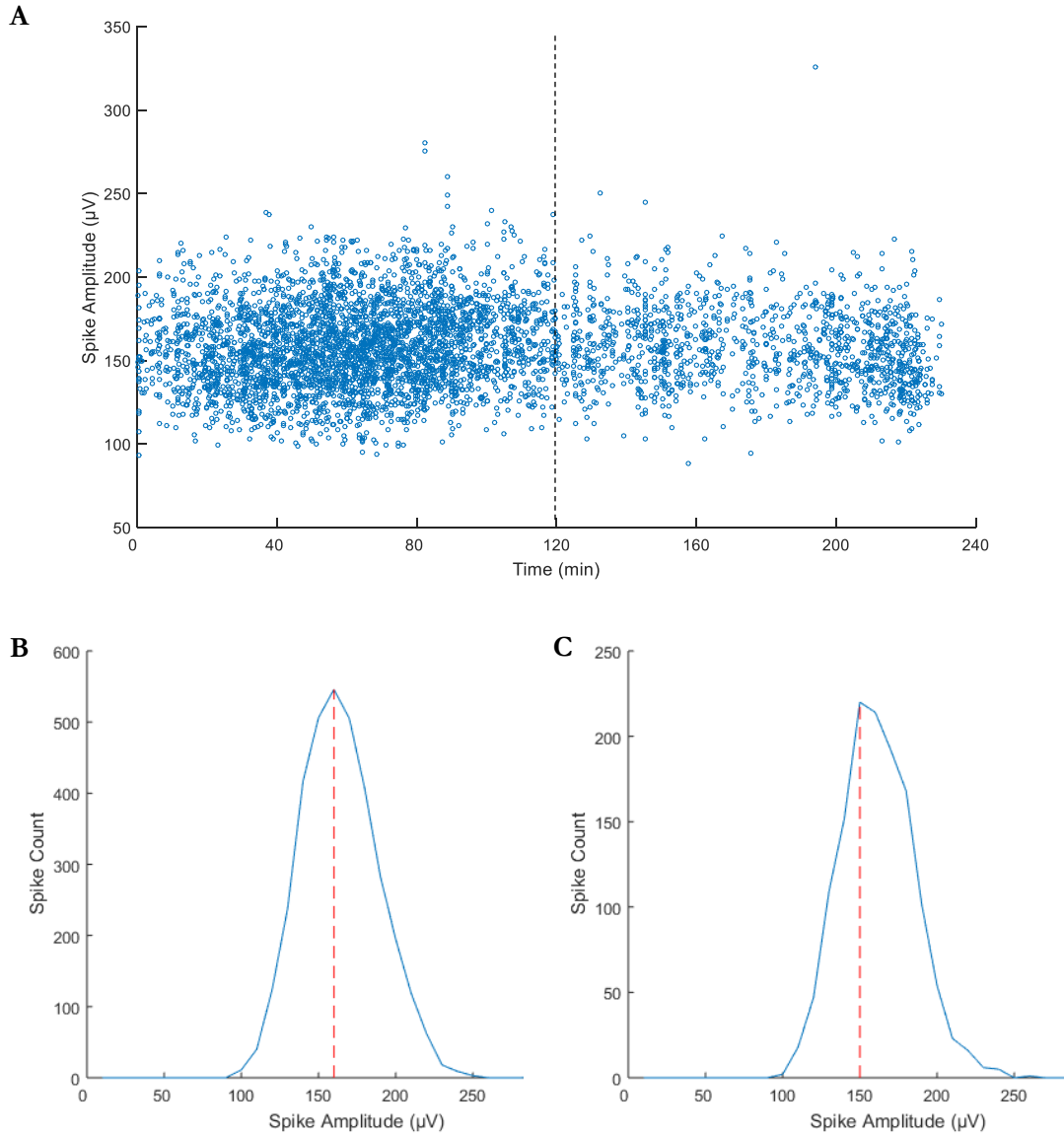


Figure 4. 12. Example of individual neuron spike amplitude analysis over time (neuron 18). (A) Neurons exhibited a disparity in spike frequency between 0-2hrs and 2-4hrs (dotted line at 2 hours into the recording). However, this decrease in activity was not related to any change in spike amplitudes; blue dots represent the time of a spike event during the 4-hour recording and the amplitude of each spike. (B) Counts of spike amplitude during 0-2hours. (C) Counts of spike amplitude during 2-4hours.

4.4 Discussion: Neuron Identification

The electrophysiological recording of neuronal activity presented here demonstrates the ability of the system to obtain high quality electrophysiological data which can be used to identify neurons. The data presented in this work is derived from a single recording which identified 78 individual units following the application of appropriate spike sorting parameters. The signal to noise ratio of electrode to neuron amplitudes averaged 10:1 which was suitable to allocate a high number of extracellular spikes to neurons via spike sorting and did not suggest that spike events required significantly large amplitudes to be detected. The recording of 78 neurons simultaneously was continued for a 4-hour period as spiking activity was still observed at this point. However, the population exhibited significantly decreased activity after 2 hours of recording with only a few neurons remaining active. No corresponding decrease in spike amplitudes were observed, suggesting that the electrode-neuron interface remained stable. Due to the low activity frequencies after 2 hours, further analysis will focus on the initial half of the recording as this represents a greater volume of useable data. The reduction in spike rate is observed across the population and is unlikely to be related to inter-neuron communication. Average population values for key properties are summarised in table 4.2.

<i>Average Neuron Properties</i>	0-2 hours	2-4 hours	4 hours
Spike Count (spikes / cell)	382±569	208±654	590±965
Spike frequency (Hz)	0.06±0.08	0.03±0.09	0.08±0.13
Amplitude (µV)	161±28	158±25	160±29
System Noise Properties			
Electrode noise (µV)	15.3 ± 0.8		
Seed Electrode noise (µV)	15.5 ± 0.4		
Non-seed electrode noise (µV)	15 ± 0.7		
SNR	10 : 1		

Table 4. 2. Average neuron population properties and system noise.

The process of spike sorting consists of several stages which aim to provide high quality data which can be allocated to individual neurons. It has been shown here that using the RMS noise input value for each electrode individually provided an acceptable sigma value to apply to the amplitude distribution detected by electrodes. This was combined with a threshold setting of 6, meaning only signals which went above and then below 6σ were included in the

signal distribution (table 4.1). Therefore, voltage amplitudes greater than $\sim 80 \mu\text{V}$ were included for further analyses. Reducing the threshold setting to 5σ (comparable to amplitude threshold of $\sim 75 \mu\text{V}$) drastically increased the number of cells identified (205 compared to 74), but many became contaminated with non-neuronal signals and impacted the final dataset. Furthermore, relaxing correlation and contamination limitations had little impact on neuron numbers identified. This suggests that the settings used in this work were the most appropriate with which to maximise the quality and quantity of recordings with this acquisition system.

The suitability of the system RMS noise input was confirmed; although seed electrodes exhibited significantly higher noise values in the presence of brain tissue, increased biological activity in the electrode vicinity makes the RMS difference reasonable. No trend was observed across seed electrodes exhibiting high or low noise. Additionally, this is a comparison of 74 electrodes to 438 (5.9 times as many), and the higher deviation may account for the significant difference. The SNR is a limitation of any extracellular recording system; however, this ratio is dependent upon the signal amplitude as much as the inherent noise of the system. Extracellular signals rapidly deteriorate in amplitude with distance from the membrane¹⁰ and, although properties of neurons widely differ, the amplitudes of spikes can indicate the proximity of a neuron to its corresponding electrode. Gauging the variation of amplitudes additionally indicates how cleanly neurons have been clustered and identified, as a bimodal distribution of amplitudes suggests the miss-allocation of spikes.

The initial half of the recording demonstrated a steady increase in activity, peaking ~ 1 hour into the recording. The rise in activity could be attributed to the slicing preparation procedure. Once in the recording chamber, slices are perfused with excited aCSF containing elevated K^+ content (see section 4.1) which is warmed to 37°C via an in-line heater (temperature was measured using the heating element's thermistor placed at the bottom of the chamber pre-recording and heating adjusted accordingly). This contrasts with the prior incubation phase, where slices are maintained at room temperature in aCSF. This transition likely causes an increase in activity and could explain the subsequent drop in spike frequency as cells were dying. The decrease in activity could also be the result of increased distance between neurons and electrodes caused by the buoyancy of the tissue. If the resistance seal was not secure (see Diagram 4. 1), the slice could become dislodged from electrodes. However, this would be indicated by a change in spike amplitude as the current would dissipate in the extracellular fluid, and this was not found to be the case.

Due to the overall change in firing rate, analysis of the entire recording session becomes obfuscated. Although non-stationary firing frequencies are common in biological systems, comparing and evaluating activities of neurons becomes difficult if that activity changes significantly across the population. As fewer spikes are detected over time, the behaviour of the neuron is also interpreted as being altered. This may be the case (e.g. resulting from a change in the experimental setup, or traumatic cellular injury), but the focus of the experiment then becomes that change in behaviour, rather than behaviour of healthy neurons connected in a representative network.

Despite a significant reduction in spike frequency over the course of the recording, the relatively constant amplitudes of spikes indicate the electrode-neuron interface is unlikely to be degrading. Therefore, the first 2 hours of recording provide appropriate data which with to further analyse connectivity in acute brain slices.

Recording #	Notes	Duration	Clustered neurons	Spikes/cell
1	Too few neurons identified	1 hour	1	43
2	Too few neurons identified	4 hours	4	102
3	No results	4 hours	0	0
4	No results	4 hours	0	0
5	Clusters demonstrate abnormal (duration >4ms) waveforms	4 hours	9	59
6	Further processing undertaken, but too few cells identified	2 hours	12	112
7	Further processing undertaken, but too few cells identified	2 hours	11	180
8	Further processing	4 hours	78	531
9	Solution leaked and damaged electronics	4 hours	6	23

Table 4. 3. Summary of recording experiments

5. Neuronal Spike Features and Temporal Characteristics

Spike features extracted via electrophysiological recordings can provide insights into neuron behaviour. Relating neuron behaviour to a role in a wider network is a critical aspect in understanding neuronal connectivity. The variety of neuronal subtypes within the cortex allows for a highly heterogeneous network of activity, therefore being able to discriminate and classify neurons is important in understanding functional architecture of the network. This chapter outlines approaches to defining the characteristics of subpopulations of neurons within the recorded data. Further investigation could attempt to validate these findings in relation to specific cortical layers and known characteristics of neuronal populations, unfortunately, information regarding precise recording location is not available in this work. Analyses of neuron characteristics were performed using Matlab software to examine specific qualities of each neuron. The averaged neuron waveform describes the typical trough-to-peak spike amplitudes and temporal characteristics of neurons. Previous studies have suggested these features can provide information regarding the function of a neuronal unit and that excitatory and inhibitory cells can be distinguished based on these features alone¹². However, the reliability of this approach may depend on cell type and experimental setup¹⁶, as the targeting of specific cell types for focussed experimentation would not yield data from a variety of cellular network functions. No definitive parameters for such distinctions were identified in this work, although the unbiased sampling of a highly heterogeneous cortical population may reflect the range of neuronal features which cannot be easily classified into two categories. The greatest variation across the population was observed in the slope of the refractory period from hyperpolarisation to resting membrane potential (RMP) and the temporal differences between depolarisation and hyperpolarisation, indicating these features to be the most effective means of differentiating the heterogeneous neuron population presented here. Further discussion and investigations of these waveforms are presented in section 5.1 and concern variations in phase amplitudes (peak to trough ratios), spike widths (the time between the negative and positive phases) and the gradient of phase changes (Fig.5.1, B and Fig.5.4).

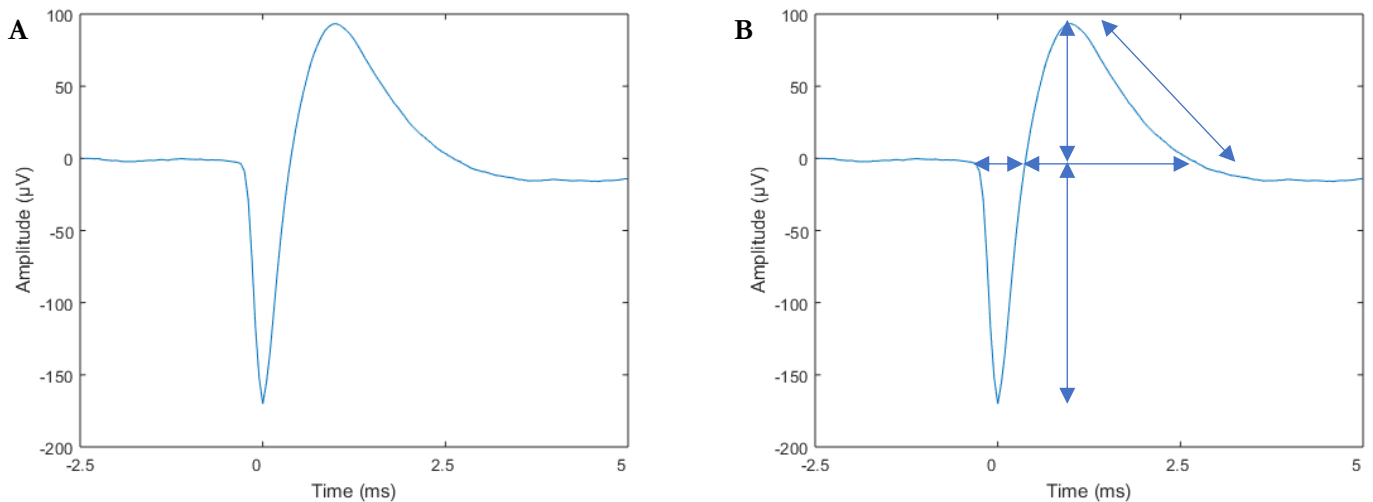


Figure 5. 1. Neuron waveforms are averaged to provide representative electrophysiological features of individual cells. The positive depolarisation of a neuron causes a negative voltage deflection in the medium surrounding an electrode; this signal is identified through spike sorting and clustered to represent the activity of a single neuron. (A) The most negative point of the signal (corresponding to peak depolarisation) is centred at $t = 0$ ms for each spike attributed to that neuron. Each sample, corresponding to every 0.05 ms on the x-axis, is averaged across every spike to produce a generalized representation of that neuron's spiking waveforms. (B) Averaged spike waveform features were analysed to discriminate neuron subtypes using temporal and amplitude properties (arrows) as discussed in section 5.1.

The elicited spike rate per neuron was relatively low compared to previous studies using a similar experimental setup⁹⁶, with most neurons displaying the greatest amount of activity in the first 2 hours of recording (see chapter 4). Firing rates generally peaked 40-80 minutes into recording, yet multiple neurons exhibited periods of relatively high frequency followed by prolonged periods of quiescence. Sporadic patterns of high frequency activity is termed bursting, and is a commonly observed behaviour in connectivity studies^{132,133,134}. However, long periods of inactivity required additional processing to provide valid interpretations of spike train temporal patterns.

It was not initially clear whether rapid changes in spike frequency were directly related to the relatively low firing rates of neurons or if spike sorting had inadvertently favoured bursting behaviours while limiting the recording of regular, or low frequency, firing rates. A possible source of bias could be increased spike amplitudes, which would provide a greater SNR and, consequently, be included throughout the spike sorting process indicating a false-positive result of increased spike activity. However, spike amplitudes over time remain

relatively constant over the 2-hour recording in all neuron spike trains (examples in Fig. 5.2, A & C). Previous studies using similar systems have not indicated a bias towards bursting behaviours¹¹ and significant amplitude changes over time would be identifiable during manual evaluation of PCA clustering. Amplitude changes would become clustered as an elongation of data points and due to the Gaussian method employed here to fit cluster data point distributions, would result in multiple overlapping clusters of distributions therefore more likely to fail the contamination criteria. Clusters in this dataset do not suggest that waveform amplitude changes impacted the clustering of spikes that would consequently result in a decreased spike rate.

The large variation between the spike frequencies of neurons prompted evaluation of spike temporal properties and is addressed in section 5.2. Inter-spike intervals (ISIs) of neurons were analysed as the temporal precision of neuron behaviour is often investigated using this quality¹³⁵. Distinctive ISI distributions can indicate simple or complex spiking patterns, however, the low spike frequency necessitated further processing for this analysis. Evaluating ISI values by limiting the maximum ISI value included in analyses exposed a population-wide change in the rate of ISI value count; the number of identified ISI values did not scale linearly with an increased allowance of maximum ISI, suggesting that certain spike frequencies were more prevalent. To evaluate ISI values relative to each neuron's spike rate, values were segregated based on each neuron's median ISI value. This provided analyses of higher (>50% of ISI values) and lower (<50% of ISI values) frequency spike rates relative to each individual neuron. A group of neurons exhibiting distinct ($p < 0.05$) behaviour at relatively higher spike frequencies was identified which indicated fast, regular, spiking activity. An additional group of neurons exhibiting bimodal distributions at higher frequencies was also identified and was found to be statistically distinct ($p < 0.05$, student's t-test). The coefficient of variation (CV) of spike trains was then analysed at high and low frequencies. This measure indicates the regularity of a neuron's spiking activity and can suggest tonic or bursting patterns of behaviour. More neurons demonstrated greater spike rate irregularity at lower frequencies, although behaviour types could not be defined with this method.

As CV values indicated many neurons exhibited bursting behaviour, a method of burst identification was performed. Many studies have utilised the ISI of neurons to evaluate bursting activities, yet numerous attempts have been made to further refine the definition of bursting. For instance, Turnbull *et al.*¹³⁶ proposed the "string" method based on electrophysiological recordings from cell cultures grown on a MEA. When plotting each spike

time against spike number (out of total recorded spikes), a more vertical slope gradient indicates high frequency neuron activity. By defining the minimum number of spikes in a burst and the maximum intra-burst ISI, “strings” of spikes can be defined as bursts. These parameters can be fitted to neuron activity to identify the potential maximum number of bursts; however, it is recommended to optimise the parameters to suit experimental conditions and is therefore not auto-adaptive, requiring manual evaluation of numerous spike trains. The mISI method developed by Chen *et al.*¹³⁵ progressed the string method and generates an auto-adaptive threshold for ISI values with which to identify periods of bursting, calculating a maximum ISI for burst identification using mean ISIs and burst durations. The use of these parameters was investigated using data from the 512-needle MEA. To the author’s knowledge these methods have been applied to EEG¹³⁷, *in vivo* (crickets)¹³⁸ and *in vitro* data^{139,140}, but not to acute rodent *ex vivo* data. The average threshold value for bursting defined by the mISI method was 9seconds, with ~50% of spikes allocated to each neuron identified as bursting. Although this method did not identify high-frequency bursting activity, the earlier use of the median ISI value to form the basis of CV analysis is partially reinforced by these findings.

The final section of this chapter focuses on a novel method of bursting analysis developed by the author and based on the mISI method. This method identifies the ISI value at which the greatest number of sequentially bursting spikes can be identified and uses only ISI values below this limit. Histograms of groups of bursting spikes were developed which were used to identify repeating ISI patterns and further segment spike trains. This adaptive method was able to reliably threshold high frequency bursting activity and demonstrated greater variation in bursting activity than the mISI method.

Information regarding neurons, and individual spikes, were extracted using the 512MEA acquisition system. This allowed for detailed investigations of the behaviour of neurons in acute *ex-vivo* cortical slices. The following sections will detail the features assessed prior to evaluation of connectivity in chapter 6. Spike features were categorised into two groups: waveform properties (such as amplitudes and trough to peak spike ratios) and temporal properties (such as inter-spike intervals and burst durations). Results are summarised in table 5.1 at the end of the chapter.

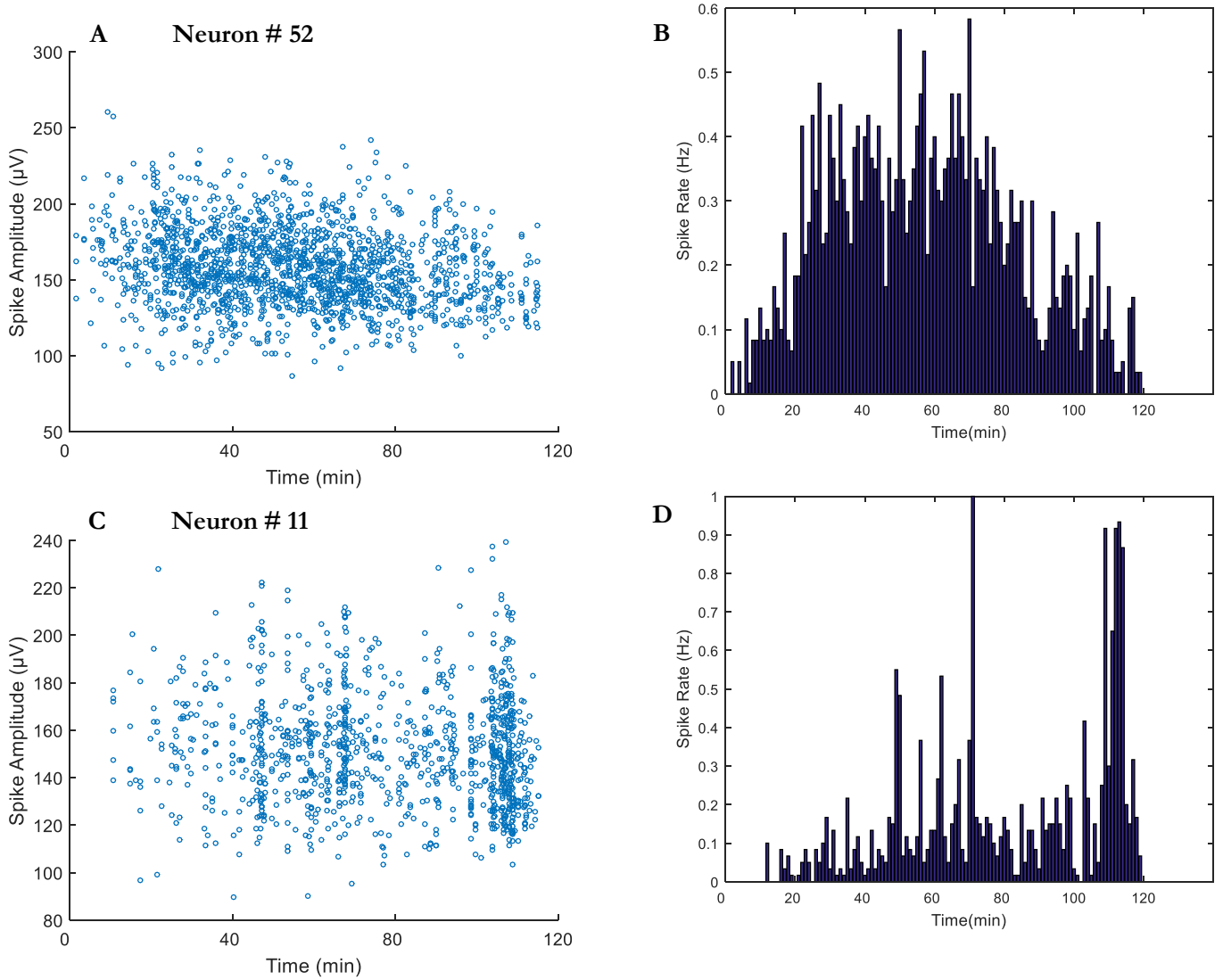


Figure 5. 2. Example of verification analysis of amplitude over time (A & C) and spike rate (B&D) from two individual neurons. Top row: this neuron (#52) demonstrates a typical increase in spike rate during the first two hours which dramatically drops 120minutes into the recording (B), and no significant change in spike amplitude occurred over this period (A). Bottom row: other neurons (e.g. #11) exhibited distinct behaviours, where spike rates dramatically and sporadically increase - a sustained increase is observed towards 120 minutes of recording, however, this rate rapidly decreases after two hours of recording.

5.1 Classification of Cell Types: Excitatory or Inhibitory

Differentiating functions of individual neurons within a network is an important goal in understanding how cells interact and communicate. Broadly, neurons can be separated into two classes; excitatory or inhibitory. Excitatory neurons most commonly utilise the transmitter glutamate postsynaptically to elevate membrane potentials closer to spiking threshold, while GABA is usually transmitted by inhibitory interneurons to achieve the opposite effect (see section 2.1.6). A variety of molecules are secreted by neurons and discrimination of the neurotransmitter utilised by an individual neuron by electrophysiological data alone is not currently validated. Classifying cells as excitatory or inhibitory would greatly assist the interpretation of neuronal networks and their underlying functions, for example, interneurons provide a timing mechanism for network computations¹⁴¹ and can dampen firing rates through feed-forward inhibition¹⁴². While there have been numerous technical approaches, several studies have attempted to discriminate cells through analysis of electrophysiological features alone. Such features are appropriate for analysis through the temporal precision and amplitude resolution afforded by the 512MEA presented in this work.

Excitatory pyramidal cells and inhibitory interneurons of the hippocampus have been shown to be reliably separated using extracellular features^{143,144,145}. The primary difference used in identification is the faster (narrower) negative spike amplitude that inhibitory neurons exhibit, relative to excitatory counterparts, which is associated with the Kv3 family of potassium channels¹⁴⁶. Previous analyses of extracellular *in vivo* cortical recordings using MEAs successfully distinguished inhibitory and excitatory neurons^{147,12,148}. This was achieved by applying parameters to waveform features and the precise timings of spike frequencies. However, subsequent studies applying a similar approach to cultured neurons *in vitro* and could not confirm the applicability of these parameters¹⁶. The high-density MEA presented in this work presented a novel opportunity to evaluate this approach using *ex vivo* acute slices with needle-based electrodes recording from healthy, intact, neuronal networks.

The spike-sorted data generated via Vision was extracted and manipulated in Matlab software to study waveform details. An average neuron waveform can be extrapolated via the acquisition system, representing the average spike elicited by a neuron. This was generated by averaging each sampling point surrounding a spike time. During spike sorting, a peak amplitude polarity (negative in this case) is identified after the signal passes the spike sorting threshold voltage. This signal is time stamped, PCA analysis is performed on the

electrode signal before and after the event, and finally a raw (system filtered) data waveform can be observed. The system samples the electrodes signal every $50\mu\text{s}$ (20 kHz) - which is the temporal resolution of each waveform. By aligning every spiking event, each sampling frame can be averaged to provide a representative waveform. Presented in figure 5.3 is the neuron spike sorted, averaged, waveform for 78 neurons recorded from across the 512-MEA. All averaged spikes are centred at 0 ms. Waveform amplitudes at -2 ms are centred at $0\ \mu\text{V}$ to account for the variation in DC offset across individual channels and for ease of comparison. The dotted boxes in the figure outline the trough and peak features of the waveforms which are the basis for waveform analysis.

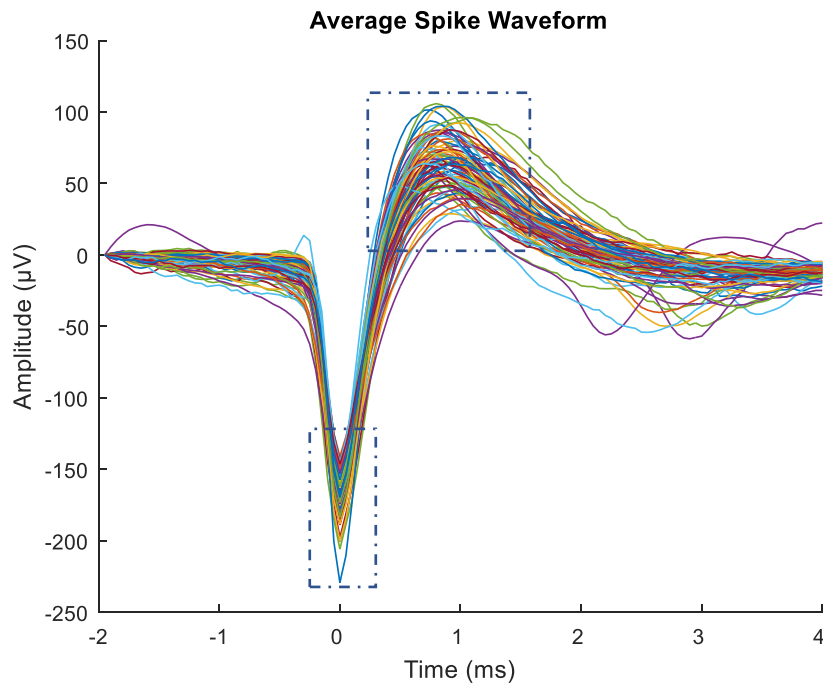


Figure 5. 3. The average spike waveform for each neuron recorded in a single experiment from the 512 MEA. Lines represent the waveform resulting from averaging the spikes allocated to an individual neuron. Averaged waveforms were assessed at the final stages of spike sorting: the shape of the wave; the temporal qualities of the positive and negative phases and reasonable amplitudes were considered. All identified neurons are represented in this figure ($n=78$). The most negative amplitude (trough) of each waveform was centred on $t = 0$ as this was defined as the spike time. The average amplitudes 2 ms prior to the spike time was centred at $0\ \mu\text{V}$. Variations in the ratios of troughs to peaks (dotted boxes) potentially underlie functional differences.

Past studies have used combinations of features to differentiate between fast-spiking inhibitory and broad-spiking excitatory neurons (Fig. 5.4). These features are termed: the peak to trough ratio¹² (compared amplitudes of depolarisation to hyperpolarisation), the spike width (trough to peak time), trough width, peak width¹⁴⁷ and the peak to resting membrane potential (RMP) slope (gradient from refractory period hyperpolarisation to RMP). Waveform analysis focussed on the averaged waveform for each neuron which was then compared across the population.

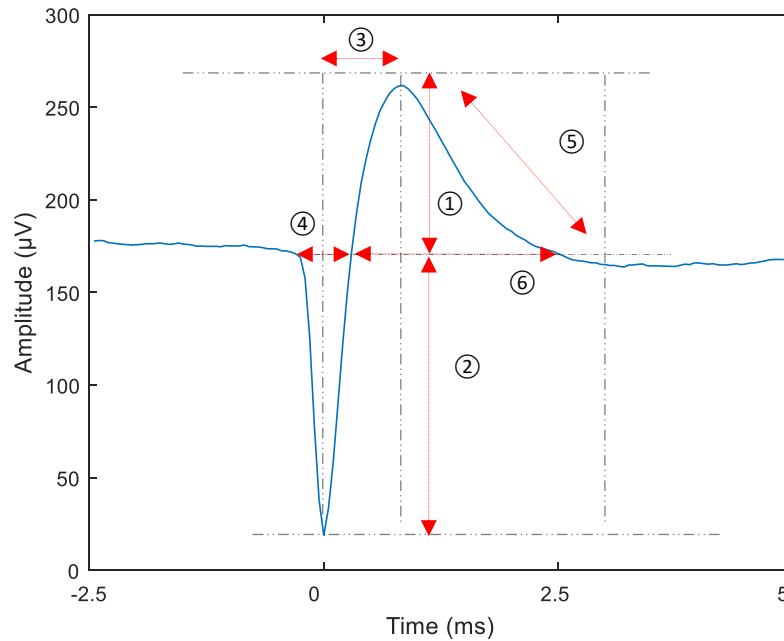


Figure 5. 4. Diagram showing features used in waveform analysis. Five parameters were used to distinguish recurring spike differences between neurons based on previous studies. (1/2) The peak to trough ratio, where a value ≈ 1 indicates a fast spiking inhibitory neuron. The spike width (3) is the time (ms) taken for the spike to reach peak positive amplitude following the spike event, while the trough width (4) is the time required to depolarise and repolarise the extracellular medium. The gradient to return to RMP from the peak was termed the end slope (5) and the peak width refers to the duration of the positive phase (peak) to occur (6).

The justification for each parameter is discussed in turn below:

1/2) **Peak to trough ratio.** The value of this feature has been associated with inhibitory neurons when ≈ 1 while excitatory neurons typically exhibit a value of ~ 0.5 ^{12,16}. Although narrow spiking is also associated with interneurons, the parameter alone does not account for changes to amplitudes and ignores the peak of the waveform. Variation between slopes

of the initial depolarisation is very small (see troughs in Fig 5.3) while the peak phase is more variable in this dataset.

- 3) **Spike width.** The trough to peak time provides a further dimension to the peak to trough ratio and could potentially suggest membrane dynamics of channel kinetics as this phase would correspond to the speed at which potassium channels open.
- 4) **Trough width.** The width of the trough has been repeatedly reported to be able to identify narrow-spiking neurons and reliably classify them as inhibitory interneurons. This feature relates to the kinetics of sodium channels opening and becoming inactivated as well as opening of potassium channels and can underlie major differences in ion channel expressions.
- 5) **End slope.** The end slope corresponds to the return to baseline (RMP) from the positive peak. A steeper slope (i.e. faster return to baseline) has been reported as a useful measure of narrow-spiking (inhibitory) neurons¹² and can be used to corroborate differences in peak to trough ratios.
- 6) **Peak width.** The duration of the peak can be used in a relative ratio to the trough width. A value approximating 1 would suggest a narrow-spiking interneuron even if the trough width was not especially narrow compared to other neurons.

5.1.1 Analysis of Averaged Neuron Waveforms

The initial stage of waveform analysis was shifting the offset of spike amplitudes. The waveforms in Figure 5.3 overlap as the amplitude at -2 ms is aligned to 0 μ V but aligning the spike trough to 0 μ V at 0 ms enables an easier comparison between neuron averages (Fig. 5.5). The extent of variation between neurons can then be better viewed and subsequent calculations are simplified. Total peak to trough amplitudes for most neurons range from \sim 175 μ V to \sim 275 μ V, while three outliers (highlighted in black dashed boxes) are visible. The large amplitude (blue – neuron #64) waveform consists of a particularly large amplitude negative phase, but the dimensions of the waveform are consistent with other waveforms. An average waveform with additional troughs during return to RMP (purple – neuron #53) could indicate signal contamination from a nearby neuron that has not been thoroughly separated by spike sorting. One neuron exhibits an erratic average waveform (orange – neuron #72), which has not elicited enough spikes in the first two hours of recording to be averaged effectively (see section 4.4). Neuron #72 was excluded from further analysis due to the low spike count in this half of the recording.

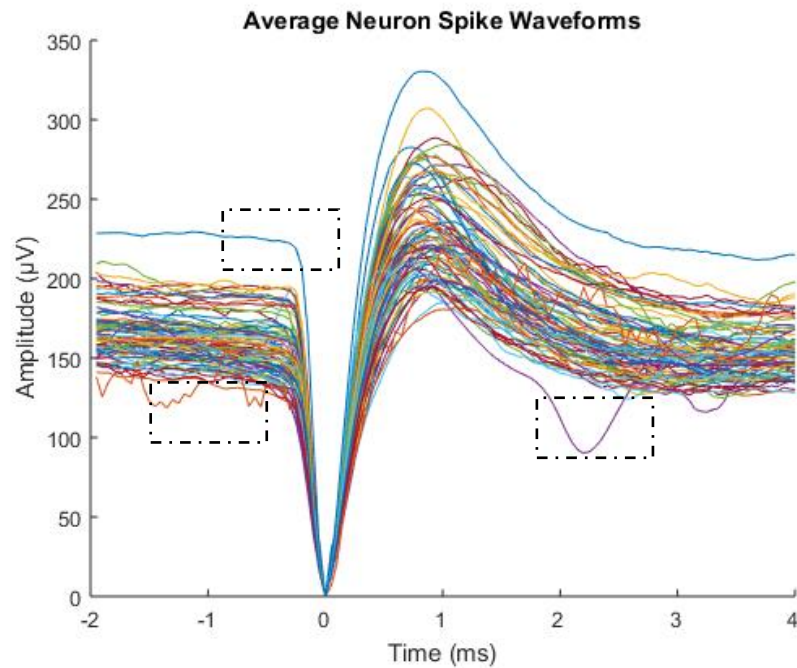


Figure 5. 5. Averaged neuron waveforms. For comparisons between neurons, averaged waveforms were offset by centring the spike time ($t=0$ ms) to $0 \mu\text{V}$. This is the same data as presented in Fig. 5.3, however, aligning time and trough amplitude highlights differences in peak to trough ratios and spike width across the population. This is performed as part of the spike sorting process, however the high-resolution amplitude data presented here is extracted from electrode data files once neurons have been identified. Three outliers are identified in black, dashed, boxes.

With the waveform trough value centred at 0 ms, $0 \mu\text{V}$, an approximate voltage for the RMP was required to define the start of the negative phase. The waveforms presented in Fig 5.5 consist of 120 data samples; 40 prior to spiking event and 80 samples after the event. The initial 30 samples (-2 to -0.5 ms in Fig.5.5) were averaged to define a resting amplitude (RMP) and an amplitude of 4 sigma below this average was used as the threshold of the beginning of the negative phase. This was due to several neurons exhibiting a shallower gradient of signal amplitude where the averaged RMP would not be applicable. A 4-sigma deviation was assessed as the most appropriate parameter (see Appendix 6), however, alternative values were tested with limited consequences to the results. The peak signal amplitude was then identified as the point of most positive voltage amplitude in the waveform and sample point recorded. The peak and trough amplitudes (①/② in Fig.5.4) and spike width (③ in Fig 5.4) could then be compared. For each parameter evaluated, histograms were generated and binned according to the square root of the number of elements in the data (i.e. $n = 78$

neurons) with a Gaussian probability density function fitted. Clustering of scatter plots was then performed in Matlab via k-means clustering with centroids based on Euclidean distances. Where discrete clusters were identified an additional histogram of each cluster is included.

5.1.2 Neuron Subtypes Discrimination via Waveform Analysis

Peak to trough amplitude ratios and spike widths demonstrated a normal distribution (Fig 5.6, B & D), indicating neurons could not be separated into sub-types using these parameters as previously reported¹². The scatter plot used to compare these features (Fig. 5.6, A) did not suggest this combination of analyses could highlight distinct groups of cells and k-means clustering was performed (Fig. 5.6, C). The average spike width was 0.89 ms (S.D. ± 0.13), however, a single neuron exhibited narrow spiking at 0.48 ms (Fig 5.6 C & D, neuron #62). The spike widths of each cluster were compared, and each found to be significantly different from each other ($p < 0.05$, student's t-test), with the greatest difference observed between clusters 2&3, however the lack of visual clustering and the approximately normal distribution does not suggest a distinct population based on this feature. The peak to trough ratio (peak amplitude divided by trough amplitude) averaged 0.7 (S.D. ± 0.05) and did not highlight any distinct waveform differences between neurons (lowest t-test value when comparing clusters $p = 0.09$, clusters 2&3).

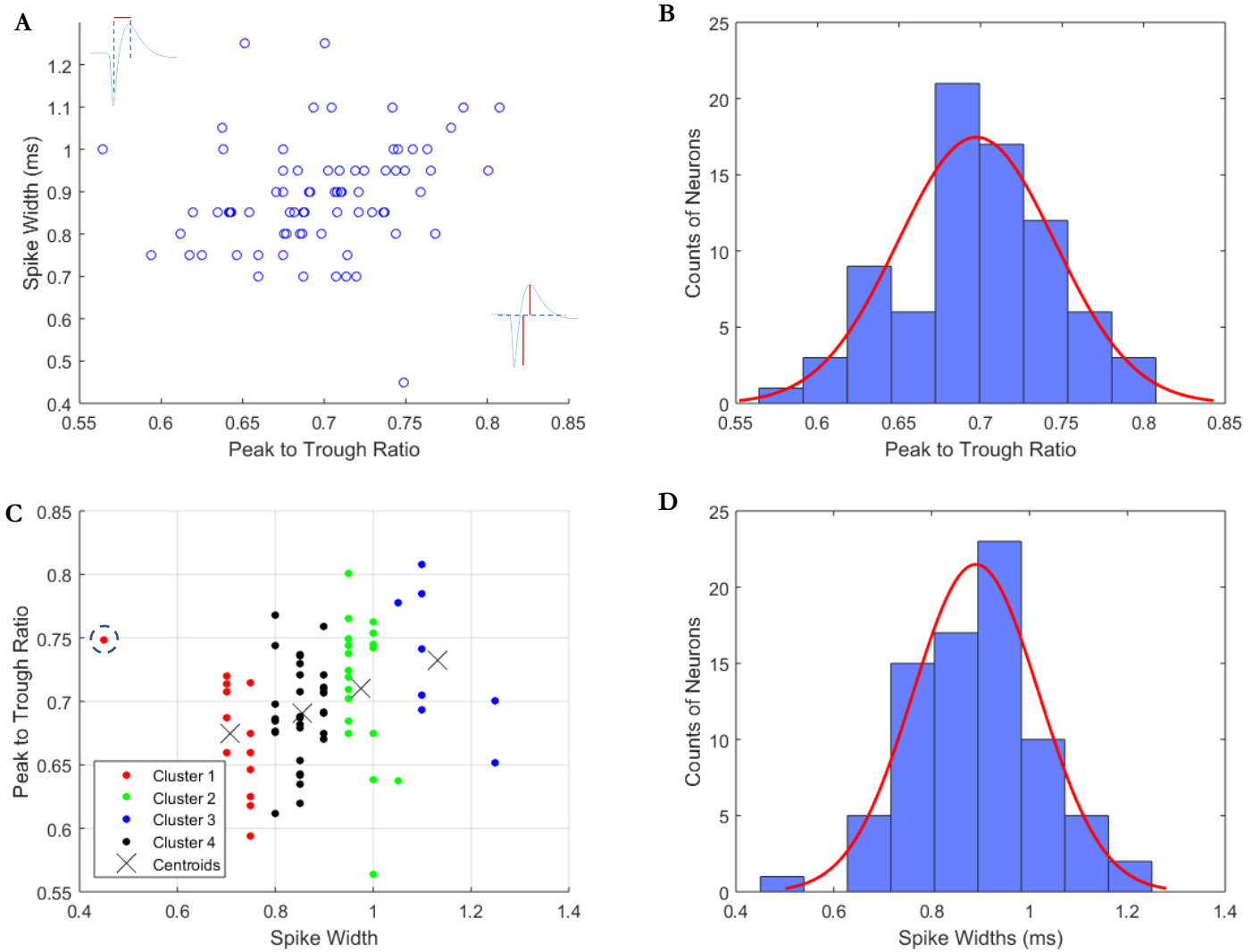


Figure 5. 6. The average peak to trough ratio per neuron and average trough to peak time. Analysis was performed on the averaged waveform per neuron. The time taken for the signal to change polarity following a spike (trough to peak time) has been reported to indicate a fast-spiking inhibitory interneuron or a slower excitatory neuron. An additional parameter is the amplitude ratio of the maximum polarities (peak: trough), which accounts for the amplitude change that occurs during the trough: peak phase. A ratio value ≈ 1 and low time value suggests a fast-spiking inhibitory neuron. No discrete clusters of neurons were identified using these waveform features. (A) Scatterplot of peak-trough ratios and spike widths. (B & D) Histograms of peak-trough ratios and spike widths respectively with normal probability distribution function fitted (red line). (C) Additional k-means clustering of the scatterplot (A) did not achieve separation of neurons, however a single neuron exhibited a small spike width (dotted blue circle).

The temporal features of waveforms have been suggested to be the main indicator of inhibitory interneurons as a narrow trough width (④ in Fig.5.4) is associated with a faster spike. The trough widths measured in the data presented here exhibit a normal distribution (Fig. 5.7, B) averaging 0.63 ms (± 0.08 S.D.). Two neurons (#55 and #72) exhibited trough widths < 0.5 ms, however, this does not correspond to a peak width correlation due to neuron 72's low spike count (see Fig. 5.5). Comparisons of each cluster's trough width values did not highlight any significant differences (lowest $p = 0.39$, student's t-test).

Peak widths (⑥ in Fig. 5.4) demonstrated greater variation and a normal probability density function could not be effectively fitted to the data (Fig. 5.7, D; average 1.17 ms, ± 0.38 S.D.). Neurons with longer peak widths could be clustered (Fig. 5.7, C), and each cluster's peak width values were significantly different ($p < 0.05$). However, cluster 3 is the most distinctive and the 5 neurons of this cluster skews the distribution (highlighted by the lack of a Gaussian fit) indicating a longer refractory period is unusual in the population.

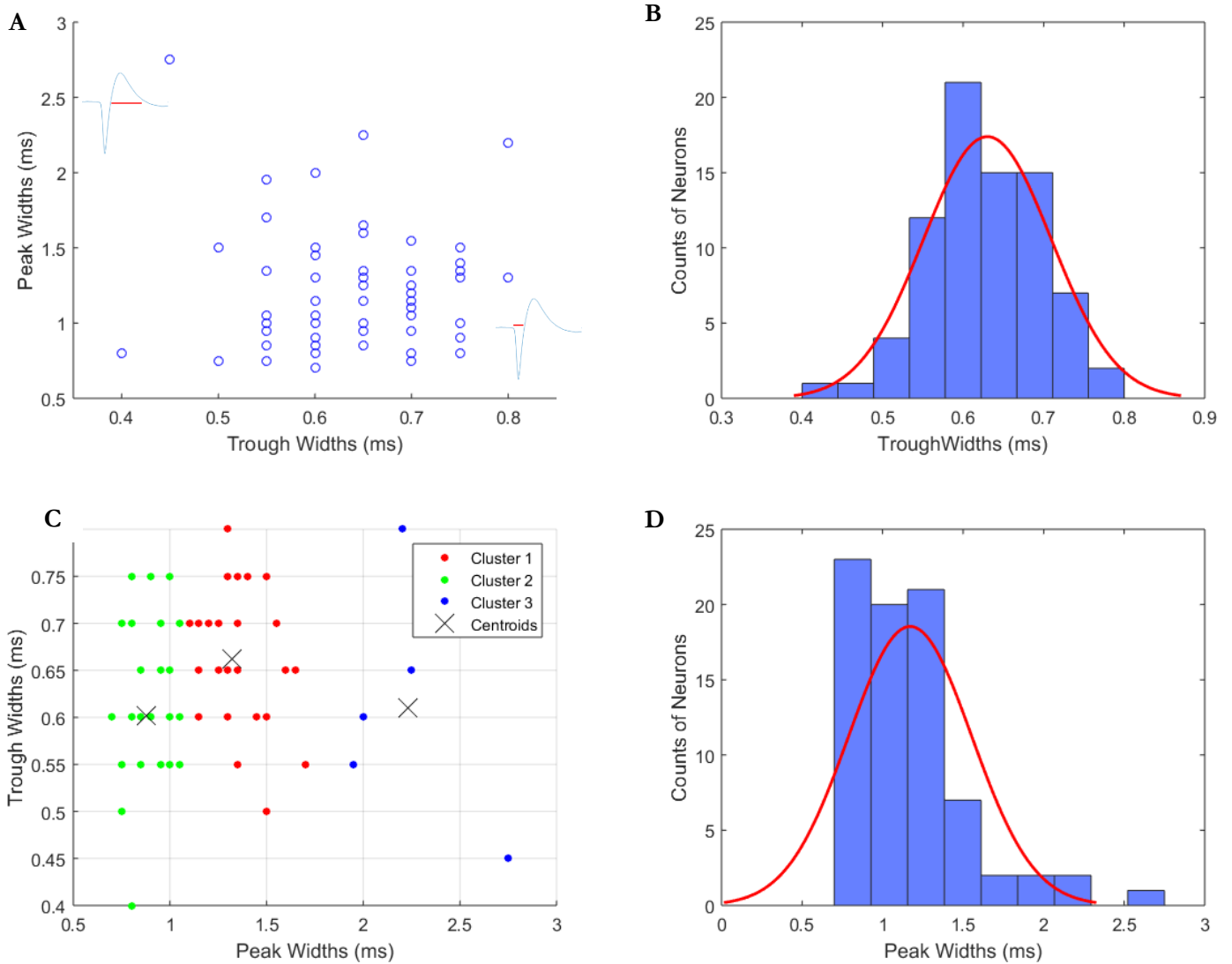


Figure 5. 7. Temporal features of average waveforms. (A) Scatter plot of trough and peak widths. (B) No distinction between neurons was observed using trough width waveform parameters. The 2 neurons with a trough width <0.5 ms demonstrate opposite peak width features suggesting that a narrow trough does not correlate with refractory period. (C & D) Peak widths exhibit a skewed distribution which does not fit a Gaussian probability function. Five neurons possessed long average peak widths (C, cluster 3), however, were not convincingly separated from the bulk of the data (Appendix 7).

The end slope of the signal (⑤ in figure 5.4: the negative gradient from the peak positive amplitude to the RMP) was then calculated using the sample point at which the slope reached 1 sigma above the RMP as defined in the peak to trough ratio calculation. This gradient

Chapter 5

represents the rate of change in extracellular voltage during the return to RMP from refractory period hyperpolarisation. This feature showed greater variation than previously discussed features (mean -1.46 , ± 0.86 S.D.). End slope values did not fit a normal distribution (Fig 5.8 B) and comparing against peak to trough ratios indicated a distinct group at an end slope value of approximately -2 (Fig 5.8 A).

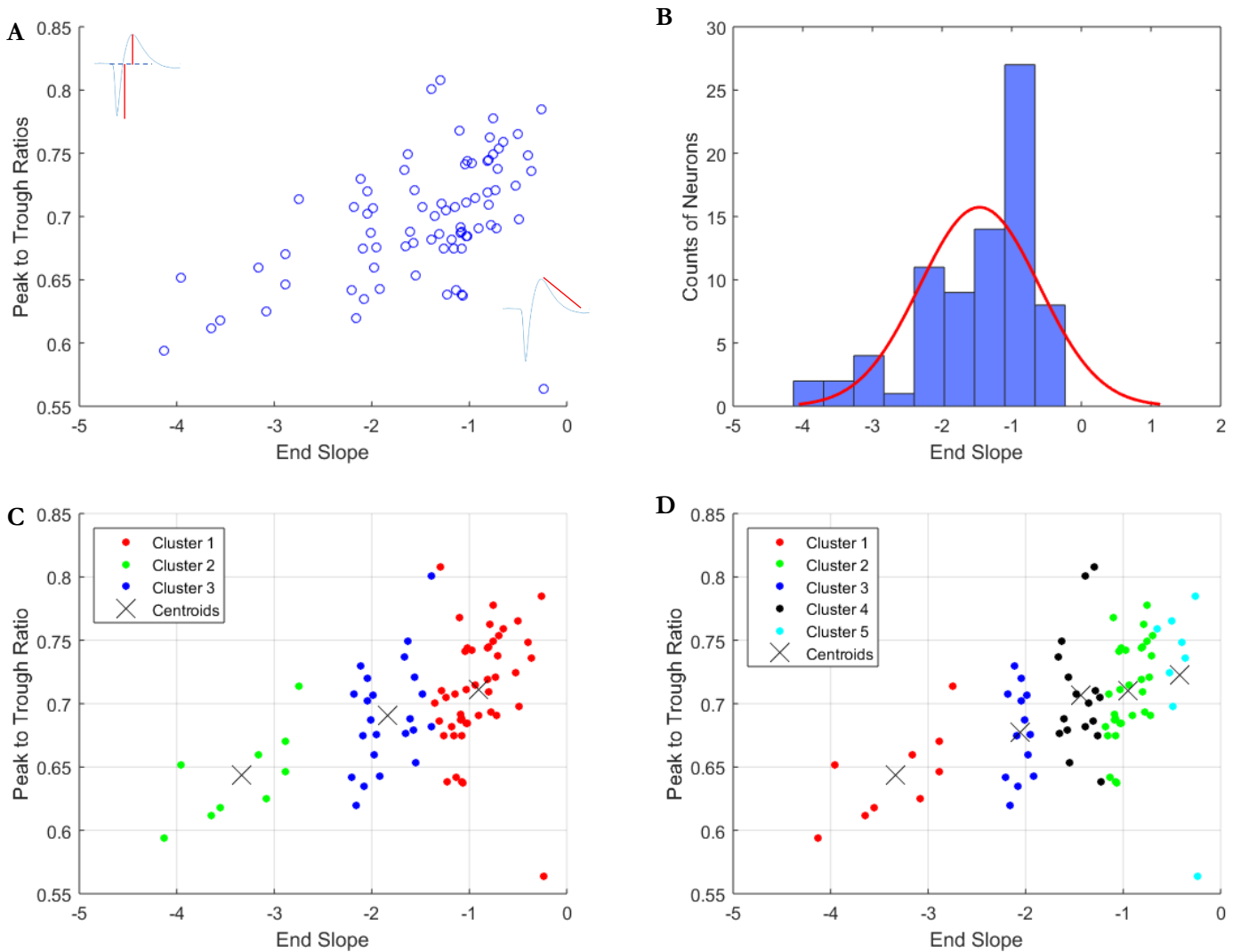


Figure 5. 8. The end slope of the waveform is the gradient of the signal from the peak amplitude to resting membrane potential and therefore represents the extracellular voltage change during action potential refractory period. Left: scatter plot of end slopes vs. peak to trough ratios. A larger peak, relative to the trough amplitude, is associated with a shallower end slope gradient as the membrane potential would take longer to return to rest. Nine

Chapter 5

neurons (#8, 36, 50, 51, 53, 55, 60, 66 & 69) exhibited particularly steep gradients greater than -2.5 and were noticeably clustered.

Neurons with steeper slopes (< -2.5) were clustered as an individual group and were found significantly different from the neighbouring cluster ($p < 0.05$). However, the use of 3 clusters was insufficient to distinguish the potential population centred at an end slope value of -2 (Fig 5.8, C, cluster 3). Histograms of individual clusters (Fig. 5.9, A) further suggested this group to be discrete, as two populations were identified. Following further clustering (Fig. 5.8, D) the distributions of these populations were observed to no longer overlap (Fig 5.9, B) and values of these clusters were found to be significantly different from neighbouring clusters ($p < 0.05$, student's t-test). This required 5 clusters, only two of which demonstrated uncontaminated distributions (Fig. 5.9, B, clusters 1 & 3). The centroids of these clusters (see Fig. 5.8 D) suggest a correlation between the end slope and peak to trough ratio as a larger trough amplitude, relative to the peak amplitude, indicates a steeper end slope. Yet, peak to trough ratios are not effective in clustering neurons (Fig. 5.6) and each cluster identified via end slope analysis exhibits a wide range of ratio values which overlap with neighbouring cluster distributions.

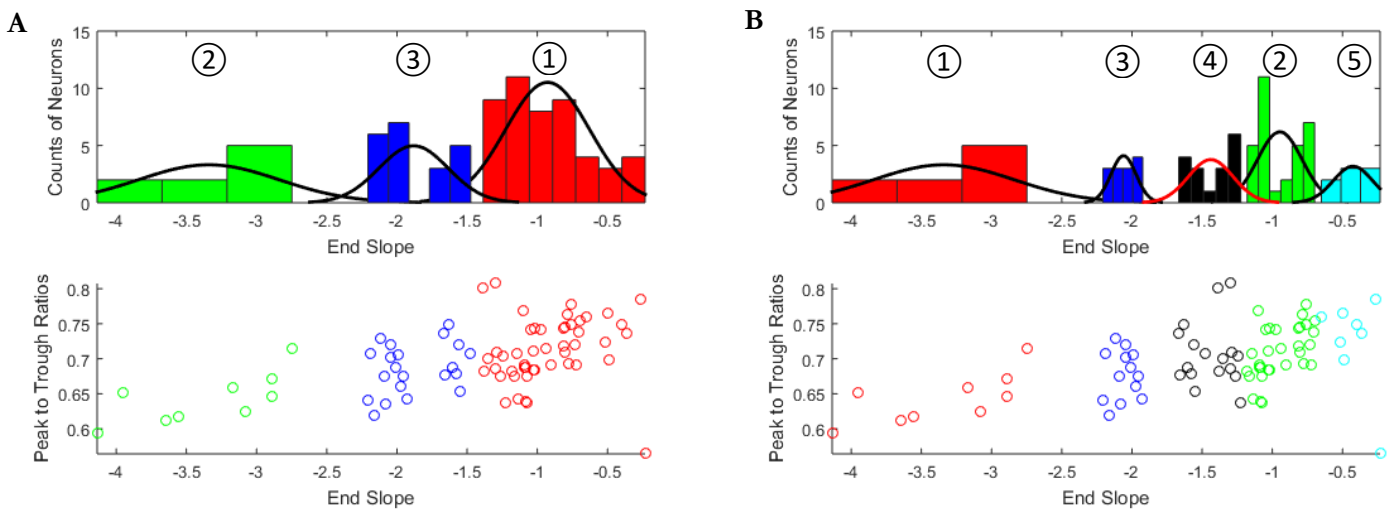


Figure 5.9. Histograms and k-means clustered scatterplots of average waveform end slopes. (A) Clustering with 3 clusters highlights a discrete group of neurons with a steep end slope (cluster 2), however a further cluster is noticeable in the histogram of cluster 3. (B) Further clustering was able to separate this population (cluster 3), but no additional populations were identified in the data. The neuron with very shallow gradient and low peak to trough ratio in

both scatterplots is neuron 72 which displays unusual waveform properties due to low spike count impacting the average waveform.

Finally, the ratios of the peak to trough amplitudes and peak to trough widths were compared (Fig. 5.10, A). This assesses the relative voltage and time differences for each neuron, where a width ratio >1 indicates a longer positive peak than the negative trough (as would be expected).

Histograms of width ratio values (peak width divided by trough width) did not fit a normal probability function (Fig. 5.10, B) and ranged from 1.06 to 3.54 (mean 1.88, ± 0.07 S.D.). Six neurons possessed a value greater than 2.7 (Fig. 5.10, C) and this population was found to have significantly different values from the neighbouring cluster ($p < 0.05$, student's t-test). The remaining two clusters were observed to be part of the same distribution (Fig. 11A). Increasing cluster numbers to 4 did not effectively separate this distribution further as clusters 4 & 1 (Fig. 11, B) were not found to be significantly different ($p > 0.05$). Waveforms with a significantly longer refractory periods than depolarisation are unusual in this population.

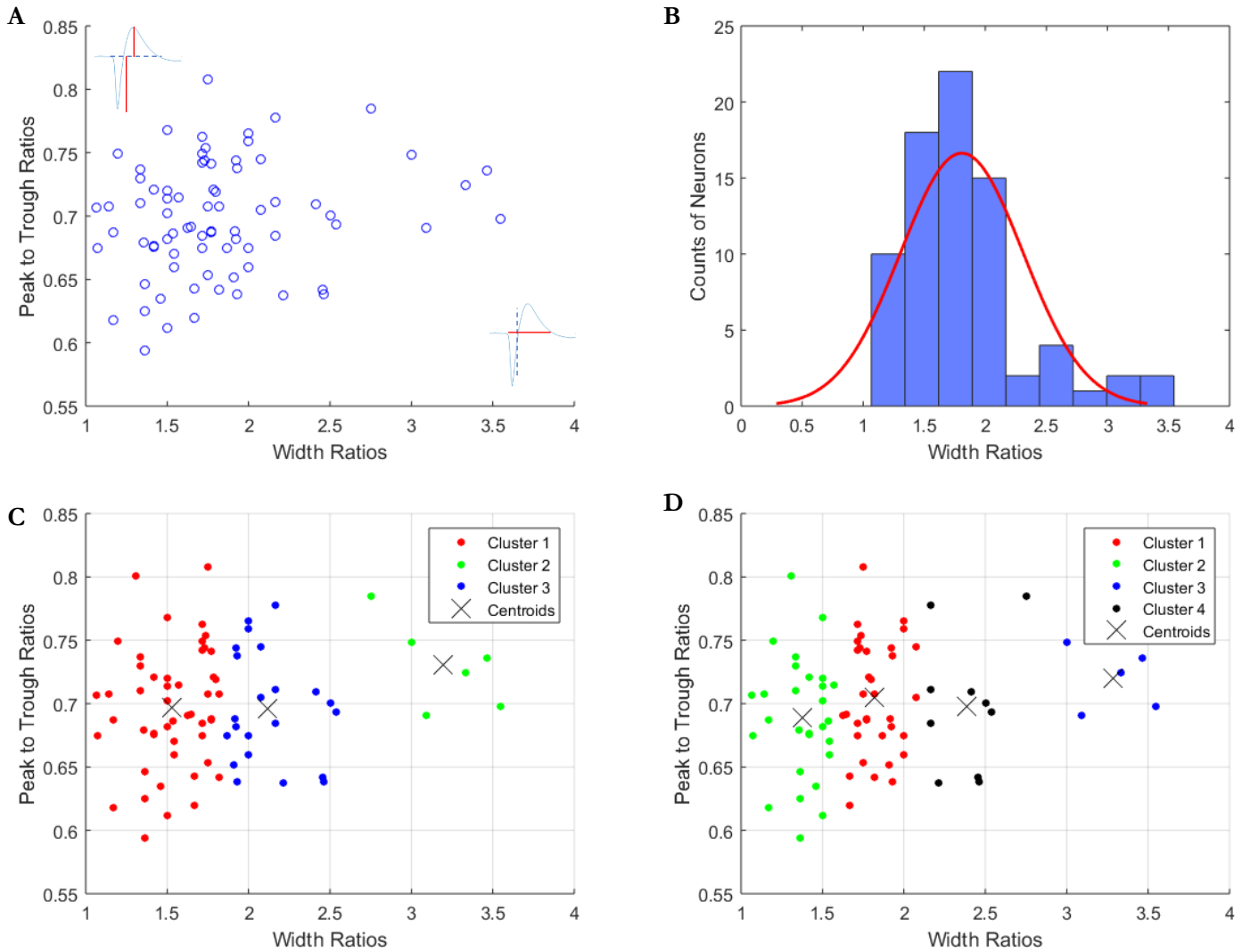


Figure 5. 10. Amplitude and temporal ratios. (A & B) Width ratios exhibited a non-Gaussian distribution across the population (mean 1.87, ± 0.07 S.D.). (C & D) Although 6 neurons with large ratio values (#10, 27, 44, 56, 62 & 73) could be interpreted as a cluster, k-means clustering did not cleanly separate the distributions. Five of these neurons possessed either large peak widths or a short spike width, but not distinctly separate from the population. Neuron #44 exhibited no other unusual waveform properties.

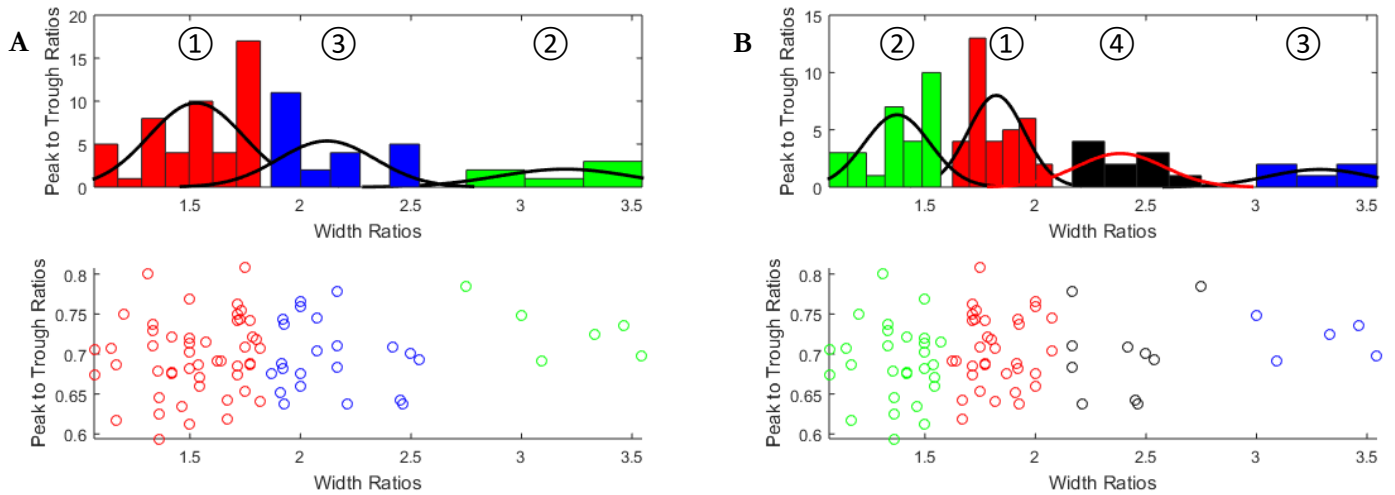


Figure 5. 11. Histograms and k-means clustered scatterplots of clustered width ratios compared to peak to trough ratios. (A) Neurons with greater width ratios were initially interpreted as a cluster, however k-means clustering did not effectively separate these distributions from the rest of the data. The sample size of the potential cluster is also low with a large range of ratio values. (B) Increasing cluster numbers did not improve cluster resolution.

The parameters described in figure 5.4 were not as effective in categorising the recorded population as previous studies have suggested. The end slope, relating to the rate of membrane refractory period, did suggest some distinct clusters of neuron behaviour, however, inferences from this parameter alone was not sufficient to further categorise neurons. The parameters addressed here may not be applicable to *ex-vivo* tissue in the proposed setup and previous studies have favoured specific combinations while consensus for the most reliable analyses appears contentious.

A repeat analysis of waveform parameters was performed for each neuron across all elicited spikes. During spike sorting clustering, spike feature variation is maximised to improve clustering of individual units. Therefore, waveform variation between spikes of a discrete unit should be low. However, as discussed in previous sections, the spike rate of each neuron varies significantly over the time of recording. The decreasing spike rate could be associated with acute cellular trauma and changes to waveform features have been shown to occur in response to inflammatory cytokines¹¹⁰. Such responses are unlikely to have progressed during the short timescale of the recording but were reviewed for reassurance. Each neuron was analysed in turn, and no discrete clusters of spikes with significant waveform feature

differences were identified. However, many neurons were observed to have a tail-off in several features, particularly peak widths and trough widths, indicating some waveform characteristics are more variable than others. Waveform features were additionally examined in ten-minute time bins to evaluate changes over time that could correspond to spike rate fluctuations. As with spike amplitudes (Fig. 5.2, A & C), no corresponding patterns were observed over time.

5.2 Spike Train Temporal Properties Indicate a High Proportion of Bursting Neurons

No definitive difference in waveform characteristics was observed within the recorded population which could suggest functional differences. Similarities in network functionality were therefore evaluated for other characteristics. An important aspect of neurons are the temporal properties of elicited spikes, which is incorporated into key models of neuron information coding – the mechanism of information transfer between neurons – and differentiating neurons based on spike activity patterns could distinguish cellular subtypes. Approaches to investigate temporal coding commonly utilise the ISIs to discern functional differences between neurons^{149,134}. This property is also used in determining periods of high-frequency activity without using an arbitrary time window. Spontaneous periods of high frequency action potentials are commonly observed in cultured neurons^{150,151} and organotypic slices of brain tissues¹¹⁵. These events, termed bursts, are believed to be critical in network formation as they have also been associated with long-term potentiation and may therefore have a role in learning and memory¹⁵². Bursts have been shown to increase the reliability of information transmission as a bursting neuron has a higher probability of eliciting an action potential postsynaptically. Additionally, bursting can be induced by pharmacological agents, for instance by increasing the activity of sodium channels¹⁵³, while acute cellular damage can trigger burst-like behaviour via cytokine 2nd messengers¹¹⁰. The cellular mechanisms and role of this function within a network remain poorly understood and separating physiological bursting from experimentally induced bursting remains a concern for acute slice preparations. The aim of the 512-needle MEA presented in this work is to record cellular activity from cells unaffected by the sectioning procedure and limit the damage to localised networks. Therefore, this setup presents the potential for a more valid interpretation of physiological network bursting.

Distributions of ISI values were assessed to investigate changes in temporal activity. These findings suggest that some recorded neurons demonstrate more complex activity patterns occur at relatively higher frequencies of spiking. The regularity at which these ISI values occur was then evaluated based on the coefficient of variation for each neuron sequence. Half (49%) of the population exhibited more irregular activity at relatively low frequencies. The MISI approach to bursting identification developed by Chen *et. al*¹³⁵ was then performed and was found to be unsuitable for the spike trains presented here due to the large range in ISI values and indicated that ~50% of each neuron's activity represented spiking behaviour. Therefore, a novel approach to burst activity analysis was developed based on proximity of periods of (relatively) high frequency activity within ISI sequences. This method highlights a greater variation of bursting behaviours across the population suggesting it is more sensitive to changes in temporal activity.

5.2.1 Inter-spike Interval Distributions

The ISI values for each neuron spike train were calculated using Matlab software. The ISI distribution curve, for all neurons, is presented in figure 5.12 (A); the peak ISI value is 5 ms. Distributions of each neuron spike train ISI values were also examined (example Fig. 5.12, B). A surprisingly large number of 2 ms and 3 ms ISI values were identified and could be attributed to relaxed correlation and contamination parameters during spike sorting as well as manual re-clustering evaluations (see section 4.1.3). Although concerning, these intervals represented a low proportion (3%) of values overall. Distributions of ISI values have been used to indicate a threshold ISI value to differentiate between regular and sporadic firing rates^{133,135,140} and this temporal feature was initially evaluated for each individual neuron.

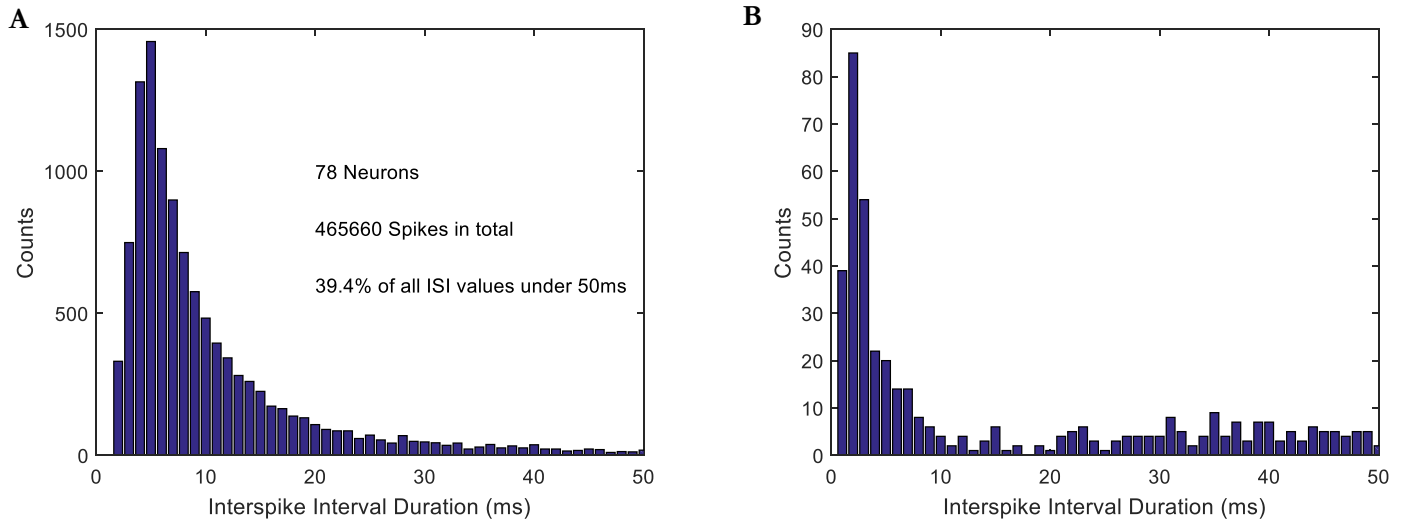


Figure 5. 12. Counts of inter-spike interval values. (A) Histogram of all neuron spike train ISI values (1 ms bins). The peak ISI value for the population as 5 ms, while a large number of ISIs under 3 ms are identified which is improbable due to the refractory periods of neurons. The range of ISIs extends far beyond 50 ms, however the bulk of cumulated values are presented within this timeframe; see Fig. 4.9,B. (B) Example histogram of ISI values for a single neuron. Most neurons exhibited a large range of ISI values.

Histogram counts of ISI values were plotted on a logarithmic axis (Fig. 5.13) where a bimodal distribution suggests the presence two distinct patterns of activity^{133,149}. Some distributions displayed an identifiable threshold (e.g. neuron #11, see Fig. 5.13, A), however most spike trains exhibited a peak of low value ISIs and a large spread of higher values (Fig. 5.13, B). The proportion of high value ISIs was striking; the average population ISI over the initial 2 hours of recording was 44 seconds (± 29.6 S.D.). Although outlier values could skew this average, intervals exceeding 1 minute were common and the range of average ISIs per neuron was between 2s (± 4.5 S.D.) and 118 s (± 142 S.D.). High value ISIs are related to the low spike frequency reported in earlier chapters as, for the duration of the recording, spiking activity is separated by long periods of inactivity (see Appendix 8 for individual neuron example).

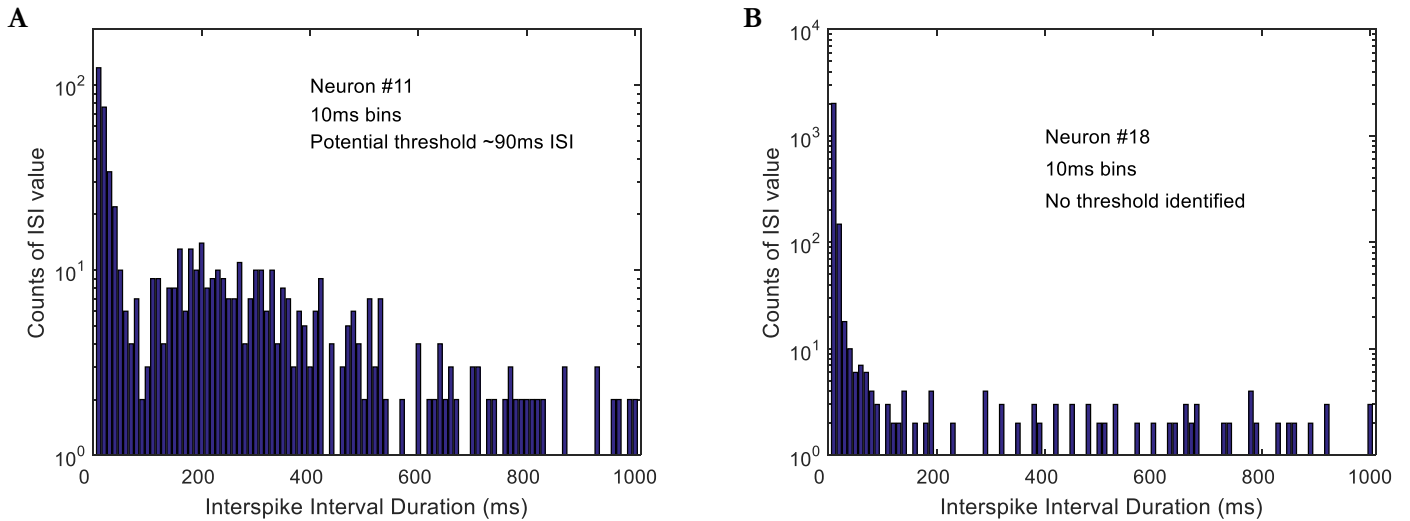


Figure 5.13. Histograms of ISI values per neuron plotted on a logarithmic scale. Threshold ISI values to identify periods of high-frequency bursting can be inferred from a bimodal distribution (A), but the large proportion of low-frequency activity made this approach difficult to meaningfully apply to most neurons of the dataset (B).

5.2.2 High Frequency Spike Rates Identify Distinct Activity in a Subset of Neurons

Sequences of ISI values were processed using a range of limiting values. A limit of, e.g. 100 ms, was set and ISI values exceeding the limit were excluded. The percentage of remaining values were then calculated as a percentage of the total, original, ISI values. For summary analysis, this data was then averaged across the population. The results indicate that, as a population, 49.97% of all ISI values in the recording are less than 7.5 seconds (Fig. 5.14, A, dashed red line); i.e. when the limit is set to 7.5 seconds the average remaining percentage of ISI values is 49.97%. The averaged percentage of ISI values under a limit was plotted against the ISI limit which can suggest a change in spiking behaviour was observed. The gradient of the curve changes when the limit is increased beyond 1s (Fig. 5.14, A, dashed black line). As this relationship is not linear, it could indicate distinct activity patterns.

The variation across spike trains for a range of limiting values can be seen in Fig. 5.14 (B) and highlights the requirement of an adaptable method of processing ISI values for distinguishing neuron behaviours at high and low spike frequencies. While resembling the pattern observed in the population analysis (Fig. 5.14, A), some spike trains exhibit 60% of ISI values under a limit of 50 ms (population average is 27.6% at 50 ms). A method was therefore developed to generate a dynamic limit based on the median ISI value of each spike train to segregate

relatively high frequency activity periods from lower spiking patterns. These were then compared to classify neurons based on the temporal qualities of spiking activity.

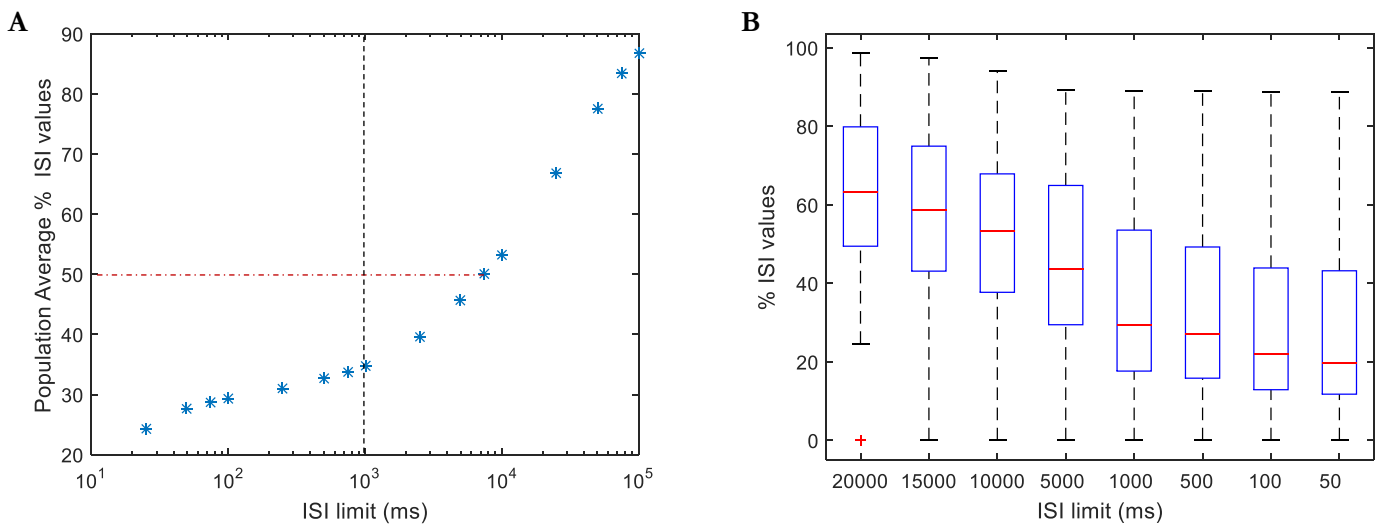


Figure 5. 14. Percentage of ISI values under a given limit. (A) Inter-spike intervals less than 7.5seconds represent 49.97% of the entire population's ISI values (red, dashed, line). A limit of 100 seconds accounts for 86.8% of all ISI values. The gradient of the slope becomes steeper at limits greater than 1 second, indicating a change in spiking behaviour. (B) Boxplot of percentages of individual spike train ISIs below a given limit. The variation of ISI values between spike trains indicates a generic limit is inapplicable. Red lines represent median values; edges of blue boxes are 25th and 75th quartiles; whiskers extend to extremes of dataset not considered outliers; outliers represented by red crosses.

The variation in counts of ISI values per neuron was analysed using the standard deviation in ISI distribution plots. Distributions with a narrow single peak, or no peak, would demonstrate a lower variation in ISI counts than distributions with broader or bimodal distributions. To account for the wide range of values, this was performed for values above and below the median ISI value of each neuron (Fig. 5.15).

A linear trend is observed between increasing mean ISI and ISI variance, however, at relatively higher spike frequencies (Fig. 5.15, A), a group of 18 neurons exhibit significantly lower variance ($p = 0.00014$, 2-tailed student's t-test). The ISI distributions of these plots were individually evaluated and exhibited narrow peaks of low value ISIs (high frequency) with a mean of 4.6 ms (± 3.5 , S.D.). Although less defined, a second cluster of 6 neurons with a variance of between 90 and 300 ms consistently demonstrated broad or bimodal ISI distributions and was statistically distinct from the higher variance group ($p = 0.013$, 2-tailed, student's t-test). At lower frequency ISIs (Fig. 5.15, B), no change in ISI distribution was

identified that showed a relationship with increasing ISI variance. This data suggests that, at relatively higher frequencies, some neurons demonstrate more complex patterns of temporal activity.

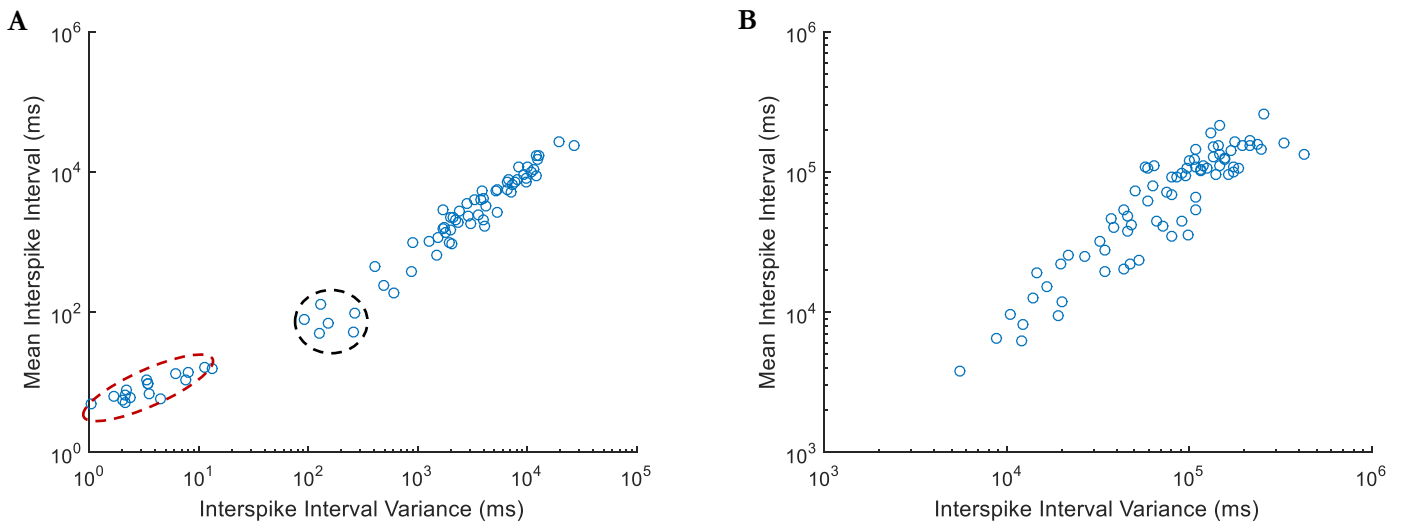


Figure 5. 15. The variation of counts of ISI values per neuron were evaluated. The linear trend indicates that a small mean ISI corresponds to a narrow distribution of ISI values. (A) The variation of counts of ISI values less than the median ISI value per neuron. (B) The variation of counts of ISI values greater than the median ISI value per neuron.

5.2.3 Coefficient of Variation of Inter-Spike Intervals

Coefficients of variation (CV) have been successfully applied in previous studies to differentiate inhibitory and excitatory cells *in vitro*^{77,147} and to evaluate variation in spike train activity^{154,113,155}. This approach divides the spike interval standard deviation by the mean ISI value to quantify the width of the ISI distribution. A CV value can indicate the regularity of spiking, i.e. if a neuron's behaviour is dominated by tonic or bursting firing rates. A CV value >1 suggests high variability in activity as the deviation exceeds the mean.

The 2-hour recording was analysed per neuron and all neurons exhibited a CV value greater than 1 (mean 1.98 ± 0.72 S.D.), suggesting all neurons exhibit irregular firing patterns (Fig. 5.16). Neuron #72 was not appropriate to analyse with this parameter as only two spikes were elicited in the first two hours. The CV is a measure of spike train variability and large ISI values would increase this variation dramatically without high frequency bursting being apparent. Therefore, high and low frequency activity was compared across neurons by limiting the ISIs analysed to above or below the median ISI value for each neuron.

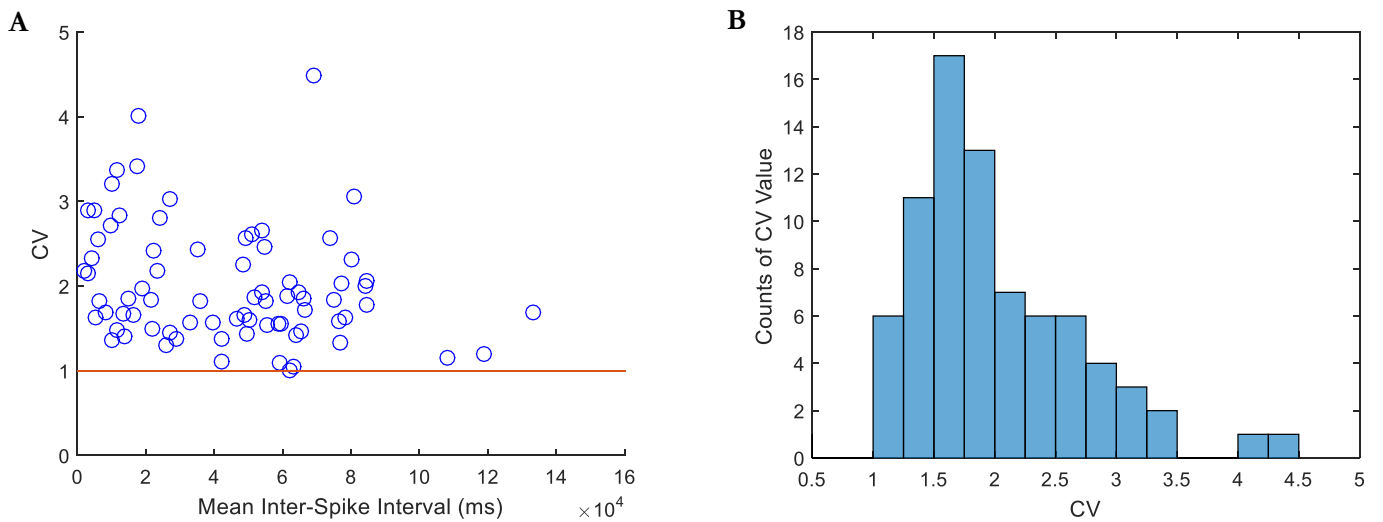


Figure 5. 16. Coefficient of variation over the 2hour recording. (A) All neurons exhibited a $CV > 1$, indicating ISI variation exceeds the mean value. (B) Histogram of CV values over the 2hour recording demonstrates the peak CV value is 1.75 with two outlying neurons exhibiting a CV value > 4 .

Neuron ISI values lower than the median represent the highest frequency spiking for each neuron. These spike rates demonstrated a $CV > 1$ (mean 1.16 ± 0.76 S.D.) in 39 neurons (50%), suggesting half of the population display irregularly elicited firing rates when firing at high frequencies relative to that neuron (Fig. 5.17 A). When ISI values are limited to values greater than the median ISI, 51 neurons (66%) possess a $CV > 1$ (Fig. 7.18 C&D, mean 1.28 ± 0.54 S.D.). When these neurons are firing at relatively low rates these frequencies are less likely to be repeated. This suggests that more neurons display greater spike rate variability when firing at lower frequencies.

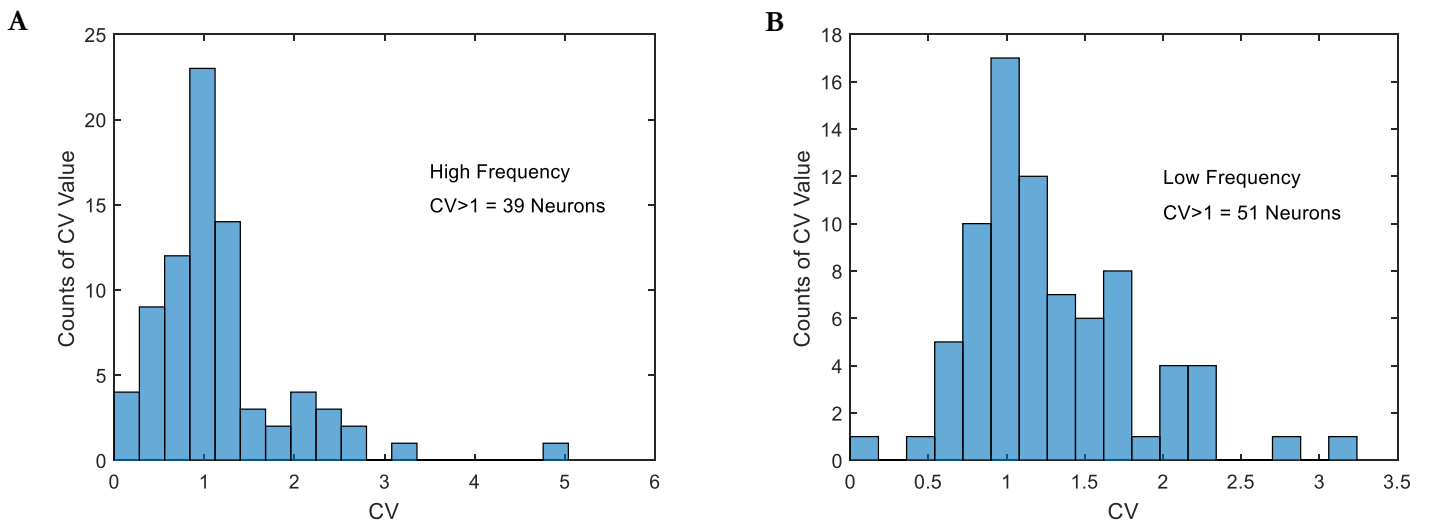


Figure 5. 17. Coefficient of variation values, per neuron, calculated with ISIs above or below the median ISI value for each neuron. (A) ISI values exceeding the median ISI were excluded from analysis, leaving relatively high frequency spike rates with which to calculate CV values. At higher frequencies, 50% of neurons display a high degree of spike train variation, i.e. $CV > 1$. (B) At lower relative frequencies, 66% of neurons displayed a $CV > 1$ indicating greater spike rate variation at lower frequencies.

The CV values at relatively high and low frequencies were then directly compared (Fig. 7.18). Of the 77 neurons (#72 excluded), 35 neurons (45%) exhibited a greater CV value at relatively higher firing rates and 38 (49%) demonstrated greater variation at lower rates. Four neurons displayed less than 0.005 difference and were therefore determined to have an equal degree of variation throughout the recording.

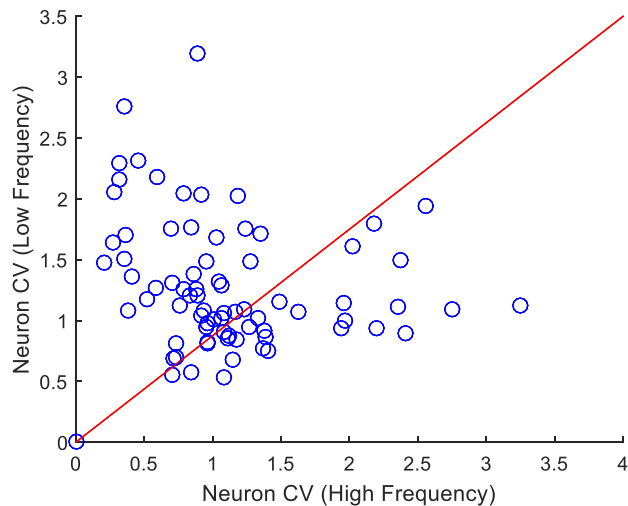


Figure 5. 18. Comparison of CV values per neuron at relatively high and low frequencies. The population was roughly split (45% to 49%) with greater variation at either frequency band. Four neurons (6%) demonstrated no difference between frequencies. The point at 0,0 is neuron 72 which exhibited no variation.

5.3 Defined Periods of Bursting Behaviour

Spontaneous periods of high frequency action potentials are commonly observed in cultured neurons and organotypic slices of brain tissues^{155,156}. These events, termed bursts, are believed to be critical in network formation, however, they have also been associated with long-term potentiation and may therefore have a role in learning and memory^{152,157}, while rate of bursting events as been shown to alter in pathological states such as Parkinson's¹⁵⁸ and Alzheimer's disease¹⁵⁹. Bursts have been shown to increase the reliability of information transmission (a bursting neuron has a higher probability of eliciting a postsynaptic action potential), however, the cellular mechanisms and role of this function within a network remain poorly understood.

The definition of a burst is variable, and studies have developed identification parameters based on: their experimental setup (e.g. cell culture¹⁵⁵ or *in vivo*¹⁶⁰), cell types employed (e.g. cortical pyramidal neurons¹⁶¹ or granule cells) and the technologies used to record activity (patch clamp, EEG, extracellular). Burst detection analyses often utilise ISI values of a neuron, rather than frequencies spanning arbitrary time windows. The deficiencies of using spike rate parameters alone relate to the significant variation in activity levels observed across

numerous cell types within a network. The use of an arbitrary value does not account for this variation and a dynamic value based on features of the spike train is more relevant.

This section evaluates the applicability of the burst identification MISI method to the recorded data and then describes an alternative approach to identifying bursting activity within a spike train termed the MBISI method. The MISI method, developed by Chen *et al.*¹³⁵, indicates that ~50% of the activity of each neuron is defined as bursting, while 30 neurons exhibited bursting in more than 50% of active periods. However, these assertions are relative to each neuron's firing rate and identified intra burst intervals (IBI) of >10seconds; a low firing rate to define as a burst. This method demonstrated low variation between neurons suggesting that they are all behaving similarly to each other despite large spike train variability. In comparison, the novel MBISI approach exhibited a large deviation in bursting behaviours between neurons, providing greater resolution to discriminate activity differences.

5.3.1 Mean Inter-spike Interval Method

The MISI method of burst identification generates an auto-adaptive threshold value (ML) which is relative to each neuron. It is performed by calculating the mean of ISI values less than the mean of the original sequence, i.e.: calculate the mean ISI value in a spike train (MISI); identify ISI values less than MISI; values less than MISI are maintained as a sequence, termed Ln; calculate the mean of Ln, termed ML; define bursts in the original ISI sequence as two or more successive ISI values less than ML. Interval values before and after each spike are plotted to survey the activity of each neuron and compare to the ML value (Fig. 5.20). Intervals preceding and after a spike below ML are designated as a bursting sequence of 3 spikes.

The method indicates an average of 49.6% ($\pm 12\%$, S.D.) of each neuron's activity consists of bursting (Fig. 5.19, A; a histogram of percentages of bursting spikes can be found in appendix 9). The MISI method generates a bursting threshold relative to each neuron with a mean ML value of 9.7seconds ($\pm 8.4s$, S.D.). A sequence of 3 spikes with ISI values of ~10s represents a low spike rate and is arguably not bursting activity due to the low frequency of activity. Eight neurons exhibited an ML value less than 1s (Fig. 5.20, B) and a greater percentage of spikes identified as bursting correlated with a lower ML value (Appendix 10).

Due to the low spiking frequency observed across neurons, the MISI method identifies a relative threshold of burst activity greater than what would be considered high frequency

spike activity (e.g. the population average of 9.7seconds). Additionally, this method suggests that, on average, half of all neuron activity is bursting and does not demonstrate a large degree of variation between neurons which could be used to differentiate functional roles. Therefore, an alternative method was developed to further distinguish neuron behaviours based on patterns of inter-burst interval values and the sequences at which these occur.

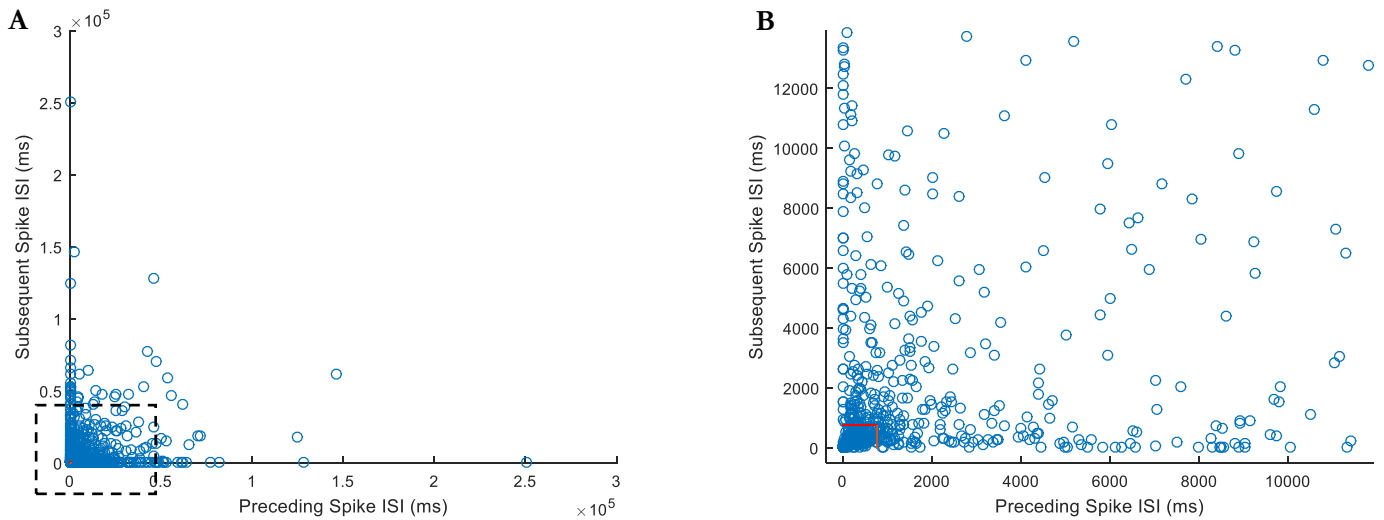


Figure 5. 19. Example of the MISI method of burst detection. The ISI value preceding a spike (x-axis) and subsequent to the same spike (y-axis) are plotted. The value of ML for this neuron is shown as a red line. Spike ISI values less than MISI both before and after the spike are part of a burst of three spikes. (A) The large range of ISI values makes the MISI threshold difficult to discern; a black, dashed, box outlines the region of interest which is presented in (B) where the red lines are visible.

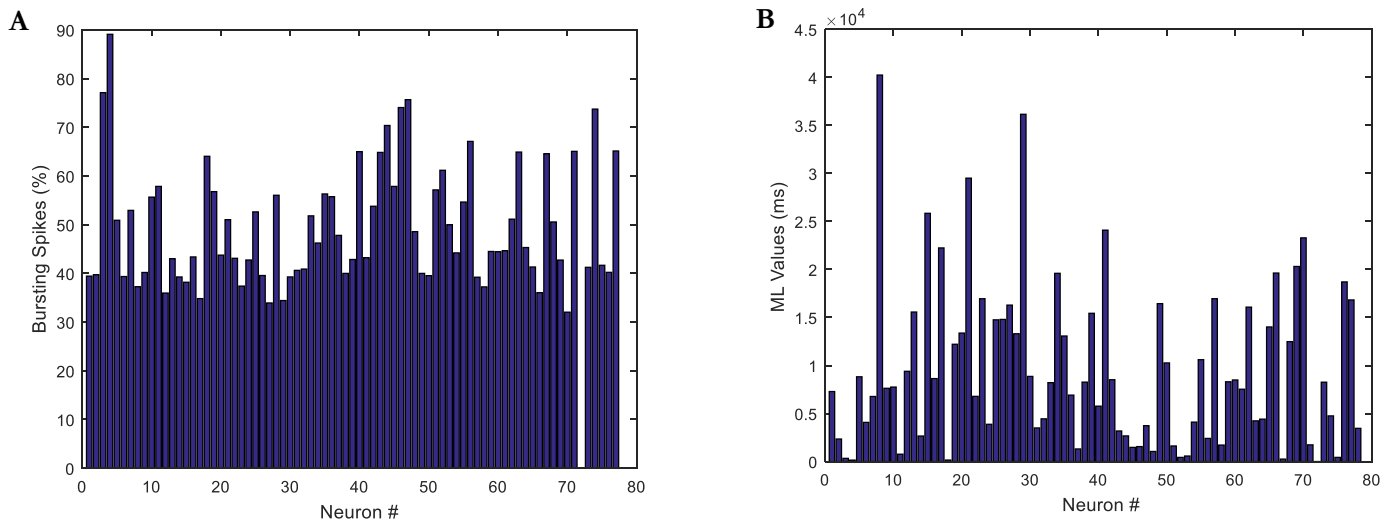


Figure 5. 20. Evaluation of the MISI method of bursting activity detection. (A) The percentage of each neuron's ISI value lower than ML threshold value (identified as bursting activity); mean 49.6% ($\pm 12\%$, S.D.). (B) The ML value calculated per neuron; mean 9.7seconds ($\pm 8.4s$, S.D.).

5.3.2 MBISI analysis

As an alternative method of ISI sequence analysis, a novel approach was developed based on proximity of periods of (relatively) high frequency activity within the sequence. This approach calculates the maximum number of groups of three or more spikes that can be defined with a given ISI value and separates the sequence into ISI values and inter-burst intervals (IBI), where $ISI < IBI$. The ISI value which identifies the maximum number of bursts (3 or more spikes) in a spike train was termed MBISI (max bursts) and reflects the ISI at which the sequence can be maximally segmented. Changes in the rate of burst identification over increasing ISI values were consistently identified across the population and provided a basis for a temporal threshold for burst activity. Peaks in histograms of the numbers of bursts detected were then used to calculate an ISI value to identify periods of bursting activity in each neuron spike train.

Briefly:

- 1 Spike train ISI values are calculated
- 2 MN is a limiting ISI value which increases by 1 ms each iteration from 0 to the maximum ISI within a given spike train.

- 3 The spike train ISI values are analysed for values less than MN, the times at which the corresponding spikes were elicited are then recorded
- 4 Then sequences where 2 or more adjacent ISI values (minimum 3 spikes) less than MN are identified
- 5 These sequences with a minimum of 2 ISI values are defined as bursts.
- 6 The number of identified bursts throughout the spike train is recorded
- 7 Subsequent to analysis of the entire spike train, the next iteration begins with MN increasing by 1 ms.

As the MN value increases, more bursts are identified, each consisting of greater numbers of spikes. This value peaks as the ISI value exceeds the time between bursts and approaches the maximum ISI, reducing the number of identified bursts (Fig. 5.21, A). Plotting the number of spike train bursts against increasing MN values (the maximum intra-burst value included in analysis) highlights bursting activity separated by large ISI values. Changes to the gradient of the curve describe characteristics of temporal proximity; i.e., a plateau indicates bursts are separated by greater ISI values while a steep gradient suggests a temporally variable spike train (Fig. 5.21, B).

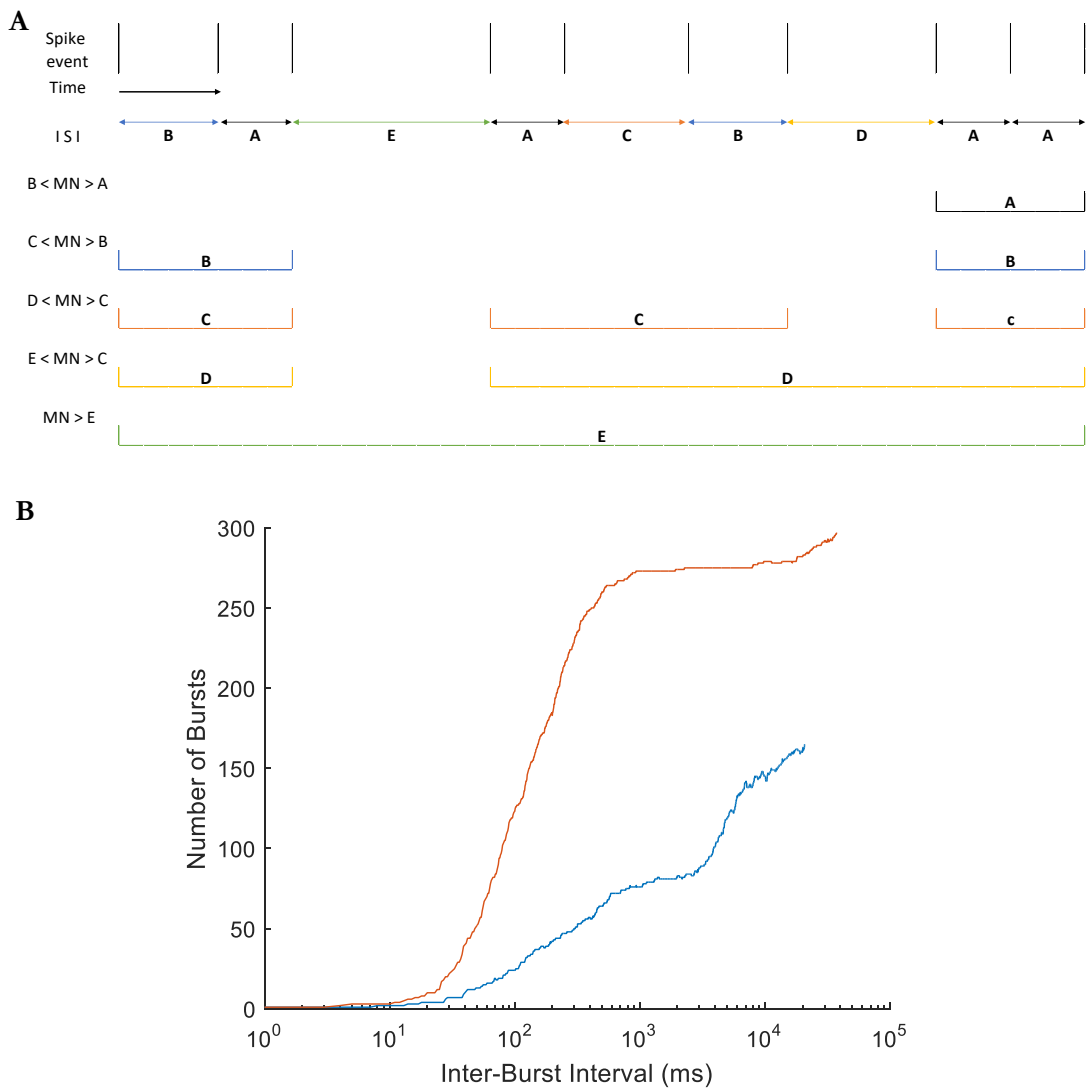


Figure 5. 21. MN burst analysis indicates the proximity of high frequency periods within a temporal sequence and identifies the ISI value at which the sequence can be most segmented into discrete periods of activity. (A) As MN increases, more groups of sequential spikes are identified as bursts. MN approaches the maximum ISI value and the number of spike groups decreases. (B) Example plot of MN analysis of two neurons. Both neurons exhibit a plateau preceding a further increase in burst number, indicating several large ISI values separating bursts. A plateau approaching the peak burst value suggests that a small proportion of spikes are separated by large ISIs (orange line).

With the number of identified bursts plotted against MN (1 ms less than the inter-burst interval), neurons consistently demonstrated a plateau in the numbers of bursts identified (Fig. 5.21, B) suggesting a regular pattern within the distribution. Histograms of MN values

were generated which highlight repeated burst number values (Fig. 5.22, A). A greater count of burst ISI value indicates that the burst sequence has not changed despite a more relaxed (increasing) ISI limit which should identify more bursts. The average value in these distributions was found to precede the initial plateau observed across the population (Fig. 5.22, B). The average number of bursts identified by this method was then used as a threshold for burst identification and spike groups identified at MN lower than this value are designated as bursts.

The peak number of bursts represents the maximum segmentation of each spike train. The number of bursts identified at MBISI value were calculated as a percentage of the maximum burst number (5.23, A). The mean population value of bursting activity (% of spikes exhibiting bursting activity) was 48.86%, comparable to the MISI method (49.6%), however, the population distribution exhibited double the deviation (± 24 S.D compared to ± 12 for MISI). Due to the relative nature of this method, neurons with high spiking frequencies do not necessarily demonstrate a high percentage of bursting periods. The variation between neurons is more observable using this method than the MISI although it is based on three or more successive spikes, not two.

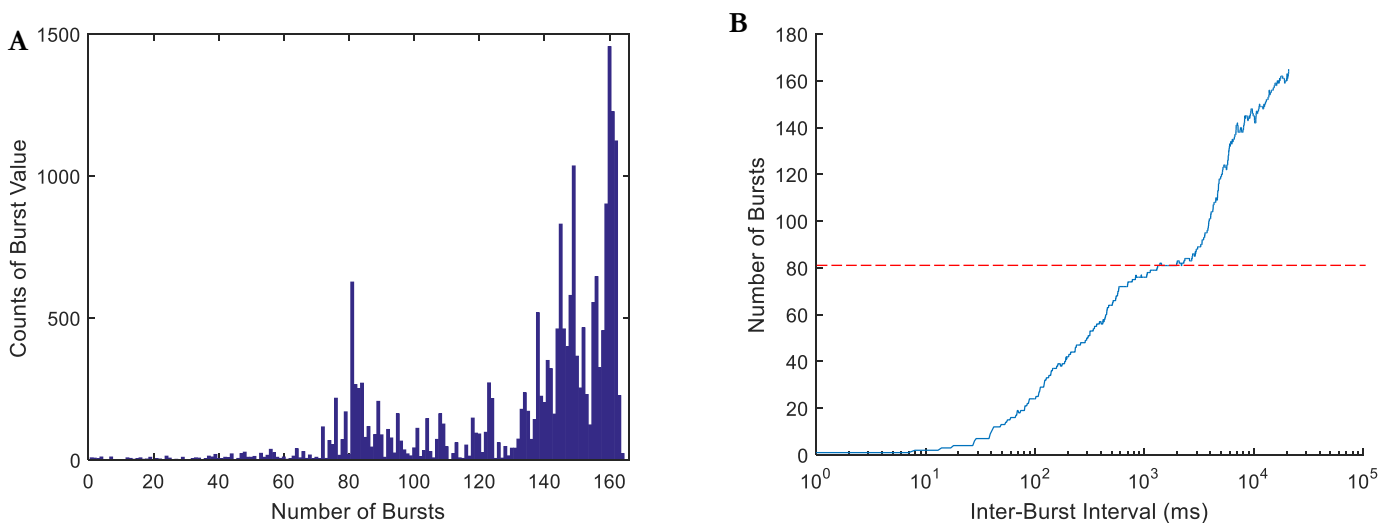


Figure 5. 22. Frequency of burst count identifies discrete populations of bursts at varying limiting ISI values. (A) Histogram of neuron #11 MBISI burst analysis. Counts of burst value refer to the count of incidences a count of bursts occurs in analysis, i.e. $MN = X$, number of bursts = Y ; $MN = X+1$, number of bursts = Y ; there are 2 counts of Y . Over 500 ISI values used as MN identify 81 bursts; despite the limiting ISI value increasing, no change to the number of identified bursts is observed. The average burst count in this histogram is 76 bursts. (B) The average of 76 bursts is plotted against the results at increasing MN values (red dashed line a

80). This identifies the MN value of 827 ms as an appropriate threshold of bursting activity for this neuron.

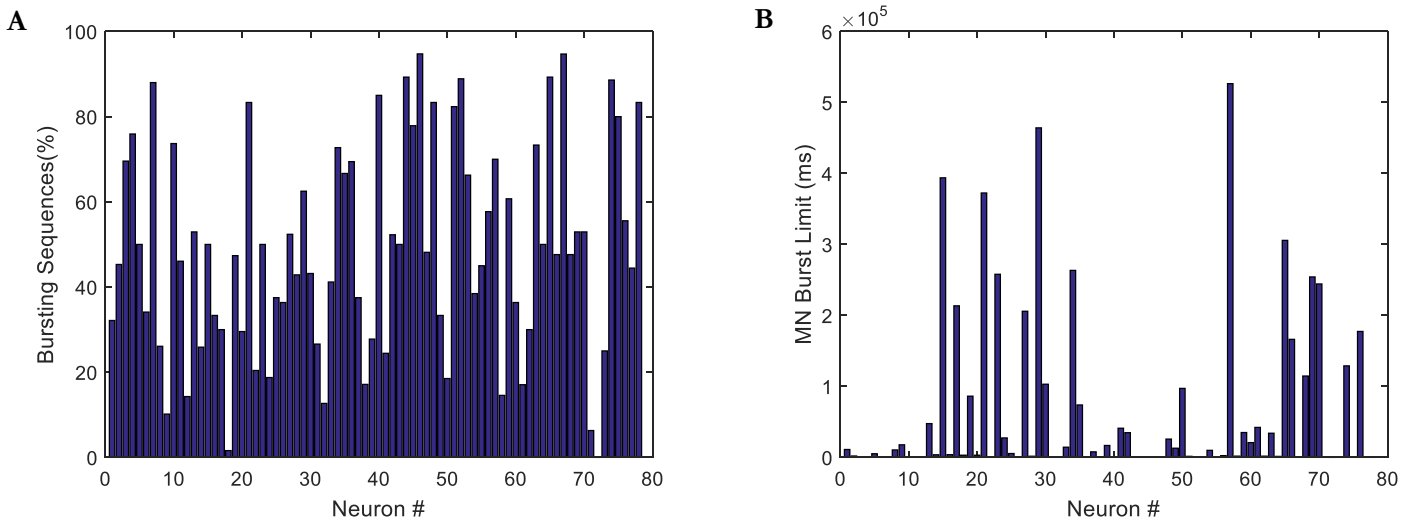


Figure 5. 23. Temporal qualities of neurons measured using the NBISI method. (A) The number of identified bursts below the MN limiting threshold as a percentage of maximum identifiable spike groups per neuron. Mean 48.9%, ± 24.8 S.D. (B) The MN limit is the ISI value at which the average number of bursts occurs; sequences of 3 or more spikes with ISI values well than the MN limit are defined as a group of bursting spikes.

5.4 Discussion: Spike Features and Temporal Characteristics

The temporal and amplitude features of extracellular waveforms have been reported to indicate if a neuron is exert an inhibitory or excitatory role within a network¹². An approach is presented in this work which attempted to discriminate between these two broad classes of cell. These features are suggested to indicate a class of neuron because the function of a cell requires specific types and densities of ion channels embedded in the cell membrane. Such discrepancies may be reflected in the speed and magnitude of ion currents. No clear distinction between cell types was identified, however, some features exhibited greater distribution than others which highlights the heterogeneity of the population. The end slope and width ratios possessed the highest deviation across the population (± 0.86 and ± 0.71 respectively) and k-means clustering of these data suggest significant differences between neurons. Both features are related to temporal characteristics of the average spike (end slope is the time taken to return to RMP from peak amplitude and width ratios are based on the

time of each phase of the AP) which is important as this approach is based on the observation that inhibitory neurons exhibit a faster, narrower, spike^{162,163}.

Although trough widths did not indicate significant variation across the population ($p = 0.39$, Fig. 5.7, B) a cluster of neurons demonstrated longer refractory periods (peak widths; Fig. 5.7, D). This feature becomes more significant when compared to the trough width and the relative ratios may be more representative of faster spiking (Fig. 5.10, B). A potential cluster of 6 neurons with significantly ($p < 0.05$) larger width ratio values indicates that these cells have a longer positive peak than the duration of the negative trough. However, this does not necessarily equate to a narrow spiking inhibitory cell as a longer refractory period has not associated with this class of cells.

A steeper (more negative) end slope gradient has been associated with inhibitory neurons¹² and two potential neuron populations were identified, but, this was not correlated with peak or trough widths measured independently. The end slope represents the rate of voltage change following peak amplitude (intracellular hyperpolarisation) in returning to RMP. It can be seen from figure 5.3 that the greatest variation in averaged waveforms occurs around the refractory period and these differences were found to be significant when clustered in groups of 3 or more (Fig. 5.9). Histograms of the end slope value distributions identified three clusters, however, not all clusters exhibited a convincingly specific identity. Particularly steep slopes (Fig. 5.9, A, cluster #2) were observed to have a distinct distribution, yet the large range of values does not suggest specificity. Low-gradient slopes (Fig. 5.9, A, cluster #1) indicated a normal distribution if portions of cluster #3 were re-assigned, however, attempting to re-define this cluster did not improve the resolution of the distribution (Fig. 5.9, B, clusters # 4,2,5). The most interesting waveform identity was centred on a slope gradient value of -2 and exhibited a significantly distinct and specific distribution (Fig. 5.9, B, cluster #3). Previous studies have not reported waveforms possessing end slope gradients of this values (max ~ -0.15 ¹²) and no investigation known to the author has described three separate clusters of populations defined using this method.

Although relaxed contamination and correlation parameters used to improve spike sorting may admit anomalous refractory period signals, averaging of the waveform limits the impact a minority of abnormal spikes could cause. It is possible that shallow gradient slopes may have been recording from somatic areas closer to the axon hillock where hyperpolarisation is attenuated¹⁶⁴, however, this suggests that the majority of neurons were recorded from this specific area which seems unlikely.

Steep slope suggests quick return to RMP and therefore would be able to fire again (high frequency) and a large amplitude extracellular peak is associated with fast spiking¹⁶⁵. This suggests that the more negative slope neurons are fast spiking inhibitory neurons, yet these cells do not demonstrate significantly narrow trough widths.

Pyramidal neurons have been reported to exhibit prominent afterdepolarisations^{166,167} a feature which was clearly identified in neuron #53 (purple waveform in fig. 5.6). However, neurons exhibiting afterdepolarisations were not identified as a distinct population when analysed using the waveform features presented in this work. Additionally, they were not found to consistently demonstrate similar temporal features. see appendix 12)

The applicability of these features in determining neuronal subtype is not universally accepted, although the inability to reproduce such findings may highlight the diversity of approaches in regards electrophysiological hardware, experimental technique and tissue preparation. Weir *et al.* utilised trough width in analyses of neuron cultures derived from new-born mice, and found no significant difference between trough widths of inhibitory and excitatory cells which had been independently classified by immunohistology techniques¹⁶. Spike widths and ratios have been used to successfully cluster inhibitory cells^{168,169}, yet have also been shown to be ineffective in distinguishing cells¹⁷⁰ and omitted from analysis due to claims of unreliability¹².

End slopes are associated with a greater distribution range (Fig. 5.8B compared to Fig.5.10B) and this feature is the best discriminator for this dataset, however, currently any conclusions regarding subtypes of neurons could be interpreted as experiment-specific and relative only within that data. It is commonly reported that the proportion of inhibitory interneurons to excitatory neurons in the cortex is in the region of 1:5¹⁷¹, yet this analytical approach does not suggest 15 (n= 78) distinct neurons. However, it is notable that there is a wide variation in waveform properties and an outlier in one waveform feature analysis is not repeatedly identified as an outlier in other analyses. The large variation in the number of spikes attributed to individual neurons may bias the resolution of each averaged waveform, therefore further investigations necessitate a high number of spikes to ensure waveform properties are representative.

It was not initially clear whether rapid changes in spike frequency were directly related to the relatively low firing rates of neurons or if spike sorting had inadvertently favoured bursting behaviours while limiting the recording of regular, or low frequency, firing rates. Increased spike amplitudes would provide a greater SNR and, consequently, be included

throughout the spike sorting process indicating a false-positive result of increased spike activity.

Previous studies using similar systems have not indicated a bias towards bursting behaviours¹¹ and significant amplitude changes over time would be identifiable during manual evaluation of PCA clustering. Amplitude changes would become clustered as an oval, or an elongation of data points, and would not fit the contamination criteria. Clusters in this dataset do not suggest that waveform amplitude changes impacted the clustering of spikes that would consequently result in a decreased spike rate.

A traditional proposal of neuron coding is based on the firing rate of a neuron (“rate coding”), where the frequency of action potentials determines the information to be relayed throughout the network. Sensory neurons have been observed to increase firing rates in response to increasing stimulus intensity, indicating a corresponding change in the manner of neural coding. Additionally, neurons exhibiting high spiking frequencies are more reliable in eliciting postsynaptic spikes whereby the stimulus is interpreted as being of greater importance to network processing. An alternative mechanism to relay information has been proposed as temporal coding. The temporal resolution of action potentials (millisecond scale) allows for a large-degree of variability within a spike train which could transmit highly complex information¹⁷². For instance, the frequency of action potentials within a defined time frame could be highly similar between two neurons, however, the possible arrangement of spikes in this time could afford large variability in temporal spiking properties between the two neurons. The regularity of spiking is a highly variable feature of this dataset and bursting neurons may play a critical role in the connectivity of this network.

Bursting neurons are characterised as eliciting spontaneous periods of high frequency spiking. However, definitions of bursting are variable as high frequency activity is relative to each neuron and a dynamic threshold is required to define this. Initially, a burst detection parameter described by Bakkum et al.¹³³ was attempted, but results did not clarify an appropriate ISI threshold for this dataset (see appendix 11 for neuron #11 comparison). The method was developed for analysis of cultured neurons on an MEA - the low spike count and high proportion of large ISIs in the dataset presented here likely impacted the outcome of this analysis. Therefore, the simpler MISI method was applied to the dataset to identify neurons with a high percentage of bursting spikes and suggested that >30% of spikes are bursting in each neuron’s spike train (Fig. 5.20, A, mean 49.6%, $\pm 12\%$, S.D.). This method identified 14 neurons with a high percentage of bursting spikes (>60%), yet the population

demonstrated a narrow distribution and therefore was limited in its ability to distinguish neurons based on this feature. An alternative method was developed and termed MBISI analysis which identifies sequences of spikes over a range of ISI values. Histograms of sequences identified as each ISI value consistently identified regular patterns of ISI sequences and the mean of the ISI distributions was found to proceed this repeated ISI value. This ISI value was therefore used as a threshold for bursting analysis and indicated a much more variable dataset.

The neurons population presented in this work exhibited high variation across multiple waveform and temporal features, however, in most cases these distributions were continuous and did not indicate discrete populations which could underlie opposing or alternative functions within a network. Waveform analysis appears to be useful to identify typicality in the dataset, yet here outliers in one feature were not consistently identified as abnormal in others. In contrast, the temporal features of the population demonstrated large variation and required further processing to address these discrepancies. Using the median ISI value to segment spike trains provided a useful comparison for relatively high and low frequency spiking, and irregular spike trains evaluated using the CV, MISI and MBISI methods do suggest a heterogeneous population. Incorporating a reliable method of recording from specific cortical layers would assist in validating conclusions regarding neuronal characteristics, as this would potentially limit the neuronal subtypes recorded from.

<i>Spike waveform properties</i>	<i>Average</i>	<i>Standard Deviation</i>
Trough Width	0.63	0.08
Peak Width	1.17	0.38
Width Ratios	1.88	0.71
Spike width (ms)	0.89	0.13
Peak to trough Ratio	0.70	0.05
End Slope	-1.46	0.86
<i>Spike Temporal Properties</i>	<i>Average</i>	<i>Standard Deviation</i>
Mean ISI (s)	44	29.6
Low Frequency ISI (s)	50.48	6.3539e+04
High Frequency ISIs (ms)	4.6	3.5
CV ISI	1.97	0.72
CV high frequency	1.16	0.76
CV low frequency	1.28	0.54
MISI Bursting ISIs (%)	49.6%	12
MISI ML value (s)	9.7	8.4
MBISI Bursting ISIs (%)	48.86	24.78
MBISI MN value (s)	24.2	57.3

Table 5. 1. Summary of neuron waveform and temporal features.

6. Connectivity Analysis of Recorded Neurons

The MEA and acquisition system are designed to define the electrophysiological activities of discrete neuronal units in healthy acute slices. The device presented in this work possesses high spatial resolution of electrodes spread over an area of 0.9X1.8 mm with the potential to identify and record activity from hundreds of neurons. The spatial resolution enables high accuracy in determining neuron locations over the array, while the effective spike sorting approach can attribute small amplitude activity (putative axonal signals), detected over several electrodes, to individual units and trace signal propagation across a network. These spatial features can be combined with temporal patterns of activity to investigate neuronal connectivity in a healthy brain slice representative of physiological network activity.

Investigations of neuronal networks can provide information to changes in plasticity; the ability of networks to re-model the strength of inputs and alter the dynamics of the network. Plasticity is a key mechanism associated with learning and memory¹, and underlies neurodevelopment¹⁷³. Furthermore, neuron network connectivity is impacted in pathological states such as Alzheimer's disease and schizophrenia¹⁷⁴. Therefore, elucidating the role of local networks within larger brain structures could greatly assist in identifying early markers of diseases.

The functions of neuronal interactions throughout a network are not fully understood. Difficulties in investigating functions can be attributed to the diversity of cell types, such as between inhibitory interneurons and pyramidal cortical neurons¹⁷⁵, and the large number of connections that exist between neurons. Technical considerations include the simultaneous investigation of as many units of the network as possible to determine the role of each within the network. A key challenge in this regard are silent (sometimes referred to as "dark") neurons¹⁰. Such neurons are visualised histologically yet exhibit extremely sparse electrophysiological activity and are therefore typically unobserved in recording experiments. Estimates suggests that only 10% of cortical neurons can be reliably detected by extracellular electrophysiological methods^{9,176}, impeding the ability to study the network fully. This is proposed to be due to sparse activity patterns of many neurons and that active subsets of neurons respond only to specific stimulus triggers¹⁰. However, increased electrode spatial resolution could help to reduce the gaps in network knowledge by increasing the numbers of neurons recorded from to determine the proportion of low-activity neurons in a population

Investigations into the mechanisms of acquiring, processing and storing information within a network of neurons involve mathematical modelling beyond the scope of this work. However, the data acquired through the recording presented here can be assessed in terms of (1) effective connectivity i.e. local interactions with a neuron downstream of the network and (2) functional connectivity i.e. temporally correlated activity suggesting equivalent functions²². Effective connectivity can be evaluated using spatial information derived from neuron locations and compared to the degree of correlation in activity patterns. Functional connectivity evaluation also relies on temporal properties of spikes but could suggest a similar input into two distant cells, e.g. two interneurons providing inhibitory feedback signals to the same neuron, but not directly interacting. The temporal properties used in this analysis were based on the results of peristimulus time histograms (PSTHs). This commonly used method to infer causal activity¹⁷⁷ counts the cumulative spike rate within a defined time window following an event such as electrical stimulation. In this work, a PSTH is a measure of delay in activity between one neuron and another.

The following sections will describe correlated neuron activity patterns resulting from PSTH analysis. Although steps were taken to mitigate the impact of spike rate discrepancies on this measure, the number of significant PSTH results (where spikes were recorded within the time window) demonstrated a near linear relationship with spike rate and indicated an ineffective approach to quantify correlated activity. Neuron locations, and distances between neurons, were then included in analysis and suggested proximal neurons exhibit greater similarities in activity patterns, indicative of effective connectivity. However, directed graphs were generated which indicated that, while clusters of proximal neurons exhibited similar activities, several separated units possessed similar levels of correlation. The propagation of axonal signals was then summarised for the population, the direction of which could be estimated for 48 neurons based on the time delay between the seed electrode and small amplitude signals on surrounding electrodes. These analyses describe the potential for this system to investigate connectivity across hundreds of neurons in a network with high temporal and spatial resolution across a large area.

6.1. Peristimulus Time Histograms

In the recording presented here, each spike was treated as an event and the activity of other neurons following each event was surveyed to gauge correlated activity changes. The variable, and large, ISI values for the dataset meant that coherent PSTH combinations were

uncommon with few spikes occurring within 500 ms of a spike event. However, neurons with high spike count, such as #2 and #52 (910 and 1887 spikes, respectively), provided sufficient spikes within 500 ms time window to generate meaningful PSTH plots (Fig. 6.1). The PSTH plots presented here (examples in Fig.6.1, B&C) are produced by the following steps:

- 1) Identify each spike time for a neuron (*Stime*)
- 2) Defining a time window (*t*) following the spike time
- 3) For each neuron being compared to, identify spikes of those neurons that occur within (*t*) of (*Stime*)
- 4) Bin the time window, e.g. every 10 ms, up to (*t*)
- 5) Sum the number of spikes which occur within each bin, i.e. the number of spikes which are elicited by that neuron at 10-20 ms after (*Stime*)

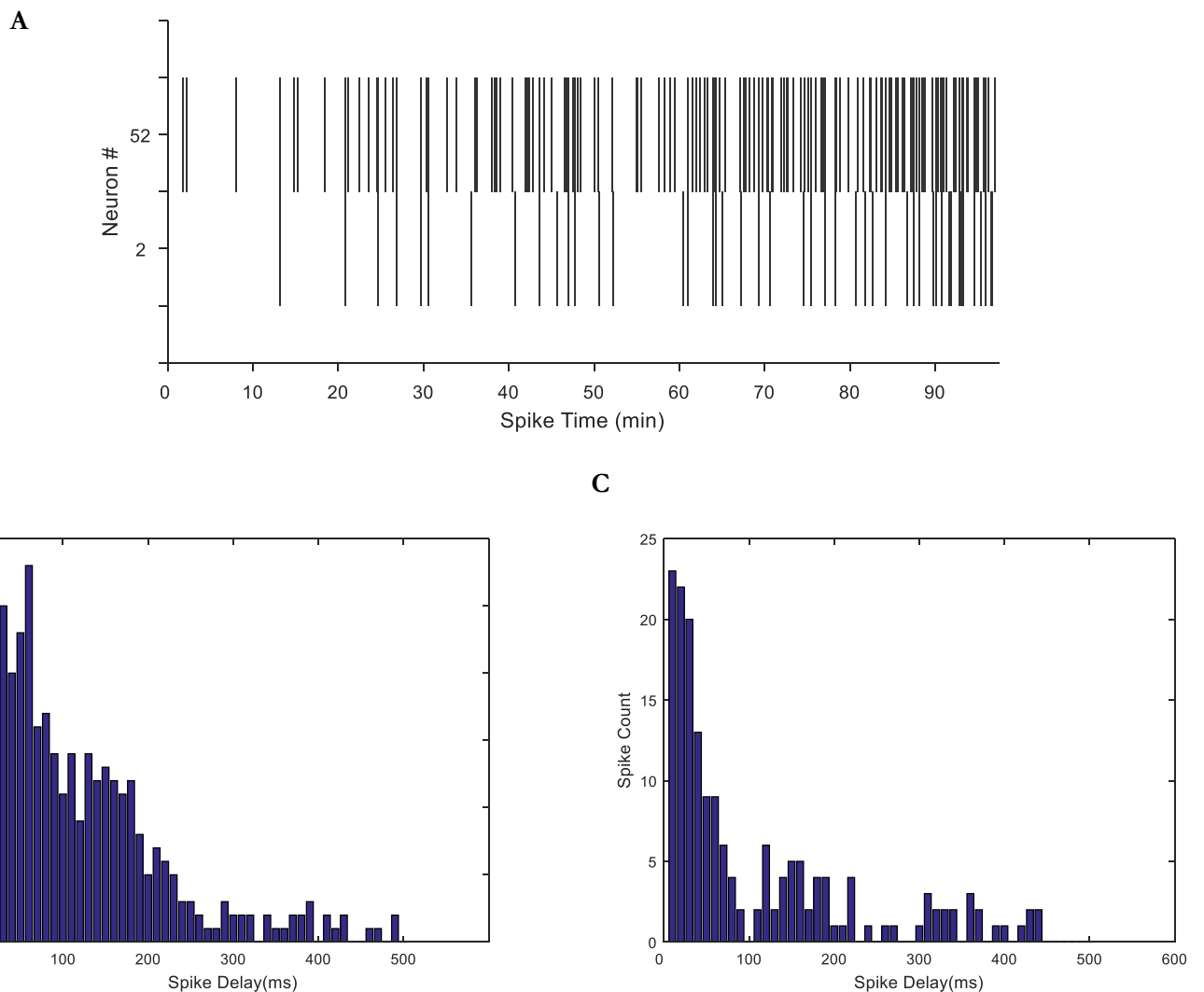


Figure 6. 1. Excerpt of a raster plot of neurons #52 & #2 with corresponding PSTH plots calculated over the 2 hours of recording. (A) The initial 90minutes of recording from neurons

2 and 52, where each spike is represented by a vertical line. (B) Histogram of the time delay between neuron #52's spike activity ($n = 1887$) and neuron #2's subsequent spikes ($n = 910$) within 500 ms. Each of #52's spikes are a trigger (centred at time 0, x-axis) and for each of #2's spikes occurring within 500 ms the time delay between events is binned into the PSTH. Neuron #2 elicits 23% of its recorded spikes within 500 ms of neuron #52' spikes. (C) Converse analysis with neuron 2 spikes used as a stimulus trigger. Although suggesting a peak of activity within 100 ms, this represents 3.8% of neuron 52's spikes.

These plots indicate a correlation in periods of activity and could suggest functional connectivity. However, a generous post-spike time window was required to accumulate enough data to generate meaningful plots due to the low spike rate. Spike counts included in PSTH plots represent a low proportion of each neuron's overall spikes; for example, neuron #52's activity within 100 ms of a neuron #2 spike (Fig. 6.1, B) accounts for 3.8% of neuron 52's spike events. Therefore, relying on PSTH plots accumulating large numbers of spikes alone is not an effective approach to identifying correlated activity in this dataset.

The low number of correlations in PSTHs are likely the result of large IS values observed throughout the dataset and drastically reduces spike timing coincidences. Correlated, functional activity should still be observable, however, the low number of neurons identified within an area of 2 x 1 mm indicates that far fewer correlated activities could be recorded. Other studies of connectivity using patch clamp techniques have had more success in identifying correlated activity between neurons over distances of $100 \mu\text{m}^{178}$, suggesting that the number of spikes assigned per neuron in this setup may significantly impact this measure. The number of spikes present in the PSTH can be misleading due to imbalances of recorded spike numbers between neurons. A neuron with high frequency activity has a higher probability of detecting another neuron's spikes within a given time window. The fraction of each neuron's spikes present in each PSTH was calculated to improve interpretation of correlation (Fig. 6.2). These 78x78 tables were used to generate a colourmap of 6006 values; excluding the neuron comparing against itself (red diagonal in Fig. 6.2). Columns represent the PSTH stimulus neurons with rows as the neuron spikes subsequent to the event. Neurons 1:32 show the greatest degree of correlation with neighbouring neurons, while neurons 18, 37, 52, 53, 58 and 74 demonstrate consistent activity correlation with other neurons. These neurons have higher number of elicited spikes (> 1000 spikes) relative to the population average (382 spikes) which would enhance the appearance of correlated activity, however, two neurons (48 & 67) also elicit >1000 spikes and demonstrate little correlated activity with

other neurons, even within a 500 ms time window (Fig. 6.2, B). A total of 2770 combinations (46%) found at least one spike within a 100 ms PSTH window (defined here as a positive combination). This analysis was repeated with a time window of 500 ms following each spike and predictably increased the fraction of spikes included within the PSTH (Fig. 6.2, B) and produced 4108 (68%) positive combinations.

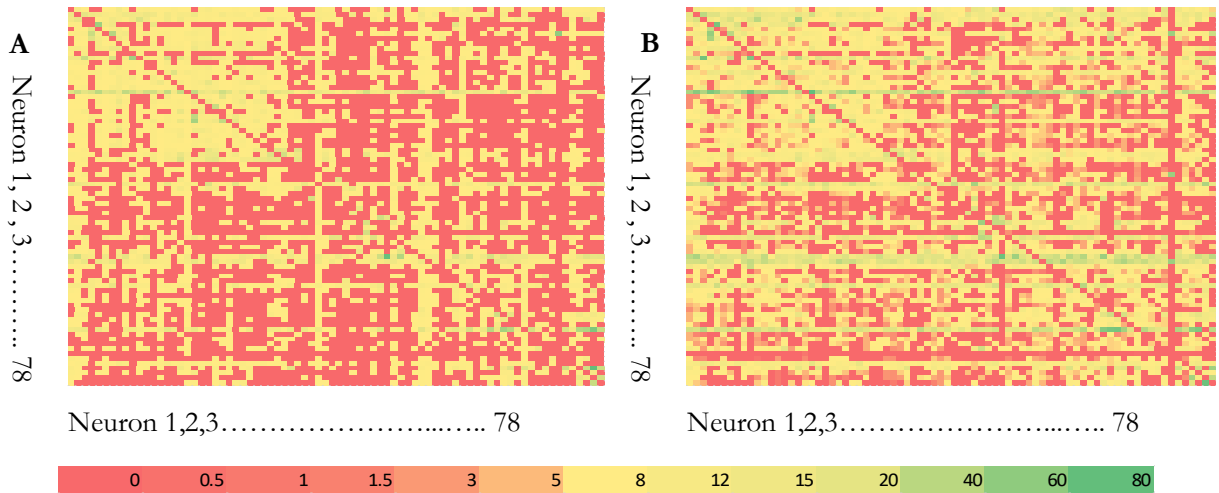


Figure 6. 2. Colourmap of the percentage spikes per neuron occurring within a given PSTH time window. Spike times function as a stimulus and each row represents the PSTH of a neuron with the column the corresponding neuron being compared to. Following a spike (row) any spike activity of another neuron (column) within the time window is recorded. The sum of each neuron’s activity in the time window is then divided by that neuron’s total spike count. The colour scheme is red (lowest value – 0) to green (highest value- 69%). A colour scale is provided showing how percentage values are binned. Red boxes indicate low percentage of a neuron’s spikes occurred within the given timeframe and neurons were not compared to themselves (red diagonal). (A) Fraction of spikes within a 100 ms PSTH time window highlights very few correlated neurons, with neurons 1:32 exhibiting the greatest consistency of similar spike activity. (B) Fraction of spikes within a 500 ms PSTH time window.

The low number of correlations is a result of the low spike count that many neurons exhibited over 2 hours of recording and are distributed across large interspike intervals. To determine the impact of spike count on the likelihood of a spike occurring within the PSTH time window, the number of spikes per neuron was compared to the number of positive PSTH combinations (Fig. 6.3). This was calculated as the number of combinations where a neuron’s spike is subsequent to a spike stimulus (i.e. the rows in figure 6.2). No change in trend was

observed when analysis was based on the number of combinations with a neuron's spike as the stimulus (columns in Fig. 6.2; appendix 13). As expected, there is a trend of increasing numbers of positive combinations with larger neuron spike counts, however, deviation from a linear dependence indicates that some neurons demonstrate limited correlated activity despite a relatively high spike count. The percentage of spikes each neuron exhibited within the time window of another neuron's spikes was averaged and included as a colour code. Although high spike count and number of positive combinations correlate, the percentage of each neuron's spikes present in the PSTH time window (colour-coded) are observed to be less dependent on these factors. For instance, at a 500 ms interval (Fig. 6.3, B), the greatest number of positive combinations consisted of, on average, 19% of that neuron's total spike count, yet another neuron exhibited fewer positive combinations but consisting of an average of 31% of its total spikes. This data does not provide information regarding individual neuron:neuron activity dependancies and the neurons presented here demonstrate low correlation in activity, however, accounting for spike count and the percentage of spikes included within PSTH time windows suggests underlying correlated activity in many neurons.

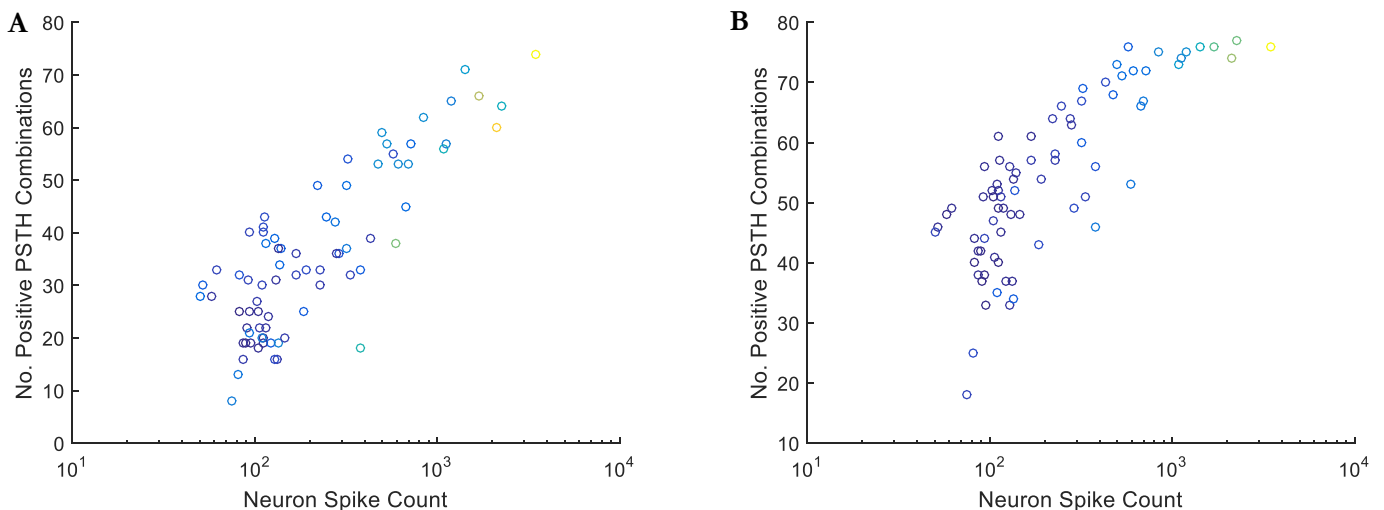


Figure 6. 3. Increasing spike count results in a trend of increasing numbers of neuron combinations with more than 1 spike within a PSTH time window. Point colours are based on the average fraction of neuron spikes occurring within each possible neuron combination time window. Colour coding scheme; dark blue (low), yellow (high). (A) At a PSTH window of 100 ms spike count correlates with increased spike; neuron 18 exhibits the highest number of positive combinations (74) with an average percent of its spikes included in combinations as 10.3%, the lowest is neuron 47 with 8 positive combinations and 0.48% of its spikes included. (B) A PSTH window of 500 ms reduces the linearity of the data as more combinations

approach the limit of 78 possible combinations. Neuron 53 exhibited the highest number of combinations at 77, with 19% of spikes. The highest fraction of spikes included was 31%(neuron 18) and the lowest was 1% (neuron 34).

6.2. EI mapping

Peristimulus time histograms provide indirect evaluation of activity dependence between neuron and can be suggestive of functional connectivity as this data does not include any indication of direct effective connectivity. The spatial resolution of the MEA presented here enables the relative distances between neurons to indicate locally clustered cells. These distances can be incorporated into connectivity analysis and proximal and temporally correlated activity could suggest local, effective, connectivity between neurons.

The locations of seed electrodes were plotted using a map of electrode positions (Fig. 6.4). During spike sorting the 6 electrodes surrounding a seed electrode are evaluated for signal amplitudes as repeated correlated activity on two neighbouring electrodes indicates a duplicate signal. Spikes can then be more accurately discriminated and allocated to an individual neuronal unit. Signals detected on neighbouring electrodes also increases the resolution of the cell location as signal amplitudes can be used to triangulate the source of the largest amplitude.

The locations of detected neurons were not evenly distributed across the MEA, suggesting that many electrodes did not come into proximity with functional neurons. This may be due to incomplete penetration of needles past damaged tissues, greater extent of cellular damage, the needles may not have been inserted or the slice detached from the needles before sufficient data could be acquired to identify neurons.

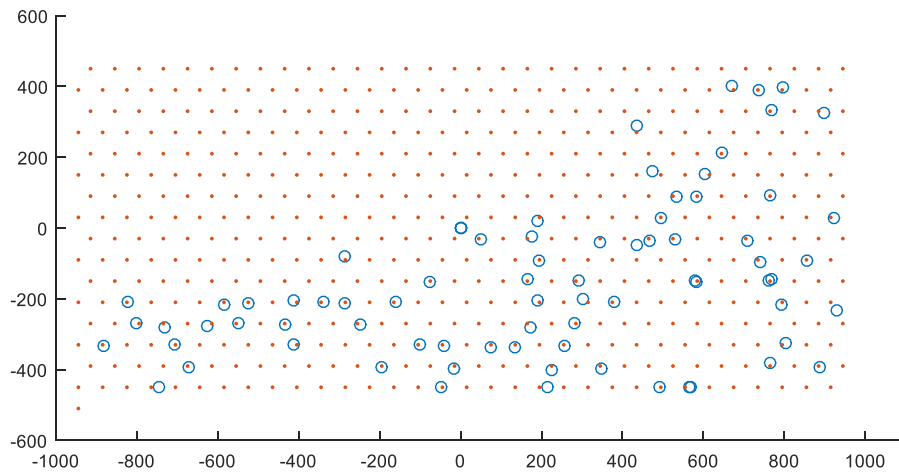


Figure 6. 4. Electrophysiological mapping of neuron locations across the MEA. When a supra-threshold spike is detected on an electrode the signal is compared to its 6 neighbours. Comparing the spike amplitudes between electrodes (orange dots) allows for triangulation of the signal and provides an approximate location of the cell (blue circles). The locations of detected neurons were not evenly distributed across the MEA.

6.2.1 Proximal Correlated Activity

Distances between neuron locations were calculated and compared to the percentage of each neuron's spikes elicited within 100 ms and 500 ms of each other neuron's spike time. Comparing the PSTH percent to cell distance provides supporting evidence of neurons comprising the same network pathway and could indicate effective connectivity; i.e. distal neurons exhibiting a high PSTH correlation are probably separated by several network nodes and correlation is either functional or coincidental. The largest distance between neurons was 1930 μm and the smallest was 4 μm .

At a time-window of 100 ms (Fig. 6.5, A), spike PSTH combinations below 10% demonstrated no relationship with cell distances. Two neuron combinations demonstrate a PSTH percentage >60% (spikes of neuron #52 subsequent to neuron #47 spikes and neuron #75 subsequent to neuron #77 spikes). The distances of these neuron combinations are 162.5 μm (52:47) and 62.3 μm (75:77). Due to the small distances and high spike correlation, these neurons are likely closely linked within the same network path. A similar trend is observed at a time window of 500 ms (Fig. 6.5, B), where higher correlated activity combinations between each neuron (PSTH%) occur with smaller distances between neurons.

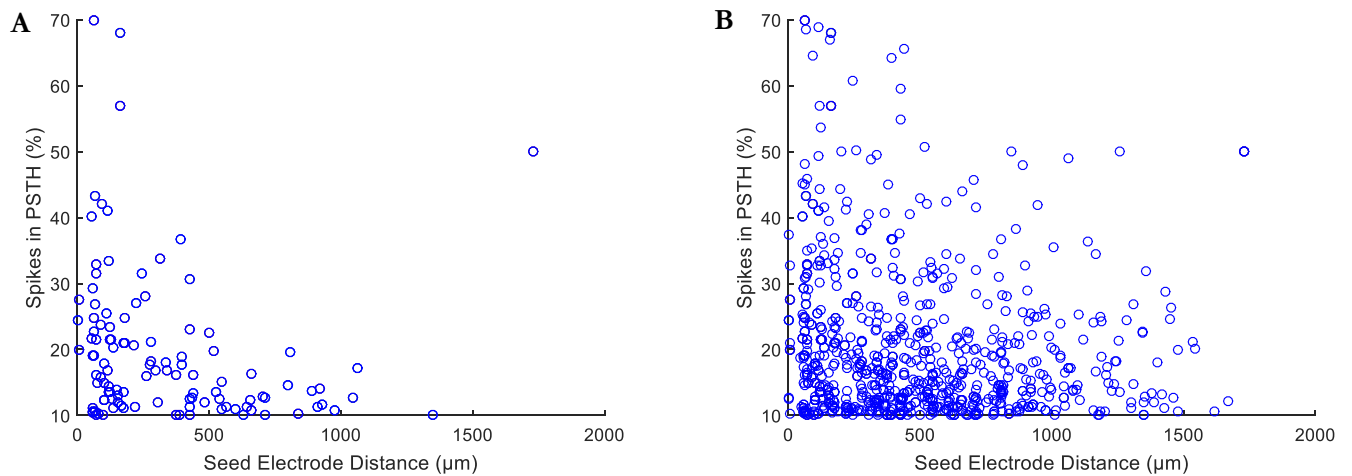


Figure 6. 5. The percentage of each neuron's spikes included within the PSTH time window of each other neuron compared to the distance between seed electrodes. Spikes percentages <10% are excluded. (A) A PSTH time window of 100 ms. (B) A PSTH time window of 500 ms. The outlier at 50% PSTH spikes in both plots is neuron #72

The percentage of each neuron's spikes within a given interval of another neuron's spikes can be visualised across the array to demonstrate that a large PSTH spike percentage is more likely to be identified at shorter distances- suggesting effective connectivity. This is achieved using the digraph (directed graph) function of Matlab, where nodes are the coordinates of each neuron and edges (connections between nodes) are positive PSTH combinations. An example of a digraph is presented in figure 6.6. A node (neuron) is represented with a red circle tagged with the neuron ID number. The radius of a node increases with a larger number of outputs; i.e. the number of neurons exhibiting activity following a spike. Edges (arrowed lines) originate from a neuron eliciting spikes within the PSTH time window of spikes from another neuron, which the arrow points at, indicating an output signal. Therefore, the arrow direction indicates activity dependency on another neuron. Line colour is based on the weighting of connection and is calculated using the percentage of each neuron's spikes present within the PSTH time window.

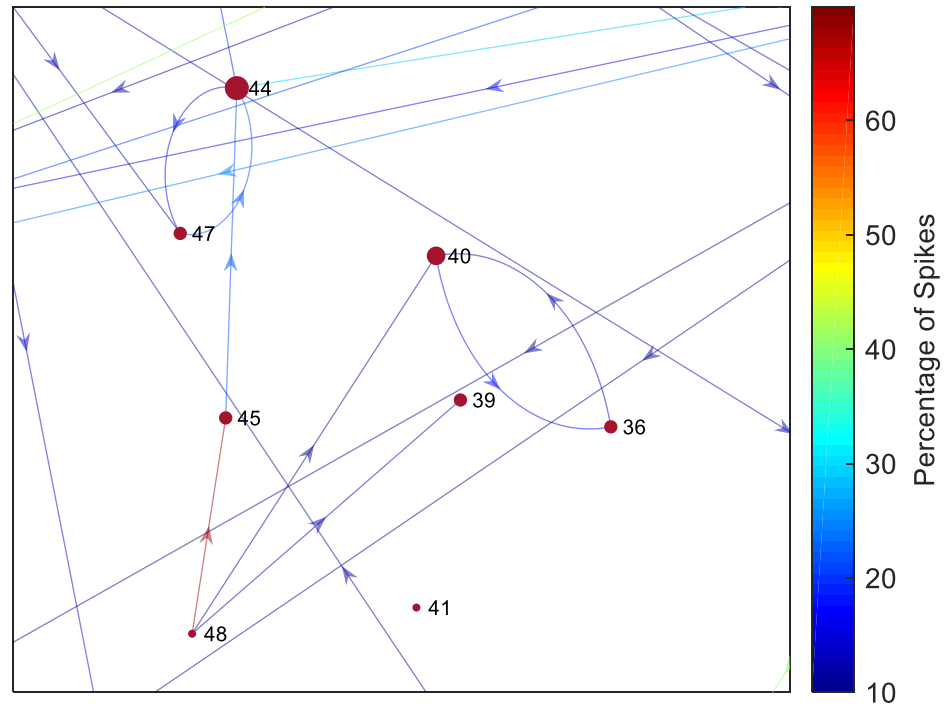


Figure 6. 6. Example of a digraph plot utilised to demonstrate activity correlations across neuron positions on the MEA device. Neuron 44 has a large node radius as it has the highest number of other nodes eliciting activity following its spikes (outputs), while neuron 41 has no identified outputs. Direction of arrows indicate neuron dependency; neuron 48 demonstrates high correlation of activity with neuron 45 as 52% of its spikes occur within 100 ms of neuron 45's spikes.

Directed graphs were generated for PSTH time-windows of 100 ms (Fig. 6.7) and 500 ms. (Fig. 6.8). As per figure 6.6, at 100 ms PSTH percentages less than 10% were excluded as these represented coincidental spiking times and were unlikely to reflect correlated behaviour. Several clusters of correlated activity can be observed, suggesting effective connectivity between member neurons. With a time-window of 500 ms (Fig. 6.8) PSTH percentages less than 30% were excluded from the graph to improve identification of edges. The greater time window increases the percentage of spikes included (corresponding to a more colourful plot) but reduces the definition of many of the clusters identified at 100 ms. These findings demonstrate how the data simultaneously recorded from hundreds of electrodes can be used to investigate effective connectivity in neuronal networks and identify clusters of correlated activity using a range of parameters.

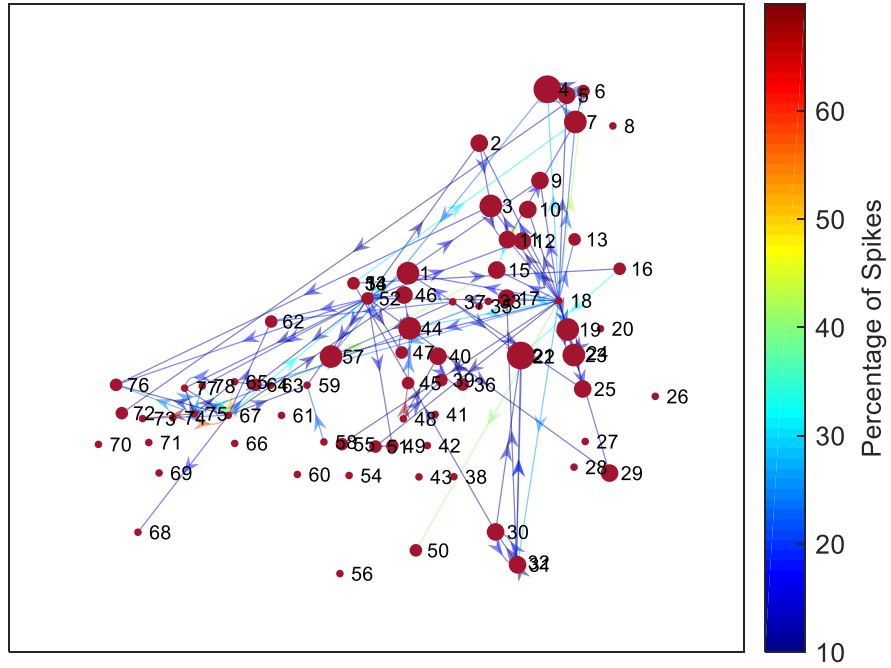


Figure 6. 7. Directed graph based on neuron locations used as nodes and edges as the percentage of spikes present within 100 ms of each other neurons' spike times.

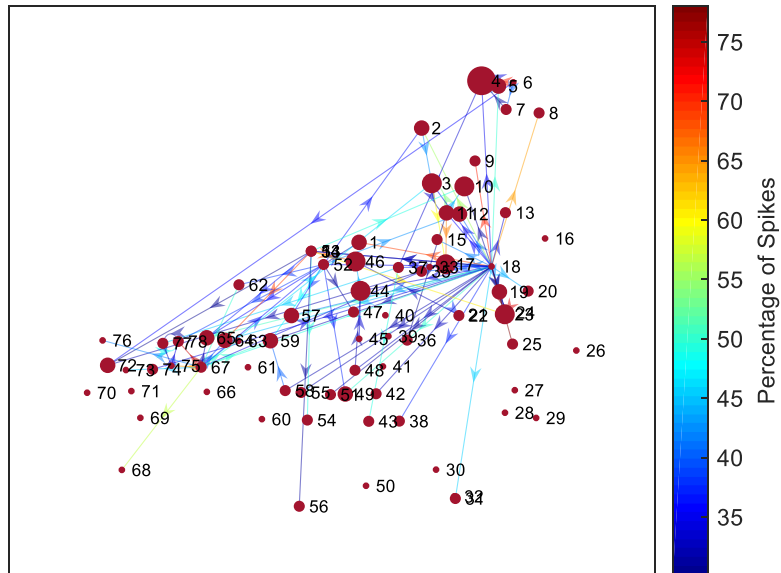


Figure 6. 8. Directed graph based on neuron locations used as nodes and edges as the percentage of spikes present within 500 ms of each other neurons' spike times.

6.2.2 Signal propagation

Simultaneous recording from 512 electrodes enables the flow of electrical charge through the extracellular space to be recreated where axonal signals are of sufficient amplitude to be detected. During spike sorting, the electrophysiological signals associated with an individual neuron are compared to the activity on the electrodes surrounding the seed electrode. Voltage fluctuations detected on surrounding electrodes immediately subsequent to a spiking event can be allocated to an individual neuron detected on a seed electrode as these low amplitude events occur within the neuron's refractory period and cannot emanate from an alternative source. Spike sorting is not based on these small amplitude signals, however, once spikes are assigned to a neuron further processing can eliminate interfering signals while averaging these potentials allows for visualisation of the waveform. The high spatial resolution of electrodes (60 μm pitch) enables axonal signals emanating from the cell body to be detected by the seed electrode's 6 neighbours by detecting amplitude changes during the milliseconds following the spike event. These signals can be used to plot the direction of signal propagation which could be used to help infer effective connectivity between cells. The original development of this array and acquisition system focussed on retinal recordings¹⁴, where neurons are more regularly arranged than in the cortex, and enabled the visualisation of signal propagation. Unlike retinal ganglion cell projections, cortical neuron outputs are myelinated, a lipid coating which increases membrane resistance and inhibits the tracking of signal propagation over large distances. Additionally, cortical projections are not predictably arranged, and the axon path may extend beyond the range of electrode detection; typically, $\sim 100 \mu\text{m}$. Although cortical neurons exhibit more complex network architectures, these features provide information regarding somatic and axonal activity elicited by multiple neurons recorded simultaneously and could be further developed to study network electrophysiology.

Spikes allocated to an individual neuron were mapped to specific electrodes and the activity on surrounding electrodes immediately following spike events were evaluated. This highlights the path of axonal projection (Fig. 6.9, A). As with averaged neuron spike waveforms generated from seed electrodes signals immediately following identified spike times can be averaged to produce a waveform of the axonal signal (Fig. 6.9, B). These waveforms exhibit triphasic signals (hyperpolarisation, depolarisation and repolarisation) and, considering the distance from the somatic signal, are putatively axonal^{150,179}.

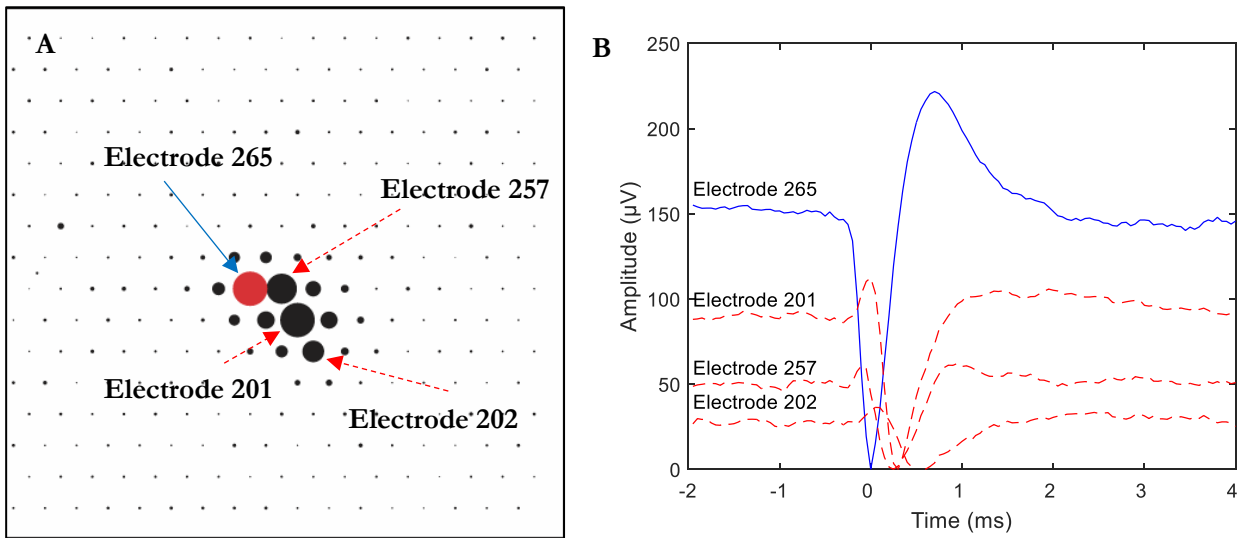


Figure 6. 9. Signal propagation across the MEA. (A) Electrophysiological image generated by Vision software showing the averaged action potential of neuron #35 propagate across electrodes. The seed electrode (red circle) detected the greatest amplitude, while surrounding electrodes record subsequent, decaying, signal attributed to the neuron through PCA spike sorting. (B) The averaged waveforms detected on seed (blue line) and surrounding electrodes (red dashed lines). The signal is detectable 134 μm away 0.5 ms after the initial spike event on the seed electrode

A total of 57 neurons exhibited (sub-spike sorting threshold) electrical activity on more than one electrode in the immediate aftermath of an elicited spike; indicating that axonal signals were detected on neighbouring electrodes (as in Fig. 6.9). An electrode was counted as detecting electrophysiological activity if an amplitude $>25 \mu\text{V}$ was recorded within 1 ms of a somatic spike. Excluding neurons where no additional electrodes were identified, the number of electrodes per neuron detecting axonal signals (Fig. 6.10, A) averaged 2.8 electrodes (± 1.9 , S.D.), while the time lag between seed electrode spike time and maximum delayed axonal signal (Fig. 6.10, B) was 0.21 ms (± 0.09 ms, S.D.). Nine neurons were noted as having additional electrodes detecting signals but no calculated signal delay (e.g. neuron 5); this was due to small amplitude signals being detected near the seed electrode at the time of the somatic spike and these neurons were located at a greater distance from seed electrodes than other neurons.

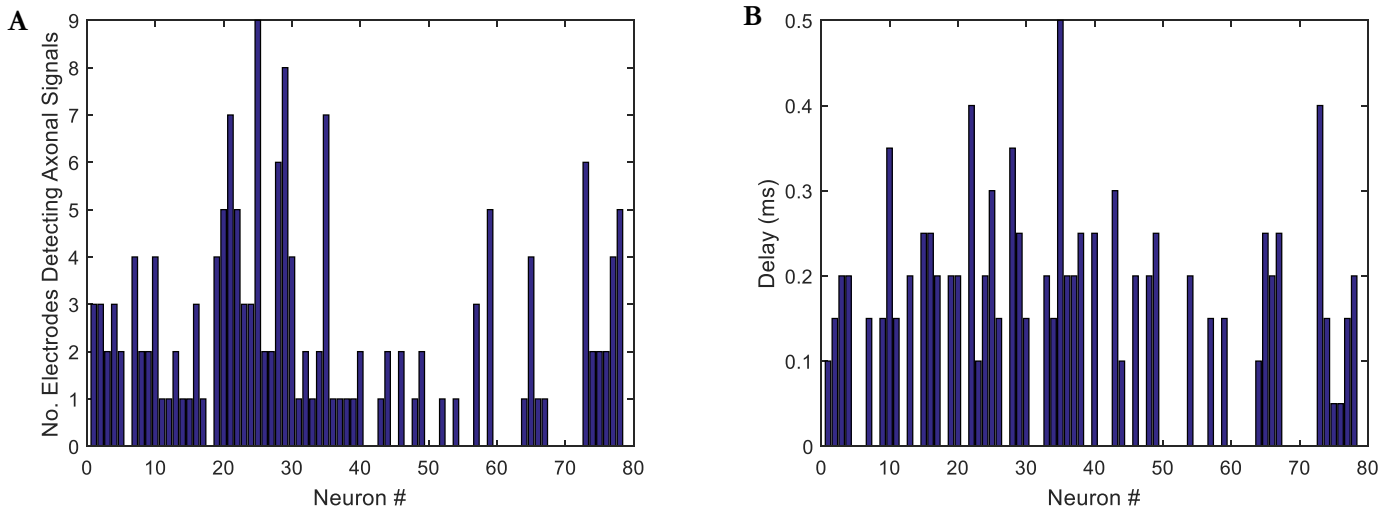


Figure 6. 10. The average amplitude of electrodes at each spike time for an individual neuron can indicate the path of signal propagation across the MEA. (A) Non-seed electrodes exhibiting an average signal amplitude $>25 \mu\text{V}$ within 1 ms of each neuron's spike time were counted per neuron. (B) The time lag between the somatic spikes detected at a seed electrode and the maximum time of signal detection at additional electrodes.

These findings demonstrate the capabilities of the MEA acquisition system to investigate the propagation of neuronal electrophysiological signals. This is achieved by the high spatial resolution of electrodes and the spike sorting approach which can detect axonal activity associated with a single neuron over several electrodes and trace the direction of signal propagation. This setup can therefore advance investigations into effective connectivity and network dynamics.

6.3 Discussion: Connectivity

This section presented several methods with which to quantify connectivity between neurons and identified limiting factors in this approach. Correlated activity can be indicated through PSTH plots which use comparisons of temporal patterns of activity to highlight repeated, functional, connectivity. However, very few neurons in this dataset demonstrated correlated activity even based over a relatively long duration of time window (e.g. 500 ms) and only a handful of PSTH plots produced coherent, meaningful results. Therefore, the spike count of each neuron was factored into analysis to calculate the fraction (%) of each neuron's spikes present within a time window of each other neuron's spikes (Fig.6.2). To an extent,

this analysis created a dependency on the spike count of each neuron, however, that many neurons deviated from this trend suggests that underlying correlated activity was present in numerous combinations (Fig. 6.3).

Temporally correlated activity is a useful measure of functional connectivity but omits the proximity of each neuron combination. The MEA presented here possesses sufficiently high spatial resolution to define the location of a neuron with an accuracy of $\sim 10 \mu\text{m}$. The locations of detected neurons were not evenly distributed across the MEA, suggesting that many electrodes did not come into proximity with functional neurons. This may be due to incomplete penetration of needles past damaged tissues or the extensive cellular damage observed. Equally, the needles may not have been inserted or the slice detached from the needles before sufficient data could be acquired to identify neurons. However, the (2-dimensional) distances between neurons could be calculated and combined with earlier PSTH analyses to evaluate temporal activity patterns in comparison with neuron proximity. This method highlighted that neuron combinations with high temporal correlations tended to more proximal. Additionally, with a PSTH time window of 100 ms, combinations with less than 10% of spikes correlated were found to have no dependency on distance and, in terms of effective connectivity, could be defined as noise. This was increased to 30% for a time window of 500 ms.

7. Histological Evaluation of Acute Slice Damage

A key design novelty of the MEA presented in this work is the 3-dimensional needles on top of which the electrodes are based (see Fig. 3.1). The intention of the design is to penetrate beyond tissue damaged by the sectioning procedure and record from healthy, intact, neuronal networks in acute brain slices. Neurons alter their electrophysiological behaviour in response to acute damage and having communication to surrounding cells severed impacts the validity of studying connectivity activity within a local network. To provide assurances that the needle electrodes can bypass this layer of damage, and the viability of sections is maintained for recording purposes, histological evaluations of acute cortical sections were performed.

Acute brain slices are often avoided in studies of neuron connectivity due to the acute damage resulting from the sectioning procedure¹⁸⁰. More commonly, cultures of neurons are grown on the surfaces of planar MEAs, which can be maintained in a healthy state for 23-28 days¹⁸¹. The relatively low density of cultured cells also assists in spike sorting and microscopy analysis^{77,182}. However, interactions between neurons are limited in their representation of physiological network functions as the architecture of the network is not directed¹⁸⁰. Advances to overcome this include the use of microfluidic devices combined with MEAs, which can pattern cell locations according to their design¹⁸³. Defining the network structure has been used to study axon guidance during network development¹⁸⁴ and degeneration of neural projections¹⁸⁵, while connectivity studies have achieved large-scale analyses of thousands of neurons¹⁸⁶. Alternative approaches have used organotypic slice cultures where a brain slice is cultured in a protective environment for several days to allow cells to regain stability following the trauma of sectioning^{187,188}. Such slices maintain the global network structure and maintain physiological interactions between neurons, however it has been reported that the boundaries of brain structures (such as the hippocampus) exhibit reduced definition⁹⁶, suggesting that the network architecture becomes altered at a local level after several days in culture. Neural probes inserted *in vivo* enable representative activity analyses of network functions^{189,116}. These devices are highly useful in studying functional connectivity but are limited in the number of recording sites that can be inserted to study connectivity of deep brain structures, such as the hippocampus, due to their invasive nature.

Sectioning of brain tissue enables access to deep structures with maintained representative network architecture. Therefore, although physiologically valid neuronal networks of the

cortex and hippocampus can be accessed, damage to tissue is inevitable. The device presented in this work consists of 512 electrodes spread over an area of 1x2mm at a spatial resolution capable of discerning multiple local networks of tens of neurons. The electrodes are based at the tips of 90 μm tall silicon needles designed to bypass tissue damaged by sectioning. It is necessary to define the extent of damage to tissues caused by the experimental setup to ensure that this design goal is achieved. A series of experiments were performed using the membrane impermeable fluorescent dye propidium iodide (PI) to assess the extent of membrane rupturing. A suitable protocol for the use of (PI) was developed for use on free-floating (FF) sections and demonstrated widespread damage to section surfaces. This dye is not neuron-specific and indicates damage to glial cells in addition to neurons. These PI stained sections were imaged at depth (z-plane) using confocal microscopy and fluorescence intensity was measured. Results suggest tissue incubation for 1hour in aCSF does not impact cell survival (t-test $p = 0.55$). However, limitations in effectively imaging through thick sections with high cell density raised concerns regarding the impact of light scattering on fluorescence measurements. This was partially confirmed by comparable experiments using TritonX, a detergent which permeabilises cell membranes, as a positive control which demonstrated a decrease in fluorescence signal at depths $>50 \mu\text{m}$. To overcome this limitation, sections were embedded in agar, re-oriented and re-sectioned to provide a cross-sectional view of PI stained tissues. These findings confirmed a high proportion of cells were PI-positive up to $\sim 100 \mu\text{m}$ into the tissue from the sectioned edge. The poor resolution in these sections, likely caused by the additional processing, prevented effective quantification of PI-stained cells, therefore, alternative verification of the extent of damage was performed using optical clearing techniques. These methods alter the refractive index of tissues to reduce light scattering and enable a greater depth of imaging. The techniques SeeDB and ClearT2 indicated a high proportion ($>80\%$) of cells exhibited PI fluorescence up to depths of $\sim 135 \mu\text{m}$ and $\sim 125 \mu\text{m}$ respectively.

The experiments outlined in this chapter demonstrate extensive acute cellular damage occurs following tissue preparation using the protocol presented in this work (section 4.1.1). This experimental setup would require inserting electrodes up to at least $100 \mu\text{m}$ beyond the edges of sectioned brain tissues for effective recordings of an intact viable neuronal circuit as a worst-case scenario. The device was designed to circumvent cellular damage to the surfaces of sections; however, previous studies have indicated that patch clamp recordings are achievable in superficial layers of brain sections^{59,190}. Patch clamping is a targeted

approach to recording, i.e. recordings would not be attempted on damaged/unviable cells, while the recording presented here is unbiased towards healthy neurons. Yet, the extensive damage observed in this preparation suggests that the sectioning procedure was detrimental to the tissue's health and that improvements, such as a more advanced vibratome¹⁹¹ or alternative cutting mediums¹⁹²⁻¹⁹⁴ (or temperature¹⁹⁵), could drastically reduce the 100 μm damaged layer observed here and enable high quality recordings of potentially hundreds of healthy neurons. This issue is further discussed in section 8.5.

7.1 Summary of Experimental Procedures

The aim of these experiments was to indicate at what depth cells are impacted by tissue preparation and to quantify cell viability at a depth appropriate for needle insertion. Several fluorescence staining approaches were performed, the methods for each are outlined in separate sections below. These methods were developed progressively to circumvent disadvantages which became evident in each setup. Initial evaluations were attempted using standard paraffin embedding techniques, however, dehydration procedures altered the tissue dimensions and made interpretations of results unreliable. Therefore, subsequent histology experiments were performed using FF sections. The use of FF sections is often avoided where possible due to poor antibody penetration, greater time required to allow diffusion of reagents and imaging difficulties due to slide mounting procedures. Furthermore, needles of the MEA are typically fabricated with a height of 90 - 120 μm to bypass damaged cells and FF sectioning is typically performed on sections <100 μm thick. Electrophysiological recordings are typically performed on 350 μm thick sections, and this section thickness was used in histological experiments.

To identify damaged cells, sections were incubated in PI, a DNA intercalating molecule which emits peak fluorescence at 617nm upon binding. As PI is membrane impermeable due to its high polarity, it stains cells with compromised membrane integrity and is indicative of cell death^{196,130}. PI is not cell-type specific, therefore emitting fluorescence in damaged glial and neuronal cells. Investigations were performed to validate the use of PI on 350 μm thick FF sections (section 7.1.1). Thick tissues exhibit high fluorescence background interference due to cell densities, therefore, the nuclease RNase was combined with PI to reduce fluorescence resulting from PI-RNA binding throughout the cell and limit the fluorescence signal to nuclei. Once a suitable protocol had been developed for PI, fluorescence intensity was quantified using a confocal microscope and ImageJ software. Image stacks were acquired at depth (z-

plane) to analyse changes in PI fluorescence as lower signal levels would suggest healthier tissue. Imaging across several trials achieved fluorescence signals at depth of 105-155 μm . The depth of imaging was likely limited due to light scattering caused by high cellular density of the cortex. Scattering could also provide a false-positive result as reduced PI signal may not necessarily be caused by fewer damaged cells.

To circumvent the problem of imaging at depth, sections were embedded in agar gel and re-orientated to enable access to a cross section of tissue slices (section 7.4). This was effective in imaging PI across the section; however, the clarity of imaged cells may have been impacted by this processing. To develop the approach, sections were applied to sample microneedles – the needle structures had been etched on a silicon substrate, but no further fabrication had been completed. Cross sections of the impacted areas could then be imaged for evaluation. A protocol was developed to differentiate PI stained cells from cells that came into direct contact with microneedles using DiI (1,1'-Dioctadecyl-3,3,3',3'-Tetramethylindocarbocyanine Perchlorate), a readily diffusing lipophilic chemical which increases fluorescence (emission $\sim 565\text{nm}$) once bound to membranes. This dye is non-selective to membranes exposed to the chemical and was applied to microneedle samples before being inserted into tissue, which was then embedded in agar and sectioned (section 7.1.4).

The density of cells in the cortex and the presence of high-scattering components like collagen and lipids creates technical challenges for imaging at depth, while tissue fixation with PFA increases scattering in mammalian tissues - imaging depth is typically limited to $<300\ \mu\text{m}$ using 2-photon microscopy^{197,198}. Alternative verification of the extent of PI-positive cells was attempted using optical clearing techniques SeeDB and ClearT2 (section 7.1.5). These protocols alter the refractive index of tissues to reduce light scattering, enabling greater depth of imaging. Optical clearing agents have a high osmolarity and higher refractive index (RI) than extracellular fluid – displacing this fluid increases the extracellular RI to match that of cellular components. Several optical clearing methods use organic solvents (BABB / 3DISCO), but these have been known to quench fluorescence¹⁹⁹, while the method CLARITY is expensive and complex to perform. The protocols used in this work were chosen due to their relative simplicity and previous studies have approved their applicability to clear thick tissue sections^{200,201,202}. The greater cellular resolution obtained through these methods allowed for quantification of the proportion of damaged cells.

Fluorescence images were acquired using an epifluorescence upright microscope (Nikon Eclipse E600) or a Leica SP5 confocal microscope. Image processing was performed using ImageJ software and analysed with Matlab.

Chemical	Supplier
Propidium iodide	ThermoFisher, P3566
PFA	Sigma, P6148
RNase	ThermoFisher, EN0531
PBS	Sigma, P4417
Triton X	Sigma, X-100
DiI	Thermo Fisher, D3911
Fructose	Sigma, F0127
Formamide	Sigma, 11814320001
PEG	Sigma, 81253
DAPI	Sigma, F6057

Table 7. 1 Chemical agents used in histological analysis.

7.2 Propidium Iodide Demonstrates Extensive Damage to Tissue Surfaces

An appropriate method of staining free-floating sections with PI was developed and demonstrated extensive damage to surfaces of tissues. Confocal images were then acquired in a z plane to gauge PI fluorescence throughout the section. Initial evaluations focussed on the impact of incubation in aCSF for 1 hour and to provide an indication of the extent of damage prior to the insertion of electrodes. This stage is commonly used in electrophysiological recordings to allow time for neurons to stabilise activity following acute trauma. Slices are sectioned in a low temperature ($\sim 1^{\circ}\text{C}$) cutting solution with high sucrose content to limit inflammatory mechanisms initiated by sectioning and reduce neuronal activity. Incubating in oxygenated aCSF at room temperature allows the return of stable neuronal activity, and the dissociation of ruptured cells from the slice. Investigations suggested the incubation period had no impact on cell survival, however, subsequent studies into the impact of needle insertions on cell survival cast doubt on the reliability of imaging at depth due to the density of PI-positive cells and the ability of the stain to effectively penetrate the medial part of the section.

To accurately reflect the tissue damage that occurs during sectioning, and over the course of other procedures prior to recording such as section incubation, studies were designed to mimic the recording procedures as closely as possible. Immediately following tissue sectioning, slices were placed in an incubation chamber resembling the setup used in recording procedures (see Fig. 4.1) containing standard aCSF (see section 4.1.2). For electrophysiological recordings, slices are incubated for 1 hour prior to being placed on the array, therefore, the impact of this stage was compared between incubated and non-incubated sections. Sections were made at a thickness of 350 μm as per the recording procedure. Staining protocol was as described above (section 7.1.2), and slices were fixed for 1 hour in PFA then incubated with 5 $\mu\text{g}/\text{ml}$ PI as earlier results indicated these parameters as appropriate.

7.2.1 Validation of Propidium Iodide Staining of Free-Floating Sections

Following cervical dislocation, rat brains were removed and dissected as described earlier (see section 4.1.1). Once glued on the vibratome stage and bathed in cutting solution, coronal brain sections were made at a thickness of 350 μm and immediately placed in 4% paraformaldehyde (PFA, *Sigma* P6148) for either 1, 2 or 3 hours at room temperature. Sections were then transferred to well plates using a plastic scoop and washed 4 x 10mins in PBS (pH 7.4). Next, sections were incubated in PI at either 2 or 5 $\mu\text{g}/\text{ml}$ for 1 hour at room temperature on a vibrating platform. Selectivity of staining was enhanced via enzymatic removal of RNA with the use of ribonuclease A (RNase) included in the PI stain solution at a concentration of 0.5 $\mu\text{g}/\text{ml}$. Following incubation, a further 4 x 10minute washes in PBS were performed before slide mounting. A non-hardening mounting medium was applied (*Vectashield*, H-1000) and a coverslip placed on top. Edges of the slide-coverslip were sealed with nail varnish to contain the medium and section. Sections were then imaged with an epifluorescence microscope.

Stage	Step	Time (minutes)
1	Incubation	60
2	Fixation – 4%PFA	60 / 120 / 180
3	Wash – PBS	10 (x 4)
4	Stain – PI (5 or 2µg/ml) + RNase	60
5	Wash – PBS	10 (x 4)
6	Slide mounting with medium	-
7	Seal slides with varnish	-

Table 7. 2. Protocol summary for propidium iodide staining of free-floating sections. Comparisons were made between the fixation time required (1, 2 or 3 hours) and the concentration of PI used (2 or 5 µg/ml) to determine an appropriate PI staining method for free-floating sections.

Surfaces of sectioned tissue displayed nucleic fluorescence following PI staining (Fig. 7.1). The dye is not cell-type specific, resulting in a high density of PI-positive cells, however background interference fluorescence was minimal. No difference was observed between the 2µg/ml and 5µg/ml groups; therefore, the lower concentration was adopted in further experiments. Tissue thickness necessitated longer fixation time in PFA to allow permeation of the agent, but prolonged immersion in PFA has been reported to cause diffusion of the PI signal and increase non-specific, background, fluorescence²⁰³. No difference was observed between sections fixed for 1 or 2 hours. Fixing for 3 hours in PFA resulted in high background fluorescence despite the cellular resolution on the superficial focal plane of sections (Appendix 14). Further experiments fixed tissues for 1 hour in 4% PFA.

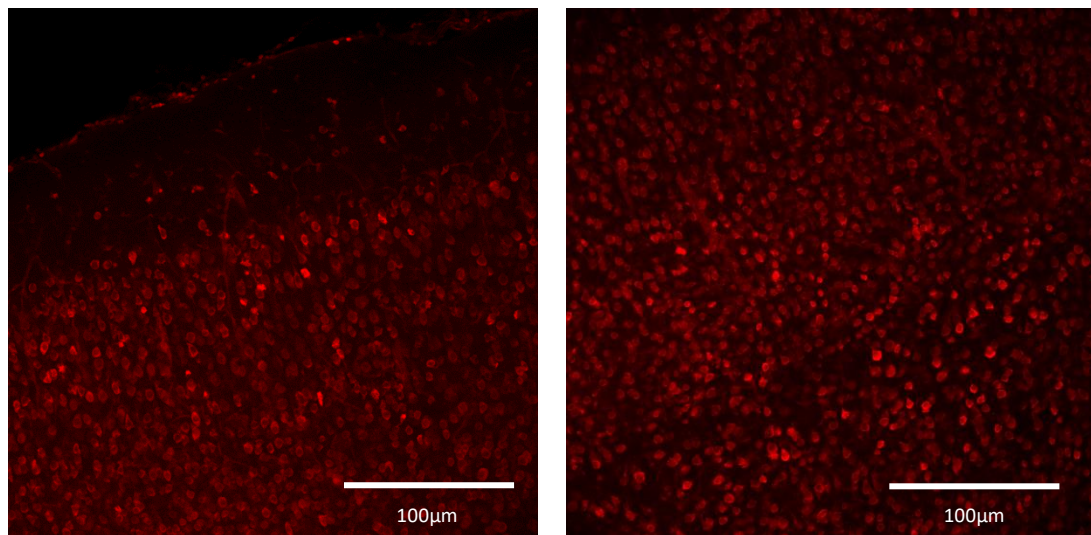


Figure 7. 1. Free-floating sections were effectively stained by PI to identify cells with compromised membrane integrity. Lateral surfaces exhibited extensive PI fluorescence and minimal background fluorescence despite high PI-positive cell density. Images taken from two separate coronal sections of cortical areas each fixed for 1 hour in PFA and stained with $2\mu\text{g/ml}$ PI. Scale bars $100\ \mu\text{m}$.

7.2.2 Incubation in aCSF Demonstrated Limited Impact on Fluorescence Signal

Following sectioning in an ice-cold sucrose-based cutting solution, acute slices are routinely incubated in aCSF for one hour at room temperature to allow neurons time to adjust to environmental change and return to stable activity. The impact of incubating tissue for 1 hour in aCSF at room temperature was estimated by the PI fluorescence signal of confocal images taken at increasing depths through the slice. Incubated slices were compared to slices immediately placed in 4% PFA following sectioning. The $350\ \mu\text{m}$ thick sections were stained as described in section 7.1.2 and z-stacks of images were acquired using a confocal microscope (Leica SP5) with an appropriate PI filter channel. Images were taken at $5\ \mu\text{m}$ steps into the section until no signal was detected and image processing was performed using ImageJ software. Fluorescence signal of PI-positive cells was calculated as “mean gray area” (averaged binary value, i.e. white to black, across pixels) via ImageJ with measurements starting when the average greyscale across the image exceeded a value of 20. The unit of mean gray area is arbitrary units (a.u.).

Peak fluorescence signal was observed superficially in slices that did not undergo incubation: incubated sections exhibited an averaged peak of $135.2\ \text{a.u.}$ ($\pm 11\ \text{S.D.}$) at a depth of $40\ \mu\text{m}$;

non-incubated section fluorescence peak of 129.1 a.u. (± 9.4 S.D.) occurred 30 μm deep (Fig. 7.2). Sections left to incubate in solution would experience dissociation of ruptured cells, which may account for the shallower fluorescence gradient over a depth of 5-40 μm . Averaged fluorescence profiles (Fig. 7.2, B) indicate incubated slices exhibit greater damage than non-incubate at a depth of 40-60 μm , however, the criteria for defining the start of analysis may result in this difference as the signal profile for incubated sections has shifted ~ 10 μm . A greater signal intensity in superficial layers would achieve inclusion criteria, therefore the shifted peak is likely caused by an increased signal in superficial layers of non-incubated slices as ruptured cells have not dissociated as would occur during incubation. Averaged conditional results found no significant differences between fluorescence signals ($p = 0.55$, 2-tailed student's t-test).

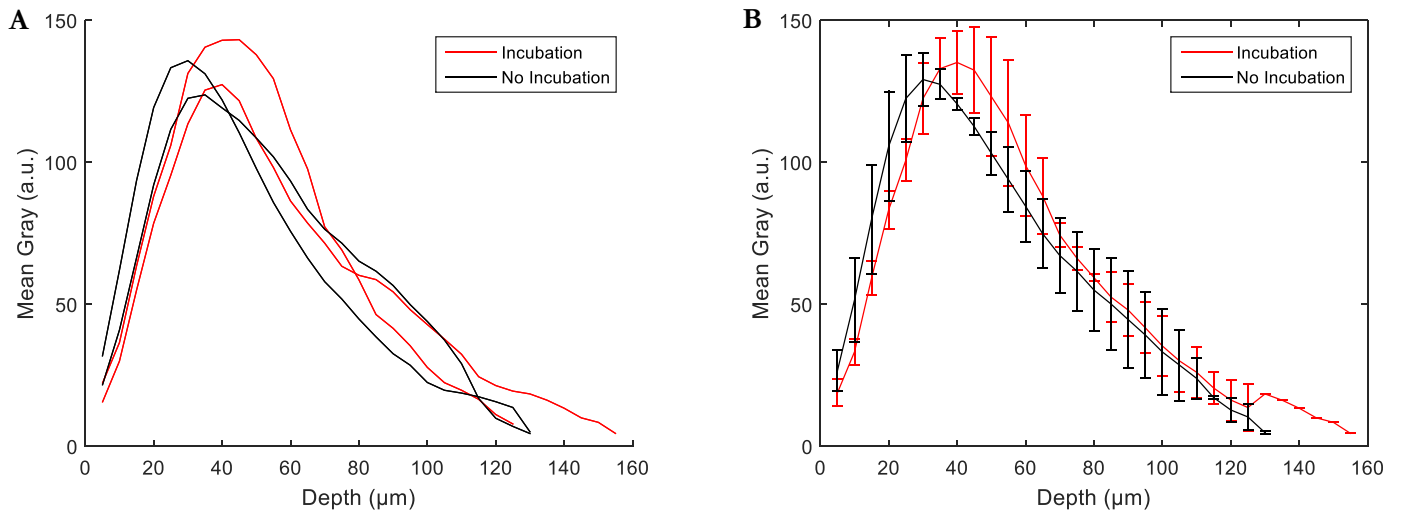


Figure 7. 2. Impact of aCSF incubation on PI fluorescence in free-floating tissue sections. (A) Non-incubated sections exhibited an elevated signal intensity in superficial layers and peak signal occurred at a shallower depth than incubated sections (30 μm compared to 40 μm). (B) Averaged fluorescence signal profiles (error bars standard deviation). Incubated sections demonstrate an increased PI fluorescence at a depth of 40-60 μm , however, no overall significant difference was identified ($p = 0.55$, student's t-test).

7.2.3 Baseline Propidium Iodide Fluorescence Signal Determined by TritonX Incubation

Imaging at depth through tissue is limited due to light scattering through cellular components with varying refractive indices. Therefore, further experiments were performed to include a positive control to quantify PI fluorescence at depth. Triton X (Sigma Aldrich, X-100) is a detergent commonly used in histology protocols to permeabilise membranes, permitting high molecular weight antibody constructs entry into cells at concentrations $>0.15\text{mM}^{204}$. Triton X is non-selective to cells, allowing PI to permeate every cell of the tissue section. After PFA fixation and washing stages, 3 sections were immersed in a solution of 1% Triton X in PBS for 30minutes at room temperature on a vibrating platform and washed 4x 10minutes in PBS before PI staining (table 7.2).

The PI fluorescence profile of TritonX-treated sections analysed at depth was found to closely resemble that of aCSF-incubated sections (Fig. 7.3). Both conditions exhibited an equivalent increase in signal, with TritonX-treated sections exhibiting a peak fluorescence of 124 a.u. (± 10.6 S.D.) at 35 μm depth and incubated slices peaking at 135 a.u. (± 11 S.D.) at 40 μm . At greater depths (>60 μm), TritonX sections exhibited greater fluorescence intensities, indicating more cells have been permeabilised by the detergent. This suggests that damage at section surfaces are equivalent, but that less cellular damage occurs in towards the centre of the section in aCSF incubated sections. However, this disparity could be the result of different cell densities in imaged regions and the impact of TritonX on the molecular interactions of PI is unknown.

Stage	Step	Time (minutes)
1	Incubation in aCSF	60
2	Fixation – 4% PFA	60
3	Wash – PBS	10 (x 4)
4	(optional) Permeabilization – Triton X	30
5	(optional) Wash – PBS	10 (x 4)
6	Stain – PI + RNase	60
7	Wash – PBS	10 (x 4)

Table 7. 3. Summary propidium iodide staining protocol including aCSF incubation and Triton X incubation stages.

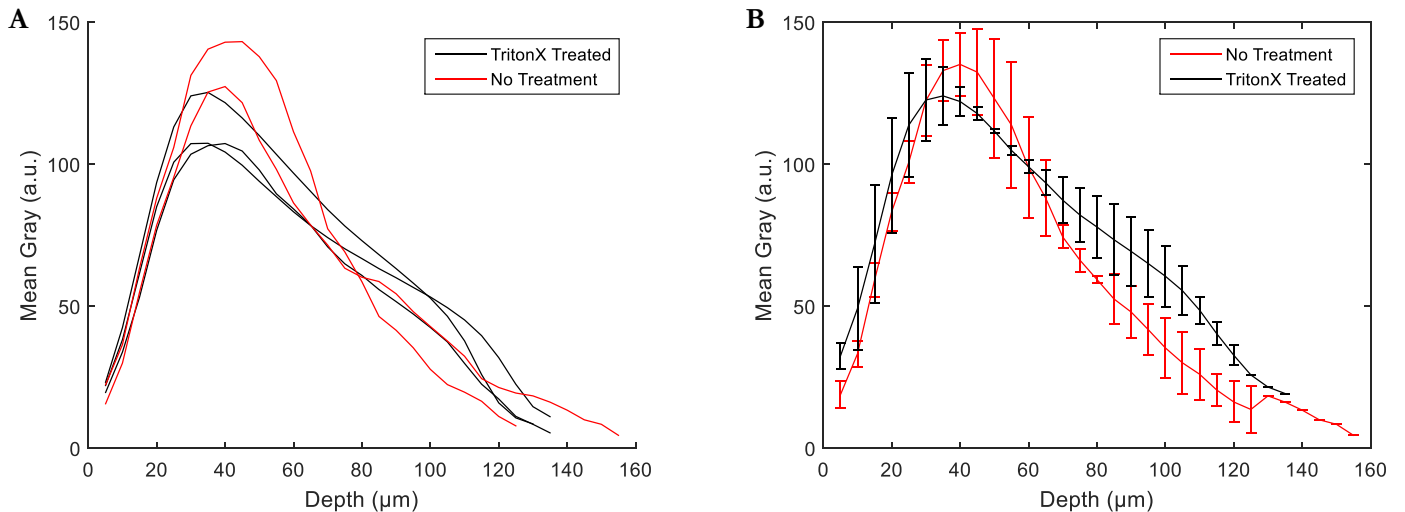


Figure 7. 3. Comparison of TritonX-treated and aCSF-incubated slices. (A) Fluorescence profiles of sections imaged at depth ($5\ \mu\text{m}$ z-plane increments) treated with Triton X (red lines, $n = 3$) or incubated in aCSF only (black lines, $n = 2$). (B) Averaged fluorescence profiles for each condition remain equivalent up to depths of $\sim 60\ \mu\text{m}$. TritonX-treated slices demonstrate greater PI fluorescence intensities at depths $>60\ \mu\text{m}$.

7.3 Assessing the Impact of Microneedle Insertion.

To assess the impact of inserting microneedles into tissue, this process was simulated using sample silicon wafers with representative needles etched on the surface (Image 7.1). Following the incubation period in aCSF, tissues were placed onto representative MEA sample needles $\sim 90\ \mu\text{m}$ high (5x5 tapered tip and $30\ \mu\text{m}$ diameter base) and a resistance seal (see diagram 4.1) applied on top to ensure tissues contact with microneedles as per the recording procedure. Initially, sections were immersed in PFA while remaining in contact with the needles and stained with propidium iodide. However, this caused a large volume of tissue to be ruptured upon slice removal (Image 7.1, B), therefore, tissues ($n = 3$) were briefly applied to needles before being detached.

Mean gray values of images for needle-applied, triton-X treated and aCSF incubated conditions were compared across the z-plane to evaluate PI fluorescence at depth (Fig. 7.4, B). Peak fluorescence values for all conditions were found at a depth of $30\text{-}40\ \mu\text{m}$. The gradient of needle-applied and TritonX-treated sections at $5\text{-}30\ \mu\text{m}$ were closely aligned and exhibited fluorescence values $\sim 14\text{a.u.}$ higher than incubated sections. The increased disparity between these groups at more medial regions could be the result of different cell densities

in imaged regions and the impact of TritonX on the molecular interactions of PI is unknown. No difference was observed between averaged group values ($p = 0.28$, 2-tailed student's t-test).

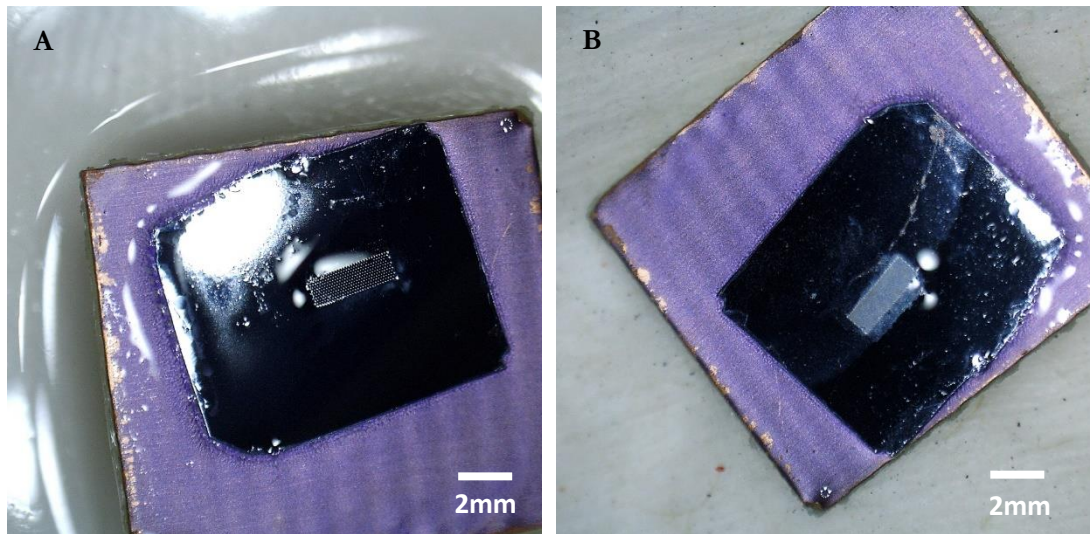


Image 7. 1. Surplus silicon-based needles produced during trials of etching fabrication techniques were used to mimic the placement of sections on needles. (A) The silicon wafer was glued to a plastic support before sections were applied. Sections were removed from the silicon wafer before fixation as fixing in PFA, whilst on top of the needles, caused a large amount of tissue to remain (B). Scale bar 2mm.

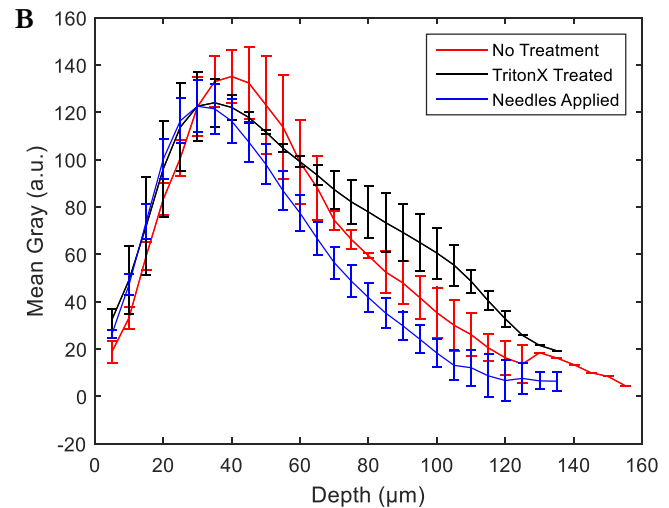
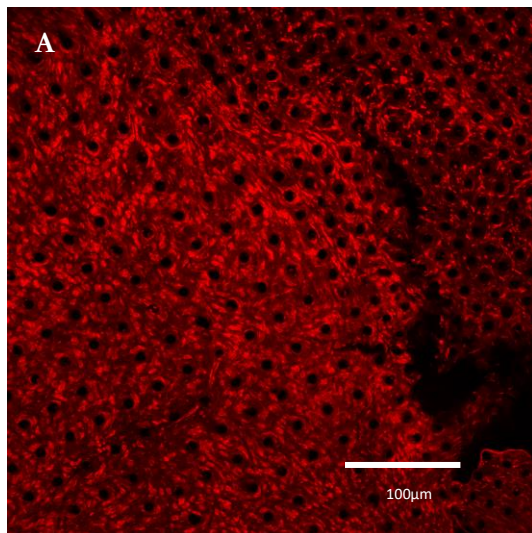


Figure 7. 4. Visualisation of silicon needle punctures in tissue sections. (A) Puncture marks of needles are visible on the surfaces of sections stained with PI (red). (B) Greyscale fluorescence

values of successive images taken in a z-plane (n=6). Sections incubated in TritonX detergent displayed a greater signal at depths >60 μm . Units A.U. = arbitrary units.

Image stacks were acquired along the z-plane and allowed a 3-dimensional image to be generated to visualise needle puncture marks in sections (Appendix 15). A layer of high PI fluorescence signal is observed superficially, which extends 50-60 μm into the tissue. The sample needles used in these experiments had dimensions representative of those used in the final MEA device, but with a reduced height of between 60-90 μm depending on sample used. These findings suggest needles with a height >70 μm would extend beyond the area of high PI fluorescence corresponding to damaged cell membranes. However, imaging depth is constrained by the scattering and a reduction in measured signal may not correspond to a decrease in fluorescence. Therefore, an alternative method was used to verify these findings.

7.4 Cross-section Imaging of Agar-embedded Tissues

Imaging of the surfaces of coronal sections provided verification of the setup and of staining procedures, yet the depth of needle penetration, and damage to surrounding cells, could not be easily resolved. Triton-X incubated sections exhibited greater PI fluorescence in medial portions of sections than tissue treated in a manner representative of the recording procedure. However, confirming the condition of tissue at depths corresponding to the height of electrode needles (~90 μm) was prevented due to light scattering in high cell density tissue.

A method was developed to obtain cross-sectional images of slices by embedding tissue in low boiling point 1% agar gel (Sigma, A0169) following the staining procedure. Agar was initially poured into a petri dish and allowed to set before a slice was placed in liquid agar and left to set for 24 hours at 4°C. A cube of agar including the sectioned tissue was removed, rotated 90°, and sectioned again (see Diagram 7.1). Re-sectioning could be reliably performed by the vibratome at a thickness of 50 μm . However, tissue rupture occurred at an increasing rate at lower thicknesses. Tissue ruptures were particularly consistent during separation of tissue from the surrounding agar. Secondary sections were placed in a large petri dish of PBS before being separated from agar and placed on slides using histology mounting medium, fluoroshield, containing DAPI (Sigma, F6057).

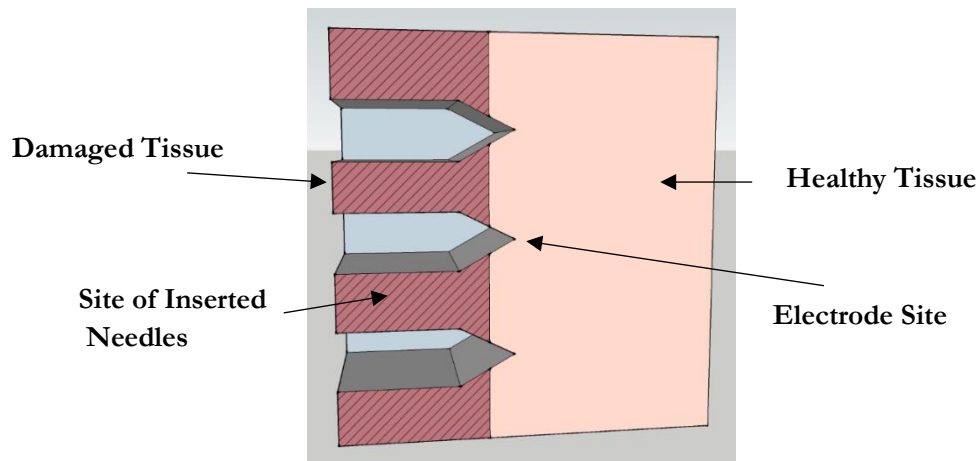


Diagram 7. 1. Secondary sectioning of agar-embedded sections. Following propidium iodide staining, sections were embedded in low boiling point agar gel, rotated 90degrees and sectioned in the new orientation. The new orientation allowed visualisation of a cross-section of the areas where needles had been inserted on the surface of the coronal section. The red, hatched, area indicates the proposed extent of tissue damage resulting from the initial sectioning and the grey gaps suggest the aimed penetration depth of the needles – electrodes are located at the tips of the needles and should extend into healthier tissue (pink). Diagram drawn using SketchUp software.

Sections had been embedded in agar and rotated perpendicular to the original plane of sectioning to provide a cross-section $\sim 50 \mu\text{m}$ thick (z-plane) and spanning the $350 \mu\text{m}$ (x-y plane) section. Acquired confocal images confirmed a layer of cell-specific PI fluorescence signal extending $\sim 150 \mu\text{m}$ (x-plane) into the medial part of the tissue from the initially sectioned edge (Fig. 7.5). This layer was not uniform to both surface edges (Fig. 7.6), indicating that the sectioning procedure used in the recording with MEA can impact the quality of recordings, yet the unequal depth of PI fluorescence was not consistently observed- either a single sectioned side of tissue exhibited a $\sim 150 \mu\text{m}$ layer of PI fluorescence or both section planes did. Analyses therefore focussed on the maximally damage edge of sectioning to provide a worst-case scenario. It was believed that the top of the slice (edge sectioned first) incurred damage repeatedly, but this was not confirmed. This discrepancy was likely due to the vibratome blade vibrational magnitude, which has been shown to impact slice quality at vibrations $> 0.5 \mu\text{m}^{205}$, or the blade angle which could not be changed on the vibratome.

Indentations of needle penetration were visualised in embedded tissues, but accurate quantification of neuronal damage was limited by non-specific fluorescence and poor cellular definition, which may have been caused by signal diffusion during the secondary sectioning. Agar-embedded tissues are cooled overnight at 4°C and immersed in PBS on the vibratome stage during re-sectioning which may have caused diffusion of the PI signal.

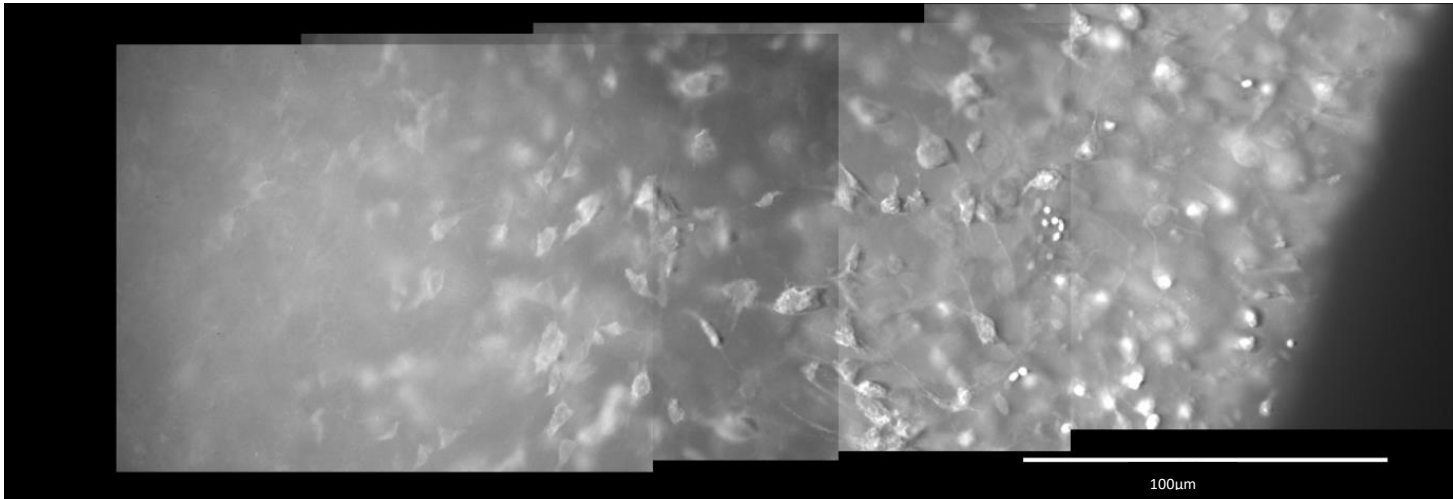


Figure 7. 5. Stitched images of PI-positive cells taken in a cross-sectional view (greyscale). Coronal sections were stained, rotated 90° (dorsal to lateral), embedded in agar and re-sectioned to provide 50 µm thick cross-sections. Edges of tissues where original sectioning occurred to provide coronal sections exhibit more distinct cellular PI fluorescence suggesting greater cellular damage. The area of specific PI-positive cells extends to ~150 µm (total section thickness 350 µm). Background interference increases in the centre of the section, indicating cells are less permeable to PI, however, section thickness could inhibit staining efficacy.

Tissues that had been placed on surplus silicon sample needles (image 7.1) were also embedded and cross-sectioned. A high intensity PI fluorescence signal was detected in areas proximal to needle puncture marks and decreased ~150 µm from the surface (Fig. 7.6). Cross-sectioning highlighted an unequal intensity of fluorescence signal on each surface (i.e. left and right of cross sectioned tissue). This did not correspond to the site of needle penetration and was likely caused by the sectioning procedure. The unreliable non-uniformity of PI signal distribution was puzzling and may relate to how delicately the slices were handled or possibly the horizontal alignment and vertical vibration of the blade caused variable movements if the analogue settings of the vibratome were imprecise²⁰⁶.

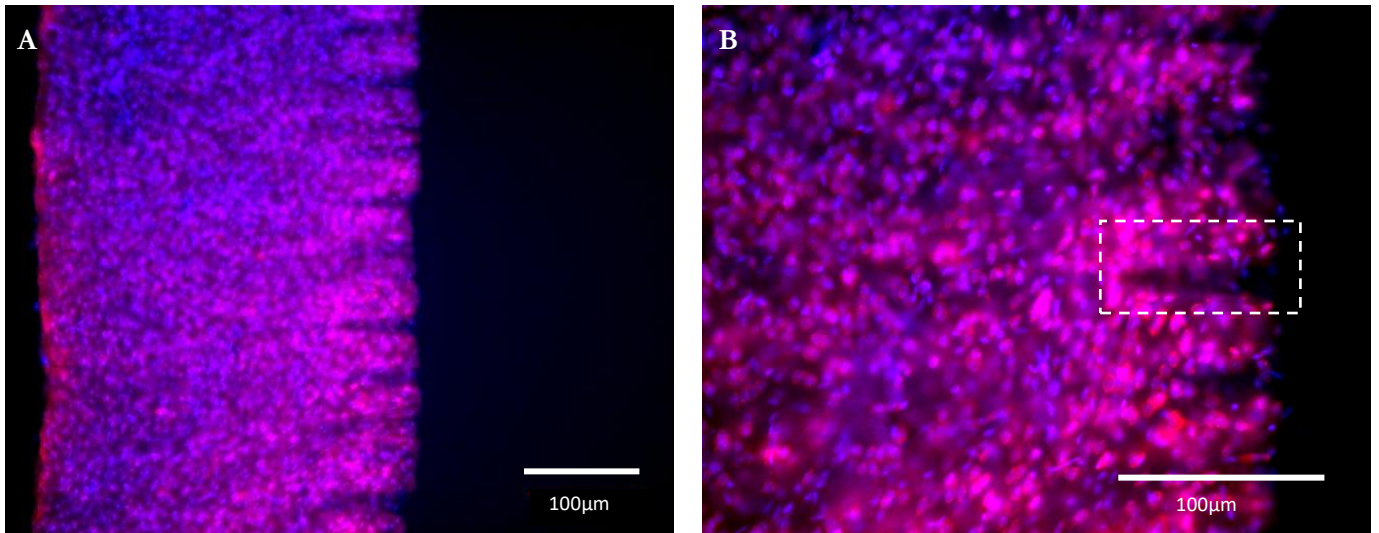


Figure 7. 6. Cross-sectioned tissues imaged following sample needle penetration. (A) A layer of high-intensity PI fluorescence extends $\sim 100 \mu\text{m}$ from the section surface medially and the signal intensity decreases at depths $>100 \mu\text{m}$. (B) Profiles of inserted needles can be visualised in cross sectional images (dotted box) and circumvents light scattering issues associated with imaging through tissue. Red: PI, blue: DAPI nucleic stain.

7.5 Neuron Tracing with Dil Lipophilic Dye

Visualising the inserted electrode and the surrounding tissue could assist to distinguish the impact of inserting high-density needle electrode from the sectioning procedure, therefore, a non-selective cell tracer dye, Dil, was used to highlight cells which had contacted needles. This dye was selected due to its reported speed and ease of application²⁰⁷. Dil has been previously used to outline the insertion paths of neural probes^{208,209}, however not to distinguish membrane contact at a scale of single-cells and not reportedly applied to studies using inserted devices of this size (i.e. $90 \mu\text{m}$ needle electrodes). More commonly, Dil is applied to cultures²¹⁰ for single cell resolution. In the context of acute slices it has been used to trace the insertion of gene transfer beads during viral vector gene transfer²¹¹ and has been combined with optical clearing to visualise vasculature²¹².

Staining with Dil was performed on fixed sections which were then embedded in agar. Crystals of Dil were dissolved in ethanol at 2mg/ml , applied to microneedles and left to dry in the absence of light. Sections fixed in PFA were then placed on top of the microneedles and pressure was applied with a resistance seal (see diagram 4.1) for one hour at room

temperature. A minimal volume of PBS was continually pipetted onto the tissue to prevent tissue desiccation. Sections were then carefully removed from the sample needles, inverted, and imaged with a confocal microscope.

Microneedles were coated in Dil stain prior to tissue placement and left to dry (see section 7.1.4). Microneedle puncture marks could not be clearly identified, and intense fluorescence signal aggregated in sporadic areas (Fig. 7.7). This was likely the result of tissue rupture during removal of tissue or incomplete dissolution of Dil crystals in ethanol solvent. Despite a failure to image the puncture area, Dil provides clear visualisation of neurons and their processes and is even capable of resolving dendritic spines (Fig. 7.8). The application of Dil on microneedles was also attempted via secondary sectioning in agar, but no conclusive results were achieved.

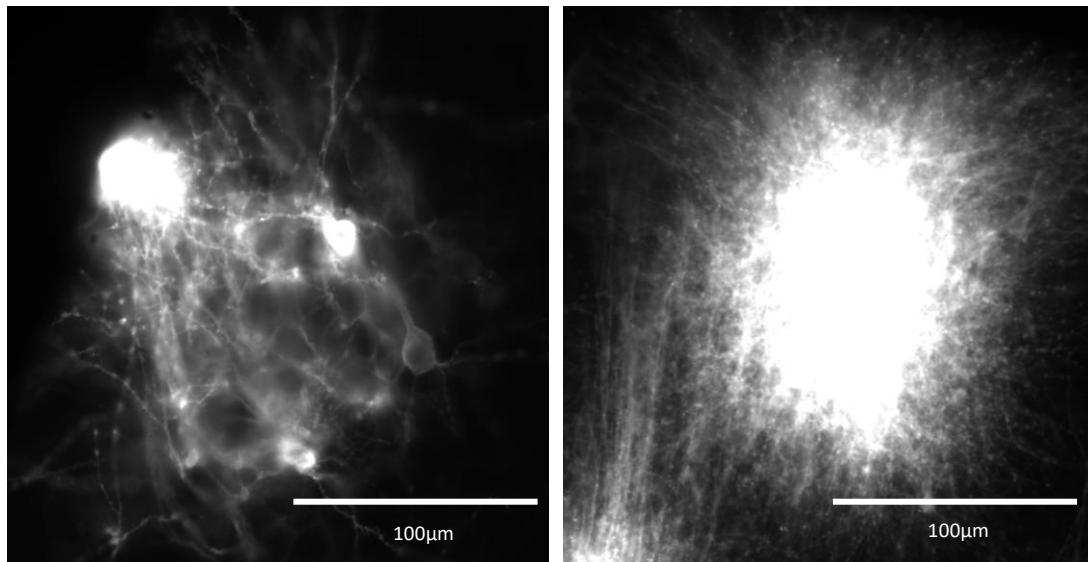


Figure 7. 7. Staining of brain sections with cell tracer dye Dil resulted in areas of aggregated dye and did not indicate locations of microneedle insertion.

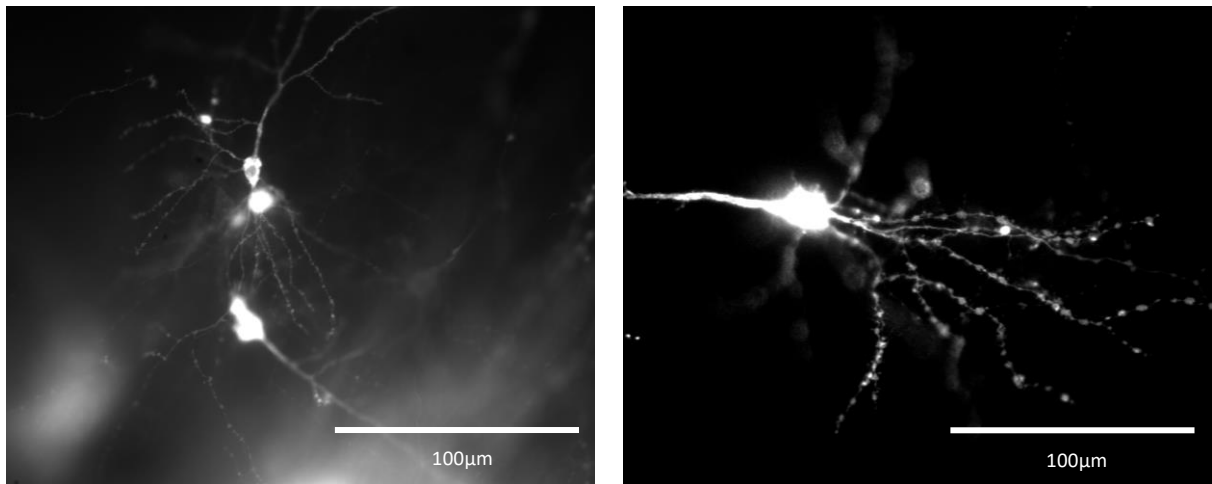


Figure 7.8. Dil staining of brain tissue provided high resolution of individual neurons and their processes.

7.6 Optical clearing

Cross sections of agar-embedded tissues enabled imaging of distortions caused by dummy MEA needle insertion, but the processing involved may have impacted the quality of staining and had a low success rate in identifying areas needles had been applied to. An alternative means of verification was explored via optical clearing of brain tissues. The comparative ease and costing of the SeeDB method¹⁹⁷ made this protocol an ideal candidate, and an additional technique, ClearT2 optical clearing²⁰¹, was also performed.

SeeDB utilises high concentrations of dissolved fructose and tissues are immersed in progressively higher concentration solutions over several hours (table 7.3). Previous literature focussed on increasing the transparency of whole organs, compared to sections used in this study, therefore the minimal suggested times of immersion in solutions were used. The SeeDB protocol was performed after PI staining and washing steps.

Imaging of sections whilst immersed in SeeDB solution requires optimised objective lenses for immersion microscopy, which was not available. Initial attempts were made to remove excess clearing solution to enhance cell definition. Improvements were achieved by gluing sections to a coverslip and placing sections in PBS which could then be imaged using a water immersion lens. However, the solution displaced the fructose-based SeeDB solution and imaging had to be rapidly performed. Due to working steps, slices in well plates were maintained at 4°C in darkness overnight if required.

Solution	Time (hours)
20% w/v	4 to 12
40% w/v	4 to 12
60% w/v	4 to 8
80% w/v	8 to 12
100% w/v	8 to 12
115% w/v	10 to 14

Table 7. 4. SeeDB optical clearing protocol for use on acute brain sections. Solutions in w/v – weight per volume.

While easy to perform and relatively cheap, the SeeDB method requires several hours. ClearT2 involves the immersion of tissues in poly-ethylene glycol (PEG), a hydrophilic polymer, and formamide (table 7.4). The ClearT2 protocol was performed after PI staining and washing steps. Imaging of ClearT2 sections was performed in the same manner as SeeDB-cleared sections.

Solution	Time (minutes)
25% formamide / 10% PEG	10
50% formamide / 20% PEG	5
50% formamide / 20% PEG	30 to 60

Table 7. 5. ClearT2 optical clearing protocol for use on acute brain sections.

Optical clearing techniques were employed to verify earlier results and with the aim of visualising sample MEA needles while still in contact with tissue sections. Increased transparency at depth enhanced cellular resolution and enabled analysis via imageJ software to distinguish DAPI and PI stained cells. The proportion of damaged cells surrounding the MEA needles could then be quantified and compared to the medial portions of tissue.

The two methods employed, SeeDB and ClearT2, were successfully performed to increase the transparency of tissue sections and the proportion of damaged cells could then be quantified and compared throughout the tissue. However, the use of a water immersion lens prevented the aim of visualising microneedles within tissue which was not achieved. The verification of these techniques suggested earlier assertions arising from secondary cross-sectioning studies were valid. Propidium iodide and DAPI staining can be successfully

combined with both SeeDB and ClearT2 optical clearing techniques and provided higher cellular resolution compared to secondary sectioning method. These studies suggest ClearT2 provides more reliable PI signal profiles than SeeDB due to reduced variation between stained sections imaged at depth. Additionally, ClearT2 tissues analysed for the percentage of PI-stained cells at depth exhibited a more coherent result and indicates that the combination of dyes with this method can be more readily interpreted.

7.6.1 SeeDB Optical Clearing

The SeeDB protocol was performed as described above (table 7.3) and was effectively combined with a double-staining of DAPI and PI (Fig. 7.9). Enhanced cellular resolution was observed compared to cross-sectioned images, enabling quantification of both DAPI and PI positive cells at depth (Fig. 7.11). Images of DAPI and PI positive cells were acquired up to a depth of 190 μm with the surface of the section defined as the first image with a DAPI mean gray value exceeding 20 (a.u.). Mean gray values at depth demonstrated a lower peak PI fluorescence intensity compared to non-cleared sections (Fig 7.9A; see Fig. 7.1 for comparison), likely a result of reduced background fluorescence. Additionally, peak fluorescence intensities were observed at greater depths than previous results indicated (50-65 μm compared to 25-45 μm). Optical clearing techniques can cause expansion of the tissue volume altering the dimensions of the layer of high-PI fluorescence, however, SeeDB has been shown to result in tissue shrinkage by up to $\sim 25\%$ ²⁰⁰ and, although the entirety of sections could not be imaged, the profile of PI fluorescence at depth is consistent with earlier results.

Cell counts of each image were measured for both DAPI and PI positive cells and compared (Fig. 7.11B) and DAPI images consistently displayed a higher cell count than depth-equivalent PI images. The peaks of PI cell counts occurred at greater depths (65-80 μm) than the mean gray peaks, suggesting more cells were identified with a lower fluorescence intensity at this depth. This could be a result of increased cell density limiting the fluorescence signal due to light scattering, or that a lower concentration of PI has permeated the tissue to this depth. These results were averaged and presented in figure 7.11C, highlighting an increase in cell count at 135 μm which may be related to a change in anatomical structure location in the section. The proportion of averaged PI cells was then calculated (Fig.7.11, D) and indicated higher cell viability at depths $>135 \mu\text{m}$, however, the reduced cell count and fluorescence intensity at this depth makes this assertion difficult to confirm.

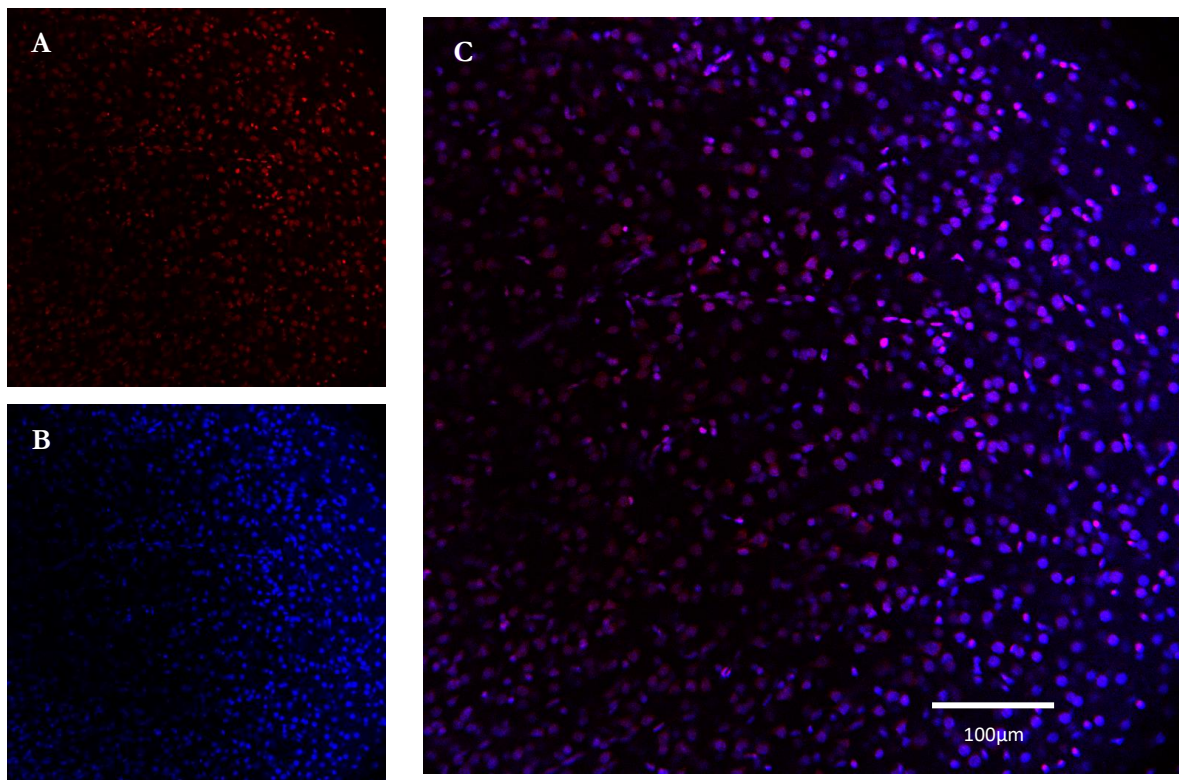


Figure 7. 9. SeeDB optically cleared sections. (A) PI staining (red) can be achieved in SeeDB-cleared sections. Background fluorescence was reduced in cleared sections compared to non-cleared, improving cellular resolution. (B) DAPI nucleic staining (blue) was included in the protocol to provide a measure of the proportion of cells exhibiting PI fluorescence. (C) Merged image of PI and DAPI images. Image acquired 85 μm medially into cleared section of cortex, scale bar 100 μm .

Background PI fluorescence was reduced in cleared sections, improving the reliability of cell identification analysis via ImageJ which was performed using the particle count measurement tool. Briefly, background was subtracted by rolling ball (surrounding pixels of every pixel are averaged to identify a threshold for signal, Fig. 7.10, A), an appropriate threshold between 0 and 255 (8-bit images) was set and visually verified for each image (Fig. 7.10, B). Particles of a size >10 pixels, and circularity 0.1 to 1, were then included for analysis (Fig. 7.10, C).

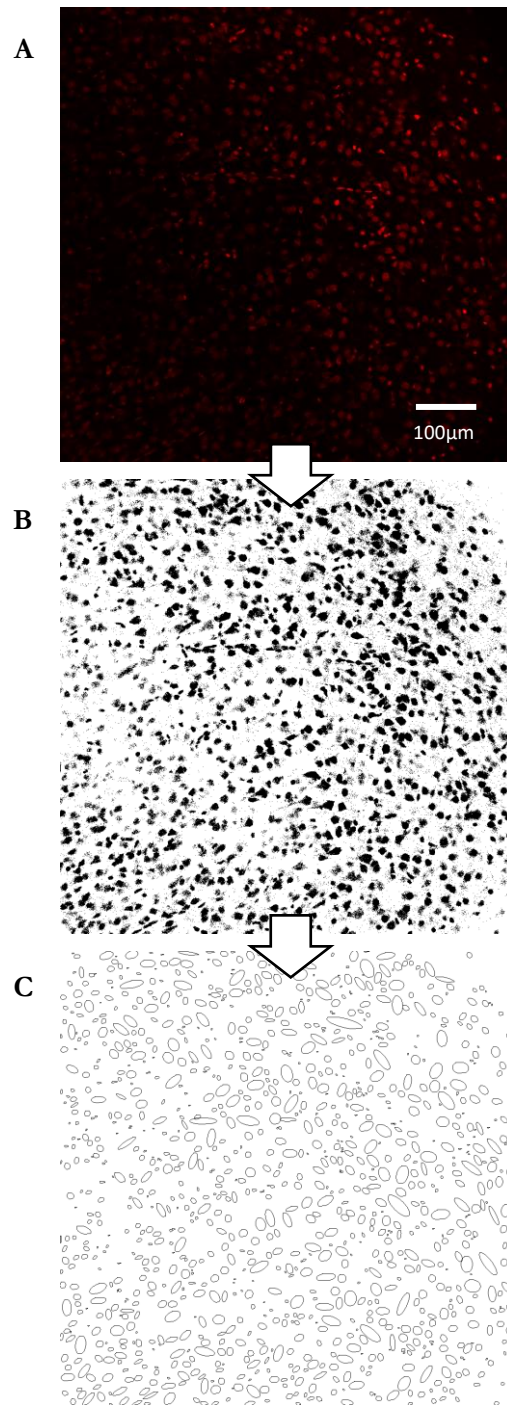


Figure 7. 10. Particle analysis of SeeDB optically cleared sections. (A) Background PI fluorescence is subtracted and (B) a pixel threshold was manually evaluated for each image. (C) The particle count is then measured for each image.

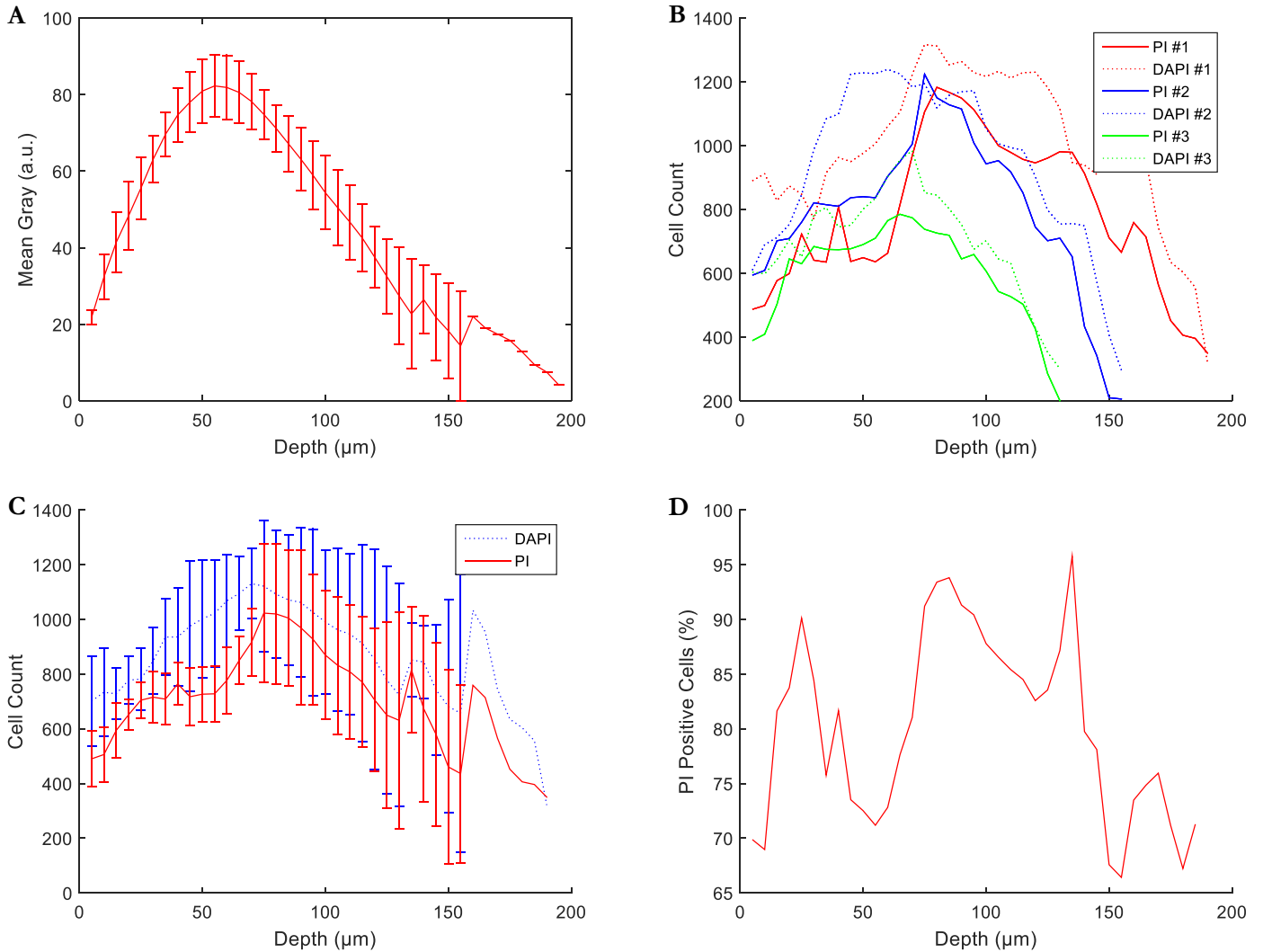


Figure 7. 11. Analysis of SeeDB-cleared sections. (A) Mean gray values of PI images demonstrate a fluorescence profile consistent with non-cleared sections and signal was detected up to a depth of 190 μm . Staining intensity peaks 50-65 μm into sections at 73-88 (a.u.). (B) Counts of PI and DAPI positive cells for each image acquired at depth. Most images exhibited a greater DAPI cell count than PI as would be expected. (C) Averaged cell counts of PI and DAPI images. Peak cell counts occur at a depth of 65-70 μm , aligning with mean gray values, however, two later peaks (135 μm and 160 μm) are not observed in mean gray measurements. Error bars standard deviation. (D) Percentage of averaged DAPI stained cells which are also PI-positive based on average values. Although the numbers of identified cells decrease > 100 μm deep, the proportion of PI stained cells rapidly decreases at depths greater than 135 μm , suggesting a greater number of viable cells at this depth.

7.6.2 ClearT2 Optical Clearing

Optical clearing by the ClearT2 method utilises graded solution concentrations of formamide and PEG as described in table 7.5. Sections were observed to have become more transparent following clearing and expanded in size $\sim 2\text{mm}$ laterally (image 7.2), consistent with previous studies²⁰¹.

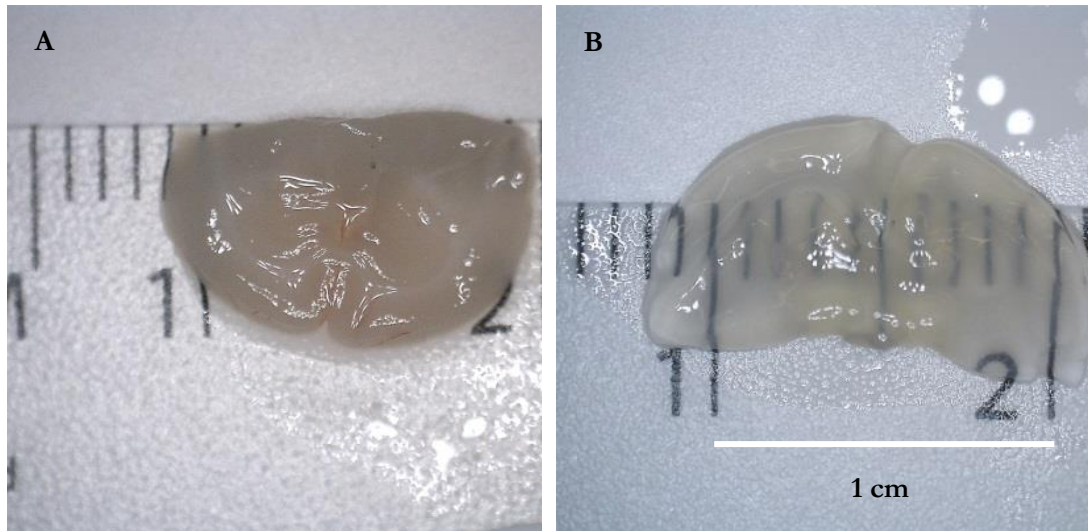


Image 7. 2. Optical clearing of brain tissue with the ClearT2 method. (A) Paraformaldehyde-fixed tissue, (B) same tissue following clearing by ClearT2 protocol (see table 7.5 for details). Sections expanded $\sim 2\text{mm}$ laterally and exhibited increased transparency.

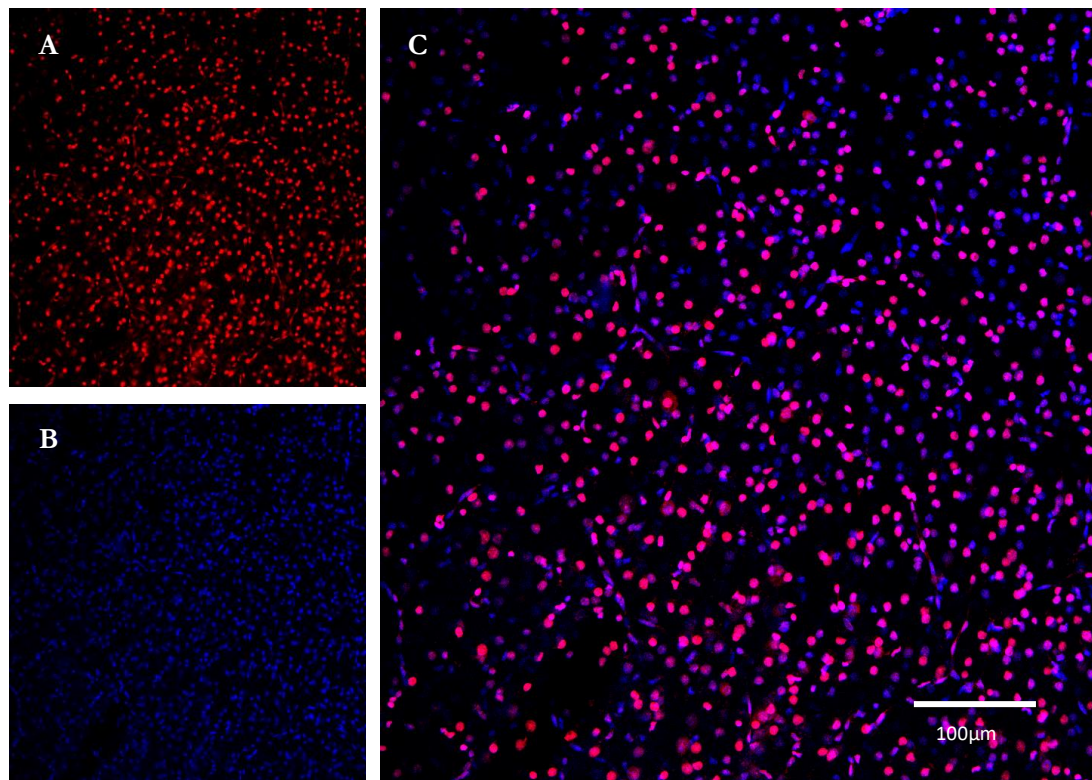


Figure 7. 12. ClearT2 optically cleared sections. (A & B) PI (red) and DAPI (blue) stained cells. (C) Merged images taken at a depth of 130 μm into tissue.

Mean fluorescence intensity of PI was measured for each image and particle count calculated using imageJ software (as described in Fig. 7.10). Fluorescence signal of PI-stained cells was detected up to a depth of 225 μm with peak signal occurring 40-60 μm into tissue (Fig. 7.13, A), consistent with SeeDB results. Sections demonstrated a reliable pattern of numbers of identified cells at depth (Fig. 7.13, B) and cell numbers peaked at a depth of 65 - 90 μm . Peak cell counts were comparable to SeeDB results; however, more cells were identified at superficial depths in ClearT2-cleared sections. For example, average PI count at 5 μm (Fig. 7.11, C) was 634 (± 159 , S.D.), but 490 (± 103 , S.D.) for SeeDB sections. The percentage of DAPI-stained cells exhibiting PI fluorescence remained >80% up to depths of ~ 125 μm (Fig. 7.13, D), similar to earlier results.

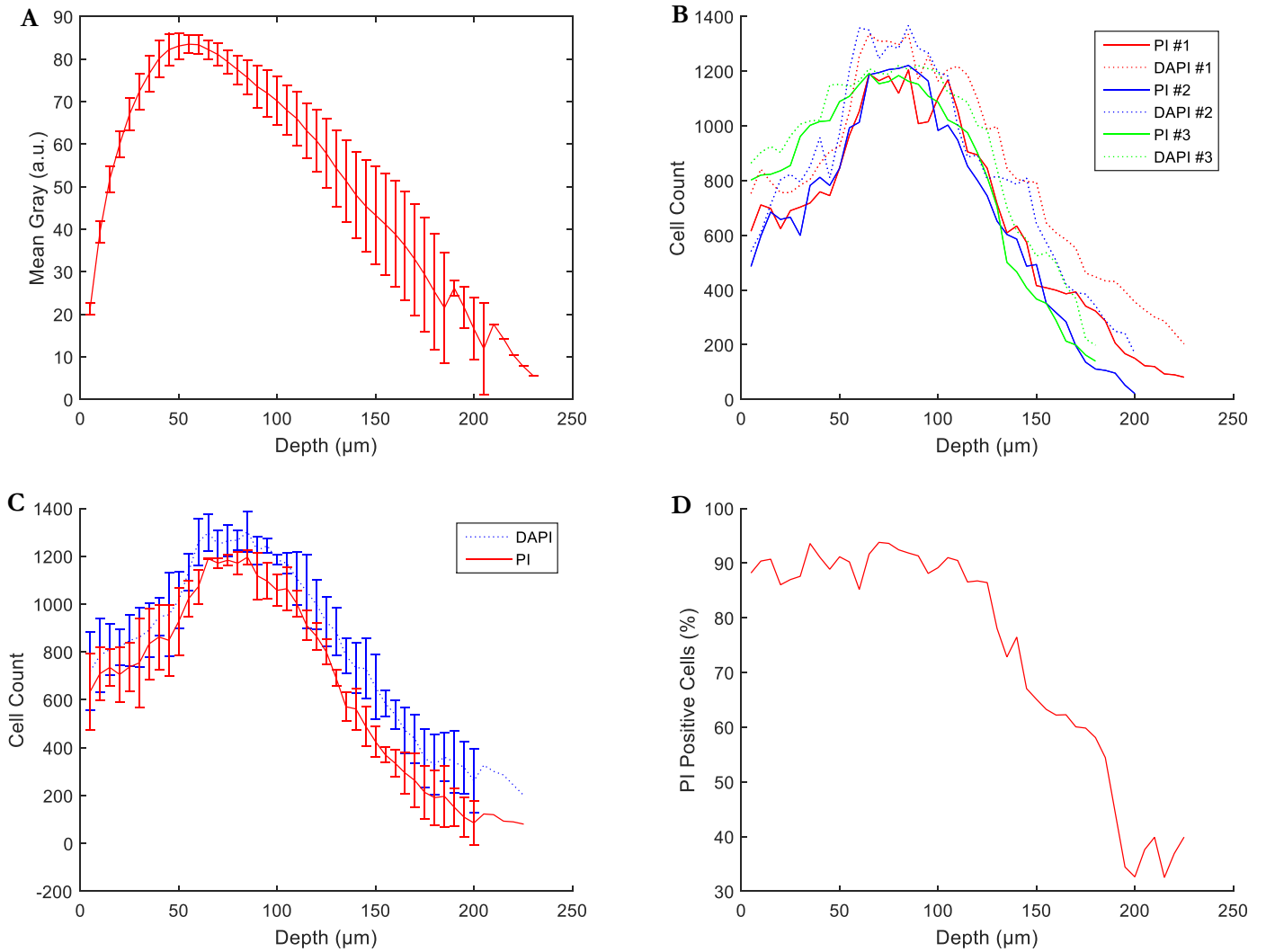


Figure 7. 13. Analysis of ClearT2 optically cleared sections. (A) ClearT2 method enabled detection of PI fluorescence signal up to a depth of 225 μm with a peak average of 83.5 (a.u.) at ~ 50 μm depth. (B) Particle count analysis of PI and DAPI positive cells. Peak cell count occurred between 65 - 90 μm deep into tissue. (C) Averaged cell counts of PI and DAPI images. ClearT2-cleared sections demonstrated low variation between analysed image stacks (error bars S.D.). (D) The percentage of DAPI cells exhibiting PI fluorescence based on average values. A high proportion of cells exhibit PI fluorescence up to a depth of ~ 125 μm before rapidly decreasing.

7.7 Discussion: Histological Evaluation

The studies presented in this chapter suggest the procedures used to prepare acute cortical slices for electrophysiological recordings result in extensive tissue damage up to 100 μm from sectioned surfaces. However, the viability of cells beyond this depth have not been reliably confirmed using PI staining protocols.

An appropriate method for staining and imaging thick sections of brain tissue with PI was developed. This stain is typically used in flow cytometry assessments or to indicate specific stages of mitosis and is not commonly combined with FF tissue sections. Without further tissue processing, PI fluorescence signal could be detected via confocal microscopy up to an average depth of 140 μm . The impact of section incubation for 1hour in aCSF, as per the electrophysiological protocol, was then assessed and found no significant differences ($p = 0.55$, t-test). Light scattering caused by high cell density limited the validity of these results, however, this effect would be less pronounced at the section surfaces, suggesting that the initial 50-60 μm accurately reflect the extent of cellular damage (Fig. 7.2). Incubated sections exhibited a shallower gradient of fluorescence signal, but larger peak values at greater depths than non-incubated sections. Dissociation of ruptured cells during incubation would reduce the density of cells at surfaces and cells would be less compacted. If the fluorescence signal in this low cell density area still achieved inclusion criteria, this expanded area of damaged cells may be interpreted as a thicker section. The greater peak values may be caused by additional cell damage at the surface which occurred during the hour of incubation. However, this impact appears marginal. Although no overall difference was observed between groups, conclusions regarding PI-positive cells at depth could not be asserted.

Sections were placed on sample microneedles to determine any additional impact on PI-fluorescence and were compared to a positive control group utilising TritonX detergent (Fig. 7.3). Disappointingly, TritonX-treated sections displayed a shallower positive gradient at surfaces and a lower peak fluorescence value than sections placed on needles; the opposite of what was expected. However, a greater signal was observed across lower depths in TritonX-treated sections, suggesting that the number of PI-positive cells decreases in the medial portions of sections. This discrepancy is noticeable at depths greater than 65 μm .

Technical difficulties caused by light scattering prompted an alternative approach which was to embed sections in agar and re-section at a new angle. These images of 50 μm thick cross-sections indicated a layer high fluorescence intensity PI-positive cells 100-150 μm thick. Although re-sectioning provided reasonable visualisation of PI fluorescence across sections,

poor cellular resolution prevented quantification of the proportion of damaged cells and PI may not have effectively diffused through the entire section. This could have been resolved by including TritonX positive control in agar re-sectioning experiments to determine if a similar staining pattern was observed. Interestingly, a discrepancy in PI fluorescence on each sectioned edge was evident in several agar embedded sections (Fig. 7.6). This was not correlated to the insertion of needles and was not consistently observed. The quality of the vibratome blade and angle of sectioning may be responsible²⁰⁶. However, handling of slices during transportation to and from the vibratome could additionally impact this outcome. The use of a small paintbrush to direct slices was limited due to potential damage reported from their use²¹³, but it is highly possible that the protocol lacked proper control measures in this regard. Attempts were made to ensure sections did not rotate to examine each surface individually, however, this was not achieved. The fluorescence discrepancies on edges may explain greater imaging depth in a single section observed following SeeDB clearing (Fig. 7.11, A).

Optical clearing techniques SeeDB and ClearT2 were effectively used to reduce the light scattering in thick brain sections, detecting PI fluorescence signal up to depths of 135 μm and 125 μm , respectively. However, these techniques have been shown to provide fluorescent imaging of depths up to 2000 μm . In this case, the depth of imaging was limited by the availability of an optimised magnification objective. Therefore, imaging had to be performed with immersion objectives in PBS which would begin to reverse the clearing of tissue as clearing agents began to diffuse into the solution.

Previous studies have indicated SeeDB protocol causes limited alterations to tissue dimensions¹⁹⁹, and no noticeable expansion or shrinkage was observed in this work. ClearT2 clearing has been compared favourably to SeeDB in terms of maintaining consistent tissue dimensions²⁰⁰ and has been reported to have no impact on expansion of individual cell size. Studies have reported that ClearT2 does not cause tissue expansion in brain sections >800 μm thick²⁰¹ or only cause mild expansion in thinner sections¹⁹⁹. Lateral tissue expansion of ~2mm was observed following ClearT2 optical clearing in this work (Fig. 7.2), however the cause of this ~20% lateral expansion is unclear as the protocol was adapted from work recommending use on sections 200-1000 μm thick.

The resolution of the acquired images (examples in Fig. 7.9 & 7.12) were greatly enhanced compared to re-sectioned tissues and enabled accurate quantification of PI-positive cells which could be compared to the cell count of non-selective DAPI-positive cells. The ClearT2

method has been reported to have poor clearing capability when compared to SeeDB²¹⁴, however in this work a more reliable profile of cell count at depth was observed in ClearT2-cleared sections (Fig. 7.11,C compared to Fig. 7.13, C). Both optical clearing techniques suggest that a significant reduction in the number of PI-positive cells occurs at a depth of ~125-135 μm into sections. This result would be impacted if PI fluorescence signal at depth decreases at a greater rate than DAPI and a greater imaging depth was expected in these studies, yet these results are consistent with the fluorescence profile in earlier results. An additional future investigation could include the optical clearing technique RTF (Rapid clearing method based on triethanolamine and formamide) which is based on the ClearT2 method and has been reported to enhance the clearing capabilities in a variety of tissue preparations²¹⁵.

These findings across a range of tissue processing methods are difficult to directly compare due to differences in staining efficacy, cell resolution, imaging depth and tissue expansion, however, the results of staining in the superficial regions of sectioned tissue edges remain the most valid as they are impacted less by light scattering and more effectively permeated by fluorescent dyes. Therefore, these results indicate extensive PI staining of cells, corresponding to acutely damaged cell membranes, up to a depth of between 80-100 μm into sections in this setup. For the experimental setup described here, electrodes located at tips of MEA microneedles should be inserted to this depth at minimum to record from viable neuronal circuits.

Previously described procedures have achieved slices with viable cells at the section surface. This suggests that the sectioning procedure described in this work damaged section surfaces to a greater extent than in comparable studies and this could have been minimised with greater investment in vibratome technology. Patch clamping at the surface of brain sections has been reliably demonstrated^{59,190,216,217}, suggesting that the extent of cellular damage observed here can be overcome with alternative preparations and procedures. Further experiments should focus on improving the viability of acute slices and validating the health of the surfaces of sections prior to adjustments to the device's design. The damage observed here may be the result of poor vibratome or blade quality – ceramic blades have demonstrated enhanced section surface viability¹⁹³ – although alternative solution preparations could validate this approach. Alternative cutting and incubation mediums such as NMDG^{193,218} could be utilised, while slicing at higher temperatures have been shown to yield improved recording quality. Despite the extensive damage observed in sections

presented here, the MEA was capable of resolving the activity of 78 neurons which suggests great potential for the study of hundreds of neurons given further experimental setup validation.

8. Conclusions & Discussion

This work describes an approach to record highly spatially and temporally defined neuronal electrophysiological activity in acute rat brain slices using a novel MEA. Electrodes were effectively platinised to exhibit appropriate SNR values with which to record neurons while the acquisition system and custom Java software reliably classified neurons. However, the data presented in this work is limited to 78 neurons identified in a single recording and comparisons between recording datasets were not completed. Numerous recording attempts were made, however, electrical artifacts and insufficient electrophysiological data inhibited the identification of neurons.

The population of neurons elicited 71% of their activity within the first two hours of a 4-hour recording, indicating a physiological change which reduced activity after two hours. This is likely attributable to the dissection and sectioning procedure, which is discussed in greater detail in sections below. Therefore, analysis was limited to the initial 2 hours of recording. Yet, identified neurons were well defined and consequently analysed for discriminatory features that could suggest the presence of discrete subpopulations. Averaged extracellular action potentials were compared by the time and amplitude of different phases of the signal. While findings did not confirm previous reports of distinctions based on trough widths and peak to trough ratios, the end slopes of the population (representing the amplitude change from hyperpolarisation peak to return to RMP) demonstrated the greatest variance and discrete clusters were identified. Temporal characteristics were difficult to classify due to large ISI values and therefore the data required further processing by being segregated into high and low frequency ISIs with a threshold set at each neuron's median ISI value. This method identified a discrete population of neurons at high frequency values which exhibited significantly lower variance and smaller mean ISI values; this subpopulation was not identifiable at lower frequency ISIs.

High frequency behaviour known as bursting has a variable definition and the sporadic spike rate of the population led to the use of a bursting identification method. The MISI method which dynamically adapts a threshold based on the mean of ISI values less than the mean of the spike train ISI (section 5.3.1). This method suggests that on average 49.6% of each neuron's spikes occur during periods of bursting with all but one neuron (#72) exhibiting bursting for more than 30% of their activity. For comparison, an alternative method of burst identification was developed which demonstrated a similar average value of bursting spikes

(48.9%), but a greater variation from this value, suggesting this approach may be a more powerful discriminator of irregular bursting behaviour.

To determine the viability of acute slices following the tissue preparation procedure, cells were stained with propidium iodide: a membrane impermeable dye which fluoresces upon binding with DNA. This dye will therefore only emit fluorescence if a cell's membrane has been ruptured which would indicate acute trauma. To circumvent the problem of light scattering while imaging at depth, alternative approaches were developed which included embedding sections in agar and rotating them to provide a cross sectional image and the optical clearing techniques ClearT2 and SeeDB. Collectively, these results indicate a layer of $\sim 100\ \mu\text{m}$ of severely damaged cells exists at the plane of sectioning. The depth of this layer is similar enough to the height of the electrode needles ($90\ \mu\text{m}$) to cause concern regarding the efficacy of the MEA design, however, the microfabrication technique utilised in the fabrication of this device permits the production of needles with heights greater than $90\ \mu\text{m}$ and further experimentation would indicate if greater depth yields a higher rate of neuron identification. Importantly, future steps should be taken to minimise the damage to brain slice tissue (further discussed in section 8.5).

Several technical challenges arose during the progression of this project and a major impediment of the project was ensuring that the fragile electronics of the acquisition system and silicon wafer MEA were sealed off from electrolyte solutions being perfused over tissue. On two occasions, liquid passed between the MEA and the neuroboard allowing salt to accumulate around wire bonds. This resulted in a failure of the recording system and reduced the possible number of recording attempts. It remains unclear if this occurred over time (potentially reflected in electrical noise which impeded neuron identification) or in a single drastic incident. These events limited the acquisition of data for this project, however, there is great potential for large datasets to be acquired through this approach.

8.1 Discussion: Electrical Characterisations

The MEA demonstrated electrical characteristics suitable for the extracellular recording of multiple neurons simultaneously: tungsten electrodes could be effectively platinised to reduce impedances to $\sim 200\text{k}\Omega$ at $1\ \text{kHz}$ (Fig. 3.5); this resulted in a system electrical RMS noise level of $10\text{-}12\ \mu\text{V}$; immersed in saline and with tissue placed on the electrodes, the device exhibited an average RMS noise of $15.4\ \mu\text{V}$ (Fig. 3.8). This is an appropriate noise level with which to record extracellular neuronal activity¹¹. Additionally, the silicon substrate of the MEA exhibited coupling to the channels, but only minimal coupling between channels

(Fig. 3.6), highlighting a reliable fabrication process. All electrodes demonstrated decreased impedance values following platinisation, however, the impact of various protocols was indistinguishable as no electrode exhibited values lower than 200k Ω and the decrease did not correspond with increased current and time (Fig. 3.5, B). The surface area of exposed tungsten was not uniform, as can be seen from the variation in tungsten electrode impedance values. As granular platinum-black is deposited at these sites the surface area increases and impedance is reduced. The surface area to volume ratio increases with irregular shapes, yet once the electrode surface is covered in platinum this ratio appears to be only marginally increased. Therefore, increasing the current and time of platinisation in the electrodes presented here has minimal impact on impedance values and the electrode can be effectively platinised by applying 100nA for 20s.

8.2 Discussion: Neuron Identification

Future experiments aim to compare recordings taken from identical brain regions; therefore, it is important to keep spike sorting parameters as similar as possible and necessitates consistent levels of electrical noise. System noise analysis based on 15 seconds of data collected at three intervals of 5 seconds at the very start of the experiment were used to quantify the noise of electrodes inserted into tissue and to determine spike sorting parameters. The mean RMS noise of all electrodes inserted into tissue was 15.4 $\mu\text{V} \pm 0.8(\text{S.D.})$ and, taking account of the noise of each electrode and average spike amplitude detected on relevant electrode, the SNR ranged from 8:15 (average 10.4) which is consistent with earlier reports using a similar system¹⁵. Variation across electrodes is likely the result of slight inequalities in the etching process, which exposes the tungsten electrodes, which in turn alters the surface area on which platinum is deposited. Sources of noise have been minimised through earlier developments of the acquisition system and how the neuroboard is insulated, while platinisation of electrodes was limited to ~ 200 k Ω and would not be further reduced without applying an unnecessary increase in current. Alternative sources of noise could derive from contact with the metallic perfusion tubes while the platinum wire circulating the recording chamber acts as an electrical grounding and improved insulation of this component could marginally improve the SNR. Electrical lighting consistently interfered with recordings due to the photoelectric effect on the silicon MEA wafer, consequently recordings were performed in the absence of light.

A key aspect of the data identified in chapter 4 is the dramatic decrease in spike rate observed after 2 hours of recording. Of all recorded spikes from across the population, 71% were

identified during the initial 2 hours with a peak in activity ~1hour from the start of recording. This could be interpreted as the length of time required for excited aCSF to perfuse into the tissue, remove incubation solution, and increase activity of neurons, however at a minimum perfusion rate of 2ml/min this assumes that 120mls is required to flush out the chamber with a volume less than ~3ml of solution when filled with tissue, mesh and perfusion pipes. Potentially the weight of the resistance seal acted slowly, and needles were only fully inserted after a prolonged period. The resistance of solution passing through the mesh seal prevented direct application of pressure and may have taken time before tissue was not physically disturbed by perfusion. It is more likely that cells had been damaged during the tissue preparation procedure and the decrease in activity is the result of necrotic cells no longer able to maintain ionic homeostatic regulation and unable to initiate action potentials. This is further discussed in section 8.5. Alternatively, following the peak of activity, electrodes may have moved to more superficial tissue layers if the buoyancy of tissue resulted in it being raised within the solution. This would diminish the cell: electrode interface and spikes would no longer be associated with the same neuron. However, this movement would also attenuate spike amplitudes which is not observed (Fig. 4.10) and was not observed in the manual evaluation spike sorted clusters.

8.3 Discussion: Spike Features and Temporal Characteristics

The aim of chapter 5 was to demonstrate analytical approaches to distinguish neuronal subtypes based on electrophysiological features alone. Temporal and amplitude features of averaged waveforms of each neuron were analysed with the aim of identifying inhibitory cells, as had been successfully performed in previous studies^{12,143,147,148}, and inter-spike interval values were interrogated and compared between neurons to highlight similar patterns of behaviour^{149,134}. Of the waveform features analysed, the end slopes of the population (representing the amplitude change from hyperpolarisation peak to return to RMP) demonstrated the greatest variance and discrete clusters were identified (Fig. 5.8). Three distinct clusters were identified and the least specific (poorly clustered) distribution has been associated with inhibitory neurons, having steeper end slope gradients¹². However, the remaining neurons exhibited a discrete distribution centred around a gradient of -2; particularly steep in comparison to previous reports in the range of 0.1 to -0.2¹². Previous reports have not suggested this method capable of categorising cells with greater resolution than excitatory or inhibitory neurons, yet the distribution presented here consists of a spectrum of properties. The specific cluster around -2 may represent excitatory neurons and

more shallow end slopes could be recorded from neuronal areas proximal to the axon hillock, where hyperpolarisation is attenuated¹⁶⁴, however these assertions are not supported by other waveform characteristics which have been more repeatedly used as a successful discriminator. It is worth noting that studies have utilised features that clearly demonstrate clear discrimination and the only consistent indicator of inhibitory neurons is a narrow trough width which is not observed in this work. Yet trough width was not found to be a reliable indicator of inhibitory neurons when cell type was verified by immunohistology techniques¹⁶ suggesting waveform features may only be useful for identifying neuronal subtypes in certain cell preparations.

Temporal analysis of spike trains aimed to differentiate regularity of neuronal activity which could underlie functional roles within a network¹⁴¹. This analysis was impacted by the low spike rate of most neurons, spread out over 2 hours of recording. Bimodal distributions of ISI values can be used to indicate complex patterns of activity¹⁴⁹, yet few neurons exhibited this distribution (Fig. 5.13). Therefore, spike trains were segregated into high and low frequency spiking by analysing the variance of ISI values above and below the median ISI value for each neuron. At higher frequencies, a discrete population was identified with low variance and relatively low mean ISI values (Fig. 5.15), suggesting a group of neurons – when spiking at high frequencies – elicit a regular high rate of spikes. While this distinction is an interesting identifier the processing involved to highlight these, relative, differences subtracts from the method's usefulness and it is unclear if this behaviour correlates to relevant functional roles. The coefficient of variation was calculated for each neuron as an additional approach to assessing the regularity of spiking activity. This approach divides the spike interval variation by the mean ISI value to quantify the width of the ISI distribution, therefore a CV value >1 suggests high variability in activity as the deviation exceeds the mean. Again, the low spike rate impacted this approach and indicated all neurons exhibited highly irregular spike trains (Fig. 5.16). The segregation of spike trains above and below the median ISI value was repeated and CV value re-calculated; this analysis suggested that more neurons exhibited a more variable spike train at lower frequencies, consistent with ISI distribution analysis. The irregularity observed in low frequency activity may be due to the use of the median value and the range of ISI values as such large ISIs occupy a large temporal space, i.e. high frequencies (low-value ISIs) could exist between 6-250 ms, but low frequencies could range from 251-20000 ms. Further investigation could employ a more dynamic threshold to identify an appropriate ISI value for each neuron or by eliminating statistically anomalous ISI values.

Finally, temporal analysis was performed to identify spontaneous high frequency activity termed bursting. The difference to high frequency ISI activity is the spontaneity and duration of these periods, however definitions of a burst are variable. Attempted here is the MISI method which identifies sequences of two or more ISI values lower than an auto-adaptive threshold based on the mean of ISI values. This method suggested at least 30% (average 49.6%) of each neuron's activity is relatively spontaneous high frequency activity (Fig. 5.20) which, while consistent with the irregularity evaluated through CV analysis, does not match with the low spike rate observed in the population. It is therefore likely that this method is highly susceptible to changes in spike frequency. As an alternative, a method was developed to identify repeated patterns of 3 or more sequential ISI values. The average value of the number of identified bursts was found to precede regularly repeated ISI values (Fig. 5.22) and was therefore used as a threshold for burst identification. This analysis provided a more variable assessment of each neuron's bursting activity and appears more adaptable to irregular spike trains than the MISI method. However, a key difference is the analysis of 3 or more ISI spikes opposed to MISI utilising only 2 and altering this minimum value may enhance the MISI applicability.

The inapplicability of these parameters to this dataset may arise from the health of the recorded tissue. The parameters were developed based on neuronal culture^{16,77} and *in vivo*¹² recordings where the proportion of cell viability is expected to be greater than acute slices. As discussed above, improving slice viability and validating the preparation could align recordings with this device more closely with previous studies or, at a minimum, provide a larger dataset with which to reinforce these findings.

8.4 Discussion: Connectivity Analysis of Recorded Neurons

Presented in chapter 6 are approaches to analyse the functional and effective connectivity of neurons utilising the high spatial and temporal resolution of the 512-needle MEA. These developed from the generation of peri-stimulus time histograms (Fig. 6.1), which highlight correlated activity between neurons, and limiting activity of interest to neurons with a high proportion of their spikes plotted in these histograms (Fig. 6.2). This method is dependent on the number of spikes elicited by a neuron; however, this relationship was not linear (Fig. 6.3) and suggested a degree of connectivity could be discerned in the data. Using the triangulated locations of neurons across the array (Fig. 6.4) the distance between neurons could be combined with PSTH data to indicate neurons both proximal to each other and

demonstrating a high proportion of correlated activity (Fig. 6.5). Consequently, the direction of connectivity, locations of cells and weight of correlation were presented as directed graphs (Fig. 6.7 & 6.8). The resolution qualities of the array also allowed the visualisation of the immediate direction of electrophysiological signals for 57 identified neurons (Fig. 6.9). These approaches to connectivity analysis can be used to identify spatially clustered cells which may be functionally similar within a network. Increased spike numbers per cell and a greater population of neurons would greatly enhance the validation of these methods. Additionally, further analysis of the immediate direction of signal propagation and comparisons with the directed graph approach could help to differentiate functional and effective connectivity in acute slice recordings.

8.5 Discussion: Histological Evaluation of Acute Slice Damage

The integrity of cell membranes in brain slices were histologically evaluated using the fluorescent dye propidium iodide. Results indicated that the tissue preparation presented here cause significant trauma to sections, evidenced by high PI fluorescence signal observable up to approximately 100 μm from sectioned edges. This represents substantial damage compared to contemporary studies^{216,217} and is potentially due to the quality of the dissection procedure, vibratome quality or the handling and incubation of sections.

This conclusion suggests that the needle heights of the MEA used in this work (90 μm), if fully inserted, were close to the boundary of the region of acute cellular damage and may account for decreased spike frequency following the initial two hours as these cells experienced necrosis. However, it is notable that PI is not commonly applied to free-floating sections and is more often used in low cell density cultures^{203,219} or flow cytometry to determine stages of mitosis^{220,221}, therefore further validation of this technique is required to ensure these findings are appropriate for conclusions based on free-floating sections.

To circumvent the challenges of developing a protocol for the use of PI on FF sections, more common paraffin embedding techniques were attempted. Previous studies reported prolonged PFA fixation causes diffusion of the PI signal and results presented here indicated a decrease in signal specificity by 3hours fixation (see section 7.2.1). Yet, paraffin dehydration protocols require several hours of formalin fixation prior to desiccation²²², and limiting this fixation time likely impacted further embedding stages which resulted in drastic tissue shrinkage.

Minimising acute cellular trauma is a critical factor to improve neuron yield and maintain high quality signal acquisition during this recording approach. Therefore, identifying and

limiting potential sources of damage must be addressed before developing this method further. Of particular concern is the sacrifice and dissection procedure employed in these studies. Here, cervical dislocation was performed followed by decapitation. Investigations focussing on improving the health of acute brain slices repeatedly state that the preferred method of sacrifice is anaesthetisation by isoflurane prior to decapitation^{180,223–227} which may confer neuroprotective benefits in young animals²²⁵. It is believed that compression of the spine during cervical dislocation applies pressure on the cerebral spinal fluid and results in the rupture of blood vessels in the brain. This method was performed due to Home Office legal requirements which limited the exploration of alternative animal procedures.

The unpredictable and unequal distribution of PI on either edge of sectioning (Fig. 7.6) may have resulted from handling during tissue transfer, yet vertical blade vibration and speed of sectioning would also impact the severity of damage¹⁹¹. Sections need to be taken rapidly to be placed in incubation aCSF and maintain viability, but sectioning too fast can result in pressure on the tissue which is particularly evident if the blade does not achieve sufficient purchase in the tissue (i.e. not vibrating adequately). Vibrational movement is required to match the lateral speed of the blade; too slow, and the blade will move forward before the tissue is properly cut, too fast and the blade can cause friction against tissue already cut. Additionally, the angle of the blade could not be altered in the vibratome used here which could explain a difference in PI fluorescence between edges as the surface area and sharpness of the blade would differ between the top and bottom edges. However, this was not confirmed and would be evidenced by more consistent observation of unequal lateral fluorescence in agar-embedded cross sections.

During the stages of tissue preparation, tissues were maintained in a series of solutions designed to minimise metabolism while keeping the ionic environment relatively consistent for neurons to survive. Sucrose-based cutting solutions are commonly used in acute slice preparations, however, they are not required for quality slices as it has been reported that decreased calcium and increased magnesium concentrations alone can yield superior results²¹³. The reasoning for using a sucrose-rich solution is to provide an equimolar replacement for NaCl: following an insult, inflammatory responses cause neurons to swell and become more permeable; this causes a surge in sodium entry into the cell which is followed by an increased intake in water. These mechanisms can adversely impact homeostatic regulations and result in cell death. Developments in slicing techniques have identified alternative candidates for cutting solutions such as N-Methyl-D-glucamine which

reportedly improves slice viability taken from mature adult animals¹⁹⁴ and has gained popularity in acute brain slice preparations¹⁹³. As with sucrose cutting solutions, acute slice preparations commonly cool solutions to approximately freezing point. The low temperature slows metabolisms therefore extending the viability of the slice for recording time by slowing the kinetics of apoptotic cascades as well as loss of homeostatic ion current control. However, membrane transporters have been reported to not respond uniformly to temperature changes²⁰⁵, suggesting placing the brain into cold solution immediately following dissection may impact ionic homeostasis and therefore slice viability.

Quantification by PI suggested no improved viability of slices resulting from the incubation of slices in aCSF for 1hour prior to recording (section 7.2.2). This stage of the experiment is to provide a period of cellular recovery as debris from damaged/dead cells can be removed and dissociate from healthier portions. This provides the advantage of reducing the thickness of the layer of damaged cells the needles are required to bypass. That no effect was observed in the setup presented here could indicate that damage was so severe any cellular dissociation during this period was minimal and undetectable due to the extensive depth of acute trauma. Further recording attempts could explore the state of tissue during this period of incubation to validate the viability of tissue prior to placing on the MEA.

Optical clearing techniques were employed with aim of improving the quantification of PI fluorescence at depth in thick sections. Both methods successfully increased imaging depth in 350 μm thick sections, but to different extents. SeeDB, a fructose-based clearing agent, identified a peak of PI fluorescence at a depth of 50-65 μm (Fig. 7.11, A) while the greatest number of identified PI positive cells occurred at 65-80 μm (Fig. 11, B). While the cell identification method could doubtless be improved, this could suggest the intensity of PI signal in superficial layers reduces cellular resolution or that PI has not effectively diffused through the tissue. Further studies using prolonged PI incubation or 200 μm thick slices could assist to confirm this. The proportion of PI positive cells in SeeDB-cleared sections was not readily coherent in superficial layers due to a peak between 0-50 μm (Fig. 7.11). It is possible that this resulted from an anatomical structure where cell density varies, or that loose, partially dissociate, cells formed a separate layer during incubation. The SeeDB method is easy to perform and did not cause alterations to tissue dimensions but takes several days and may not consistently affect regions of varying cell density.

In contrast to SeeDB, the ClearT2 method resulted in ~ 2 mm of lateral tissue expansion (Fig. 7.2) despite previous studies with ClearT2 on sections 200-1000 μm thick reporting limited

alterations to slice dimensions²⁰¹. This expansion was observed to similar extents in each tissue processed by this method. A possible source of this discrepancy could be handling of tissues, as this method replaces lipids in fibrous structures with PEG and may reduce tissue integrity causing in the tissue to stretch when transported under strain.

The ClearT2 method generated higher resolution images compared to the SeeDB method, despite contrary reports²¹⁴, and cell identification produced a more coherent profile (Fig. 7.13, B, C & D) which indicated that ~90% of cells are PI-positive up to a depth of approximately 125 μm . This is more aligned with results in cross sectional images. The superior resolution may be caused by an imaging challenge which also impeded the depth of image acquisition. The confocal microscope did not possess an objective optimised for the RI of these solvent solutions and imaging was performed using a water immersion lens with cleared tissue immersed in PBS. Therefore, imaging was performed quickly as these techniques are readily reversible and the solvents can diffuse into PBS. This was a major limiting factor in imaging optically-cleared tissues. It is possible that the objective used was better suited to ClearT2 and that SeeDB is more readily reversible in PBS. However, these results are relatively consistent with earlier assertions and improved procedures would likely enable a quantifiable PI profile of an entire acute slice.

Experiments utilising Dil were aimed at achieving visualisation of needle penetration depth to ensure needles were fully inserted. Previous successful applications of this approach have inserted a single silicon probe millimetres into the brain^{209,208}, while in this work needles 90 μm tall with 60 μm spacing were applied. The small electrode dimensions likely contributed to the aggregation of dye and poor discrimination of needle insertion sites. Dil is more commonly used to stain vasculature²¹² which, if additionally stained, would decrease specificity of cellular imaging in 350 μm thick free-floating slices due to the number of vessels. Aggregation of the dye limited the specificity of the stain and it has been reported that Dil diffusion into cell membranes is improved at 37°C²²⁸, however, the aim of the experiment was not to improve neuron identification but the sites of needle penetration, therefore limiting Dil diffusion would be preferable. In addition to attempting the stain at lower concentrations, further use of Dil should also be applied to lightly fixed (1.5% PFA) sections as this has been reported to improve resolution of cells^{229,230}, while sonification of the Dil solution has been reported to improve the solubility in ethanol²⁰⁷.

8.6 Summary & Future Directions

The novel 512 needle MEA presented in this work can define neurons and their signals with a high degree of precision and generates high spatial and temporal resolution data with which to interrogate the functional and effective connectivity in acute brain slices. Further validation of the recording process is required to improve the number of neurons identified and the quality of data. Future experiments should initially focus on improving the viability of slices to provide the usefulness of prolonged periods of continuous recording. This would also likely increase the yield of neurons identified and refine locations of functional units within a network.

The approaches to discriminate neuronal subtypes based on signal waveforms presented here are based on prior investigations, yet the parameters which were utilised remain contentious and few of these are universally accepted as reliable. This work does, however, highlight the variability of the repolarisation phase between neurons and further experiments with this system could determine the classification power of this criterion.

Long periods of quiescence severely impacted the temporal analysis of the dataset. These low activity periods may reflect physiological activity; however, this assertion requires further verification with larger neuron numbers obtained from several recordings and comparisons with *in vivo* recordings from the same region. If the behaviour is validated, the MEA could be used to investigate brain structures difficult to approach with current *in vivo* technologies. Segregating spike train ISI values artificially created two, more manageable, datasets and a distinct group of neurons exhibited regular high rates of activity at higher frequencies, but not lower frequencies, suggesting complex patterns of spiking behaviour. This approach may be more applicable to distorted or abnormal spike trains, yet further interrogation of these neurons could provide valuable insights into their functional roles.

The MBISI method was developed by the author and was prompted by inconsistencies observed following the application of the MISI method. Although useful, the MISI method appears to be highly influenced by the irregularity of the spike trains presented here and may be more suitable to future recordings. The MBISI method essentially identifies the ISI value in each spike train which immediately precedes ISI values which are regularly elicited, i.e. regular activity. In this sense, MBISI is a measure of irregularity of groups of 3 or more sequential spikes. Whether this method is applicable to other recorded spike trains remains to be seen.

Connectivity was evaluated using the combined temporal and spatial characteristics of the system which were designed with this purpose in mind. Temporal precision provided highly defined PSTH plots, but these were hampered by the low spike count. Adjustments were made to account for the percentage of spikes occurring within a given time window to highlight relevant correlated activity and, in parallel, the locations of neurons were defined with high spatial accuracy. These properties were effectively combined and highlighted several units with high activity correlation which were relatively proximal, suggesting the identification of a network pathway. This analysis also exhibited the direction of signal propagation and further experiments with a higher neuron yield could provide greater detail of these network. To ensure a valid interpretation, in future perhaps a more defined structure with known pathways, such as the hippocampus, should be used to verify the applicability of this approach.

Finally, the viability of acute slices following the tissue preparation procedure were evaluated to confirm the suitability of the silicon needle heights. The methods employed produced variable results; however, it seems reasonable to suggest an area approximately 100 μm thick from slice edges was severely damaged by the protocol used in this work, suggesting the needle tips were inserted into the boundary between this damaged area and healthier tissue. It seems probable that this was a major contributor to the disappointingly low numbers of identified neurons. While electrode-tipped silicon needles have been fabricated at greater heights, future work should aim to minimise tissue damage as a priority as even at healthy depths such severe trauma would likely impact the electrophysiology of neurons.

Acknowledgments

I acknowledge and thank Dr. Keith Mathieson, who has supervised this work, and Dr. Debbie Gunning who was my original supervisor.

I also thank the valuable contributions of Dr. Niall McAlinden and Paul Hynd.

I acknowledge the laboratories of Prof. Alan Litke and John Beggs for the development of spike sorting software and acquisition system, as well as their support and advice.

I acknowledge funding from EPSRC.

Bibliography

1. Colicos, M. A. Neuronal networks and synaptic plasticity: understanding complex system dynamics by interfacing neurons with silicon technologies. *J. Exp. Biol.* **209**, 2312–2319 (2006).
2. Lein, E. S. *et al.* Genome-wide atlas of gene expression in the adult mouse brain. *Nature* **445**, 168 (2006).
3. Tasic, B. *et al.* Shared and distinct transcriptomic cell types across neocortical areas. **563**, 72–78 (2019).
4. Barzegaran, E. & Knyazeva, M. G. Functional connectivity analysis in EEG source space: The choice of method. *PLoS One* **12**, 1–16 (2017).
5. Chalovich, J. M. & Eisenberg, E. Assessing Functional Connectivity in the Human Brain by fMRI. *Magn Reson Imaging* **25**, 1347–1357 (2007).
6. Neher, E., Sakmann, B. & Steinbach, J. H. The extracellular patch clamp: A method for resolving currents through individual open channels in biological membranes. *Pflügers Arch. Eur. J. Physiol.* **375**, 219–228 (1978).
7. Mathieson, K. *et al.* Large-area microelectrode arrays for recording of neural signals. *IEEE Trans. Nucl. Sci.* **51**, 2027–2031 (2004).
8. Lewicki, M. S. A review of methods for spike sorting: the detection and classification of neural action potentials. *Network* **9**, R53–78 (1998).
9. Spira, M. E. & Hai, A. Multi-electrode array technologies for neuroscience and cardiology. *Nat. Nanotechnol.* **8**, 83–94 (2013).
10. Shoham, S., O'Connor, D. H. & Segev, R. How silent is the brain: is there a 'dark matter' problem in neuroscience? *J. Comp. Physiol. A. Neuroethol. Sens. Neural. Behav. Physiol.* **192**, 777–84 (2006).
11. Gunning, D. E. *et al.* Dense arrays of micro-needles for recording and electrical stimulation of neural activity in acute brain slices. *J. Neural Eng.* **10**, 016007 (2013).

-
12. Niell, C. & Stryker, M. Highly Selective Receptive Fields in Mouse Visual Cortex. *J. Neurosci.* **28**, 7520–7536 (2008).
 13. Hottowy, P., Dąbrowski, W., Skoczeń, A. & Wiącek, P. An integrated multichannel waveform generator for large-scale spatio-temporal stimulation of neural tissue. *Analog Integr. Circuits Signal Process.* **55**, 239–248 (2007).
 14. Litke, a. M. *et al.* What does the eye tell the brain?: Development of a system for the large-scale recording of retinal output activity. *IEEE Trans. Nucl. Sci.* **51**, 1434–1440 (2004).
 15. Gunning, D. E. *et al.* Large-Area , High-Density Arrays of Micro-Needles for Acute Slice Electrophysiology. 328–329 (2014).
 16. Weir, K., Blanquie, O., Kilb, W., Luhmann, H. J. & Sinning, A. Comparison of spike parameters from optically identified GABAergic and glutamatergic neurons in sparse cortical cultures. *Front. Cell. Neurosci.* **8**, 1–12 (2015).
 17. Isomura, T. *et al.* Signal transfer within a cultured asymmetric cortical neuron circuit. *J. Neural Eng.* **12**, 066023 (2015).
 18. Leach, J. B., Achyuta, A. K. H. & Murthy, S. K. Bridging the Divide between Neuroprosthetic Design, Tissue Engineering and Neurobiology. *Front. Neuroeng.* **2**, 18 (2010).
 19. De Vico Fallani, F., Richiardi, J., Chavez, M. & Achard, S. Graph analysis of functional brain networks: Practical issues in translational neuroscience. *Philos. Trans. R. Soc. B Biol. Sci.* **369**, (2014).
 20. Vecchio, F., Miraglia, F. & Maria Rossini, P. Connectome: Graph theory application in functional brain network architecture. *Clin. Neurophysiol. Pract.* **2**, 206–213 (2017).
 21. Poli, D., Pastore, V. P. & Massobrio, P. Functional connectivity in in vitro neuronal assemblies. *Front. Neural Circuits* **9**, 1–14 (2015).
 22. Friston, K. J. Functional and effective connectivity: a review. *Brain Connect.* **1**, 13–36 (2011).
 23. Seth, A. K., Barrett, A. B. & Barnett, L. Granger Causality Analysis in Neuroscience

-
- and Neuroimaging. *J. Neurosci.* **35**, 3293–3297 (2015).
24. Waters, J., Schaefer, A. & Sakmann, B. Backpropagating action potentials in neurones: measurement, mechanisms and potential functions. *Prog. Biophys. Mol. Biol.* **87**, 145–70 (2005).
 25. Stuart, G., Spruston, N., Sakmann, B. & Hausser, M. Action potential initiation and back propagation in neurons of the mammalian central nervous system. *Trends Neurosci.* **20**, 125–131 (1997).
 26. Gentet, L. J., Stuart, G. J. & Clements, J. D. Direct measurement of specific membrane capacitance in neurons. *Biophys. J.* **79**, 314–20 (2000).
 27. Zhao, Y. *et al.* Patch clamp technique: review of the current state of the art and potential contributions from nanoengineering. *Proc. Inst. Mech. Eng. Part N J. Nanoeng. Nanosyst.* **222**, 1–11 (2008).
 28. Alberts, B., Johnson, A., Lewis, J. *Principles of Membrane Transport.* (New York: Garland Science, 2002).
 29. Martin, B. *et al.* Class II G protein-coupled receptors and their ligands in neuronal function and protection. *Neuromolecular Med.* **7**, 3–36 (2005).
 30. Vincent, S. R. Nitric oxide neurons and neurotransmission. *Prog. Neurobiol.* **90**, 246–255 (2010).
 31. Brear, R., Rintoul, D. *Principles of Biology: 10.5 Lipids.* (OpenStax College, 2013).
 32. Blaustein, M. P. & Lederer, W. J. Sodium calcium exchange: Its physiological implications. *Physiol. Rev.* **79**, 763–854 (1999).
 33. Gadsby, D. C. Principle. *Currents* **10**, 344–352 (2010).
 34. Wright, S. H. Generation of resting membrane potential. *Adv. Physiol. Educ.* **28**, 139–142 (2004).
 35. Alvarez, | & Latorre. *The constant-field equation.*
 36. Dabrowski, K. M., Castaño, D. J. & Tartar, J. L. Basic Neuron Model Electrical Equivalent Circuit : An Undergraduate Laboratory Exercise RC Circuit :

-
- Representation of concentration RC Circuit : Representation of capacitance RC Circuit : Putting it all together RC Circuit : Representation of resistance. *J. Undergrad. Neurosci. Educ.* **12**, 49–52 (2013).
37. Hodgkin, A. L. & Huxley, A. F. A quantitative description of membrane current and its application to conduction and excitation in nerve. *Bull. Math. Biol.* **52**, 25–71 (1990).
 38. Lewis, E. R. An electronic model of neuroelectric point processes. *Kybernetik* **5**, 30–46 (1968).
 39. Harmon, L. D. Studies with artificial neurons, I: properties and functions of an artificial neuron. *Kybernetik* **1**, 89–101 (1961).
 40. Sayer, R. J., Friedlander, M. J. & Redman, S. J. The time course and amplitude of EPSPs evoked at synapses between pairs of CA3/CA1 neurons in the hippocampal slice. *J. Neurosci.* **10**, 826–836 (1990).
 41. Llinás, R., Steinberg, I. Z. & Walton, K. Relationship between presynaptic calcium current and postsynaptic potential in squid giant synapse. *Biophys. J.* **33**, 323–351 (1981).
 42. Buzsáki, G., Anastassiou, C. a & Koch, C. The origin of extracellular fields and currents--EEG, ECoG, LFP and spikes. *Nat. Rev. Neurosci.* **13**, 407–20 (2012).
 43. Magee, J. C. & Cook, E. P. Somatic EPSP amplitude is independent of synapse location in hippocampal pyramidal neurons. *Nat Neurosci* **3**, 895–903 (2000).
 44. Spruston, N., Stuart, G. & Häusser, M. Principles of Dendritic Integration. (2016).
 45. Grienberger, C. & Konnerth, A. Imaging calcium in neurons. *Neuron* **73**, 862–85 (2012).
 46. Grewe, B. F., Langer, D., Kasper, H., Kampa, B. M. & Helmchen, F. High-speed in vivo calcium imaging reveals neuronal network activity with near-millisecond precision. *Nat. Methods* (2010). doi:10.1038/nmeth.1453
 47. Mohammed, A. I. *et al.* An integrative approach for analyzing hundreds of neurons in task performing mice using wide-field calcium imaging. *Sci. Rep.* (2016). doi:10.1038/srep20986

-
48. Stuart, G. & Sakmann, B. Amplification of EPSPs by axosomatic sodium channels in neocortical pyramidal neurons. *Neuron* **15**, 1065–1076 (1995).
 49. Platkiewicz, J. & Brette, R. A threshold equation for action potential initiation. *PLoS Comput. Biol.* **6**, 25 (2010).
 50. Ritzau-jost, A. *et al.* Article Ultrafast Action Potentials Mediate Kiloherz Signaling at a Central Synapse. *Neuron* **84**, 152–163 (2014).
 51. Weiss, N. & Zamponi, G. W. Control of low-threshold exocytosis by T-type calcium channels. *Biochim. Biophys. Acta - Biomembr.* **1828**, 1579–1586 (2013).
 52. Szule, J. A. & Coorsen, J. R. Revisiting the role of SNAREs in exocytosis and membrane fusion. *Biochim. Biophys. Acta - Mol. Cell Res.* **1641**, 121–135 (2003).
 53. Duncan, J. S. Neurotransmitters, drugs and brain function. *Br. J. Clin. Pharmacol.* **53**, 648 (2002).
 54. Higgs, M. H., Romano, C. & Lukasiewicz, P. D. Presynaptic effects of group III metabotropic glutamate receptors on excitatory synaptic transmission in the retina. *Neuroscience* **115**, 163–172 (2002).
 55. Chen, L. W., Cao, R., Liu, H. L., Ju, G. & Chan, Y. S. The striatal GABA-ergic neurons expressing substance P receptors in the basal ganglia of mice. *Neuroscience* **119**, 919–925 (2003).
 56. Shu, Y., Hasenstaub, A., Duque, A., Yu, Y. & McCormick, D. a. Modulation of intracortical synaptic potentials by presynaptic somatic membrane potential. *Nature* **441**, 761–765 (2006).
 57. Ray, S. Challenges in the quantification and interpretation of spike-LFP relationships. *Curr. Opin. Neurobiol.* **31**, 111–118 (2015).
 58. Iyer, R., Menon, V., Buice, M., Koch, C. & Mihalas, S. The Influence of Synaptic Weight Distribution on Neuronal Population Dynamics. *PLoS Comput. Biol.* **9**, (2013).
 59. Perin, R., Berger, T. K. & Markram, H. A synaptic organizing principle for cortical neuronal groups. *Proc. Natl. Acad. Sci. U. S. A.* **108**, 5419–5424 (2011).

-
60. Jäckel, D. *et al.* Combination of High-density Microelectrode Array and Patch Clamp Recordings to Enable Studies of Multisynaptic Integration. *Sci. Rep.* **7**, 978 (2017).
 61. Wood, C., Williams, C. & Waldron, G. J. Patch clamping by numbers. *Drug Discov. Today* **9**, 434–441 (2004).
 62. Obien, M. E. J., Deligkaris, K., Bullmann, T., Bakkum, D. J. & Frey, U. Revealing neuronal function through microelectrode array recordings. *Front. Neurosci.* **8**, 1–30 (2015).
 63. Neher, E., Sakmann, B. Single-channel currents recorded from membrane of denervated frog muscle fibres. *Nature* **260**, 799–802 (1976).
 64. Veitinger, S. The Patch-Clamp Technique. *Leica Microsystems* (2011).
 65. Sigworth, F. J. & Neher, E. Single Na⁺ channel currents observed in cultured rat muscle cells. *Nature* **287**, 447–449 (1980).
 66. Caudle, A. S., Yang, W. T., Mittendorf, E. A. & Kuerer, H. M. HHS Public Access. **150**, 137–143 (2016).
 67. Ogden, D. & Stanfield, P. Patch clamp techniques for single channel and whole-cell recording. *Currents* **2**, 53–78 (1981).
 68. Leech, C. A. & Iv, G. G. H. Application of Patch Clamp Methods to the Study of Calcium Currents and Calcium Channels. *Methods Cell Biol.* **40**, 135–151 (1994).
 69. Mortensen, M. & Smart, T. G. Single-channel recording of ligand-gated ion channels. *Nat. Protoc.* **2**, 2826–2841 (2007).
 70. Engelhard, B., Ozeri, N., Israel, Z., Bergman, H. & Vaadia, E. Inducing Gamma Oscillations and Precise Spike Synchrony by Operant Conditioning via Brain-Machine Interface. *Neuron* **77**, 361–375 (2013).
 71. Williams, A. J., Zhou, C. & Sun, Q.-Q. Enhanced Burst-Suppression and Disruption of Local Field Potential Synchrony in a Mouse Model of Focal Cortical Dysplasia Exhibiting Spike-Wave Seizures. *Front. Neural Circuits* **10**, 1–17 (2016).
 72. Du, J., Blanche, T. J., Harrison, R. R., Lester, H. A. & Masmanidis, S. C. Multiplexed,

-
- high density electrophysiology with nanofabricated neural probes. *PLoS One* **6**, (2011).
73. Gray, C. M., Maldonado, P. E., Wilson, M. & McNaughton, B. Tetrodes markedly improve the reliability and yield of multiple single-unit isolation from multi-unit recordings in cat striate cortex. *J. Neurosci. Methods* **63**, 43–54 (1995).
74. Henze, D. a *et al.* Intracellular features predicted by extracellular recordings in the hippocampus in vivo. *J. Neurophysiol.* **84**, 390–400 (2000).
75. Buzsáki, G. Large-scale recording of neuronal ensembles. *Nat. Neurosci.* **7**, 446–51 (2004).
76. Welkenhuysen, M. *et al.* An integrated multi-electrode-optrode array for in vitro optogenetics. *Sci. Rep.* **6**, 20353 (2016).
77. Becchetti, A. *et al.* Exact distinction of excitatory and inhibitory neurons in neural networks: a study with GFP-GAD67 neurons optically and electrophysiologically recognized on multielectrode arrays. *Front. Neural Circuits* **6**, 1–11 (2012).
78. Fano, U. Ionization Yield of Radiations. II. The Fluctuations of the Number of Ions. *Phys. Rev.* **72**, 26–29 (1947).
79. Tripathy, S. J. *et al.* Large-scale analysis of brain-wide electrophysiological diversity reveals novel characterization of mammalian neuron types. *BMC Neurosci.* **16**, O4 (2015).
80. Perlmutter, J. S. & Mink, J. W. Deep Brain Stimulation. *Annu. Rev. Neurosci.* **29**, 229–257 (2015).
81. Fiscella, M. *et al.* Recording from defined populations of retinal ganglion cells using a high-density CMOS-integrated microelectrode array with real-time switchable electrode selection. *J. Neurosci. Methods* **211**, 103–113 (2012).
82. Huys, R. *et al.* A novel 16k micro-nail CMOS-chip for in-vitro single-cell recording, stimulation and impedance measurements. *2010 Annu. Int. Conf. IEEE Eng. Med. Biol. Soc. EMBC'10* 2726–2729 (2010). doi:10.1109/IEMBS.2010.5626572
83. Huys, R. *et al.* Single-cell recording and stimulation with a 16k micro-nail electrode

-
- array integrated on a 0.18 μm CMOS chip. *Lab Chip* **12**, 1274 (2012).
84. Mathieson, K. *et al.* Detection of retinal signals using position sensitive microelectrode arrays. *Nucl. Instruments Methods Phys. Res. Sect. A Accel. Spectrometers, Detect. Assoc. Equip.* **513**, 51–56 (2003).
85. Bucher, V., Brunner, B., Leibrock, C., Schubert, M. & Nisch, W. Electrical properties of a light-addressable microelectrode chip with high electrode density for extracellular stimulation and recording of excitable cells. *Biosens. Bioelectron.* **16**, 205–210 (2001).
86. Müller, J. *et al.* High-resolution CMOS MEA platform to study neurons at subcellular, cellular, and network levels. *Lab Chip* **15**, 2767–2780 (2015).
87. Van Pelt, J., Corner, M. A., Wolters, P. S., Rutten, W. L. C. & Ramakers, G. J. A. Longterm stability and developmental changes in spontaneous network burst firing patterns in dissociated rat cerebral cortex cell cultures on multielectrode arrays. *Neurosci. Lett.* **361**, 86–89 (2004).
88. Srinivas, K. V., Jain, R., Saurav, S. & Sikdar, S. K. Small-world network topology of hippocampal neuronal network is lost, in an in vitro glutamate injury model of epilepsy. *Eur. J. Neurosci.* **25**, 3276–3286 (2007).
89. Law, J. K. Y. *et al.* The use of microelectrode array (MEA) to study the protective effects of potassium channel openers on metabolically compromised HL-1 cardiomyocytes. *Physiol. Meas.* **30**, 155–167 (2009).
90. Aregueta-Robles, U. a, Woolley, A. J., Poole-Warren, L. a, Lovell, N. H. & Green, R. a. Organic electrode coatings for next-generation neural interfaces. *Front. Neuroeng.* **7**, 15 (2014).
91. Yúfera, A., Olmo, A., Daza, P. & Cañete, D. Cell Biometrics Based on Bio-Impedance Measurements. (2011). doi:10.5772/21742
92. Franks, W., Schenker, I., Schmutz, P. & Hierlemann, A. Impedance Characterization and Modeling of Electrodes for Biomedical Applications. (2005). doi:10.1109/TBME.2005.847523

-
93. Geddes, L. A. & Roeder, R. Criteria for the selection of materials for implanted electrodes. *Ann. Biomed. Eng.* **31**, 879–890 (2003).
 94. Merrill, D. R., Bikson, M. & Jefferys, J. G. R. Electrical stimulation of excitable tissue: Design of efficacious and safe protocols. *J. Neurosci. Methods* **141**, 171–198 (2005).
 95. Wheeler, B. C. & Nam, Y. In Vitro Microelectrode Array Technology and Neural Recordings. *Crit. Rev. Biomed. Eng.* **39**, 45–61 (2011).
 96. Ito, S. *et al.* Large-Scale, High-Resolution Multielectrode-Array Recording Depicts Functional Network Differences of Cortical and Hippocampal Cultures. *PLoS One* **9**, e105324 (2014).
 97. Joye, N., Lavagnino, M., Schmid, A. & Leblebici, Y. Three-dimensional Tip Electrode Array Technology for High Resolution Neuro-Electronic Systems used in Electrophysiological Experiments. *IEEE Int. Conf. Nano/Molecular Med. Eng.* 2–5 (2007).
 98. Friede, R. L. The relationship of body size, nerve cell size, axon length, and glial density in the cerebellum. *Proc. Natl. Acad. Sci. USA* **49**, 187–193 (1963).
 99. Low, L. K. & Cheng, H.-J. Axon pruning: an essential step underlying the developmental plasticity of neuronal connections. *Philos. Trans. R. Soc. Lond. B. Biol. Sci.* **361**, 1531–44 (2006).
 100. Lossi, L., Alasia, S., Salio, C. & Merighi, A. Cell death and proliferation in acute slices and organotypic cultures of mammalian CNS. *Prog. Neurobiol.* **88**, 221–245 (2009).
 101. Weise, J., Isenmann, S. & Bähr, M. Increased expression and activation of poly(ADP-ribose) polymerase (PARP) contribute to retinal ganglion cell death following rat optic nerve transection. *Cell Death Differ.* **8**, 801–7 (2001).
 102. Wang, J. T., Medress, Z. A. & Barres, B. A. Axon degeneration: Molecular mechanisms of a self-destruction pathway. *J. Cell Biol.* **196**, 7–18 (2012).
 103. Kerschensteiner, M., Schwab, M. E., Lichtman, J. W. & Misgeld, T. In vivo imaging of axonal degeneration and regeneration in the injured spinal cord. *Nat. Med.* **11**, 572–577 (2005).

-
104. Knöferle, J. *et al.* Mechanisms of acute axonal degeneration in the optic nerve in vivo. *Proc. Natl. Acad. Sci. U. S. A.* **107**, 6064–9 (2010).
 105. Mandolesi, G., Madeddu, F., Bozzi, Y., Maffei, L. & Ratto, G. M. Acute physiological response of mammalian central neurons to axotomy: ionic regulation and electrical activity. *FASEB J.* **18**, 1934–6 (2004).
 106. Egert, U., Heck, D. & Aertsen, A. Two-dimensional monitoring of spiking networks in acute brain slices. *Exp. Brain Res.* **142**, 268–274 (2002).
 107. Yger, P., Spampinato, G. L. B. & Esposito, E. Fast and accurate spike sorting in vitro and in vivo for up to thousands of electrodes. *bioRxiv* 1–21 (2016).
doi:10.1101/067843
 108. Leibig, C., Wachtler, T. & Zeck, G. Unsupervised neural spike sorting for high-density microelectrode arrays with convolutive independent component analysis. *J. Neurosci. Methods* **271**, 1–13 (2016).
 109. Quiroga, R. Q., Nadasdy, Z. & Ben-Shaul, Y. Unsupervised spike detection and sorting with wavelets and superparamagnetic clustering. *Neural Comput.* **16**, 1661–1687 (2004).
 110. Clarkson, B. D. S., Kahoud, R. J., McCarthy, C. B. & Howe, C. L. Inflammatory cytokine-induced changes in neural network activity measured by waveform analysis of high-content calcium imaging in murine cortical neurons. *Sci. Rep.* **7**, 1–13 (2017).
 111. Greer, J. E., Povlishock, J. T. & Jacobs, K. M. Electrophysiological Abnormalities in Both Axotomized and Nonaxotomized Pyramidal Neurons following Mild Traumatic Brain Injury. **32**, 6682–6687 (2012).
 112. Rey, H. G., Pedreira, C. & Quiroga, R. Past, present and future of spike sorting techniques. *Brain Res. Bull.* **119**, 106–117 (2015).
 113. Nigam, S. *et al.* Systems/Circuits Rich-Club Organization in Effective Connectivity among Cortical Neurons. *@BULLET J. Neurosci.* **36**, 670–684 (2016).
 114. Roebroek, A., Formisano, E. & Goebel, R. The identification of interacting networks in the brain using fMRI: Model selection, causality and deconvolution. *Neuroimage*

-
- 58, 296–302 (2011).
115. Massobrio, P., Tessadori, J., Chiappalone, M. & Ghirardi, M. In Vitro Studies of Neuronal Networks and Synaptic Plasticity in Invertebrates and in Mammals Using Multielectrode Arrays. *Neural Plast.* **2015**, 1–18 (2015).
 116. Yague, J. G., Tsunematsu, T. & Sakata, S. Distinct Temporal Coordination of Spontaneous Population Activity between Basal Forebrain and Auditory Cortex. *Front. Neural Circuits* **11**, 1–14 (2017).
 117. Broido, A. D. & Clauset, A. Scale-free networks are rare. *Nat. Commun.* 1–10 doi:10.1038/s41467-019-08746-5
 118. Sporns, O., Honey, C.J., Kotter, R. Identification and Classification of Hubs in Brain Networks. *PLoS One* **2(10): e10**, (2007).
 119. Cunningham, W. *et al.* Fabrication of microelectrode arrays for. *J. Phys. D Appl. Phys.* **34**, 2804–2809 (2001).
 120. Sher, A. *et al.* Large-scale multielectrode recording and stimulation of neural activity. **579**, 895–900 (2007).
 121. Viswam, V., Obien, M. E. J., Franke, F. & Frey, U. Optimal Electrode Size for Recording From Neuronal Assemblies. **13**, 1–23 (2019).
 122. Dabrowski, W. *et al.* Development of integrated circuits for readout of microelectrode arrays to image neuronal activity in live retinal tissue. *2003 IEEE Nucl. Sci. Symp. Conf. Rec. (IEEE Cat. No.03CH37515)* **2**, 956–960 (2003).
 123. Ilic, B. *et al.* Preparation and characterization of platinum black electrodes. *J. Mater. Sci.* **35**, 3447–3457 (2000).
 124. Hottowy, P. *et al.* 512-electrode MEA System For Spatio-Temporal Distributed Stimulation and Recording of Neural Activity. 327–330 (2010).
 125. Rydygier, P., Fiutowski, T. & Dąbrowski, W. Design of a Low Noise , Low Power , High Dynamic Range Amplifier-Filter Circuit for Recording Neural Signals Using Multielectrode Arrays. *Mix. Des. Integr. Circuits Syst. 2009. Mix. '09. Mix. Int. Conf.* 242–247 (2009).

-
126. Viswam, V., Obien, M., Frey, U., Franke, F. & Hierlemann, A. Acquisition of Bioelectrical Signals with Small Electrodes. 1–4 (2018).
doi:10.1109/BIOCAS.2017.8325216.Acquisition
 127. Agmon, A. & Connors, B. W. Thalamocortical responses of mouse somatosensory (barrel) cortex in vitro. *Neuroscience* **41**, 365–379 (1991).
 128. Chen, W., Hobbs, J. P., Tang, A. & Beggs, J. M. A few strong connections: Optimizing information retention in neuronal avalanches. *BMC Neurosci.* **11**, (2010).
 129. Stratton, P. *et al.* Action potential waveform variability limits multi-unit separation in freely behaving rats. *PLoS One* **7**, (2012).
 130. Buskila, Y. *et al.* Extending the viability of acute brain slices. *Sci. Rep.* **4**, 5309 (2014).
 131. Fukuda, A. *et al.* Appearance of deteriorated neurons on regionally different time tables in rat brain thin slices maintained in physiological condition. *Neurosci. Lett.* **184**, 13–16 (1995).
 132. Kaneoke, Y. & Vitek, J. L. Burst and oscillation as disparate neuronal properties. *J. Neurosci. Methods* **68**, 211–23 (1996).
 133. Bakkum, D. J. *et al.* Parameters for burst detection. *Front. Comput. Neurosci.* **7**, 193 (2013).
 134. Izhikevich, E. M., Desai, N. S., Walcott, E. C. & Hoppensteadt, F. C. Bursts as a unit of neural information: selective communication via resonance. *Trends Neurosci.* **26**, 161–7 (2003).
 135. Chen, L., Deng, Y., Luo, W., Wang, Z. & Zeng, S. Detection of bursts in neuronal spike trains by the mean inter-spike interval method. *Prog. Nat. Sci.* **19**, 229–235 (2009).
 136. Turnbull, L., Dian, E. & Gross, G. The string method of burst identification in neuronal spike trains. *J. Neurosci. Methods* **145**, 23–35 (2005).
 137. Karoly, P. J. *et al.* Bursts of seizures in long-term recordings of human focal epilepsy. **58**, 363–372 (2018).
 138. Pfeiffer, M., Hartbauer, M., Lang, A. B., Maass, W. & Römer, H. Probing real sensory

-
- worlds of receivers with unsupervised clustering. *PLoS One* **7**, (2012).
139. Cotterill, E., Charlesworth, P., Thomas, C. W., Paulsen, O. & Eglen, S. J. A comparison of computational methods for detecting bursts in neuronal spike trains and their application to human stem cell-derived neuronal networks. *J. Neurophysiol.* **116**, 306–321 (2016).
 140. Kapucu, F. E. *et al.* Burst analysis tool for developing neuronal networks exhibiting highly varying action potential dynamics. *Front. Comput. Neurosci.* **6**, 38 (2012).
 141. Buzsáki, G. & Chrobak, J. J. Temporal structure in spatially organized neuronal ensembles: a role for interneuronal networks. *Curr. Opin. Neurobiol.* **5**, 504–510 (1995).
 142. Pouille, F. & Scanziani, M. Enforcement of Temporal Fidelity in Pyramidal Cells by Somatic Feed-Forward Inhibition. *Science (80-.)*. **293**, 1159 LP – 1163 (2001).
 143. Csicsvari, J., Hirase, H., Czurkó, a, Mamiya, a & Buzsáki, G. Oscillatory coupling of hippocampal pyramidal cells and interneurons in the behaving Rat. *J. Neurosci.* **19**, 274–287 (1999).
 144. Rudy, Bernardo; Fishell, Gordon; Lee, SooHyun; Hjerling-Leffler, J. Three Groups of Interneurons Account for Nearly 100% of Neocortical GABAergic Neurons. *Dev Neurobiol* **31**, 1713–1723 (2011).
 145. Kepecs, A. & Fishell, G. Interneuron Cell Types: Fit to form and formed to fit. *Nature* **505**, 318–326 (2014).
 146. Bean, B. P. The action potential in mammalian central neurons. *Nat. Rev. Neurosci.* **8**, 451 (2007).
 147. Peyrache, A. *et al.* Spatiotemporal dynamics of neocortical excitation and inhibition during human sleep. *Proc. Natl. Acad. Sci.* **109**, 1731–1736 (2012).
 148. Bartho, P. Characterization of Neocortical Principal Cells and Interneurons by Network Interactions and Extracellular Features. *J. Neurophysiol.* **92**, 600–608 (2004).
 149. Oswald, A.-M. M., Doiron, B. & Maler, L. Interval coding. I. Burst interspike intervals

-
- as indicators of stimulus intensity. *J. Neurophysiol.* **97**, 2731–43 (2007).
150. Bakkum, D. J. *et al.* Tracking axonal action potential propagation on a high-density microelectrode array across hundreds of sites. *Nat. Commun.* **4**, 2181 (2013).
 151. Gullo, F. *et al.* Atypical seizure-like activity in cortical reverberating networks in vitro can be caused by LPS-induced inflammation: a multi-electrode array study from a hundred neurons. *Front. Cell. Neurosci.* **8**, 1–18 (2014).
 152. Grover, L. M., Kim, E., Cooke, J. D. & Holmes, W. R. LTP in hippocampal area CA1 is induced by burst stimulation over a broad frequency range centered around delta. *Learn. Mem.* **16**, 69–81 (2009).
 153. T., S. S., Kristiina, H., Juha, V. & Kai, K. Intrinsic bursting of immature CA3 pyramidal neurons and consequent giant depolarizing potentials are driven by a persistent Na⁺ current and terminated by a slow Ca²⁺-activated K⁺ current. *Eur. J. Neurosci.* **23**, 2330–2338 (2006).
 154. Holt, G. R. & Douglas, J. Comparison of Discharge Variability Visual Cortex Neurons In Vitro and In Vivo in Cat C y C 7. *J. Neurophysiol.* **75**, 1806–1814 (1996).
 155. Eisenman, L. N., Emmett, C. M., Mohan, J., Zorumski, C. F. & Mennerick, S. Quantification of bursting and synchrony in cultured hippocampal neurons. *J. Neurophysiol.* **114**, 1059–1071 (2015).
 156. Bisio, M., Bosca, A., Pasquale, V., Berdondini, L. & Chiappalone, M. Emergence of bursting activity in connected neuronal sub-populations. *PLoS One* **9**, (2014).
 157. Capocchi, G., Zampolini, M. & Larson, J. Theta burst stimulation is optimal for induction of LTP at both apical and basal dendritic synapses on hippocampal CA1 neurons. *Brain Res.* **591**, 332–336 (1992).
 158. Mitchell, M. J. & King, M. R. NIH Public Access. **3**, 1–23 (2014).
 159. Disterhoft, J. F., Wu, W. W. & Ohno, M. Biophysical alterations of hippocampal pyramidal neurons in learning, ageing and Alzheimer's disease. *Ageing Res. Rev.* **3**, 383–406 (2004).
 160. Grieve, K. L., Rivadulla, C. & Cudeiro, J. Mixed burst and tonic firing in the thalamus:

-
- a study in the feline lateral geniculate nucleus in vivo. *Brain Res.* **1273**, 48–57 (2009).
161. Dégenétais, E., Thierry, A.-M., Glowinski, J. & Gioanni, Y. Electrophysiological properties of pyramidal neurons in the rat prefrontal cortex: an in vivo intracellular recording study. *Cereb. Cortex* **12**, 1–16 (2002).
162. Connors, B. W. & Gutnick, M. J. Intrinsic firing patterns of diverse neocortical neurons. *Trends Neurosci.* **13**, 99–104 (1990).
163. Erisir, A., Lau, D., Rudy, B. & Leonard, C. S. *Function of Specific K Channels in Sustained High-Frequency Firing of Fast-Spiking Neocortical Interneurons.* (1999).
164. Colbert, C. M. & Pan, E. Ion channel properties underlying axonal action potential initiation in pyramidal neurons. *Nat. Neurosci.* **5**, 533–8 (2002).
165. Silver, R. A. Neuronal arithmetic. *Nat. Rev. Neurosci.* **11**, 474–489 (2010).
166. Connors, B., Gutnick, M. & Prince, D. Electrophysiological properties of neocortical neurons in vitro. *J. Neurophysiol.* **48**, 1302–1320 (1982).
167. Jensen, M. S., Azouz, R. & Yaari, Y. Spike after-depolarization and burst generation in adult rat hippocampal CA1 pyramidal cells. *J. Physiol.* (1996).
doi:10.1113/jphysiol.1996.sp021301
168. Bruno, R. M. & Simons, D. J. Feedforward mechanisms of excitatory and inhibitory cortical receptive fields. *J Neurosci* **22**, 10966–10975 (2002).
169. Simons, D. J., Carvell, G. E. & Kyriazi, H. T. Alterations in functional thalamocortical connectivity following neonatal whisker trimming with adult regrowth. *J. Neurophysiol.* **114**, 1912–1922 (2015).
170. Atencio, C. A. & Schreiner, C. E. Spectrotemporal Processing Differences between Auditory Cortical Fast-Spiking and Regular-Spiking Neurons. *J. Neurosci.* (2008).
doi:10.1523/JNEUROSCI.5366-07.2008
171. Sahara, s., Yanagawa, Y., O’Leary, D.D.M., Stevens, C. F. The fraction of cortical GABAergic neurons is constant from near the start of cortical neurogenesis to adulthood. *J. Neurosci.* **31**, 1713–1723 (2013).

-
172. Eggermont, J. J. Is there a neural code? *Neurosci. Biobehav. Rev.* **22**, 355–70 (1998).
 173. Tien, N.-W. & Kerschensteiner, D. Homeostatic plasticity in neural development. *Neural Dev.* **13**, 9 (2018).
 174. Oberman, L. & Pascual-Leone, A. Changes in plasticity across the lifespan: Cause of disease and target for intervention. *Prog. Brain Res.* **207**, 91–120 (2013).
 175. Hoffmann, J. H. O. *et al.* Synaptic conductance estimates of the connection between local inhibitor interneurons and pyramidal neurons in layer 2/3 of a cortical column. *Cereb. Cortex* **25**, 4415–4429 (2015).
 176. Kerr, J. N. D., Greenberg, D. & Helmchen, F. From The Cover: Imaging input and output of neocortical networks in vivo. *Proc. Natl. Acad. Sci.* **102**, 14063–14068 (2005).
 177. Fournier, E., Meunier, S., Pierrot-Deseilligny, E. & Shindo, M. Evidence for interneuronally mediated Ia excitatory effects to human quadriceps motoneurons. *J. Physiol.* **377**, 143–169 (1986).
 178. Kremkow, J., Dornn, A. L. & Poulet, J. F. A. In Vivo Monosynaptic Excitatory Transmission between Layer 2 Cortical Pyramidal Neurons Report In Vivo Monosynaptic Excitatory Transmission between Layer 2 Cortical Pyramidal Neurons. 2098–2106 (2015). doi:10.1016/j.celrep.2015.11.011
 179. Barry, J. M. Axonal Activity in vivo: Technical considerations and implications for the exploration of neural circuits in freely moving animals. *Front. Neurosci.* **9**, 1–12 (2015).
 180. Heuschkel, M. O., Fejtli, M., Raggenbass, M., Bertrand, D. & Renaud, P. A three-dimensional multi-electrode array for multi-site stimulation and recording in acute brain slices. *J. Neurosci. Methods* **114**, 135–148 (2002).
 181. Thivierge, J. P. Scale-free and economical features of functional connectivity in neuronal networks. *Phys. Rev. E - Stat. Nonlinear, Soft Matter Phys.* **90**, 1–8 (2014).
 182. Franke, F. *et al.* High-density microelectrode array recordings and real-time spike sorting for closed-loop experiments: an emerging technology to study neural

-
- plasticity. *Front. Neural Circuits* **6**, 105 (2012).
183. Gladkov, A. *et al.* Design of Cultured Neuron Networks in vitro with Predefined Connectivity Using Asymmetric Microfluidic Channels. *Sci. Rep.* **7**, 1–14 (2017).
184. Sophie, R. *et al.* Neuronal Architectures with Axo-dendritic Polarity above Silicon Nanowires. *Small* **8**, 671–675 (2012).
185. Taylor, A. M. *et al.* A microfluidic culture platform for CNS axonal injury, regeneration and transport. *Nat. Methods* **2**, 599–605 (2005).
186. Ullo, S. *et al.* Functional connectivity estimation over large networks at cellular resolution based on electrophysiological recordings and structural prior. *Front. Neuroanat.* **8**, 137 (2014).
187. Egert, U. *et al.* A novel organotypic long-term culture of the rat hippocampus on substrate-integrated multielectrode arrays. *Brain Res. Protoc.* **2**, 229–242 (1998).
188. Opitz-Araya, X. & Barria, A. Organotypic Hippocampal Slice Cultures. *J. Vis. Exp.* 2462 (2011). doi:10.3791/2462
189. Schjetnan, A. G. P. & Luczak, A. Recording Large-scale Neuronal Ensembles with Silicon Probes in the Anesthetized Rat. *J. Vis. Exp.* 3282 (2011). doi:10.3791/3282
190. Feldmeyer, D., Joachim, L. & Sakmann, B. Efficacy and connectivity of intracolumnar pairs of layer 2 / 3 pyramidal cells in the barrel cortex of juvenile rats. **2**, 583–602 (2006).
191. Geiger, J. R. P. *et al.* Patch-clamp recording in brain slices with improved slicer technology. *Pflugers Arch. Eur. J. Physiol.* **443**, 491–501 (2002).
192. Zhao, S. Ting, J.T., Atallah, H.E., Qiu, L., Tan, J, Gloss, B. Cell-type Specific Optogenetic Mice for Dissecting Neural Circuitry Function. *Nat. Methods* **8**, 745–752 (2011).
193. Ting, J. T. *et al.* Preparation of Acute Brain Slices Using an Optimized N -Methyl-D-glucamine Protective Recovery Method. 1–13 (2018). doi:10.3791/53825
194. J.T.Ting, T.L.Daigle, Q. Chen, G. F. Acute brain slice methods for adult and aging

-
- animals: application of targeted patch clamp analysis and optogenetics. **1183**, 1–21 (2014).
195. Eguchi, K., Velicky, P., Hollergschwandtner, E. & Itakura, M. Advantages of acute brain slices prepared at physiological temperature in characterization of synaptic functions.
196. Kim, S. *et al.* Disparate roles of zinc in chemical hypoxia-induced neuronal death. *Front. Cell. Neurosci.* **9**, 1–9 (2015).
197. Ke, M.-T. & Imai, T. Optical clearing of fixed brain samples using SeeDB. *Curr. Protoc. Neurosci.* **66**, Unit 2.22. (2014).
198. Tsai, P. S. *et al.* Correlations of neuronal and microvascular densities in murine cortex revealed by direct counting and colocalization of nuclei and vessels. **29**,
199. Kim, S.-Y., Chung, K. & Deisseroth, K. Light microscopy mapping of connections in the intact brain. *Trends Cogn. Sci.* **17**, 596–9 (2013).
200. Boutin, M. E. & Hoffman-Kim, D. Application and Assessment of Optical Clearing Methods for Imaging of Tissue-Engineered Neural Stem Cell Spheres. *Tissue Eng. Part C Methods* **21**, 292–302 (2015).
201. Kuwajima, T. *et al.* ClearT: a detergent- and solvent-free clearing method for neuronal and non-neuronal tissue. *Development* **140**, 1364–8 (2013).
202. Ke, M.-T., Fujimoto, S. & Imai, T. SeeDB: a simple and morphology-preserving optical clearing agent for neuronal circuit reconstruction. *Nat. Neurosci.* **16**, 1154 (2013).
203. Brana, C., Benham, C. & Sundstrom, L. A method for characterising cell death in vitro by combining propidium iodide staining with immunohistochemistry. *Brain Res. Protoc.* **10**, 109–114 (2002).
204. Koley, D. & Bard, A. J. Triton X-100 concentration effects on membrane permeability of a single HeLa cell by scanning electrochemical microscopy (SECM). *Proc. Natl. Acad. Sci.* **107**, 16783–16787 (2010).
205. Huang, S. & Uusisaari, M. Y. Physiological temperature during brain slicing enhances the quality of acute slice preparations. *Front. Cell. Neurosci.* **7**, 48 (2013).

-
206. Ankri, L., Yarom, Y. & Uusisaari, M. Y. Slice it hot: acute adult brain slicing in physiological temperature. *J. Vis. Exp.* e52068 (2014). doi:10.3791/52068
 207. Rasia-Filho, A., Brusco, J., Rocha, L. & Moreira, J. Dendritic spines observed by extracellular Dil dye and immunolabeling under confocal microscopy. (2010).
 208. Jun, J. J. *et al.* Fully integrated silicon probes for high-density recording of neural activity. *Nature* (2017). doi:10.1038/nature24636
 209. McAlinden, N., Gu, E., Dawson, M. D., Sakata, S. & Mathieson, K. Optogenetic activation of neocortical neurons in vivo with a sapphire-based micro-scale LED probe. *Front. Neural Circuits* (2015). doi:10.3389/fncir.2015.00025
 210. Cheng, C., Trzcinski, O. & Doering, L. C. Fluorescent labeling of dendritic spines in cell cultures with the carbocyanine dye Dil; *Front. Neuroanat.* (2014). doi:10.3389/fnana.2014.00030
 211. Haber, M. Cooperative Astrocyte and Dendritic Spine Dynamics at Hippocampal Excitatory Synapses. *J. Neurosci.* (2006). doi:10.1523/JNEUROSCI.1302-06.2006
 212. Moy, A. J., Wiersma, M. P. & Choi, B. Optical histology: a method to visualize microvasculature in thick tissue sections of mouse brain. *PLoS One* **8**, e53753 (2013).
 213. Papouin, T. & Haydon, P. G. Obtaining Acute Brain Slices. doi:10.21769/BioProtoc.2102
 214. Wan, P., Zhu, J., Yu, T. & Zhu, D. Comparison of seven optical clearing methods for mouse brain . in **10481**, 104811I-10481–7 (2018).
 215. Yu, T. *et al.* RTF: A rapid and versatile tissue optical clearing method. *Sci. Rep.* **8**, 1–9 (2018).
 216. Wozny, C. & Williams, S. R. Specificity of Synaptic Connectivity between Layer 1 Inhibitory Interneurons and Layer 2 / 3 Pyramidal Neurons in the Rat Neocortex. (2011). doi:10.1093/cercor/bhq257
 217. Lefort, S., Tómm, C., Sarria, J. F. & Petersen, C. C. H. Article The Excitatory Neuronal Network of the C2 Barrel Column in Mouse Primary Somatosensory Cortex. *Neuron* **61**, 301–316 (2009).

-
218. Agrawal, S. K. & Fehlings, M. G. Mechanisms of secondary injury to spinal cord axons in vitro: role of Na⁺, Na⁽⁺⁾-K⁽⁺⁾-ATPase, the Na⁽⁺⁾-H⁺ exchanger, and the Na⁽⁺⁾-Ca²⁺ exchanger. *J. Neurosci.* **16**, 545–52 (1996).
 219. Macklis, J. D. & Hospital, C. Progressive incorporation of propidium iodide in cultured mouse neurons correlates with declining electrophysiological status : a fluorescence scale of membrane integrity. **31**, 43–46 (1990).
 220. Pollice, A. A. *et al.* Sequential Paraformaldehyde and Methanol Fixation for Simultaneous Flow Cytometric Analysis of DNA , Cell Surface Proteins , and Intracellular Proteins '. **444**, 432–444 (1992).
 221. Van Hooijdonk, C. A. E. M., Glade, C. P. & Van Erp, P. E. J. TO-PRO-3 iodide: A novel HeNe laser-excitable DNA stain as an alternative for propidium iodide in multiparameter flow cytometry. *Cytometry* **17**, 185–189 (1994).
 222. Grizzle, W. E. Models of Fixation and Tissue Processing. *Biotech Histochem.* **84**, 185–193 (2009).
 223. Ferrea, E. *et al.* Large-scale, high-resolution electrophysiological imaging of field potentials in brain slices with microelectronic multielectrode arrays. *Front. Neural Circuits* **6**, 80 (2012).
 224. Sullivan, B. L., Leu, D., Taylor, D. M., Fahlman, C. S. & Bickler, P. E. Isoflurane prevents delayed cell death in an organotypic slice culture model of cerebral ischemia. *Anesthesiology* **96**, 189–95 (2002).
 225. Xinhua Zhan, Christian S. Fahlman, P. E. B. Isoflurane Neuroprotection in Rat Hippocampal Slices Decreases with Aging. *Anesthesiology* 995–1003 (2006).
 226. Staal, J. a., Alexander, S. R., Liu, Y., Dickson, T. D. & Vickers, J. C. Characterization of cortical neuronal and glial alterations during culture of organotypic whole brain slices from neonatal and mature mice. *PLoS One* **6**, (2011).
 227. Pennartz, C. M., De Jeu, M. T., Geurtsen, a M., Sluiter, a a & Hermes, M. L. Electrophysiological and morphological heterogeneity of neurons in slices of rat suprachiasmatic nucleus. *J. Physiol.* **506 (Pt 3)**, 775–93 (1998).

-
228. Chen, B. K. *et al.* Optimizing conditions and avoiding pitfalls for prolonged axonal tracing with carbocyanine dyes in fixed rat spinal cords. *J. Neurosci. Methods* **154**, 256–263 (2006).
229. Kim, B. G., Dai, H. N., McAtee, M., Vicini, S. & Bregman, B. S. Labeling of dendritic spines with the carbocyanine dye Dil for confocal microscopic imaging in lightly fixed cortical slices. *J. Neurosci. Methods* (2007). doi:10.1016/j.jneumeth.2007.01.016
230. Staffend, N. A. & Meisel, R. L. Diolistic labeling in fixed brain slices: Phenotype, morphology, and dendritic spines. *Curr. Protoc. Neurosci.* (2011). doi:10.1002/0471142301.ns0213s55

Appendices

Appendix 1. Photolithographic process

The MEa presented in this work is made using a novel combination of photolithographic techniques¹¹ and the process is outlined in the steps below:

(i) DRIE etch silicon. The first step in the fabrication process is to etch arrays of 61 hexagonally close packed, high in to a 4-inch diameter, 350 μm thick silicon wafer. On aspect ratio (11:1), tapered holes to a depth of ~ 300 μm to this wafer, ten devices are fitted. Following a combined pre-bake at 150 $^{\circ}\text{C}$ (to remove moisture) and an HMDS (hexamethyldisilazane) prime (to improve adhesion of photoresist to the wafer), SPR220-7 photoresist is spun to a thickness of 7 μm , and baked on a hotplate at 90 $^{\circ}\text{C}$ for 200 s. Standard UV contact photolithography (using developer MF-26A) is used to pattern the photoresist in to arrays of holes, each having a 25 μm diameter. This patterned mask is hardened by oven baking for 1 h at 120 $^{\circ}\text{C}$. The holes are etched using a STS ICP (inductively coupled plasma) deep reactive ion etcher, which switches between CH_4 passivation and SF_6 etch steps to achieve the required etch profile (Bosch process). This profile defines the shape of the needle.

(ii) Thermal oxidation and metallization. A 2 μm thick silicon dioxide layer is thermally grown at 1050 $^{\circ}\text{C}$ to form a high-quality, uniform sidewall insulation. The tapered point at the base of the etched hole will eventually be the conducting tip of the needle making it important to have a conformal metal coating. To this end, 400 nm of LPCVD (low pressure chemical vapour deposition) tungsten (W) is deposited. Prior to the tungsten deposition, a titanium layer (50 nm) was sputtered to promote tungsten adhesion to the thermal silicon dioxide.

(iii) Readout lithography. The tungsten layer is patterned using a pre-bake and HMDS prime followed by spinning Shipley 3612 photoresist to a thickness of 1.6 μm . The photoresist is oven baked at 90 $^{\circ}\text{C}$ for 30 min before UV exposure and oven baked at 120 $^{\circ}\text{C}$ for 60 min after developing. Photoresist spun over the perforated surface of the silicon wafer is always spun relatively thin. It is baked in an oven rather than a hotplate since lower gradient temperature ramping avoids resist bubbling over the etched holes. This resist layer is used as standard for all of the remaining photolithography steps in this process. An SF_6 reactive-ion etch removes the exposed tungsten, electrically isolating each electrode.

(iv) Polysilicon deposition. For mechanical strength, 4 μm of LPCVD polysilicon is deposited and patterned to fill, or at least partially fill, the holes. A 1.6 μm photoresist mask and an SF_6 etch with 10% oxygen are used respectively to mask and etch the polysilicon. This exposes the tungsten readout for electrical contact in the next step. These first steps have essentially embedded arrays of conducting needles in to the wafer.

(v) Aluminium (Al) deposition and patterning. A short argon etch removes a few nanometres of surface material preparing the wafer surface for a 1 μm layer of sputter deposited aluminium, which makes electrical contact with the exposed tungsten. Sputtered aluminium is a well-established, reliable contact for wire bonding (which is used to connect the array to the readout electronics at a later stage). The aluminium is patterned using a 1.6 μm photoresist mask and a Al-11 chemical wet etch (pre-mixed phosphoric, acetic and nitric acid in water) heated to 40 $^{\circ}\text{C}$. The combination of tungsten and aluminium form an electrical connection between the tungsten tip of each needle (the electrode) and an aluminium bond pad.

(vi) Silicon nitride deposition and patterning. The aluminium/ tungsten tracks are protected with a 500 nm layer of low temperature (350 $^{\circ}\text{C}$) PECVD (plasma enhanced chemical vapour deposition) silicon nitride. The following steps are not shown in figure 1. To expose the aluminium bond pads, the silicon nitride is selectively etched (RIE) using SF₆ and 10% oxygen. The wafer is then diced to release individual devices.

(vii) Silicon and tip oxide etch. Two etch masks, one on each side of the device, are required before etching hundreds of microns of bulk silicon to expose the array of needles. In this process, the bulk silicon will ultimately be etched strength around the needles). To retain the mechanical to leave ~ 100 μm thickness (this provides mechanical strength of the device, a frame around the edge of the device is protected with a mask of silicon dioxide. On the backside (with holes and readout) of each device, Protek B3, an etch mask resistive to wet chemical base etches is spin-coated. A 25% concentration TMAH (tetra methyl ammonium hydroxide in water) solution, heated to 95 $^{\circ}\text{C}$, is used to remove enough of the bulk silicon to expose the oxide-coated needles. The silicon etch rate is ~ 0.9 μmmin^{-1} and so thin (325–350 μm) silicon wafers are used to avoid long etch times. The slow etch rate is beneficial for accurately defining the length of the needle and, in particular, the conductive tip. At some point during the silicon etching, the arrays of oxide-coated needles will begin to appear. When the desired length of tip (length of needle needed to be conducting) is exposed from the silicon, the device is removed from the TMAH and rinsed thoroughly in water. Using dilute (5%) buffered hydrofluoric acid, as much as 75% of the tip oxide thickness is etched. It is critical that a thin layer of oxide remains at the tip and no tungsten is exposed.

(viii) Final silicon and tip oxide etch. The silicon etch is continued to expose the required length of the needle electrode, leaving a few tens of microns of silicon as the support substrate. A 2% concentration of hydrofluoric acid (which is selective to tungsten) is used to remove the remaining oxide from the tip, exposing a small tungsten electrode. The protective Protek is removed in acetone followed by a low-power oxygen plasma clean. The silicon chip is glued to a support piece of silicon or glass (for strength) and is wire-bonded to a PCB making it compatible with the existing readout system.

Appendix 2. Measuring MEA impedances

Impedances before and after platinisation were measured prior to integrating the MEA into the neuroboard

- 1) Before inverting the MEA, the chamber was filled with saline or platinisation solution, for either impedance measurements or platinisation procedures.
- 2) To ensure electrodes remained in contact with the solution following inversion a 3D-printed lid was secured to the top of the recording chamber
- 3) The MEA was then inverted and secured in a custom-made plastic holder which prevented the substrate from moving. The holder was designed to precisely fit the chamber to prevent any movement (not shown).
- 4) Electrode readouts could then be accessed with and impedance probes applied to characterise electrical properties of the array (see Image. 8.1)

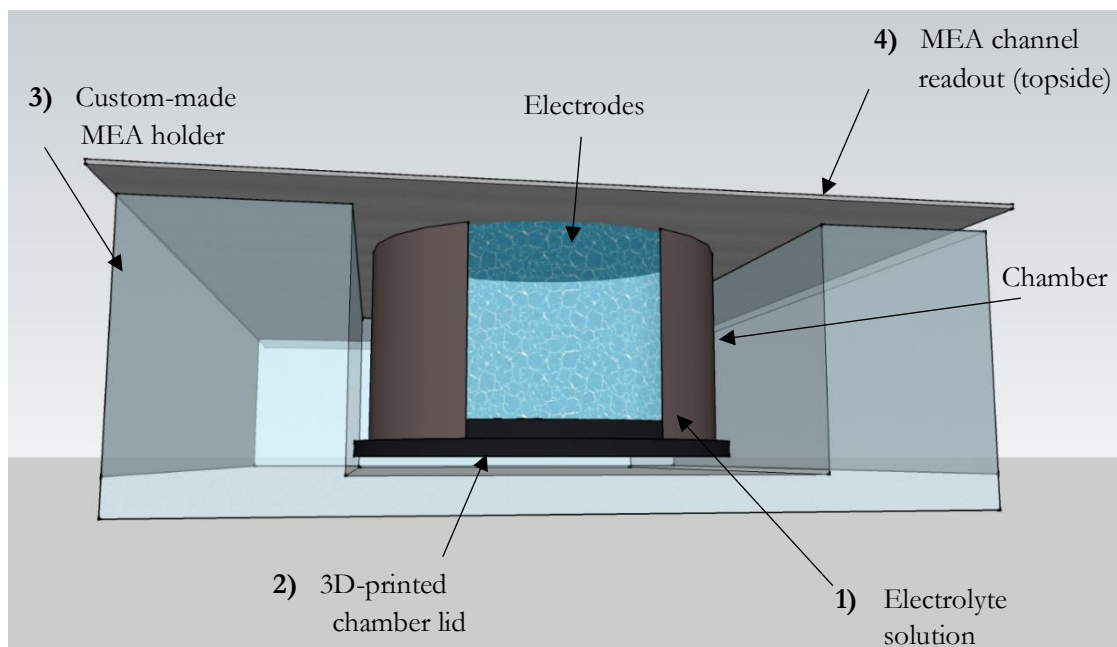


Figure 8. 1 Schematic of how the MEA is arranged to measure impedances. The recording chamber is filled with saline solution and sealed with a 3D-printed lid. The MEA is then inverted and secured in a custom-made holder. Recording probes are then applied to exposed read out

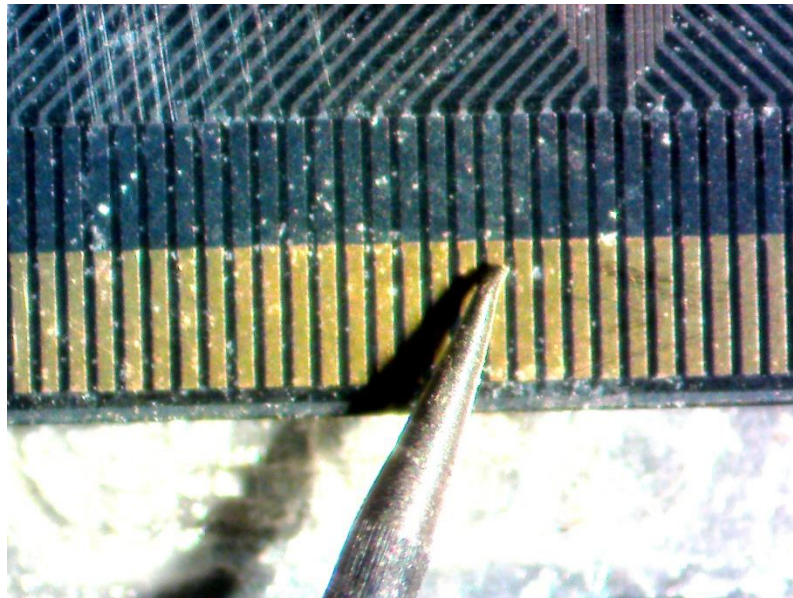


Image 8. 1. Photograph of a probe applied to electrode readout on the MEA substrate in order to measure the electrical characterisations of electrodes

Appendix 3. Block Diagram of a single PLAT-64 channel

The data acquisition system was originally developed to image the electrophysiological activity or retinal ganglion cells¹²², however, their design is applicable to studies of cortical neurons.

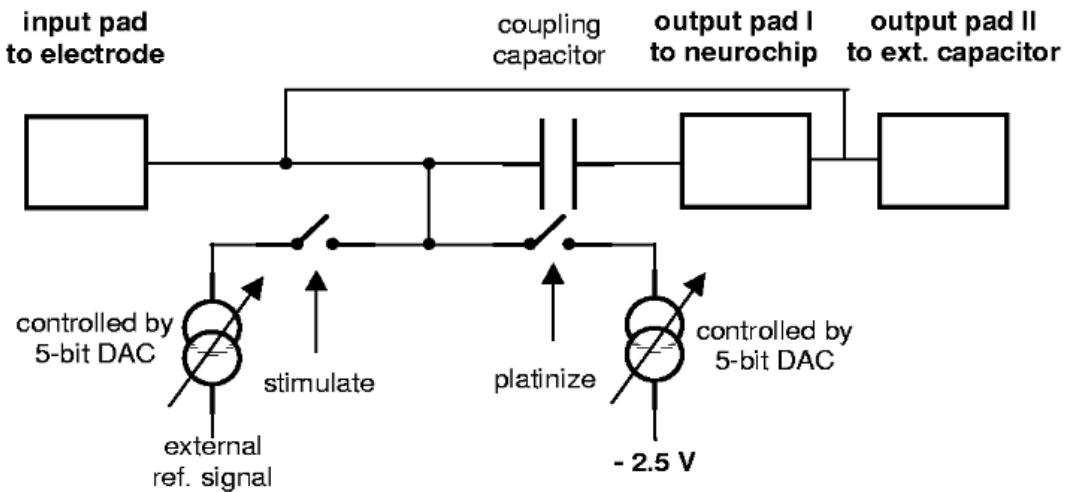


Figure 8. 2. Schematic taken from Dabrowski et al.(2003)¹²² describing the design of electrode readouts to PLAT-64 ASIC. In this case, a stimulation option is available which was not included in the work presented here.

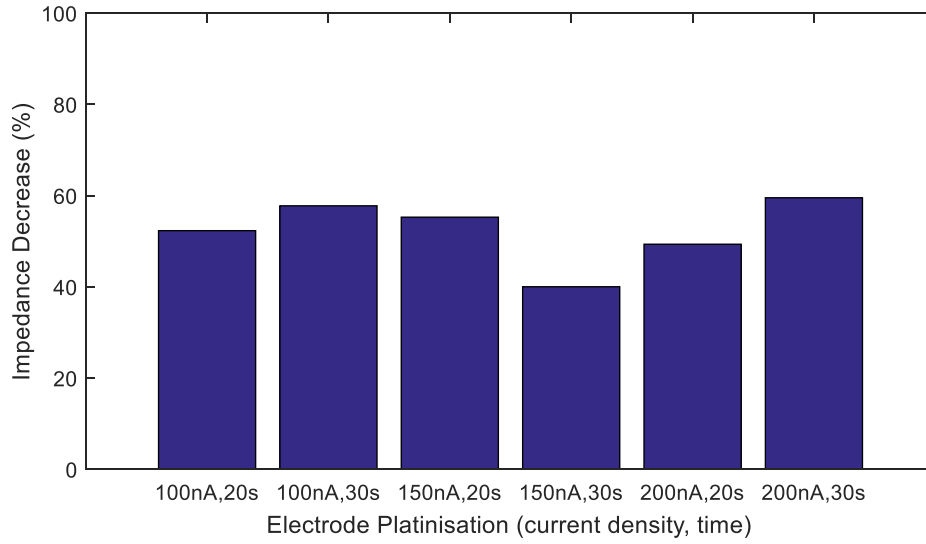
Appendix 4. Percentage Impedance Decrease following Platinisation

Figure 8. 3 Briefly electroplating with a current of 100nA for 20 seconds sufficiently reduced impedances to appropriate values of 150-300 k Ω and was found to consistently reduce impedances by ~50%.

Appendix 5. Outlier Spike Amplitudes

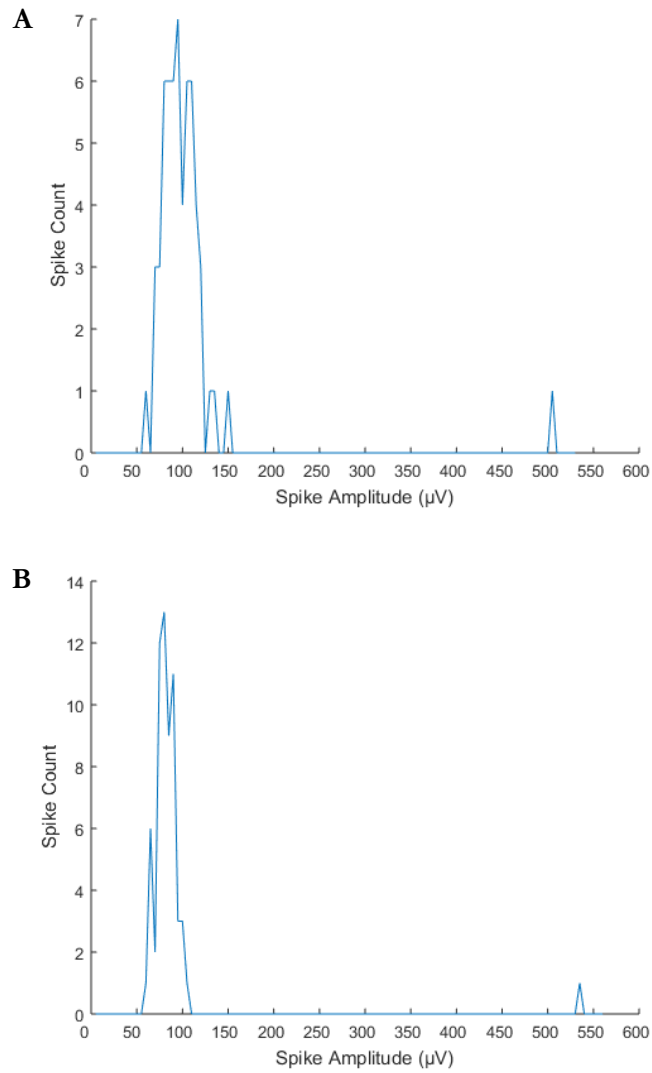


Figure 8. 4. Neurons #4 (A) and #29 (B) exhibited large differences in average spike amplitude deviation between periods 0-2hours and 2-4hours. In both cases this was the the result of single outlier spikes skewing the deviation.

Appendix 6. Calculation of Neuron Average RMP

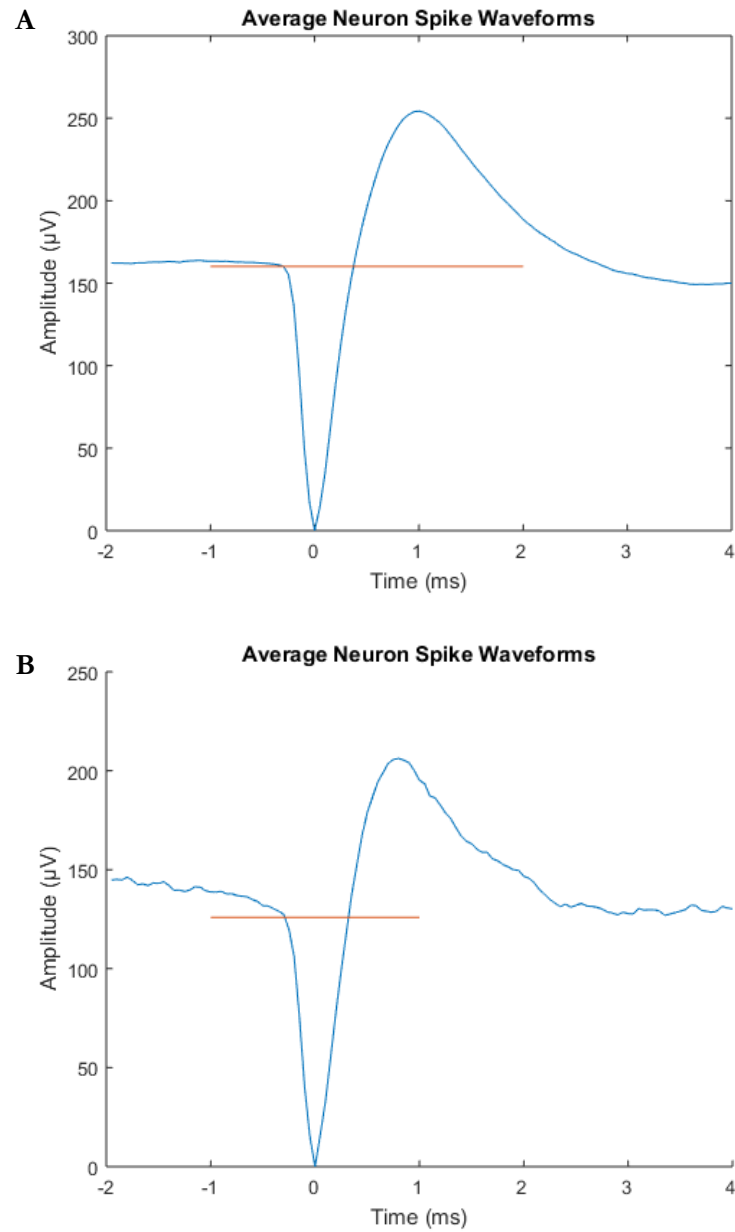


Figure 8. 5. (A) Resting membrane potential was defined by the 1.5 ms of averaged waveform amplitudes from 2 ms to 0.5 ms prior to the averaged minimum amplitude (depolarisation peak). Four sigma below the averaged 1.5 ms of amplitudes (30 samples) was chosen as an appropriate RMP (orange line) to account for variable gradients observed in some neuron wavefor ms(B).

Appendix 7. Five Neurons Possessed Long Average Peak Widths

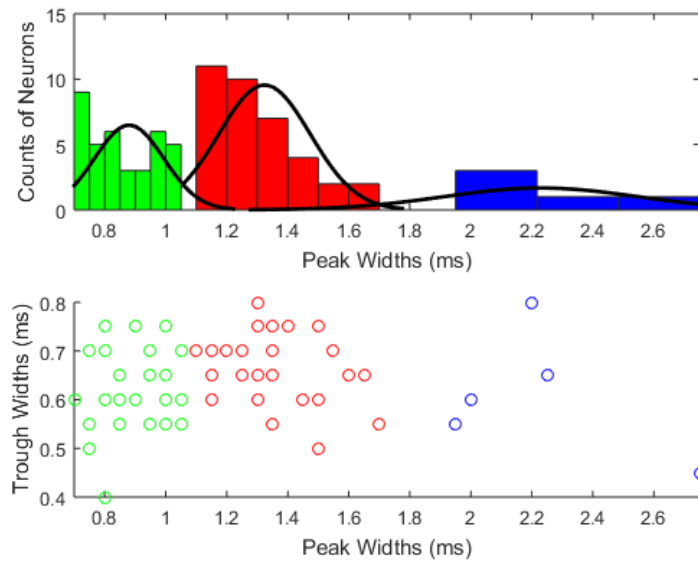


Figure 8. 6. Five neurons possessed long average peak widths (C, cluster 3), but were not convincingly separated from the bulk of the population.

Appendix 8. High Incidence of Large Value ISIs

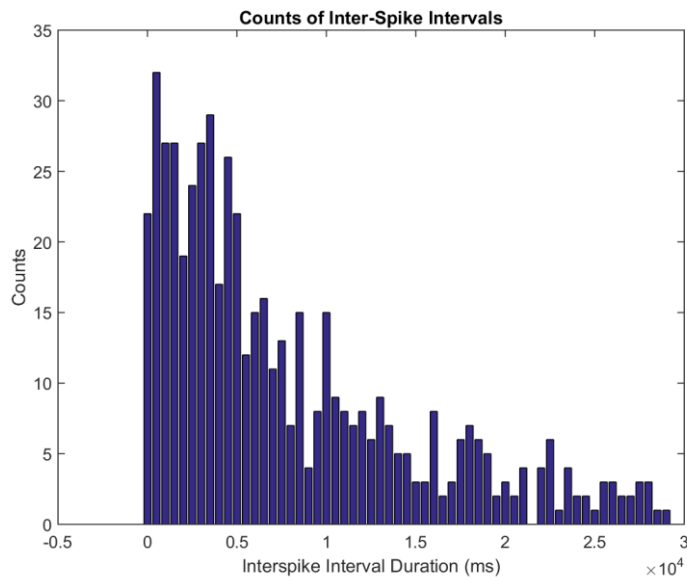


Figure 8. 7. Large inter-spike intervals are prevalent in the dataset. A histogram of ISI values from neuron #23 highlights that this property is commonly observed to exceed 10seconds (N.B. x-axis is $\times 10^4$).

Appendix 9. Neurons Demonstrating Bursting Behaviour Determined by the MISI Method of Burst Detection

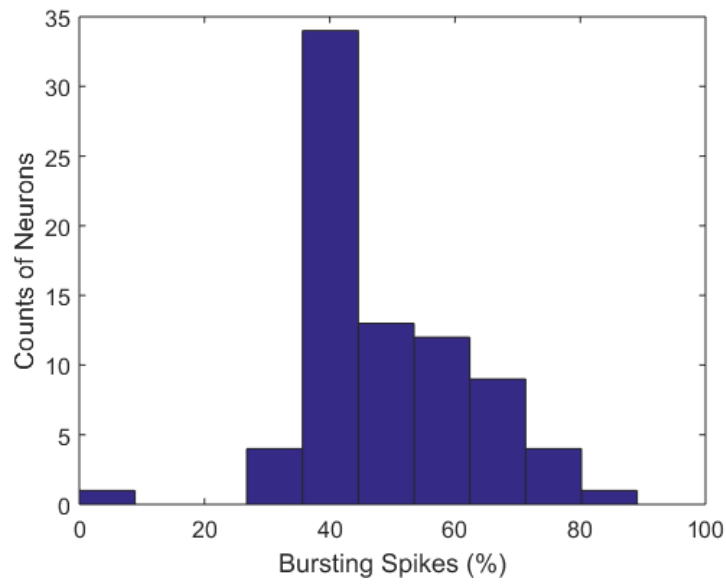


Figure 8. 8. Histogram of neurons exhibiting bursting behaviour defined as two subsequent spikes with an ISI value less than the neuron ML value.

Appendix 10. Neuron ML Values

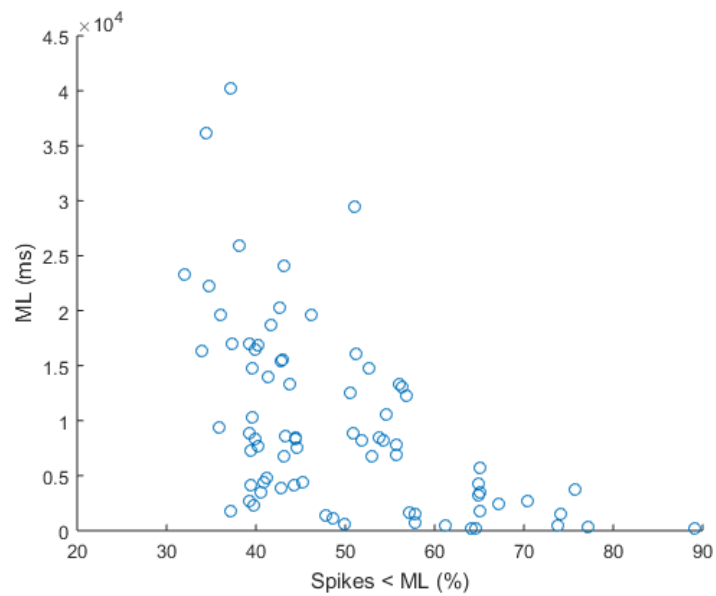


Figure 8. 9. Eight neurons exhibited an ML value less than 1second and a greater percentage of spikes identified as bursting correlated with a lower ML value

Appendix 11. Attempt at Bakkum burst detection

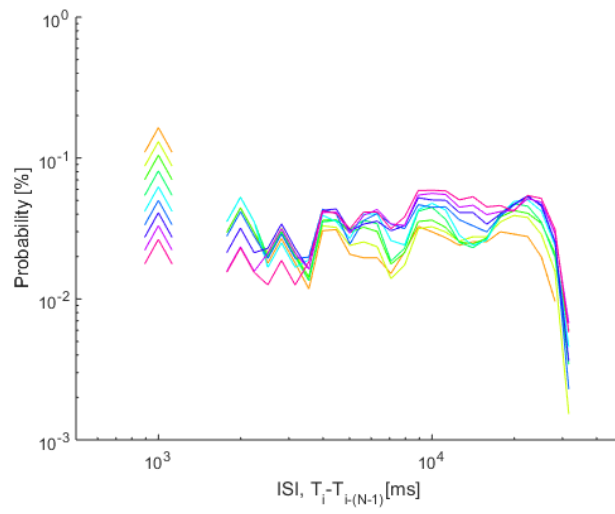


Figure 8. 10. Adapted method from ¹³³

Appendix 12. Waveform Afterdepolarisation

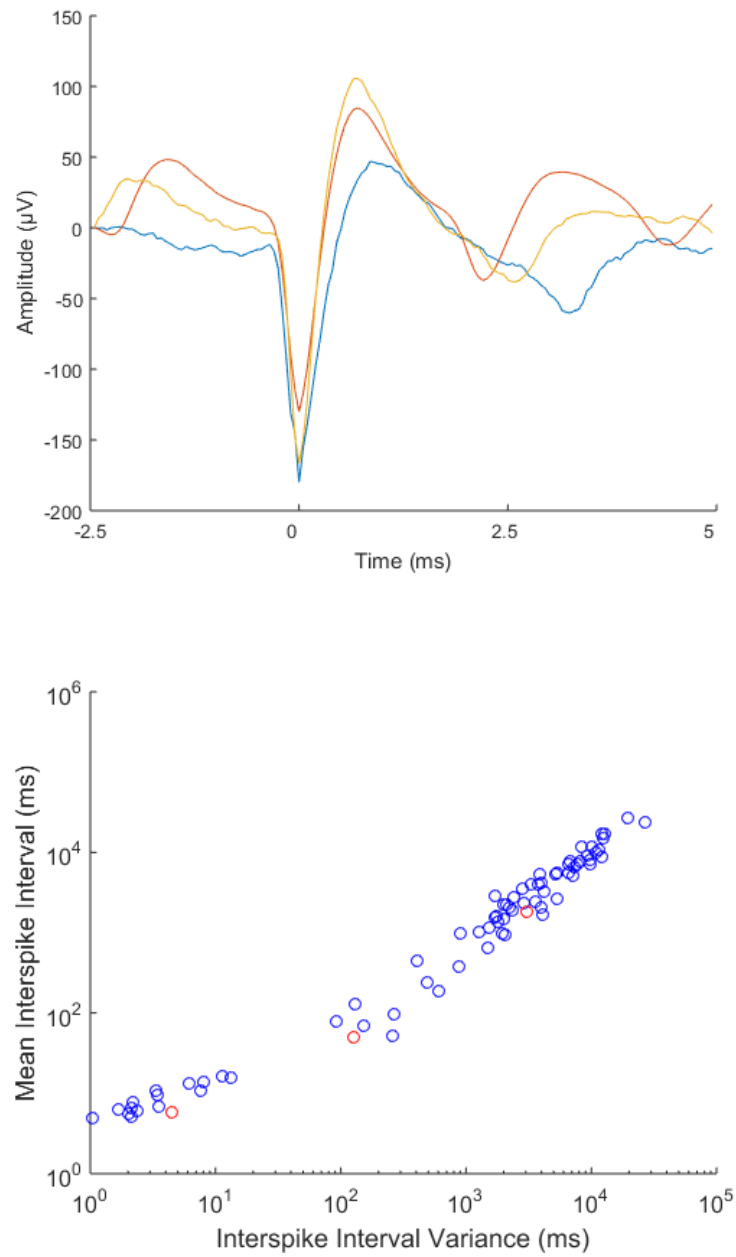


Figure 8. 11. Three neurons exhibited significant afterdepolarisation (A) and this feature has been associated with pyramidal neurons. However, these neurons did not share any other temporal or waveform characteristics and were not segregated as a discrete population

Appendix 13. Connectivity Analysis

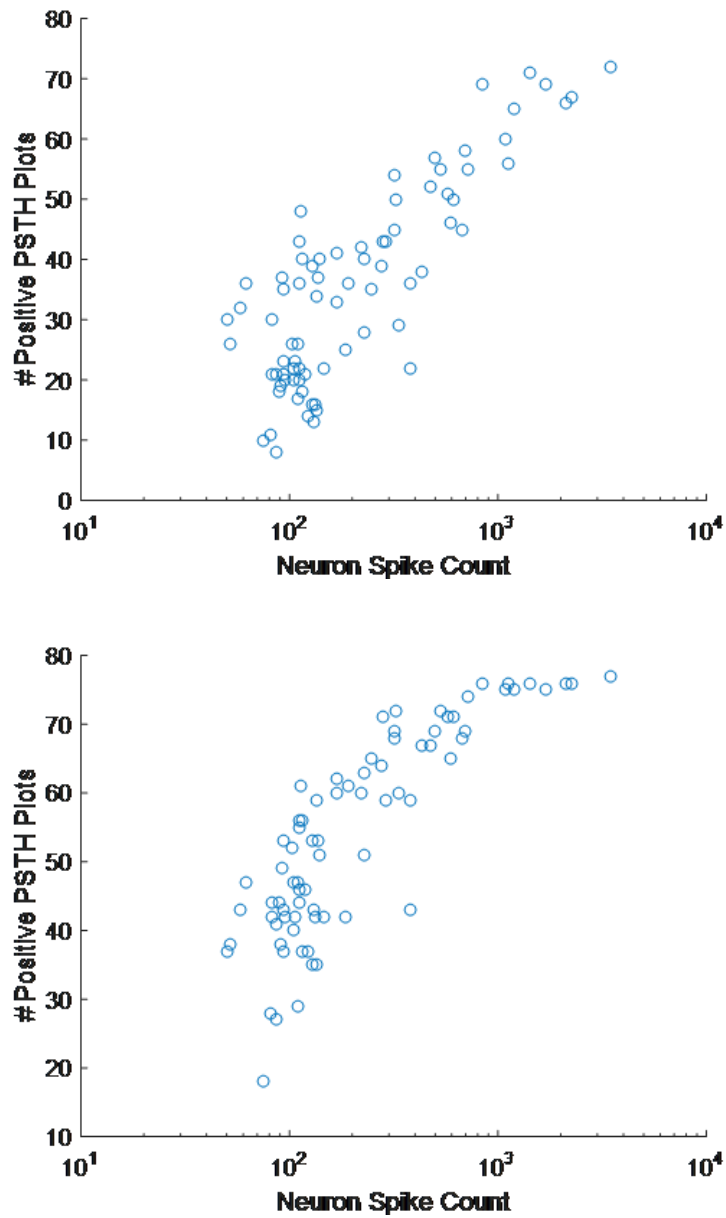


Figure 8. 12. No change in trend was observed when analysis was based on the number of combinations with a neuron's spike as the stimulus (columns in Fig. 6.2).

Appendix 14. Prolonged PFA Fixation Increased PI Background Fluorescence

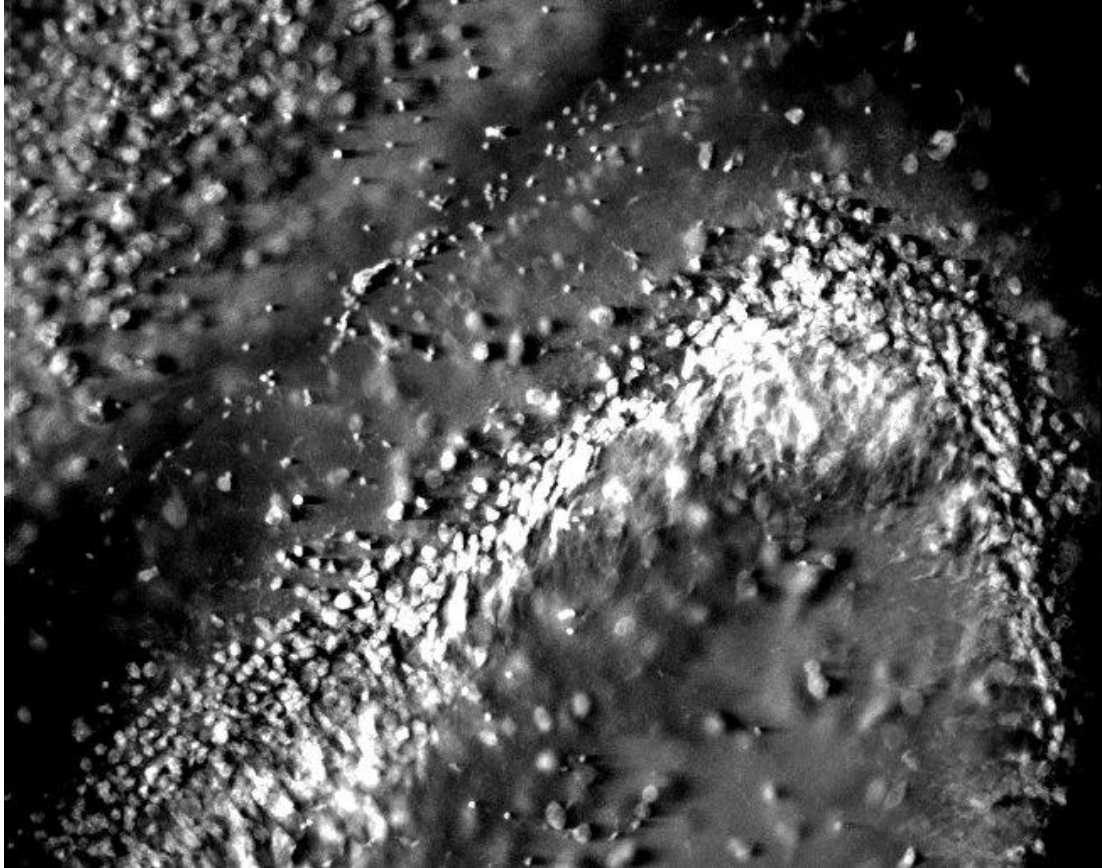


Figure 8. 13. Fixing brain sections for 3 hours in PFA resulted in high background fluorescence despite the high cellular resolution on the superficial focal plane of sections.

Appendix 15. 3-Dimensional Imaging of Tissue Punctures

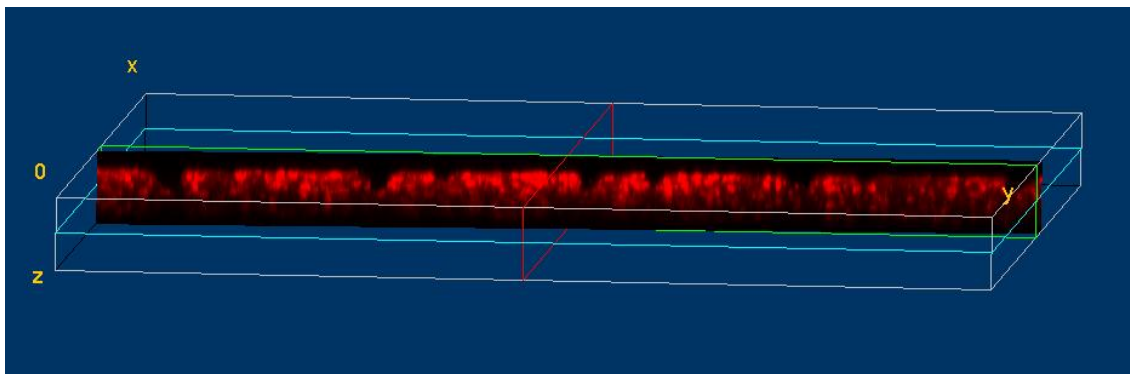


Figure 8. 14 Visualisation of silicon needle punctures in tissue sections. Confocal microscopy enabled images to be acquired in the z plane and a 3-dimensional image generated. Total depth imaged was 205um but fluorescence signal was only present for 135um. Indentations at the top surface of the generated image indicate needle penetration into tissue.